# Source Sector Analysis of Marine and Other Volatile Organic Compounds on Sable Island, Nova Scotia, Canada

by

Loay Jabre

Submitted in partial fulfilment of the requirements

for the degree of Master of Applied Science

at

Dalhousie University

Halifax, Nova Scotia

August 2017

# TABLE OF CONTENTS

# LIST OF TABLES

# LIST OF FIGURES

# ABSTRACT

Phytoplankton produce approximately 40% of the world's oxygen and play a critical role in regulating global climate by the drawdown of atmospheric carbon dioxide and, as suggested by increasing evidence, through the emission of climate-relevant volatile organic compounds (VOCs). Currently, there is a gap in knowledge surrounding long-term emissions of phytoplankton related VOCs under field conditions. In a first of its kind, this study combined continuous measurements of total and specific VOCs on Sable Island throughout 2016 with the Hybrid Single-Particle Lagrangian Integrated Trajectory model, meteorological and remote sensing data to allocate measured compounds into three different upwind source sectors. 48% of VOCs were found to originate from marine phytoplankton emissions, 40% from terrestrial biogenic sources and 11% from anthropogenic activity. These results challenge current methods and assumptions of *in situ* measurements and shed light on the likelihood of various other sources interfering with remote marine VOC measurements.

# LIST OF ABBREVIATIONS USED

| | |
|---|---|
| AFRG | Atmospheric Forensics Research Group |
| amu | Atomic mass unit |
| CCN | Cloud Condensation Nuclei |
| Chl-*a* | Chlorophyll *a* |
| CLAW | Charlson-Lovelock-Andreae-Warren |
| CO | Carbon monoxide |
| $CO_2$ | Carbon dioxide |
| df | Dry Film -thickness- |
| DMS | Dimethyl sulfide |
| DMSP | Dimethylsulfoniopropionate |
| DNA | Deoxyribonucleic acid |
| ECD | Electron Capture Detector |
| EI | Electron Ionization |
| FID | Flame Ionization Detector |
| GC-MS | Gas Chromatography-Mass Spectrometry |
| GLV | Green Leaf Volatile |
| HYSPLIT | Hybrid Single Particle Lagrangian Integrated Trajectory |
| i.d. | Internal Diameter |
| MODIS | Moderate Resolution Imaging Spectroradiometer |
| MS | Mass Spectrometer |
| m/*z* | Mass/Charge ratio |
| NAAMES | North Atlantic Aerosols and Marine Ecosystem Study |

| | |
|---|---|
| NASA | National Aeronautics and Space Administration |
| NIST | National Institute of Standards and Technology |
| ng | Nano gram ($10^{-9}$g) |
| $NO_3$ | Nitrate |
| NOAA | National Oceanic and Atmospheric Administration |
| $O_3$ | Ozone |
| o.d. | Outside Diameter |
| OH | Hydroxyl radical |
| Pg | Peta gram ($10^{15}$ g) |
| pg | Pico gram ($10^{-12}$ g) |
| PID | Photo Ionization Detector |
| $SO_2$ | Sulfur dioxide |
| SPME | Solid Phase Micro-extraction |
| SSA | Source Sector Analysis |
| SVI | Soil Vapor Intrusion |
| TD | Thermal Desorption |
| TDT | Thermal Desorption Tube |
| Tg | Tera gram ($10^{12}$ g) |
| μg | Micro gram ($10^{-6}$ g) |
| μL | Micro liter ($10^{-6}$ L) |
| UV | Ultra Violet |
| VOC | Volatile Organic Compound(s) |
| WAS | Whole Air Sample |

# ACKNOWLEDGEMENTS

I am indebted to many people and organizations for the completion of this thesis. First and foremost, I am grateful to my supervisors Dr. Mark Gibson and Dr. Susanne Craig for granting me the opportunity to work on this project, their guidance and insightful advice. I am also tremendously thankful to the present and past members of the Atmospheric Forensics Research Group who worked tirelessly on all aspects of this study to ensure its success. Special thanks also goes to Thermo Fisher Scientific for providing and maintaining the Trace 1300-ISQ GC-MS, the Nova Scotia Graduate Scholarship committee, Environmental Studies Research Funds and Natural Resources Canada for student and project funding, and Maritime Air Charter for providing transport to Sable Island. Last but not least, I want to thank my friends and family for all their -well needed- moral support.

# CHAPTER 1 INTRODUCTION

Approximately 2.3 billion years ago, planet Earth experienced an event that shifted its journey through the universe forever. The successful evolution of the first photosynthetic microorganisms, the cyanobacteria, created The Great Oxygenation Event, and within a relatively short period of time, the previously anaerobic planet transitioned to having an atmosphere composed of 35% oxygen. This caused a huge imbalance in the already functioning anaerobic systems; it reshaped the atmosphere by forming ozone, and initiated one of the most significant mass extinction events our planet has witnessed (Shields-Zhou and Och, 2011). Fast forward to today, Earth has stabilized at a 21% atmospheric oxygen composition with an ozone layer protecting the planet from harmful UV-radiation and allowing the DNA-containing biota to flourish. The ancient photosynthetic microorganisms have evolved into hundreds of species of phytoplankton inhabiting virtually every aquatic region of the globe and producing approximately half of the free oxygen that supports life (Falkowski et al., 2004). The sheer enormity of phytoplankton presence on Earth also makes them a key component of bio-geochemical cycles, the basis of aquatic food webs and an important regulator of global climate.

Other than producing oxygen, phytoplankton absorb a large portion of carbon dioxide from the atmosphere and release key gases that control climate. Some of these gases, such as halomethanes, directly impact the atmosphere by reaching the stratosphere where they can catalyze the destruction of ozone (Colomb et al., 2008) while others, such as dimethyl sulfide, have indirect effects linked to the formation of clouds and scattering

of sunlight (Malin and Kirst, 1997). Nonetheless, it is not a secret that the survival of our planet's biota is dependent on the survival of phytoplankton.

Unfortunately however, anthropogenic activity is drastically changing our planet's climate, and with that, have introduced a suite of complex alterations to oceanic phytoplankton (Barton et al., 2016). In some regions, the water column has become more strongly stratified, leading to warmer, more nutrient poor conditions that favour the growth of smaller phytoplankton species (Li and Glen Harrison, 2008; Li et al., 2006). The likely effects of these shifts are two-fold: unlike small cells, large cells are more likely to sink and bury their carbon in the deep ocean for climate-relevant time scales; smaller cells are associated with longer, less efficient food webs that may ultimately affect the success of higher trophic levels such as fisheries species. In other regions, long-term data records show statistically significant increases in phytoplankton primary productivity (Mackas, 2011) thought to be related to increased phytoplankton metabolic rates with increasing temperature (Rasconi et al., 2017; Sánchez et al., 2008).

These multi-facetted alterations can be studied from several angles, one of which is to measure marine emissions of volatile organic compounds (VOCs) to help understand the relationship between phytoplankton and the atmosphere. Many of these VOCs are produced by phytoplankton as a result of physical or biological stress, such as the changing conditions of the world's oceans (Loreto and Velikova, 2001). However, the majority of studies inspecting these compounds are performed under laboratory controlled environments, which have been shown to poorly reflect conditions in the wild (Sabolis, 2010; Sinha et al., 2006). Field studies, even though having their own

complexities and challenges, are therefore crucial for our understanding of phytoplankton produced VOCs.

Evidence of anthropogenic pollution and long range transport of terrestrial compounds have been detected even in the most remote regions of the world (Monks et al., 2009; Moore, 2000). This introduces errors in the measurements of marine produced VOCs as samples may contain several sources of compounds. As a result, and in collaboration with a 5-year National Aeronautics and Space Administration (NASA) project entitled the North Atlantic Aerosols and Marine Ecosystems Study (NAAMES, https://naames.larc.nasa.gov/), this research project aimed to achieve two main objectives; to quantify temporal variations in marine biogenic emissions in the field, and to recognize other (non-marine) contributing sources of VOCs on Sable Island.

Photoionization detection was used for continuous real-time measurements of total VOCs. Thermal desorption tube sampling with gas chromatography-mass spectrometry was used to identify VOC species, and the National Oceanic Atmospheric Association (NOAA) Hybrid Single-Particle Lagrangian Integrated Trajectory (HYSPLIT) model was utilized to reproduce twice-daily air mass back trajectories on Sable Island. Additionally, remote sensing data of chlorophyll-*a* concentrations were used to support and contextualize on-island measurements. Despite all the complications associated with remote-region research, this study confirmed important temporal trends in marine VOC emissions and the likelihood of multiple, non-marine sources being associated with remote marine measurements of VOCs.

# CHATPER 2 LITERATURE REVIEW

In 1987, Nature published one of the most controversial journal entries of this century. In this publication, Charlson et al. (1987) describe their 'CLAW' hypothesis, in which they proposed a negative-feedback-loop mechanism where phytoplankton play a role in regulating Earth's climate through the production of dimethyl sulfide (DMS). Their argument stated that with increased solar irradiance (and therefore temperature), an increased amount of DMS is released by phytoplankton into the atmosphere. DMS would then undergo a series of chemical reactions that would result in increased cloud formation, which would cool down the Earth via the albedo effect. Additionally, according to the hypothesis, the opposite is true with decreased irradiance (Charlson et al., 1987). This instigated a great number of studies and publications from various scientific branches to inspect these mechanisms. However, with mounting evidence against the CLAW hypothesis (Quinn and Bates, 2011; Woodhouse et al., 2010), we are left with large uncertainties surrounding the effects of phytoplankton on the atmosphere and how a changing climate may affect phytoplankton dynamics.

## 2.1 Ocean-Atmosphere Interactions

Oceans cover 71% of the Earth's surface and therefore play a key role in shaping our climate by having significant biotic and abiotic influences on biogeochemical cycling (Bigg, 2005). For example, more than a quarter of all anthropogenic $CO_2$ produced in the last decade was absorbed by the oceans, adding up to 2.5 Pg annually (Le Quere et al., 2012).

The interactions between oceans and other regions of the lower troposphere are multi-dimensional (absorption and/or reflection of radiation, release of climate relevant substances etc.) and can be viewed in terms of exchanges in energy (heat and light), humidity and a multitude of organic and inorganic compounds and particles. Even though each of these interactions is significant in its own way, this thesis will focus mainly on the uni-directional flow of VOCs from the ocean to the atmosphere.

### 2.1.1 Ocean Surface-Atmosphere Interaction

In order to understand the atmospheric chemistry of marine emissions, it is beneficial to understand the mechanisms through which compounds are released from ocean surfaces to the atmosphere. This happens via two main processes; the bursting of surface bubbles and surface evaporation.

The formation of surface bubbles has long been studied and recognized for its importance in the release of salts and other aerosols, also known as sea-spray. The breaking of the bubble film that forms on the surface also carries with it the release of compounds present in the upper layer of water at the time of breaking (biogenic VOCs, inorganic salts, oxygen etc.) (Cochran et al., 2017). Bubbles are formed when wind interacts with surface water, creating waves which break into visible “white caps”. Less visible, sub-millimeter bubbles are also formed as a result of precipitation (rain and snow) hitting and disturbing the ocean surface (Blanchard and Woodcock, 1957; Zhao et al., 2003). In another study inspecting the release of dimethyl sulfide (DMS), it was noted that the transfer velocity of DMS from the water to the atmosphere was larger at higher winds speeds and greater amount of wave breaking (Turner et al., 1996). The formation of surface bubbles and subsequent release of aerosols was also shown to increase in

supersaturated, hyperoxic (130% air saturation) seawater (e.g. during periods of phytoplankton blooms) irrespective of wind speed (Stramska et al., 1991). Temperature also plays an important role in bubble formation and compound release. More surface bubbles were formed at 23.5°C than at 12.9°C (Woolf et al., 1987) with Turner et al. also observing a decreased rate of DMS release at lower temperatures (Turner et al., 1996).

These effects are governed by the ideal gas law ($PV=nRT$) and Boyl's law ($P_1V_1 = P_2V_2$), which state that an increase in temperature causes and increase in partial pressure of dissolved gases. This reduces their solubility and ultimately results in increased flux of gases from seawater to the atmosphere.

Regardless of bubble formation, an increase in kinetic energy due to an increase in temperature would facilitate the release of VOCs and other gases from surface waters (Wiebe and Gaddy, 1940). There is a gap in the literature in regards to specifically describing mechanisms in which biogenic VOCs are released from the oceans through evaporation. However, many of these VOCs have low boiling points, for example, chloromethane boils at -24.2°C and would evaporate readily even in the middle of winter in the northern Atlantic (Hilal et al., 2003) . With that said, other conditions such as water salinity and the chemical/physical properties of specific compounds should also be taken into consideration when studying ocean-atmosphere interactions.

## 2.2 Phytoplankton – Biology and Ecology

It is not possible to have a good understanding of biogeochemical cycles and ocean-atmosphere interactions without considering the role played by phytoplankton; a group of hundreds of different taxa and species of photosynthetic and -generally-

immotile marine algae (WHOI, 2017). Due to their dependence on sunlight, phytoplankton inhabit the upper layers of the oceans where they drift and form seasonal 'blooms' during which they rapidly reproduce in response to suitable temperatures, sufficient solar irradiance, and adequate nutrient availability (von Dassow and Montresor, 2011).

These primary producers are at the center of all marine food webs and ecosystems. By fixing inorganic carbon through photosynthesis, they become the source of chemical energy in the oceans, supporting small zooplankton, which are fed on by virtually every marine animal, from whales, to fish and shellfish (Christaki et al., 2014; Danielsdottir et al., 2007). Carbon fixation by phytoplankton is also responsible for the removal of 35% to 55% $CO_2$ from the atmosphere (Behrenfeld et al., 2005, 2006; Jardillier et al., 2010) and the production of approximately 40% of the world's oxygen (Hader and Schafer, 1994; Jenkins and Goldman, 1985). More relevant to this project, phytoplankton produce a suite of atmospherically relevant gases, such dimethyl sulfide, halomethanes and other hydrocarbons; which influence air chemistry and cloud formation (Monks et al., 2009). These are discussed in more detail in Section 2.3.

### 2.2.1 Phytoplankton in the North Atlantic / Scotian Shelf

Phytoplankton inhabit virtually all marine and aquatic regions in the world. However, the northern Atlantic / Scotian Shelf play host to one of the largest phytoplankton blooming events on Earth due to nutrient richness and ideal water temperatures (Fournier et al., 1977; Siegel et al., 2002). This has caught the attention of researchers for decades (Riley, 1957), providing a wealth of knowledge about

oceanography, biogeochemistry, phytoplankton ecology as well as prompting new and novel methods for phytoplankton research (Craig et al., 2012; Soja-Woźniak et al., 2017).

*In situ* measurements in the northern Atlantic show distinct seasonal/temporal patterns in phytoplankton blooms. A spring bloom composed mainly of diatoms was observed, followed by an assemblage of pico- and nanophytoplankton around May-August, and a bloom of dinoflagellates in September (Craig et al., 2015; Riley, 1957; Ross et al., 2017). Additionally, a smaller autumnal bloom is often observed and occurs as a result of increased wind-driven mixing that entrains nutrient rich deeper water into the upper sunlit water column (Craig et al., 2015). These blooms correspond to periods of high nutrient availability in the area due to deep ocean mixing and advection (Fournier et al., 1977; Strain and Yeats, 2005), increasing light availability (Friedland et al., 2016) and seasonal conditions conducive to the growth of certain algal classes (Craig et al. 2015). Having previous knowledge of phytoplankton blooming patters is extremely useful in designing and timing experiments concerned with marine emissions because it allows researchers to setup instrumentation and adjust models accordingly.

### 2.3 Phytoplankton-Related Volatile Organic Compounds (VOCs)

Volatile organic compounds (VOCs) are carbon-based molecules with a low boiling point and therefore evaporate readily at relatively low temperatures (Liu et al., 2008). Tens of thousands of VOC species have been identified and are mainly produced by anthropogenic (factories, oil rigs, cement manufacturing etc.) and biogenic (terrestrial and marine organisms etc.) sources (ECCC, 2013). Phytoplankton are responsible for the production of the majority of marine-emitted VOCs and more than one third of total global VOC emissions (Palmer and Shaw, 2005; Paul and Pohnert, 2011; Sinha et al.,

2006). This is significant as many of the VOCs they produce have strong impacts on climate and atmospheric conditions.

In a similar way to terrestrial plants (Holopainen and Gershenzon, 2010), phytoplankton produce and release VOCs in response to physical (oxidative, thermal, photolytic etc.) and biological (defence against predators, inter/intraspecific competition) stress (Ekdahl et al., 1998), as well as an indirect by-product of intracellular metabolism (Loreto and Velikova, 2001; Moore and Tokarczyk, 1993; Moore et al., 1994; Palmer and Shaw, 2005). Nonetheless, marine emitted biogenic VOCs can be divided into two main categories, halogenated hydrocarbons, such as halomethanes and longer-chained halocarbons, and non-halogenated hydrocarbons, such as monoterpenes and the widely known dimethyl sulfide (Colomb et al., 2008; Liu et al., 2008).

### 2.3.1 Halocarbons

Halogenated hydrocarbons or halocarbons are organic compounds containing one or more halogen atoms such as chlorine, bromine, or iodine within their structures (Liu et al., 2008). These compounds have several environmental and climate changing effects (Monks et al., 2009; Palmer et al., 2013). Stable marine halocarbons with a relatively long life time, such as chloromethane and bromomethane (life time ~ 1-3 years) (Lof et al., 2000) can travel to the stratosphere and cause ozone destruction through photolysis (Moore and Tokarczyk, 1993), and shorter-lived halocarbons such as iodomethane, can form iodine radicals that catalyze lower tropospheric ozone destruction (Colomb et al., 2008).

These two effects are fundamentally different: depletion of stratospheric ozone causes an increase in the amount of harmful UV radiation entering the biosphere (Herman et al., 1996), leading to cancers through inducing DNA replication errors, crop damage and severe 'sun burn' on humans and animals alike (Martinez-Levasseur et al., 2013; Ravanat et al., 2001; Teramura, 1983). Conversely, tropospheric ozone is a powerful air pollutant that causes respiratory problems and its reduction is seen as beneficial (Lelieveld and Dentener, 2000). With that said, increased UV radiation reaching the troposphere due to low stratospheric ozone shielding causes an increase in biospheric ozone levels in the presence of anthropogenic pollutants such as NOx and other VOCs (Gibson et al., 2009a; Pickering et al., 1992). It should also be noted that the majority of marine halocarbons are washed out of the atmosphere with precipitation; hence, stratospheric ozone destruction remains largely due to anthropogenic causes (Goodwin et al., 1997; Moore, 2000).

The chemistry and mechanisms in which specific compounds affect the atmosphere have been well studied, however, questions regarding the collective magnitude and temporal variations of their production from phytoplankton are yet to be answered.

### 2.3.2 Dimethyl sulfide (DMS)

Contrary to common knowledge, the majority of DMS ($CH_3$-S-$CH_3$) is not directly produced by phytoplankton but is a breakdown product of dimethylsulfoniopropionate (DMSP). This is a two-step process in which DMSP is released into surface water, and is then converted into DMS. Only a small fraction of DMSP is converted into DMS intracellularly with the use of the enzyme DMSP-lyase (Malin and Kirst, 1997)

Phytoplankton cells directly excrete DMSP into surface water as a means of controlling cell buoyancy; however, this mechanism is believed to be of little significance to the overall DMSP budget (Belviso et al., 1990; Reisch et al., 2011). The main mechanism in which DMSP is released into the water is via cell rupturing resulting from grazing by zooplankton, wave breaking or natural death. This allows for aerobic and anaerobic bacterial degradation and the use of bacterial DMSP-lyase to convert DMSP into DMS (Andreae and Crutzen, 1997). During periods of phytoplankton blooms, surfaces waters become supersaturated with DMS, which is then released from the water into the atmosphere through evaporation and rupturing of surface bubbles (Turner et al., 1996).

DMS released into the atmosphere is quickly (lifetime ~1 day) oxidized by OH radicals and to a small extent $NO_3$, to form sulfur dioxide ($SO_2$) and methane sulfonic acid (MSA). Oxidation by $NO_3$ is insignificant in clean and remote ocean regions making OH the main driver of oxidation. This reaction is light dependent as the production of OH depends on the photolysis of $O_3$. This has been shown by measurements that indicated increased levels of DMS on cloudy days and decreased DMS levels on sunny days (O'Dowd et al., 1997). Further oxidation of $SO_2$ forms sulfuric acid ($H_2SO_4$), which nucleates and/or deposits on sea salt aerosols to form sulfate aerosols. These aerosols scatter and reflect solar radiation, causing a cooling effect. Further deposition and nucleation of sulfuric acid forms cloud condensation nuclei (CCN), which act as initial sites for water vapor to form cloud droplets. An increase in DMS causes an increase in sulfuric acid concentrations and hence an increase in clouds/cloud optical thickness and

solar reflection (Andreae and Crutzen, 1997; Ayers et al., 1997; Buckley and Mudge, 2004; O'Dowd et al., 1997).

It has be estimated that about 30% of CCN originate from oceanic DMS (Mahajan et al., 2015), making it a substantial source of global cooling. Further evidence of the cooling negative-feedback-loop is shown in Malin and Kirst's work where the production of DMSP in phytoplankton cells is increased with increased solar irradiance and decreased with a decrease in solar irradiance (Malin and Kirst, 1997).

With that said, there is contradicting evidence to the research mentioned above. A temperature increase by 1°C can directly affect phytoplankton metabolism and has been shown to drastically reduce the number of zooplankton, which are responsible for releasing most of the DMSP into surface waters and ultimately to the atmosphere (Reisch et al., 2011). Increasing temperatures can also cause ocean stratification where deep ocean mixing is reduced, bringing with it a reduction in nutrients entrained into the upper sunlit layers and causing weaker phytoplankton blooms with less DMS emissions (Capotondi et al., 2012).

DMS may certainly have important climate forcing effects, but many questions regarding its atmospheric chemistry and production still need to be answered before the extent of its effects are fully understood.

### 2.3.3 Other Non-Halogenated Marine Hydrocarbons

Phytoplankton also produce many other non-halogenated compounds, including isoprene, limonene, *a*-pinene, and 1-hexanol (Colomb et al., 2008; Meskhidze et al., 2015; Moore and Tokarczyk, 1993; Moore et al., 1994; Palmer and Shaw, 2005). In addition to halocarbons and DMS, these compounds play important roles climate forcing.

Substantial isoprene ($C_5H_8$) production by phytoplankton cultures was first discovered in the early 1990s (Bonsang et al., 1992; Moore et al., 1994) and was later confirmed by models and some field studies to amount up to 10 Tg of the annual atmospheric isoprene budget (Meskhidze et al., 2015; Palmer and Shaw, 2005; Shaw et al., 2010; Sinha et al., 2006). These are important discoveries, because like DMS, the oxidation of isoprene forms secondary organic aerosols (SOAs) such as glycolic acid and oxalic acid, which act as CCNs and assist in cloud formation or become particulate organic matter that can induce negative radiative forcing by reflecting and scattering sunlight (Carlton et al., 2009; Lim et al., 2005).

Biogenic, marine monoterpenes ($C_{10}H_{16}$) such as limonene and *a*-pinene also undergo oxidation to form SOAs, which have the ability to further nucleate and become CCNs and have similar climate forcing effects as isoprene and DMS (Engelhart et al., 2008; Yu et al., 1999). However, it has also been shown that in the presence of isoprene, particle formation by monoterpenes is decreased, adding to the complexity of the interactions between marine emissions and the atmosphere (Kiendler-Scharr et al., 2009). Similarly, phytoplankton-produced alcohols and aldehydes including hexanol and hexanal form their own SOAs, but may cause inhibition of SOA formation when mixed with terpenes (Liyana-Arachchi et al., 2014; Waza, 2014).

### 2.4 Non-Marine VOCs

When trying to distinguish marine VOCs from others, it is important to be aware of the different sources of VOCs and the overlap in emissions of similar VOC species by more than one source. This study examined terrestrial and anthropogenic sources that may influence marine VOC measurements and analysis.

### 2.4.1 Natural Terrestrial Sources

Terrestrial VOCs from natural sources such as vegetation and forest fires can travel long distances through the atmosphere and interfere with marine VOC measurements. Mainland Nova Scotia is the closest major source of terrestrial biogenic VOCs to Sable Island, with other possible sources such Maine and close maritime / northern Atlantic regions. These areas are rich in coniferous vegetation including numerous species of spruce, pine and hemlock, as well as many species of deciduous trees like birch, oak and maple. Several studies have identified the VOC species produced by these forests/trees and were found to be heavily composed of monoterpenes such as camphene, *p*-cymene, *a*-pinene and limonene (Holopainen, 2004; Holopainen and Gershenzon, 2010; Spanke et al., 2001; Trabue et al., 2008). Isoprene was also found to be a key VOC produced by virtually all terrestrial plants, contributing to more than one third of all biogenic hydrocarbon emissions on Earth (Kiendler-Scharr et al., 2009; Loreto and Velikova, 2001).

Green leaf volatiles (GLV) including as 1-hexanol, hexane and *Z*-3-hexenyl acetate are also widely emitted by plants in the north Atlantic region (Copolovici et al., 2012; Jactel et al., 1996). These are produced as a defense mechanism when a plant is subjected to mechanical stress, such as grazing by animals or insects (Scala et al., 2013), a common occurrence on Sable Island by the feral horses and the leaf beetle *Trichlochmaea sablensis*. This, combined with their short atmospheric lifetime, makes on-island emissions from local grasses and foliage the most likely source of terrestrial GLVs measured on Sable Island. Additionally, it should be noted that there are no known terrestrial biogenic sources of halocarbons.

Forest fires are another major source of natural terrestrial VOCs. Every year since 1990, 2.5 million hectares of land are consumed by wild fires in Canada (NRC, 2017). These fires are a significant source of $CO_2$, CO, methane, ethane, ethene, propene, hydrogen cyanide, benzene and naphthalene -to name a few compounds (Simpson et al., 2011). Wild fire plumes can travel over long distances and cause spikes in measurements thousands of kilometers away. For example, emissions from boreal forest fires and fires in western Canada have been shown to reach Atlantic Canada and Europe (Forster et al., 2001; Gibson et al., 2015; Palmer et al., 2013).

### 2.4.2 Anthropogenic Sources

Anthropogenic VOCs can act as greenhouse gases with negative impacts on human health and the environment. A report by Environment and Climate Change Canada showed a 50% nationwide reduction in anthropogenic VOC emissions since 1990 (ECCC, 2016), however, anthropogenic sources still dominate urban regions and contribute to approximately one quarter of global VOC emissions (Borbon et al., 2013).

In Canada, the majority of anthropogenic VOCs are released from the oil and gas industry, followed by paints and solvents. This is especially relevant because Sable Island is surrounded by six major offshore oil and gas drilling platforms (Waugh et al., 2010). VOC measurements on petroleum wells show the emissions of a variety of compounds including toluene, benzene, alkanes, CFCs and a variety of other aromatic hydrocarbons such as cumene (Harrison et al., 1975; Warneke et al., 2014). Fossil fuel combustion also contributes to the release of many VOC species including naphthalene, benzene, xylene, styrene and several chlorinated hydrocarbons such as tetrachloromethane, 1,4- and 1,2-dichlorobenzene (Elbir et al., 2007; Monks et al., 2009; Walker et al., 2000). With that

said, long range transport from industrialized regions of Canada and the United States can have sizeable impacts on VOC measurements on Sable Island.

## 2.5 VOC Detection

Generally, a two-step process is applied to detect VOCs; collection and subsequent measurement. Some instruments combine these two steps into real-time/near-real time measurements, where collection and detection are completed in one continuous step.

### 2.5.1 Collection Methods

Solid-phase micro extraction (SPME): Developed in the early 1990s, this technique involves the use of a thin fibre that can be coated with a variety of different sorbents. A range of VOCs are attracted to specific sorbents and adhere to the fibre as a result (Arthur and Pawliszyn, 1990). Even though SPME is a quick and easy method to use, the fibres are often very fragile and unsuitable for long term storage (Nardi, 2003). An individual would also have to manually 'expose' each fibre for every collection period, as there are no portable automated SPME samplers on the market. This made the use of SPME incompatible with long term measurements and the harsh transport conditions of samples to/from Sable Island.

Whole air sample (WAS) canisters: As the name suggests, these are containers which are used to store a volume of air for later analysis. Unlike SPME, WAS canisters are rugged and non-selectively collect VOCs present in the sampled air (Schmidbauer and Oehme, 1988). They have been used extensively for industrial hygiene monitoring, indoor and outdoor pollution studies as well as measurements of biogenic VOCs

(Holopainen and Gershenzon, 2010; Wheeler et al., 2011). However, canisters are bulky in size and the sample inside is prone to relatively quick degradation. This, combined with the large size of their auto sampler equipment made them unsuitable for use in this study.

Thermal desorption tubes (TDTs): These stainless steel cylinders contain a variety of sorbent powders and molecular sieves which adsorb VOCs as air actively or passively travels through the tube. TDTs are compact, reusable up to 300 times and can be stored with marginal sample loss for up to 3 years under proper conditions. They are commonly used in environmental monitoring programs as well as biogenic VOC sampling (Asamany et al., 2017; Dohoo et al., 2015; Batterman et al., 2002; Tholl et al., 2006; USEPA, 1999), making them an ideal collection tool for VOCs on Sable Island. It should also be noted that to my knowledge, there have been no previous publications on the use of TDTs to sample marine biogenic VOCs in the wild, making this study a first in its field.

### 2.5.2 Detection Methods

Gas-chromatography (GC) coupled with various detectors are widely utilized in analytical chemistry for VOC measurements. GC is used to separate complex mixtures into precise narrow bands of individual compounds that are injected into a detector. Many types of detectors are used for different applications, for example, an electron capture detector (ECD) is typically used for measuring halocarbons at extremely small concentrations, which would be ideal for many of the marine biogenic VOCs. However, its detection limit drops significantly when analyzing other non-halogenated VOCs (Maggs et al., 1971). Flame ionization detectors (FIDs) are also widely used for VOC

quantification, and are relatively inexpensive, robust and require low maintenance. However, they lack the ability to identify VOCs and have relatively high detection limits, making them less than ideal for the exploratory research performed in this study (Liu et al., 2005). Mass spectrometers (MS) are another type of detectors frequently used for VOC measurements. Even though they are relatively costly and challenging to maintain and operate, they provide suitably low detection limits and can be used to quantify and identify compounds. Through the use of electron ionization or chemical ionization, MS detectors can measure the mass/charge ratio (m/*z*) of fragmented ions and 'reconstruct' an identification of the original VOC in question. This is very useful when measuring unknown VOCs, and can later be supplemented with certified standards for proper quantification and a better identification match (Asamany et al., 2017; Batterman et al., 2002; Dohoo et al., 2015; van Drooge et al., 2009). GC-MS was therefore the most suitable instrument to use for identification and quantification of marine biogenic VOCs in this study.

### 2.5.3 Real-Time Detection

The collection and storage step involved in VOC detection can be omitted through the use of real-time/near-real time detection. The principle behind this is that VOCs are measured frequently and constantly in the field (or experimental setup), providing a continuous record of temporal fluxes. GC-MS coupled with direct air intake (i.e. air server-Unity 2-TD-GC-MS) would be the most ideal option to use in this study, providing near-real time identification and quantification of VOCs. However, due to its high power consumption and need for frequent maintenance, it was unmanageable to install such an instrument in a remote location such as the Sable Island supersite. Smaller

FID instruments like the Thermo 55i have been previously used on Sable Island for total VOC detection but were found to have unsuitably high detection limits for trace gases (Hayes, 2014). A photo ionization detector (PID), the ppbRAE 3000, replaced the Thermo 55i as a result. The ppbRAE has a low detection limit with a wide dynamic range of detection (1ppb-10,000ppm), is lightweight and requires low maintenance. PIDs are most commonly used for industrial exposure, indoor and ambient air quality measurements and have been utilized for biogenic VOC measurements in the field (He et al., 2005; Karlik et al., 2002; Su et al., 2007).

## 2.6 Source Sector Analysis (SSA)

Fluxes in VOCs on Sable Island may be attributed to several sources: biogenic marine, natural terrestrial sources from the island itself or the mainland, anthropogenic sources from nearby oil and gas rigs and long range transport of pollutants. With the combination of meteorological data and models, remote sensing, VOC measurements and atmospheric chemistry/biological knowledge, it is possible to deduce the likely sources of these VOCs and the fraction contributed by each source.

### 2.6.1 Air Mass Back Trajectories

As the name suggests, these models are used to compute the path an air parcel takes before arriving at a specified location. The National Oceanic and Atmospheric Administration's (NOAA) Hybrid Single-Particle Lagrangian Integrated Trajectory (HYSPLIT) model (http://www.arl.noaa.gov/HYSPLIT_info.php) is used extensively to track the three dimensional movement history of air masses over predefined periods of time, altitudes and atmospheric conditions (Gibson et al., 2009b, 2013; Palmer et al., 2013; Ryoo et al., 2011). Common uses of HYSPLIT include tracking sources of air

pollution or predicting the future path of air parcels leaving volcanic eruptions or forest fires. It is therefore a valuable tool to utilize in this study to trace back the sources of air arriving at Sable Island during period of VOC measurements.

### 2.6.2 Remote Sensing

Due to phytoplankton's location in the upper layers of the water column and the fact that they strongly absorb blue and red wavelengths of light, it is possible to observe phytoplankton activity by measuring the amount and spectral quality of light reflected by the ocean, i.e. ocean color, using spectroradiometers mounted on orbiting satellites. For example, the Moderate Resolution Imaging Spectroradiometer (MODIS) mounted on NASA's Aqua and Terra satellites is able to measure ocean color, as well as capture images in the visible light spectra of clouds and long range transport plumes of pollution (NASA-MODIS, 2016). Satellites are routinely used in the detection of phytoplankton blooms and can give invaluable data about seasonality, size and even the type of algal species in a bloom (Behrenfeld et al., 2005; Craig et al., 2006; Soja-Woźniak et al., 2017).

All photosynthetic organisms, including phytoplankton, contain the photosynthetic pigment, chlorophyll-*a*, and chlorophyll-*a* concentration (*Chl-a*; mg $m^{-3}$) is the most commonly used proxy for phytoplankton biomass. Estimates of *Chl-a* can be made from satellite ocean color using the so-called blue-green band ratio algorithms (O'Reilly et al., 1998). However, it is fully acknowledged that these estimates may be inaccurate, especially in waters where other non-covarying optically active water constituents (e.g. colored dissolved organic matter, non-algal particles) are present, such as coastal and shelf waters (Craig et al., 2006, and references therein). In an ideal

scenario, satellite estimates of phytoplankton biomass should be validated with other measurements such as *Chl* estimation from water samples (microscopy, flow cytometry or DNA analysis). Alternate ocean color algorithms may also be employed to obtain more accurate *Chl* estimates (Craig et al., 2012). However, for the purposes of this study, satellite *Chl* were used as a semi-quantitative tool that provided vital context for interpreting the complex spatiotemporal history of the air masses that were measured and analyzed at the Sable Island supersite.

# CHAPTER 3 MATERIALS AND METHODS

## 3.1 Experimental Setup

All measurements in this study were conducted on Sable Island (43.9337° N, 59.9149° W) located in the Northwest Atlantic, approximately 300 km southeast of Halifax, Nova Scotia, Canada. Figure 1 provides a Google Earth image of Sable Island with some of its main land marks labelled. Named after the French word for sand (*le sable*), this narrow sandbar island has been considered a Canadian National Park Reserve since 2011 (CBC, 2011). Sable Island is world famous for being home to hundreds of feral horses, which were brought to the island in the mid-1700s during the Acadian Expulsion (Nova Scotia Museum of Natural History, 2016).

The island has been used for decades as a meteorological monitoring site and hub for scientific research ranging from studies on the wild horses and seals to environmental geology. This prompted the construction of several buildings/sheds to house instruments and 'field laboratories' as well as lodging for visiting researchers, students, tourists and its approximately five fulltime residents.

Sable Island was chosen as the study site for several reasons. Notably, the island's location in a nutrient-rich zone along the Scotian Shelf provides a highly productive environment for phytoplankton populations to flourish (Craig et al., 2012; Fournier et al., 1977; Strain and Yeats, 2005) (Figure 2). The island's remoteness also contributes to a relatively clean environment in which marine emissions can be measured and differentiated from anthropogenic / terrestrial sources (Duderstadt et al., 1998; Gibson et al., 2009b, 2013; Waugh et al., 2010). Additionally, the island provides a fixed location

for long-term continuous measurements of ocean emissions (as opposed to a ship) and is equipped with facilities required for this study, such as insulated buildings and power generators.

Except for the meteorological services weather station, all field instruments used in this study were operated out of the Environment and Climate Change Canada air chemistry building (Figure 3). This building was strategically placed on the west side of the island, upwind of diesel generators, furnaces and other possible sources of on-island anthropogenic emissions. The building is also insulated and air conditioned to maintain the year-round environmental conditions required for instruments to operate at their optimum.

Site visits were conducted using a fixed-wing airplane operated by Maritime Air Charter Limited/Sable Aviation out of Halifax Stanfield International Airport. The island can also be reached via boat or helicopter, neither of which was used due to prohibitive costs and inopportune travel times and schedules. A typical site visit would begin with an approximately 50-minute flight from the airport and landing on a 10 km stretch of beach on Sable Island, followed by a 30-minute drive to the study site/compound. With that said, it is important to mention that unsuitable weather conditions, scheduling conflicts, mechanical failures with the aircraft and other unforeseen obstacles made field visits difficult and less frequent than desired.

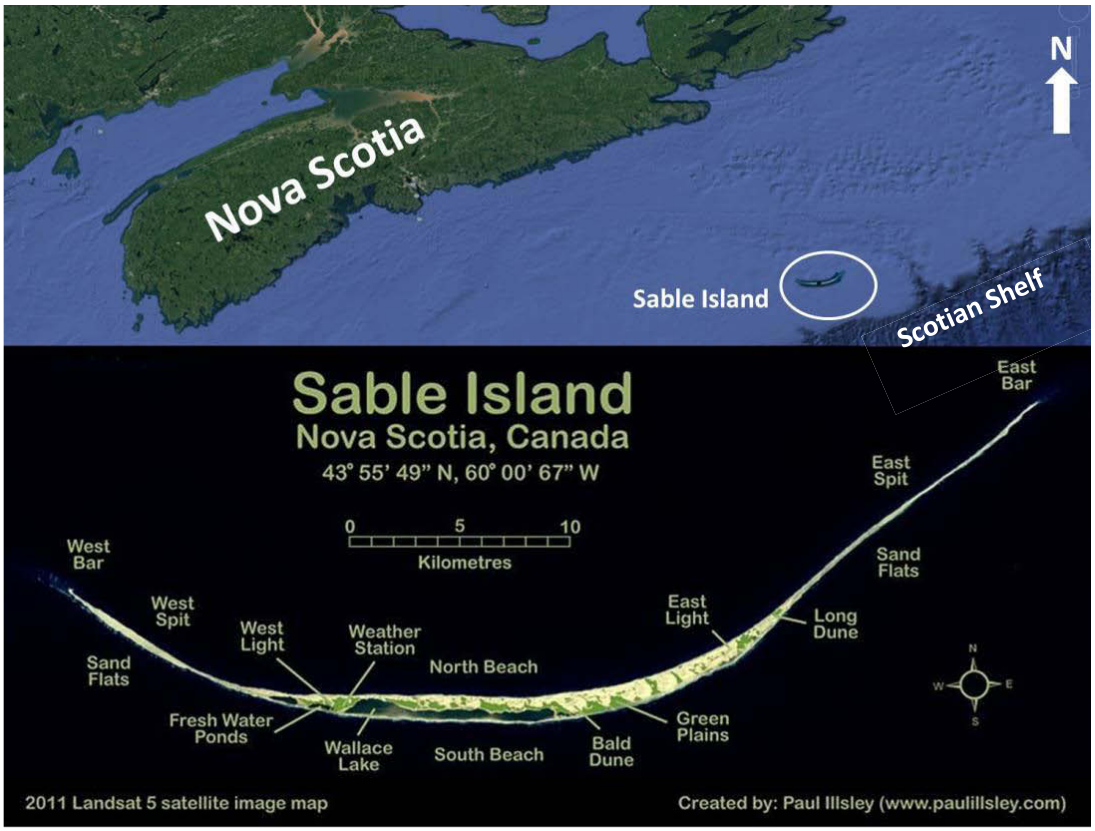


**Figure 1.** A Google Earth satellite image of Sable Island showing its location relative to mainland Nova Scotia, the Scotian Shelf, and a satellite image of labelled landmarks on the island (Paul Rogers, 2012. www.sableisland.info)

**Figure 2.** NASA MODIS' satellite image showing phytoplankton blooms around Sable Island in July, 2010. Adapted from NASA, retrieved from http://modis.gsfc.nasa.gov/gallery.

**Figure 3.** Photograph of the air chemistry building on Sable Island (Photo: Loay Jabre).

The island was visited on average once every two months between May and December, either by me or other members of Dr. Gibson's Atmospheric Forensics

Research Group (AFRG) for instrument maintenance, calibrations and data download. Full-time technicians living on the island also assisted with downloading data on a bi-weekly basis and were communicated with regularly to facilitate instrument programming and troubleshooting when needed. Aside from direct field measurements, samples were also collected from Sable Island and analyzed at the AFRG laboratory on Dalhousie University's Sexton campus. Table 1 shows a full list of instruments used in this study and their location. A detailed description of operations and procedures of instruments and software is also provided in subsequent sections of the Materials and Methods.

**Table 1.** List of instruments and equipment used, with manufacturing company and location during the study.

| Instrument | Company | Location |
|---|---|---|
| ppbRAE 3000 Handheld VOC Monitor | RAE Systems | Sable Island, inside air chemistry shed with outside inlet through wall |
| MTS-32™ | Markes International | Sable Island, outside air chemistry shed on roof |
| Unity 2 Thermal Desorption Unit | Markes International | AFRG laboratory |
| TRACE™ 1300 Gas Chromatograph | Thermo Fisher Scientific™ | AFRG laboratory |
| ISQ™ Series Single Quadrupole Mass Spectrometer | Thermo Fisher Scientific™ | AFRG laboratory |
| SVI Thermal Desorption Tubes | Perkin Elmer | N/A |
| Carbotrap® 217 Thermal Desorption Tubes | Supelco/Sigma-Aldrich | N/A |
| TC-20 ™ Tube Conditioner | Markes International | AFRG laboratory |

### 3.2 Meteorological Data

A weather station (Climate Identifier: 8204703) located approximately 100 meters from the air chemistry shed at a 1.2 meter elevation was used to measure temperature (°C), wind speed (m/s) and wind direction (10's of deg.). Data were recorded hourly for the entirety of the year 2016 and were used to generate wind-rose plots and temperature time series plots.

### 3.3 ppbRAE 3000 Portable VOC Monitor

Continuous, real-time, total volatile organic compound (VOC) concentrations were measured in parts per billion (ppb) via photo ionization detection (PID) using a ppbRAE 3000 Portable VOC Monitor (RAE Systems, 2015), placed inside the temperature controlled air chemistry shed to minimize measurement error. A Krypton, 10.6 eV ultraviolet (UV) lamp was used to ionize VOCs at 1 ppb resolution with a measurement range of 1 ppb-10,000 ppm. This instrument uses an internal pump to draw air into an ionization chamber at a flow rate of 0.5 L/min where the UV lamp ionizes incoming VOCs, separating them into positively charged ions and negatively charged electrons. After ionization, a cathode and an anode attract the ions and electrons respectively to generate an electric current, which is then converted into a ppb concentration. It should also be noted that most (but not all) VOCs are ionized at 10.6 eV, therefore giving a good representation of total VOCs in the ambient air. Figure 4 is a schematic diagram showing the underlying process of PID detection.

The ppbRAE 3000 was mounted on a wall inside the air chemistry through which a hole was drilled and Tygon® anti-static tubing was passed through to the exterior. An air inlet with a bug screen cover was then constructed on the outside to prevent insects and

course debris from entering the tube. A water trap was installed on the inside before the ppbRAE 3000 to capture condensation and any water that may have gotten drawn into the tube. The tubing was then connected to the ppbRAE inlet, which was outfitted with a RAE 0.45 mm External Filter to prevent dust from entering the system (Figure 5). Measurements were continuously recorded in 15 minute intervals for the entirety of year 2016 and data were downloaded bi-weekly using ProRAE Studio software.

Calibrations were performed with 10 ppm and 20 ppm Isobutylene calibration gas and instrument zeroing was achieved using RAE's VOC Zeroing Tubes. Other maintenance procedures, such as inlet and lamp cleaning were performed as suggested by the instrument's manual (RAE Systems, 2015).

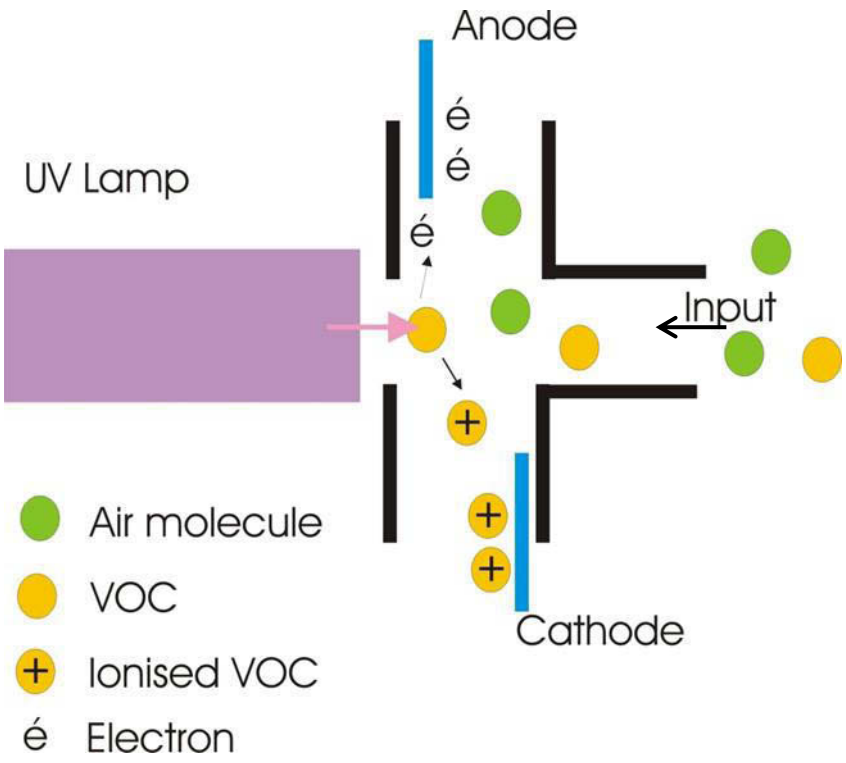


**Figure 4.** Schematic diagram of an ionization chamber showing the flow path of VOCs and their ionization by the UV lamp (Sysmatec, 2017).

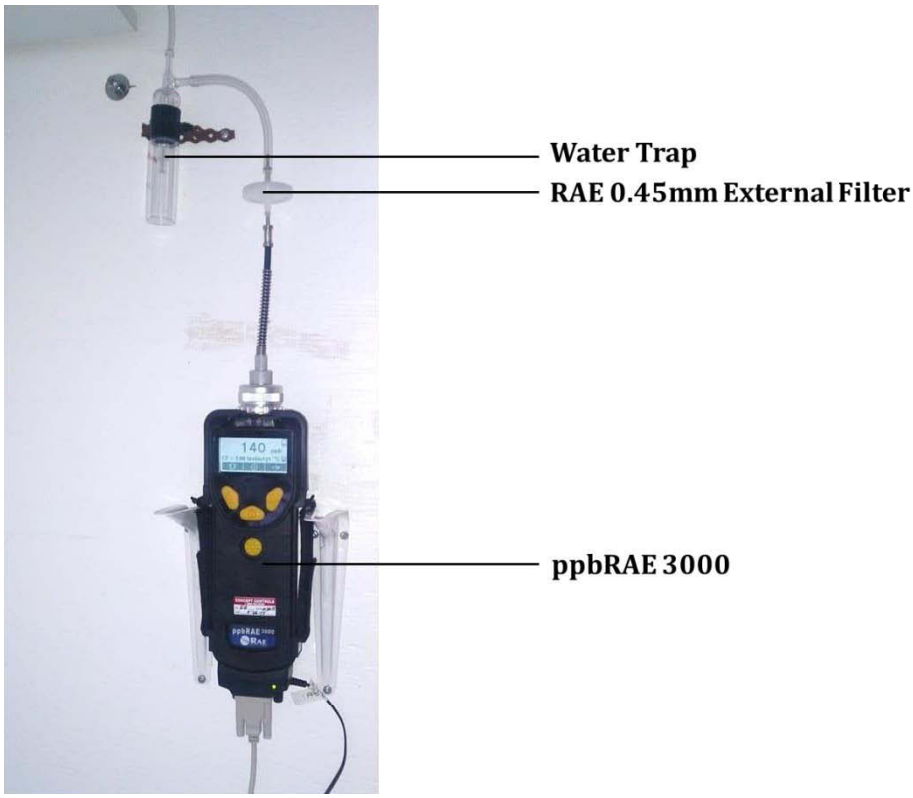


**Figure 5.** Photograph of the ppbRAE 3000 mounted on the wall inside the air chemistry building on Sable Island (Photo: Yunchen Li).

### 3.4 Thermal Desorption Tubes / TC-20 ™ Tube Conditioner

Time integrated sampling of VOC species were also performed on Sable Island via air sampling on thermal desorption tubes (TDTs). The TDTs were then analyzed by thermal desorption-gas chromatography-mass spectrometry (TD-GC-MS). TDTs are narrow, glass or stainless steel tubes that can be packed with one or more of a variety of sorbent materials and used to sample a wide range of volatile and semi-volatile organic compounds in various applications (Dohoo et al., 2015). Figure 6 shows a diagram of a typical TDT.

Two types of TDTs were used in this study, the multi-bed Soil Vapor Intrusion™ (SVI) from Perkin Elmer and the CarboTrap® 217 from Supelco (Figure 7); both of

which made of stainless steel, 89 mm in length, 6.4 mm o.d. and meet USEPA TO-14 and USEPA TO-17 regulations. The SVI tubes contained three sorbents: Carbograph 1™, Carbograph 2™ and a Carboxen 1003™ molecular sieve, while the CarboTrap® 217 tubes contained Carbotrap B® graphitized black carbon and a Carboxen 1000® molecular sieve. Sorbents in both tube types were separated by 3 mm of silanized glass wool.

The TC-20™ Tube Conditioner (Markes, 2015) was used to clean and bake out (condition) all TDTs prior to sampling (Figure 8). This instrument was operated with ultra-pure nitrogen (99.999% purity) to simultaneously flush 20 TDTs, while at the same time maintaining a specific bake out temperature for a predefined period of time. SVI tubes were conditioned at 350°C for four hours, and CarboTrap® tubes were conditioned at 400°C for one hour as prescribed by their operations manuals. The tubes were allowed to cool under ultra-pure nitrogen flow to avoid contamination by passive sampling and were then immediately sealed with air tight, brass Swagelok caps to ensure an uncontaminated environment inside the tube until sampling. The caps were cleaned by soaking in deionized water over night followed by flushing with a methanol-deionized water mixture, then allowed to air dry for 24 hours before use.

All handling of TDTs was conducted while wearing powder-free nitrile gloves and great care was taken to avoid touching the ends of the tubes.

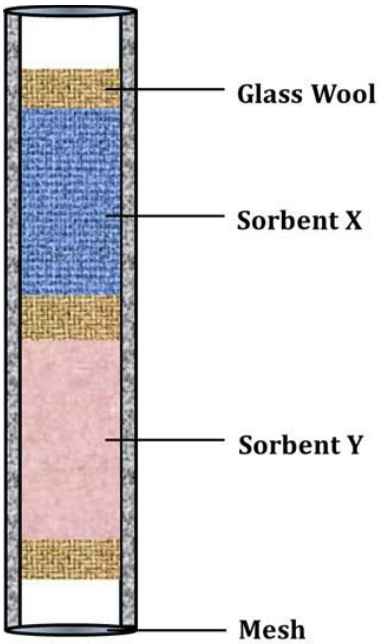


**Figure 6.** Diagram of a generic TDT with two different sorbents, separated and held together by glass wool, with a fine wire mesh on either end of the tube to prevent debris from entering.


**Figure 7.** Photograph of Carbotrap® (left) and SVI™ (right) TDTs (Photo: Loay Jabre)


**Figure 8.** Photograph of the TC-20™ Tube Conditioner, with the tube holder resting on top of the instrument (Photo: Loay Jabre)

### 3.5 MTS-32 ™

A Multi-Tube Sequential Sampler for thermal desorption tubes (MTS-32$^{TM}$) (Figure 9) was used for active VOC sampling on Sable Island (Markes, 2015). This instrument is designed for unattended, sequential sampling of air on 32 different TDTs at an adjustable flow rate for a programmable period of time. All parts of the MTS-32$^{TM}$ were inside a heated, low-emitting, weather proof box, allowing for year-round outdoor placement of the instrument for direct exposure to outside air. In this study, the sampling process began by fitting 32 TDTs with diffusion-locking caps (DiffLok™ caps) on the outflow end and inserting the sampling end into numbered (1 through 32) slots on a rotating pump manifold. Difflok™ caps only allow one-way flow of air through the tube when negative

pressure is applied, i.e. when air is drawn through the tube during sampling (Figure 10). The manifold rotates to place one TDT in the sampling port position where air from the outside is drawn into the MST-32 by an internal pumped attached to the current sampling tube. The DiffLok™ caps keep all the tubes sealed when not connected to the internal pump (Markes, 2015). To maximize the capture of VOCs, TDTs were sampled at a 100 mL/min flow rate for 24 hours per tube with two blank tubes (un-sampled) kept as a control. After the completion of each sampling episode, TDTs were removed from the instrument, fitted with Swagelok caps, and transported back to the laboratory to be stored at 0 - 4°C for subsequent analysis.

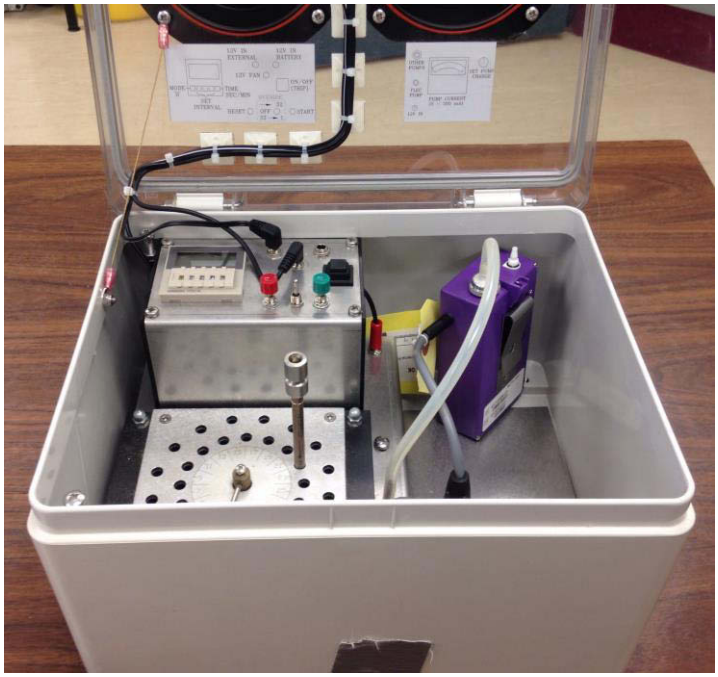

**Figure 9.** Photograph of the MTS-32$^{TM}$, with one TDT placed in the rotating pump manifold (Photo: Loay Jabre).

**Figure 10**. Photograph of a TDT with a DiffLok ™ show on the top of the tube (Photo: Loay Jabre).

### 3.6 Thermal Desorption – Gas Chromatography – Mass Spectrometry

A Unity-2 Thermal Desorption (Markes, 2012) – Trace 1300 Gas Chromatography–ISQ Elite Mass Spectrometry system (TD-GC-MS) (Thermo Scientific, 2012) was used for TDT sample analysis (Figure 11). These three instruments were used in synchrony as one unit to thermally desorb, chromatographically separate and analyse VOC species previously collected on TDTs on Sable Island using the MTS-32™. All TDTs were allowed to warm up to room temperature prior to analysis.

The Unity-2 thermal desorption unit was operated by first purging a TDT with ultrapure nitrogen (99.999% purity) for 10 minutes at room temperature to remove moisture and any residual ambient air. The TDT was then heated (SVI: 325°C, CarboTrap®: 330°C) for 10 minutes to liberate VOC species from the sorbents into a flow of ultrapure helium (99.999% purity) carrier gas. The carrier gas then transports VOC species onto a pre-conditioned, air toxics cold trap, which functions to create a narrow

band of compounds required at the start of GC analysis. Afterwards, the cold trap was heated to 330°C at a rate of 40°C/s and ultrapure helium was used to transfer VOCs from the cold trap to the GC.

The Trace 1300 Gas Chromatograph was used with a Restek fused silica, 40 meter long, 0.18 mm i.d. , 1 μm df, RTX® -VMS column to separate the mixture of compounds entering the column into distinct bands of VOC species. Initial oven temperature was set to 45°C and held for 6.55 minutes followed by an increase to 100°C at 8.4°C/min with a 1.45 minute hold. Finally, an increase to 240°C at 17.3°C/min with a 1.9 minute hold was programmed at the end of the run to clear the column from any contaminants. A continuous flow rate was set to 1.01 mL/min throughout the run, following EPA Method 524.2 and VOCs were transferred to the ISQ via a heated transfer line kept at 250°C to prevent condensation.

The ISQ™ Series Single Quadrupole Mass Spectrometer was used for compound identification and quantification. All analyses were conducted using electron ionization with the ion source temperature held constant at 300°C. The electron multiplier (detector) and filament (ion source) were turned off for the first 8 minutes of each analysis to reduce consumption by unwanted compounds/contaminants, and the quadrupole was programmed to scan at a mass range of 35-300 amu with a scan time of 0.2 seconds.

A non-naturally occurring, deuterium-labelled 1,4-dichlorobenzene was used as an internal standard to normalise daily variations in GC-MS operations, and a master-mixture of 72 different compounds including biogenic marine and terrestrial VOCs as well as anthropogenic VOCs was used as an external standard to identify and quantify

samples. Deuterated internal standards are used because they provide a signal similar to that of the analytes of interest, but are slightly heavier and therefore distinguishable. All standards were serially diluted with GC-grade methanol into 1 ng/µL, 5 ng/µL, 10 ng/µL, 50 ng/µL, 100 ng/µL, 1 µg/µL and 10 µg/µL concentrations and were stored in the freezer at -18°C until use. To create a TDT standard, a 10 µL capacity gastight precision syringe (Hamilton Company, Nevada, USA) was used to transfer 1 µL of standard of each concentration into a TDT under a 100 mL/min flow of ultra-pure helium using a Markes' Calibration Solution Loading Rig (Figure 12). External standards were loaded on pre-conditioned TDTs and internal standards were loaded on sample tubes in addition to pre-conditioned TDTs for comparison. Standards were analyzed using TD-GC-MS following the same methods for sample analysis discussed above, and retention times, m/*z* ratios and peak integration were extracted in conjunction with a built-in NIST library to quantify and identify compounds.

At the beginning of each day and before any sample analyses were conducted, an air and water test, a leak check and general system health checks were completed, followed by one control run and one 'empty' run to ensure a contamination free system. To ensure consistency in the results, internal standards were run once a day and external standards were run bi-weekly.

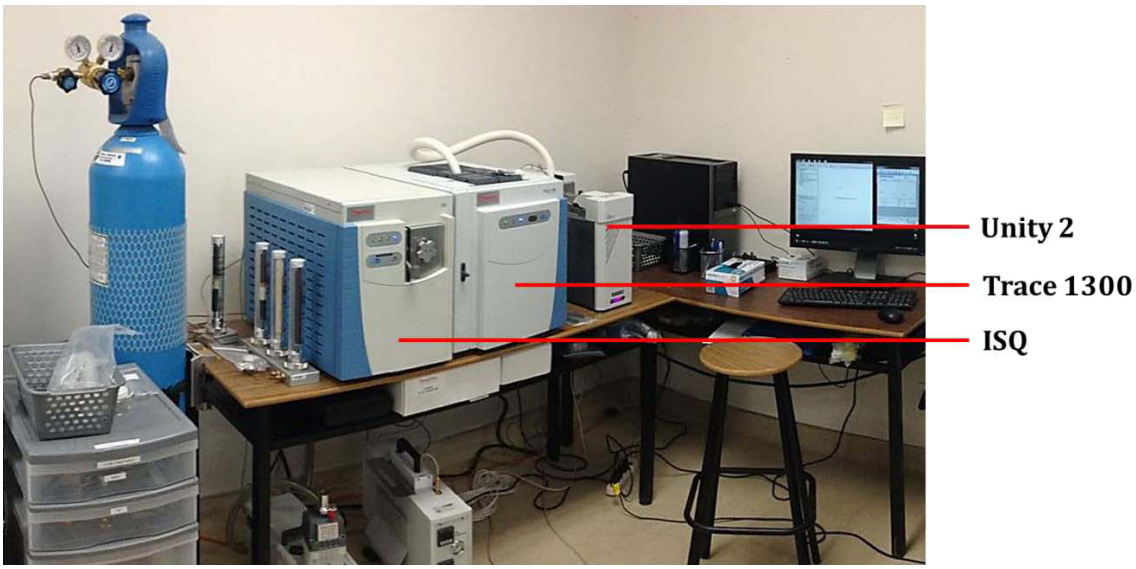


**Figure 11.** Photograph inside the AFRG laboratory showing the TD-GC-MS setup (Photo: Loay Jabre).

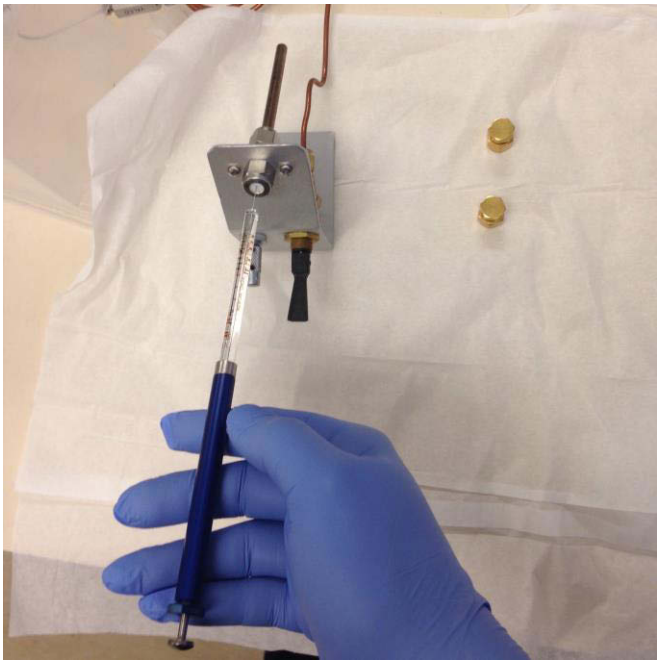

**Figure 12.** Markes' Calibration Solution Loading Rig with a 10 µL capacity gastight syringe and TDT attached

### 3.7 Hybrid Single-Particle Lagrangian Integrated Trajectory (HYSPLIT) Model

A Hybrid Single Plot Lagrangian Integrated Trajectory (HYSPLIT) model was used to create 5-day air mass back-trajectories to track possible sources of VOCs on Sable Island (ARL-NOAA, 2005). This computer model creates a 3-dimensional representation (vertical and horizontal) of selected air parcel trajectories by applying turbulence and wind field components to a hypothetical 'packet of particles', in this case, VOCs. HYSPLIT runs were compiled twice a day, at 0000 and 1200 UTC for the entirety of 2016, with 500 m chosen as the arrival height to avoid the simulation of air parcels hitting the ground before reaching Sable Island as the final destination. The model was programmed to produce full 5-day backward trajectory with 5-hour intervals between each point on the path. Meta-analysis of HYSPLIT mass back trajectories was also performed to separate the sources into four different zones: Marine, SW, NW, and North. Figure 13 is a Google image map adapted from Dr. Gibson's EVE3800: Air Quality course showing the location of these zones relative to Sable Island (Gibson, 2017).

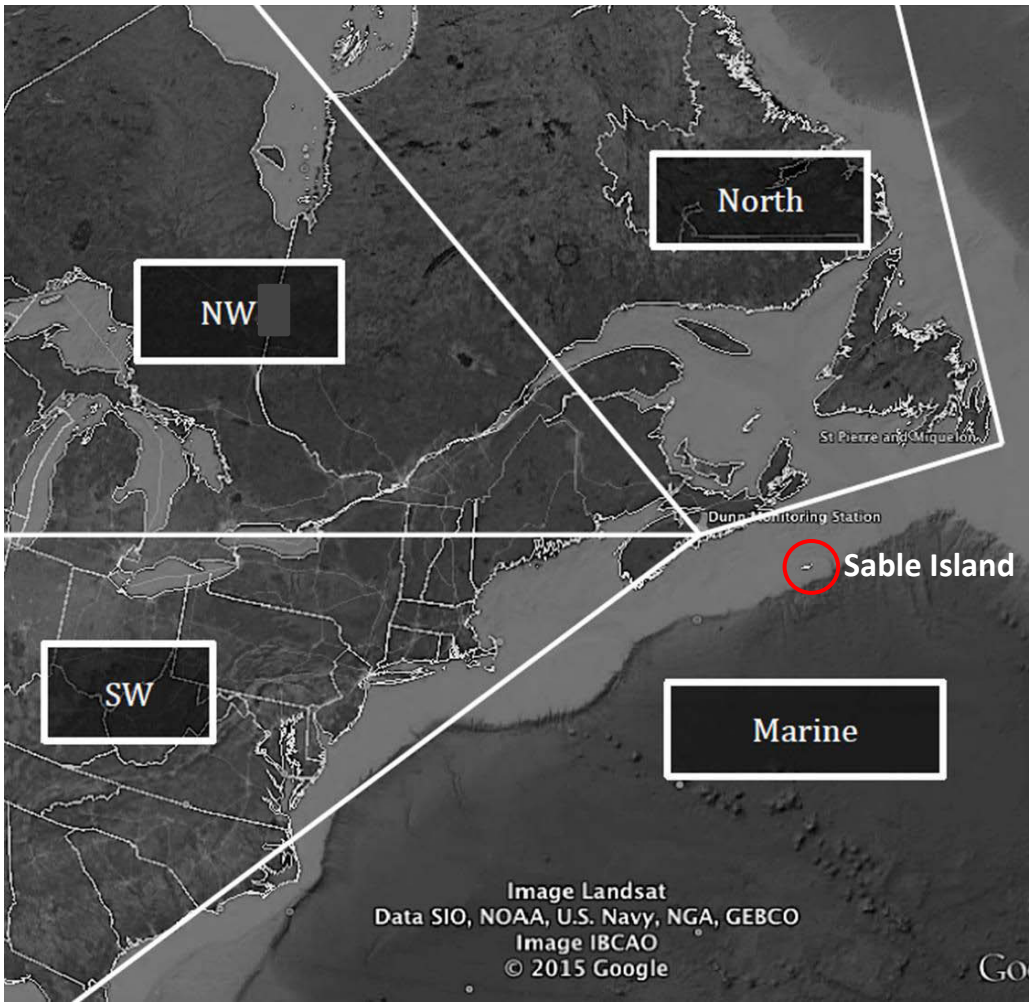


**Figure 13.** Different zones relative to wind direction. Adapted from ENVE3800:Air Quality. By Dr. Mark Gibson (Gibson, 2017).

### 3.8 Remote Sensing

Images of chlorophyll-*a* concentration around Sable Island were obtained from the MODIS Aqua satellite, at a 5-day average and 4 km resolution. Images were only downloaded for periods where VOC spikes were observed. These level-3 data (images) are publicly available for use (http://oceancolor.gsfc.nasa.gov).

### 3.9 Statistical Analysis / Graphing

Statistical software R configured with RStudio (R Studio, 2016) and OpenAir Package (Carlsaw, 2015) were used to plot data and produce descriptive and inferential statistics. Descriptive statistics included mean, median, mode, standard deviation, data completeness (%) and 25th and 75th percentiles. Inferential statistics included One-Way Analysis of Variance (ANOVA), Tukey HSD and Kruskal-Wallis tests and $X^2$ tests where applicable, all of which were performed at a significance level of $\alpha = 0.05$. Wind rose plots were created using WRPLOT View™ (Lakes Environmental, 2016) to produce a visual representation of wind speed and direction.

# CHAPTER 4 RESULTS

## 4.1 Meteorological Conditions

Temperature, wind direction and wind speed were measured hourly on Sable Island during 2016. Comprehensive descriptive statistics of these parameters are provided below in Table 2. Descriptive statistics of temperature, wind direction and wind speed on Sable Island for 2016.

**Table 2.** Descriptive statistics of temperature, wind direction and wind speed on Sable Island for 2016.

| | Temp. (°C) | Wind Direction (°) | Wind Speed (km/hr) |
|---|---|---|---|
| **n** | 8414 | 8414 | 8535 |
| **n missing** | 370 | 343 | 249 |
| **Completeness (%)** | 95.79 | 96.10 | 97.17 |
| **Mean** | 9.43 | 205.8 | 25.36 |
| **Std. Deviation** | 7.35 | 96.73 | 12.79 |
| **Minimum** | -9.7 | 100 | 0 |
| **25$^{th}$ Percentile** | 3.8 | 140 | 17 |
| **Median** | 9.4 | 220 | 24 |
| **75$^{th}$ Percentile** | 15.2 | 280 | 34 |
| **Maximum** | 53.8 | 360 | 91 |
| **I.Q.R** | 11.4 | 140 | 17 |

### Temperature

The mean annual temperature for 2016 on Sable Island was 9.43°C ± 7.35°C. January, March and February were the coldest months respectively while August, September and July were the warmest months, respectively. Mean monthly temperatures are shown in Table 3 with a visual representation in Figure 14.

**Table 3.** Mean monthly temperatures in °C on Sable Island for 2016.

| Month | Temperature (°C) | Standard Deviation (±°C) |
|---|---|---|
| **January** | 1.64 | 3.03 |
| **February** | 2.12 | 4.01 |
| **March** | 1.75 | 3.40 |
| **April** | 11.06 | 12.92 |
| **May** | 8.35 | 2.23 |
| **June** | 11.76 | 2.29 |
| **July** | 15.99 | 2.05 |
| **August** | 18.94 | 1.81 |
| **September** | 17.66 | 2.76 |
| **October** | 12.94 | 3.19 |
| **November** | 9.09 | 2.72 |
| **December** | 2.66 | 3.90 |

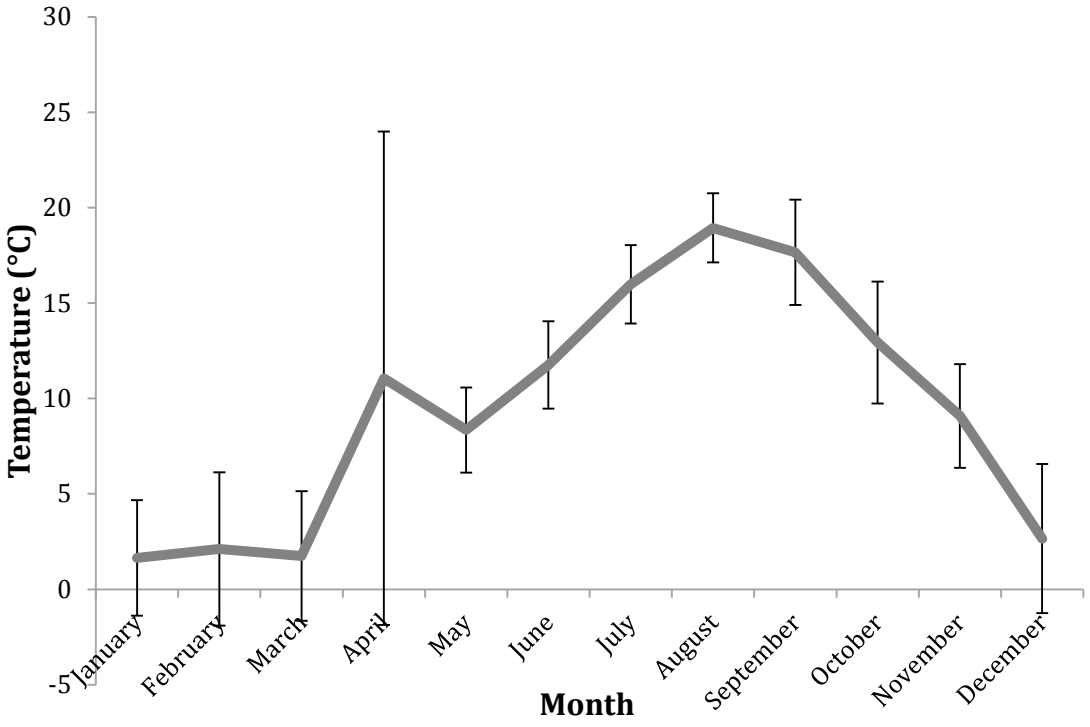


**Figure 14.** Mean monthly temperature (°C) on Sable Island for 2016. Error bars represent 95% confidence intervals.

As expected, winter was the coldest season of the year, followed by autumn, spring and summer respectively (Table 4, Figure 15) ($p = 2.2 \times 10^{-16}$). In this, and subsequent sections, the 2016 seasons were defined as follows: Summer: July - September, Autumn: October -December, Winter: January-March, Spring: April - June.

**Table 4.** Mean seasonal temperatures in °C on Sable Island for 2016.

| Season | Temperature (°C) | Standard Deviation (±°C) |
|---|---|---|
| **Summer** | 17.53 | 1.21 |
| **Autumn** | 8.23 | 3.69 |
| **Winter** | 1.84 | 3.48 |
| **Spring** | 10.39 | 5.82 |

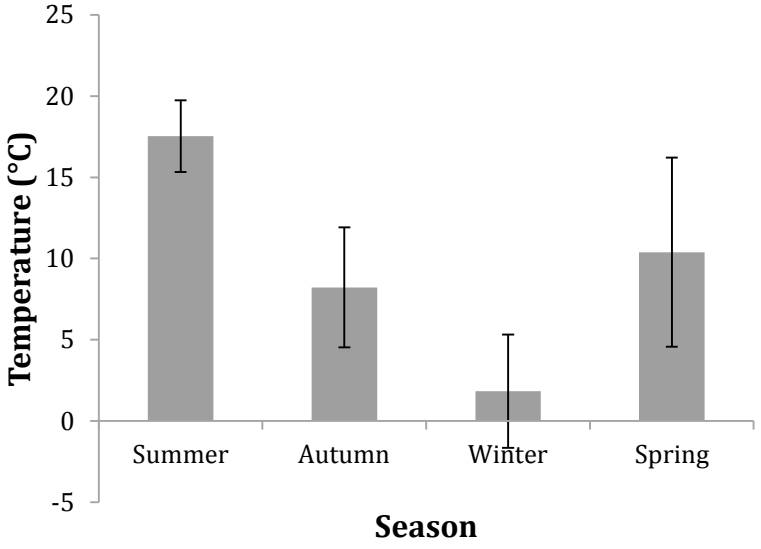


**Figure 15.** Mean seasonal temperature (°C) on Sable Island for 2016. Error bars represent 95% confidence intervals.

**Wind**

The 2016 mean annual wind direction and speed measured on Sable Island were 205.8° ± 96.73° and 25.36 km/hr ± 12.79 km/hr respectively. Wind-rose analyses show a mean annual wind direction of 256°, translating to a predominantly WSW wind blowing into the island (Figure 16, 17).

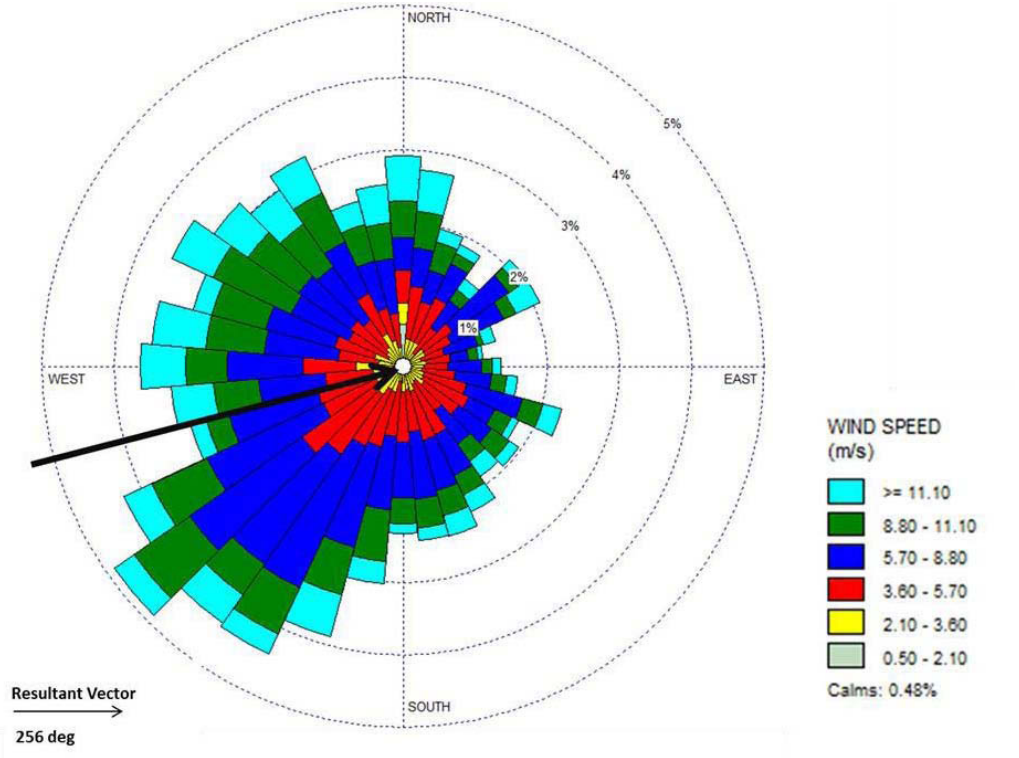


**Figure 16.** Wind rose plot of mean annual wind directions and speeds blowing into Sable Island for 2016.

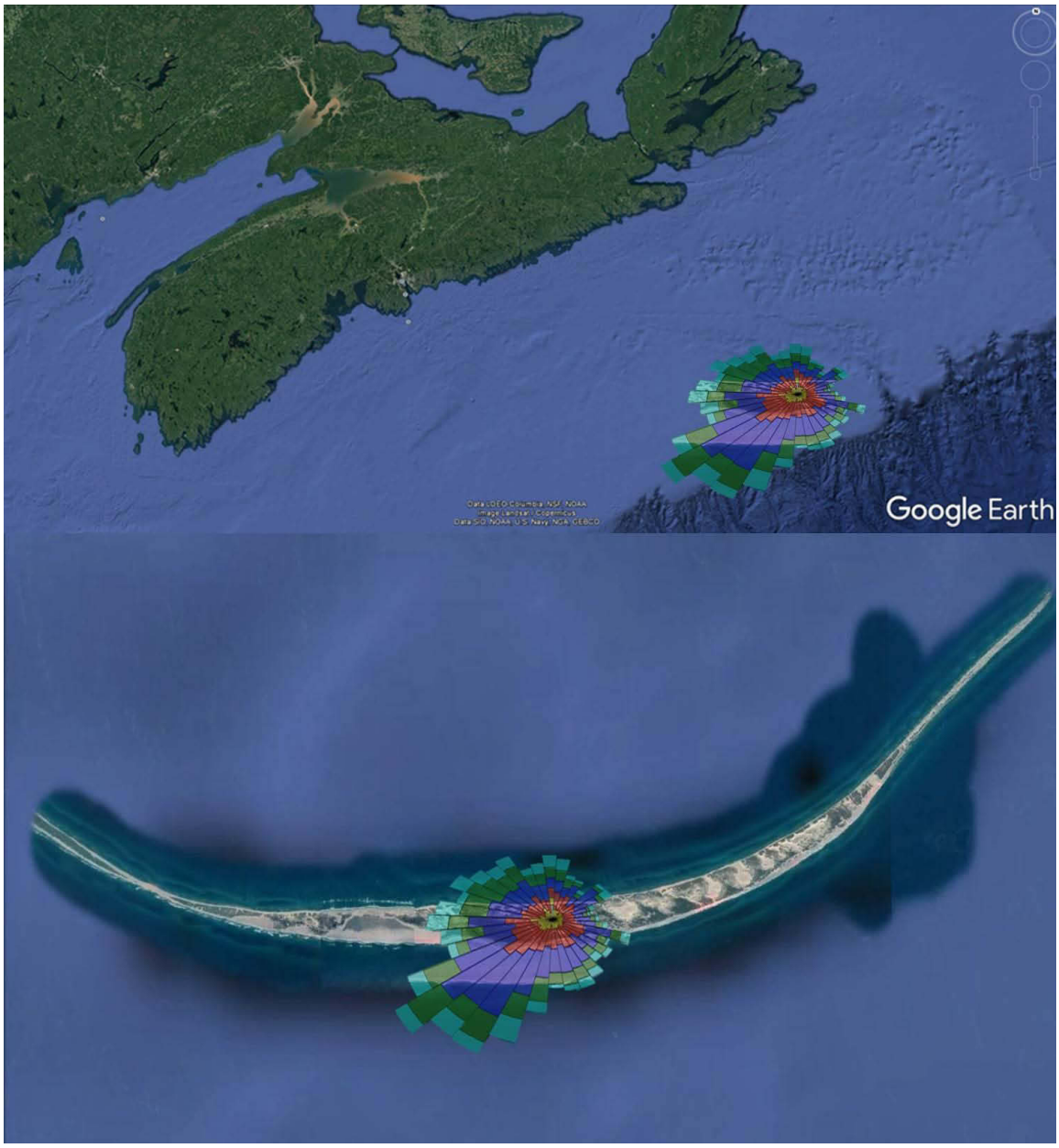


**Figure 17.** Google map image of Sable Island with a superimposed wind rose diagram.

### 4.2 Total Volatile Organic Compounds (VOCs)

Total VOC concentrations were measured in 15 minute intervals during 2016, with temporal measurements presented in UTC standard. Overall, the summer season had the highest VOC concentrations, followed by spring, autumn and winter respectively (Table 6, Figure 18) ($p = 2 \times 10^{-16}$).

**Table 5.** Descriptive statistics of Total VOC concentrations (ppb) on Sable Island for 2016.

| | **Total VOC (ppb)** |
|---|---|
| **n** | 32173 |
| **n missing** | 2963 |
| **Completeness (%)** | 91.57 |
| **Mean** | 1871 |
| **Std. Deviation** | 2097.97 |
| **Minimum** | 0 |
| **25$^{th}$ Percentile** | 200 |
| **Median** | 1871 |
| **75$^{th}$ Percentile** | 3394 |
| **Maximum** | 20030 |
| **I.Q.R** | 3194 |

**Table 6.** Mean seasonal VOC concentrations (ppb) on Sable Island for 2016.

| **Season** | Mean Total VOC Concentration (ppb) | Standard Deviation (± ppb) |
|---|---|---|
| **Summer** | 3918.20 | 1455.81 |
| **Autumn** | 349.49 | 322.05 |
| **Winter** | 170.36 | 44.03 |
| **Spring** | 2921.27 | 1104.02 |

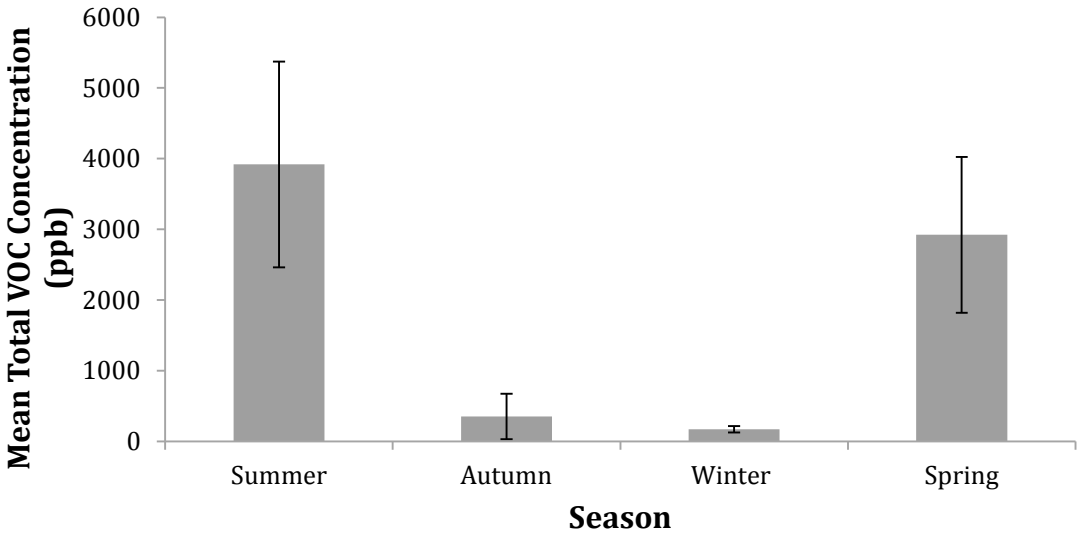


**Figure 18.** Mean seasonal VOC concentrations (ppb) on Sable Island for 2016. Error bars represent 95% confidence intervals.

As predicted, monthly mean VOC concentrations also followed seasonal trends. January and December had the lowest mean VOC concentrations of 6.6 ppb ± 30.47 ppb and 7.28 ppb ± 53.41 ppb respectively while July and August had the highest concentrations of 4060.95 ppb ± 845.09 ppb and 5384.58 ppb ± 2385.15 ppb respectively (Table 7. Mean monthly VOC concentrations (ppb) on Sable Island for 2016.; Figure 19). To minimize short temporal fluctuations, Figure 20 also provides an average trend-line of mean monthly VOC concentrations.

**Table 7.** Mean monthly VOC concentrations (ppb) on Sable Island for 2016.

| Month | Total VOC (ppb) | Standard Deviation (± ppb) |
|---|---|---|
| **January** | 6.60 | 30.47 |
| **February** | 202.21 | 48.84 |
| **March** | 302.28 | 52.79 |
| **April** | 1257.42 | 1049.19 |
| **May** | 3849.52 | 1421.98 |
| **June** | 3656.88 | 840.90 |
| **July** | 4060.95 | 845.09 |
| **August** | 5384.58 | 2385.15 |
| **September** | 2309.06 | 1137.19 |
| **October** | 684.02 | 565.34 |
| **November** | 357.19 | 347.38 |
| **December** | 7.28 | 53.41 |

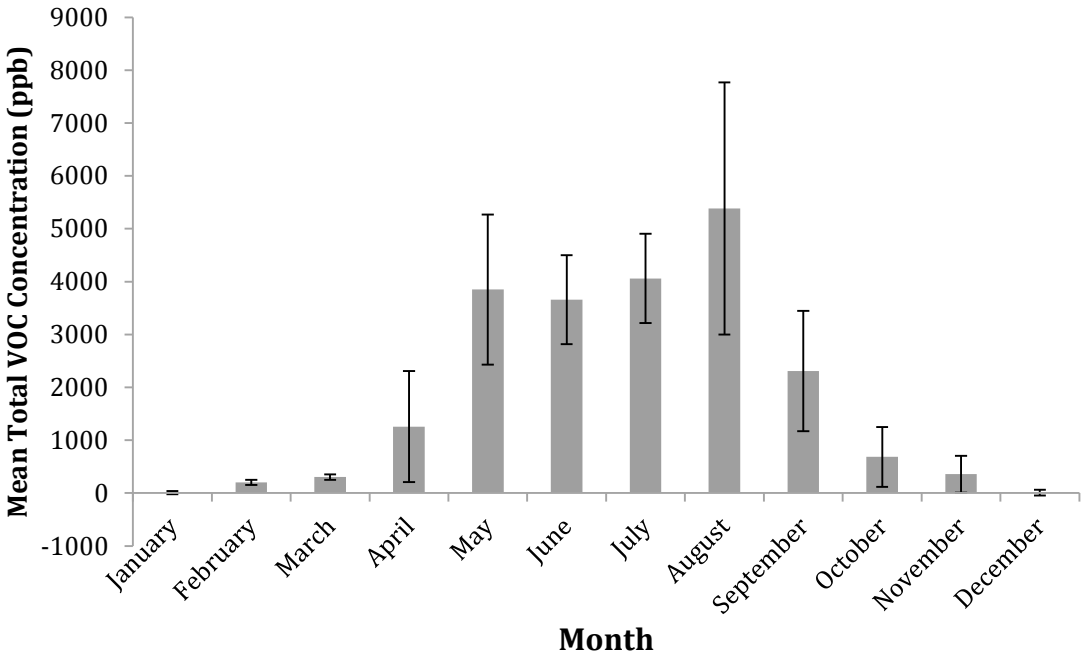


**Figure 19.** Mean monthly VOC concentrations (ppb) on Sable Island for 2016. Error bars represent 95% confidence intervals.

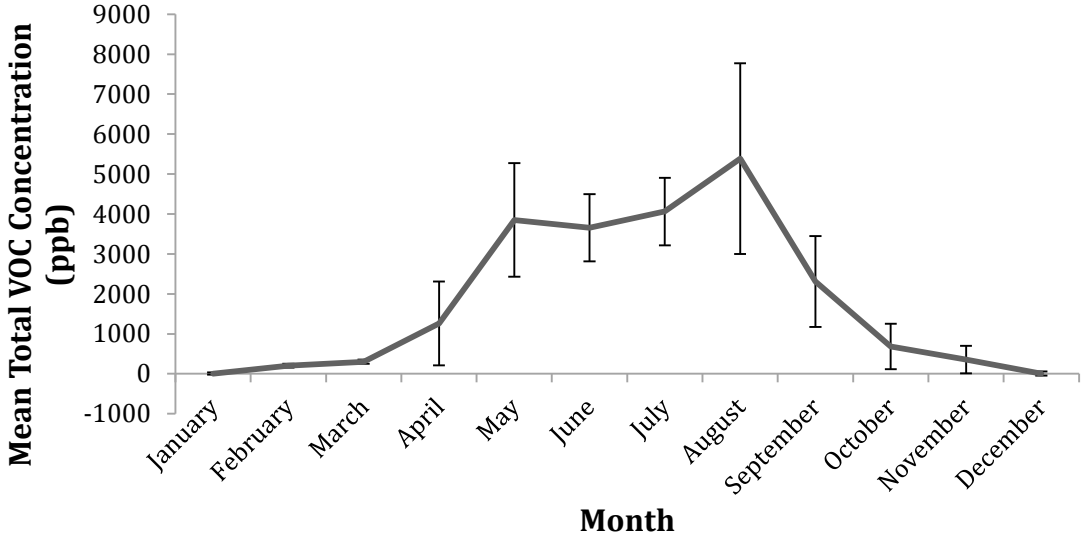


**Figure 20.** A moving average trend-line of mean monthly VOC concentrations (ppb) on Sable Island for 2016. Error bars represent 95% confidence intervals.

Diurnal / time-dependant changes in VOC concentrations were also observed in several months throughout 2016. January, February, March, April and December did not have noticeable changes in VOC concentrations (Figure 21, 22, 24) and September showed a relatively small diurnal change (Figure 23). May, June, July, August, October and November showed the most time-dependent variation in VOCs, with concentrations peaking around mid-day/early afternoon (Figure 22, 23, 24). Table 8 provides times at which VOC concentrations begin to noticeably increase, reach peak concentrations and then start to tail off.

**Table 8.** Time of day (hh:mm) (UTC) during which VOC concentrations begin to increase, reach a peak and decline for every month during 2016 on Sable Island

| Month | Start Time (hh:mm) | Highest Peak Time (hh:mm) | End Time (hh:mm) |
|---|---|---|---|
| **January** | - | - | - |
| **February** | - | - | - |
| **March** | - | - | - |
| **April** | - | - | - |
| **May** | 08:30 | 14:00 | 17:15 |
| **June** | 08:30 | 13:15 | 16:45 |
| **July** | 09:15 | 12:45 | 18:00 |
| **August** | 09:15 | 13:00 | 17:45 |
| **September** | 10:00 | 13:45 | 17:00 |
| **October** | 10:45 | 14:30 | 22:15 |
| **November** | 11:15 | 16:15 | 20:00 |
| **December** | - | - | - |

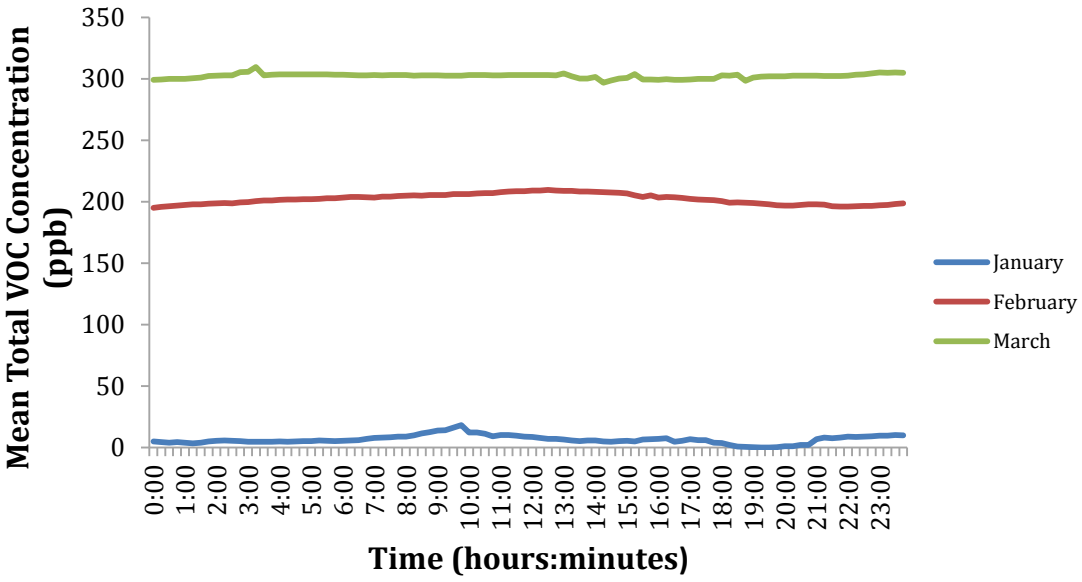


**Figure 21.** Hourly mean VOC concentrations (ppb) for January, February and March, 2016 on Sable Island.

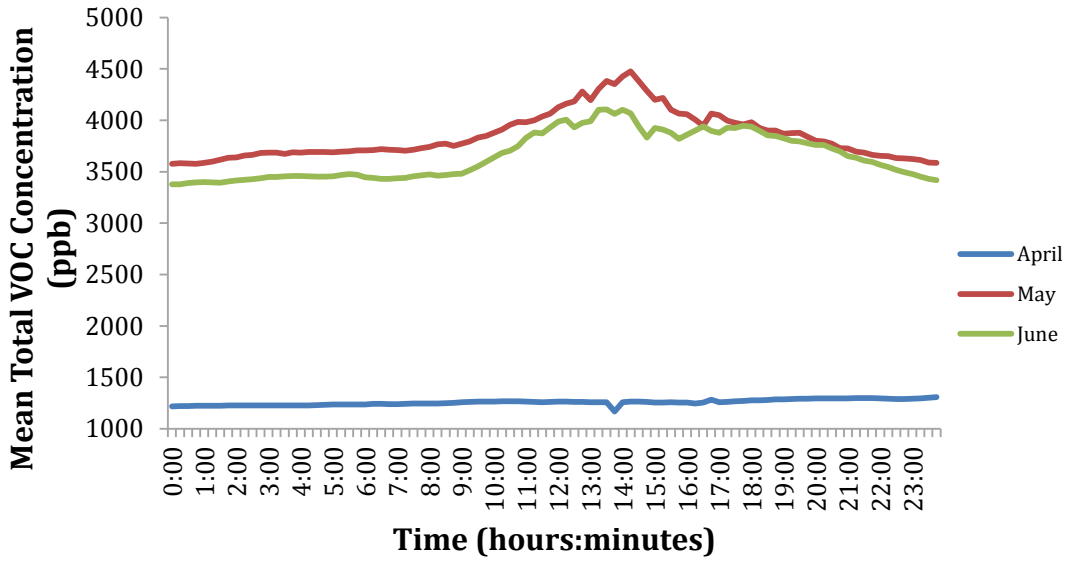


**Figure 22.** Hourly mean VOC concentrations (ppb) for April, May and June, 2016 on Sable Island.

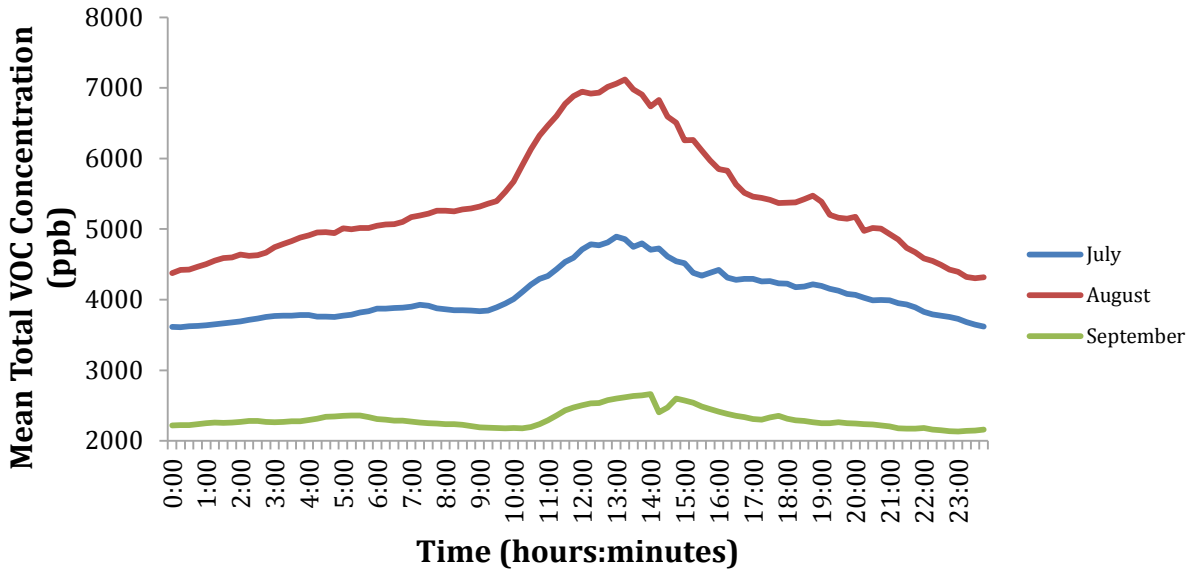


**Figure 23.** Hourly mean VOC concentrations (ppb) for July, August and September, 2016 on Sable Island.

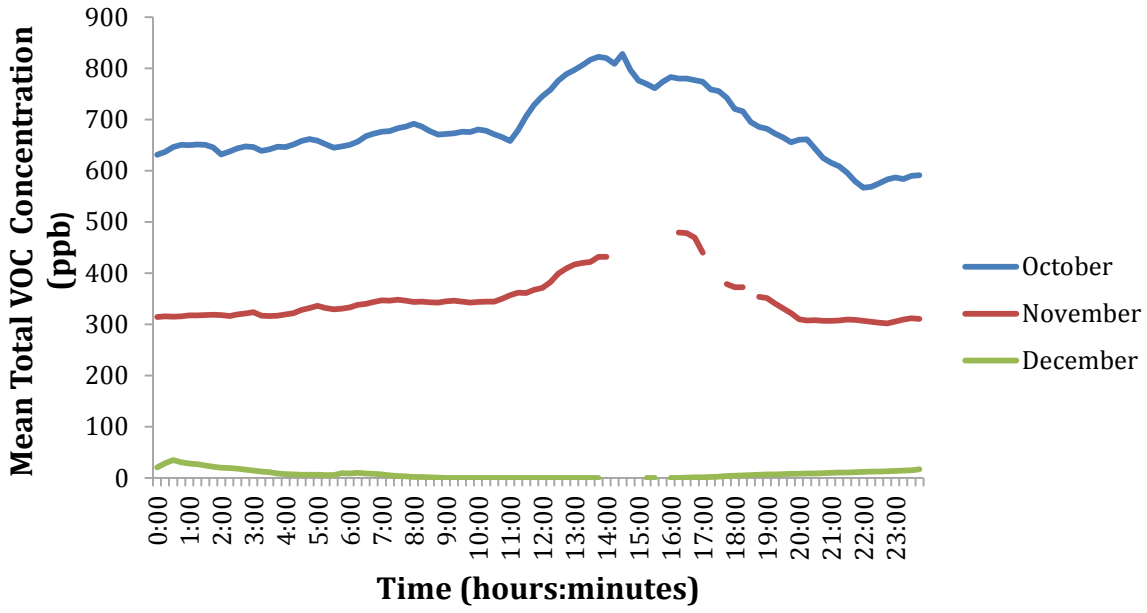


**Figure 24.** Hourly mean VOC concentrations (ppb) for October, November and December, 2016 on Sable Island.

Even though monthly and seasonal trends were observed when VOC concentrations were analyzed for the entire year at once, a visual inspection of the trend revealed 'spikes' in concentrations throughout the entire year (Figure 25). Table 9 also provides the time at which the highest concentration in each observed spike was measured.

**Table 9.** Date, Peak Time, and Total VOC concentration for each of the observed spikes in Figure 25.

| **Spike** | Date (yyyy-mm-dd) | Peak Time – UTC (hh:mm) | Total VOC (ppb) |
|---|---|---|---|
| **1** | 2016-05-08 | 14:15 | 11455 |
| **2** | 2016-05-24 | 13:45 | 9843 |
| **3** | 2016-06-08 | 13:15 | 9623 |
| **4** | 2016-06-13 | 14:00 | 7461 |
| **5** | 2016-06-29 | 12:00 | 7285 |
| **6** | 2016-07-08 | 21:00 | 6416 |
| **7** | 2016-07-16 | 14:15 | 7568 |
| **8** | 2016-07-29 | 13:00 | 10849 |
| **9** | 2016-08-14 | 19:00 | 17786 |
| **10** | 2016-08-22 | 13:45 | 20029 |
| **11** | 2016-08-27 | 14:00 | 9787 |
| **12** | 2016-09-08 | 14:00 | 7850 |
| **13** | 2016-09-20 | 13:30 | 3811 |
| **14** | 2016-09-28 | 13:45 | 2608 |
| **15** | 2016-10-10 | 14:00 | 2464 |
| **16** | 2016-10-22 | 16:00 | 1914 |

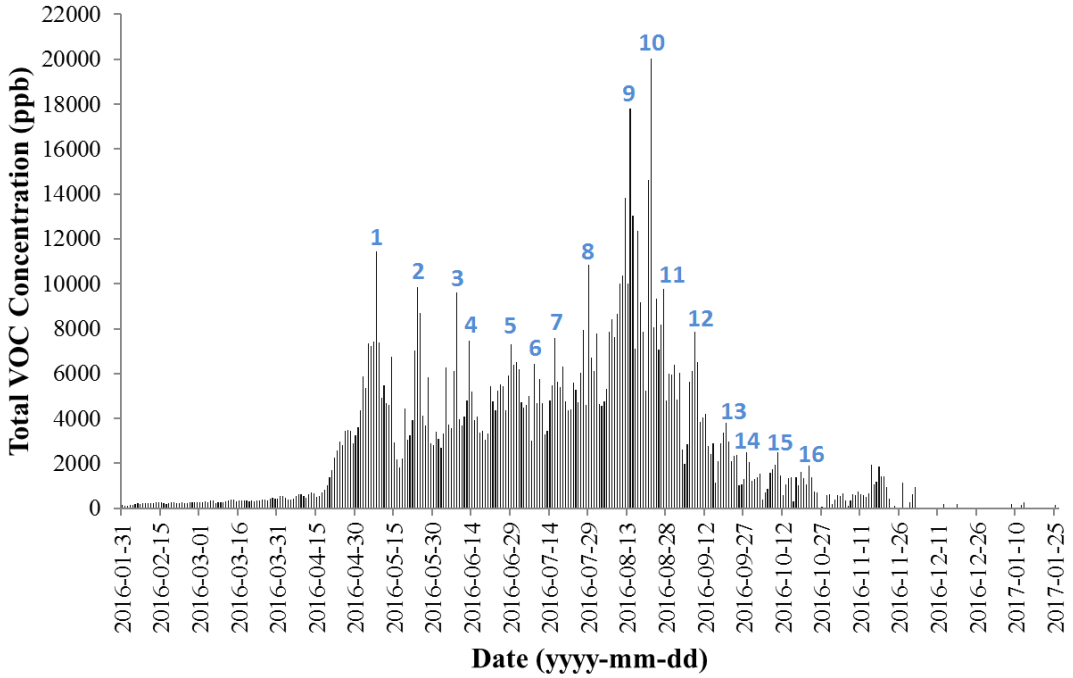


**Figure 25.** Total VOC concentrations (ppb) measured every 15 minutes in 2016 on Sable Island. Blue numbers represent spikes in VOC concentrations that were analyzed in detail.

### 4.3 Long-range and local airflow over Sable Island using the NOAA HYSPLIT Model.

Analysis of long-range and local air flow impacting Sable Island from far and near source regions was conducted using the National Oceanic Atmosphere Administration (NOAA), Hybrid Single Particle Lagrangian Integrated Trajectory (HYSPLIT) model. Five-day air mass back trajectories were performed twice a day (ending at 0000 and ending at 1200 UTC) for Sable Island for the entirety of 2016. The trajectory was then categorized into four different zones, Marine, South West, North West and North as shown below (Figure 26).

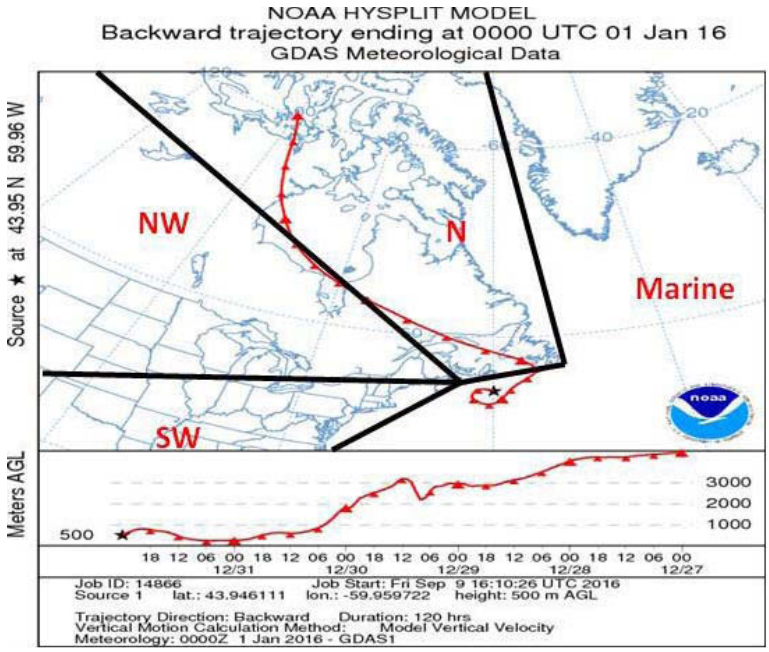


**Figure 26.** Example of HYSPLIT model output showing the four characterization zones. SW = South West, NW = North West, N = North. This example shows a 5-day air mass back trajectory that would be classified as associated with Northerly airflow.

Over all in 2016, air masses travelled mostly from the North (31.64%) and North West (28.9%) to Sable Island and approximately one quarter of the time from marine regions (26.03%). Air masses travelled from the South West direction least frequently (13.42%), as shown in Figure 27. The entire, twice daily HYSPLIT model outputs are provided in the Appendix.

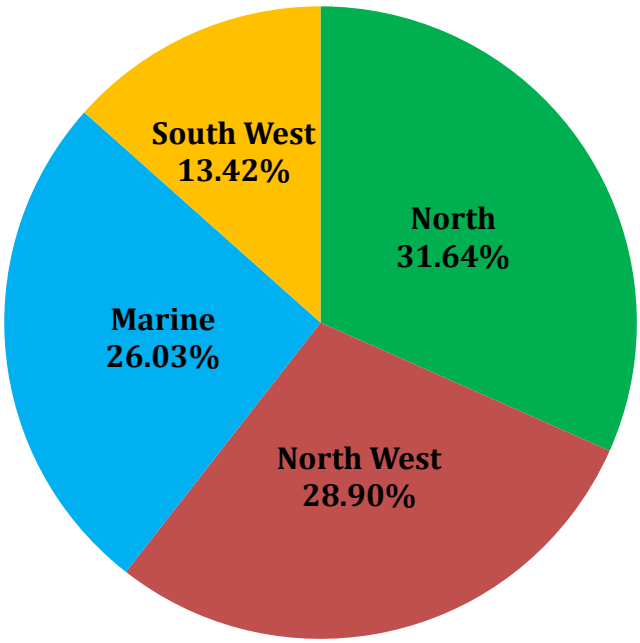


**Figure 27.** Frequency (percentage) of air mass sources into Sable Island for 2016, derived from HYSPLIT analyses.

Seasonal analysis of HYSPLIT showed that winter and autumn were dominated by North and North West wind trajectories (winter: 32% N, 33% NW; autumn: 40% N, 34% NW). Spring and summer seasons were dominated by marine trajectories, with the North being the second most frequent trajectory in the spring and North West for the summer (spring: 35% Marine, 32% N; Summer: 36% Marine, 29% NW). Except for the winter season, the South West trajectory was the least frequent in all seasons. Figure 28 provides a breakdown of the trajectory frequencies during all four seasons.

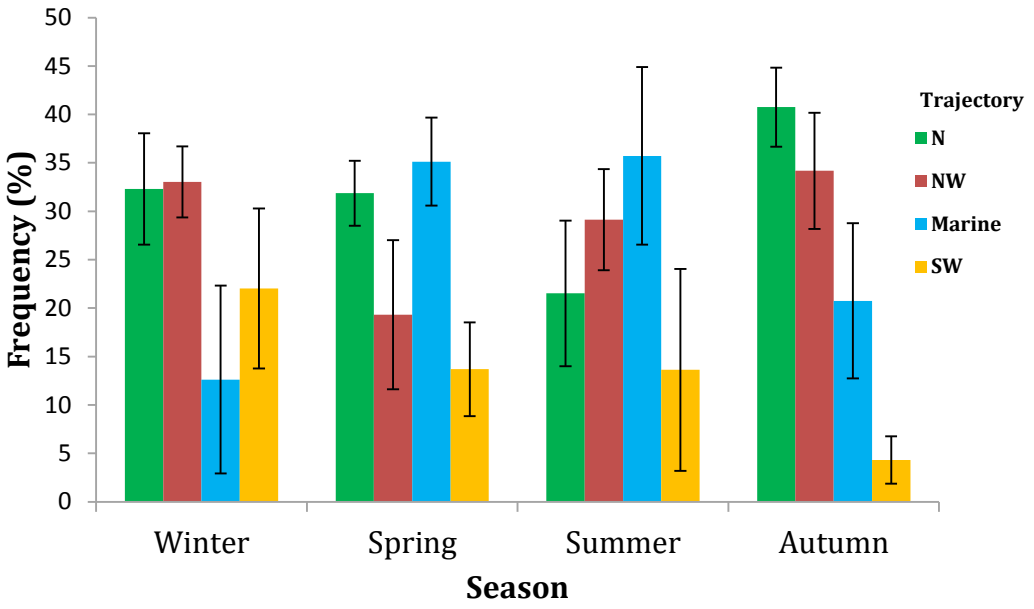


**Figure 28.** Seasonal analysis of air mass sources to Sable Island in 2016. SW = South West, NW = North West, N = North. Error bars represent 95% confidence intervals.

Monthly analysis of HYSPLIT showed that October had the highest source of Northern air masses followed by November and January respectively, while July had the smallest sources of Northern air masses, followed by August and September respectively. NW air masses were most frequent in December, followed by February and October respectively, and least frequent in May, followed by June and September respectively. Marine sources were most frequent in September, followed by May and April respectively, and least frequent in January, followed by October and December respectively. South West sources were most frequent in January, followed by February and July respectively, and least frequent in November, followed by September and October respectively. Figure 29 shows a percentage breakdown for each of the four sources for every month in 2016.

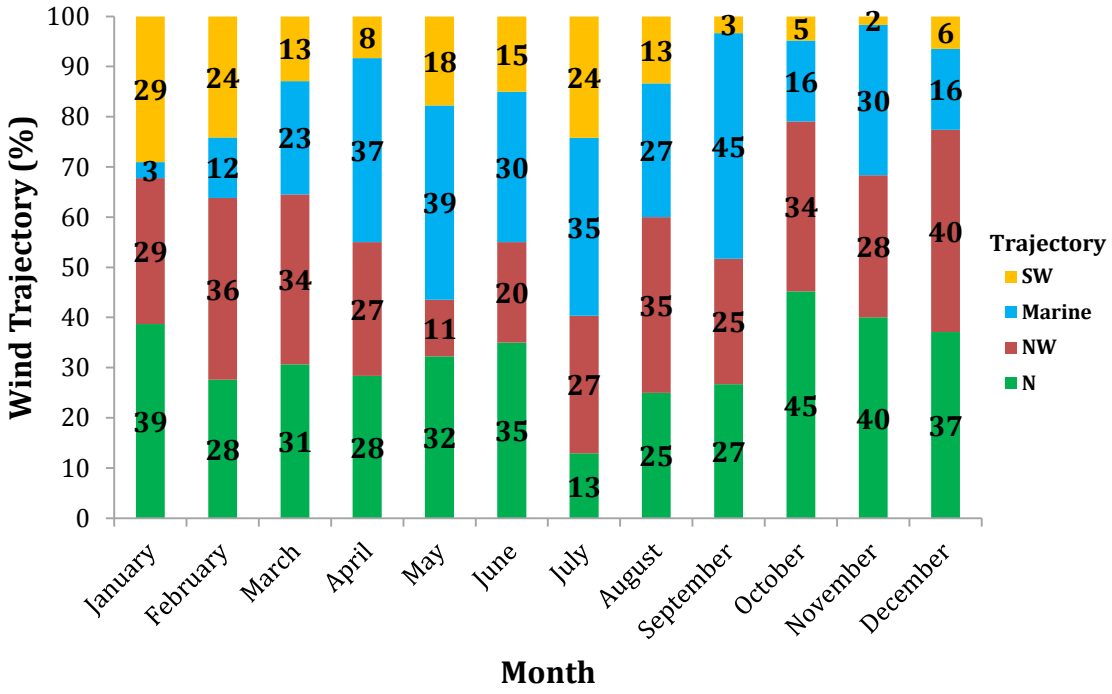


**Figure 29.** Monthly analysis of air mass sources to Sable Island in 2016. SW = South West, NW = North West, N = North.

### 4.3.1 HYSPLIT Analysis for Select VOC Spikes

16 distinct "spikes" in total VOC concentrations were observed in 2016 (Figure 25)marine. Trajectories that passed over several source areas were characterized temporally, according to the most time spent over one trajectory.

**Table 10** provides the dates during which these spikes were observed, the HYSPLIT trajectory for each spike as well as the "source". To categorize the source, each trajectory's path was examined, and if the trajectory passed over a populated area (i.e. city or industrial zone), it was considered to be industrial, if it passed over forest/areas of

low population, it was considered terrestrial, and if it was a marine trajectory, the source was considered marine. Trajectories that passed over several source areas were characterized temporally, according to the most time spent over one trajectory.

**Table 10.** Source sectoring of air-mass back trajectories on Sable Island for select days during 2016. HYSPLIT = Trajectories following zones in Figure 25. Source = Trajectories characterized by population density/industrial activity. SW = South West, NW = North West, N = North.

| Spike | Date (yyyy-mm-dd) | HYSPLIT | Source |
|---|---|---|---|
| **1** | 2016-05-08 | Marine | Marine |
| **2** | 2016-05-24 | Marine | Marine |
| **3** | 2016-06-08 | SW | Anthropogenic |
| **4** | 2016-06-13 | NW | Terrestrial |
| **5** | 2016-06-29 | Marine | Marine |
| **6** | 2016-07-08 | Marine | Marine |
| **7** | 2016-07-16 | SW | Anthropogenic |
| **8** | 2016-07-29 | NW | Terrestrial |
| **9** | 2016-08-14 | N | Anthropogenic |
| **10** | 2016-08-22 | Marine | Marine |
| **11** | 2016-08-27 | Marine | Marine |
| **12** | 2016-09-08 | Marine | Marine |
| **13** | 2016-09-20 | Marine | Marine |
| **14** | 2016-09-28 | Marine | Marine |
| **15** | 2016-10-10 | Marine | Marine |
| **16** | 2016-10-22 | Marine | Marine |

Overall, the spikes in total VOC concentration were mostly associated with marine sources (68.75%), followed by anthropogenic (18.75%) and terrestrial (12.5%) sources respectively (Figure 30).

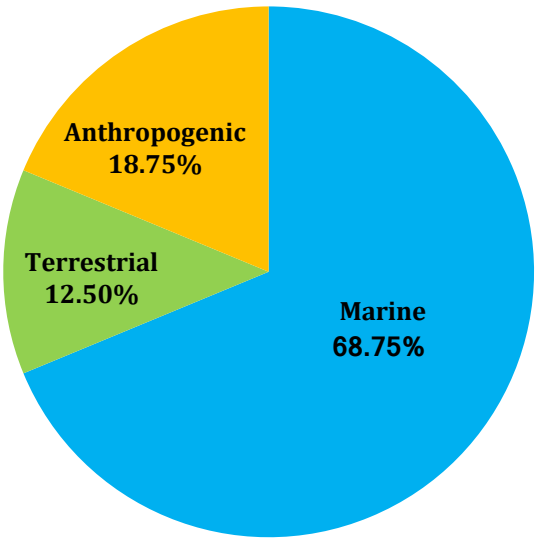


**Figure 30.** Sources of air mass back trajectories on Sable Island for select days with spikes in VOC concentrations in 2016.

Identical HYSPLIT analyses were conducted for the time period during which VOC species were measured (April, 15$^{th}$, 2016 - May 9$^{th}$, and August 13$^{th}$ - 14$^{th}$ 2016). During that period, marine sources were most common (44.44%) followed by terrestrial (25.93%) and anthropogenic (29.63%) sources respectively (Figure 31).

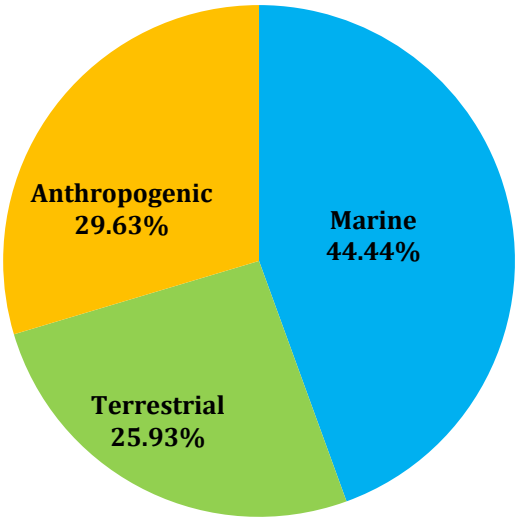


**Figure 31**. Sources of air mass back trajectories on Sable Island for days during which VOC species measurements were conducted.

### 4.4 VOC Species Meta-Analysis

TD-GC-MS was used to identify VOC species through m/*z* ratio, retention time, NIST libraries and standards. Figures 32-36 provide examples of sample runs, including a control showing no VOCs, an internal standard run showing deuterated 1,4-dichlorobenzene, a calibration curve for Toluene, and two sample runs showing dimethyl disulfide and bromomethane. Where applicable, the top panel (Relative Abundance vs Time) shows the chromatogram produced, and the bottom panel (Relative Abundance vs m/z) shows the mass spectrum. In cases where compounds are present (Figures 34-36), a third window is opened (bottom right of the figure), showing a library of possible compounds, the chemical structure of the identified compound and the probability of a correct match.

The most commonly detected VOCs are listed alphabetically in Table 11 and assigned to one or more likely sources; marine, anthropogenic, or terrestrial, based on previously published literature. A "(?)" was used to indicate the best possible source based on chemical composition when the literature survey was insufficient in determining the source.

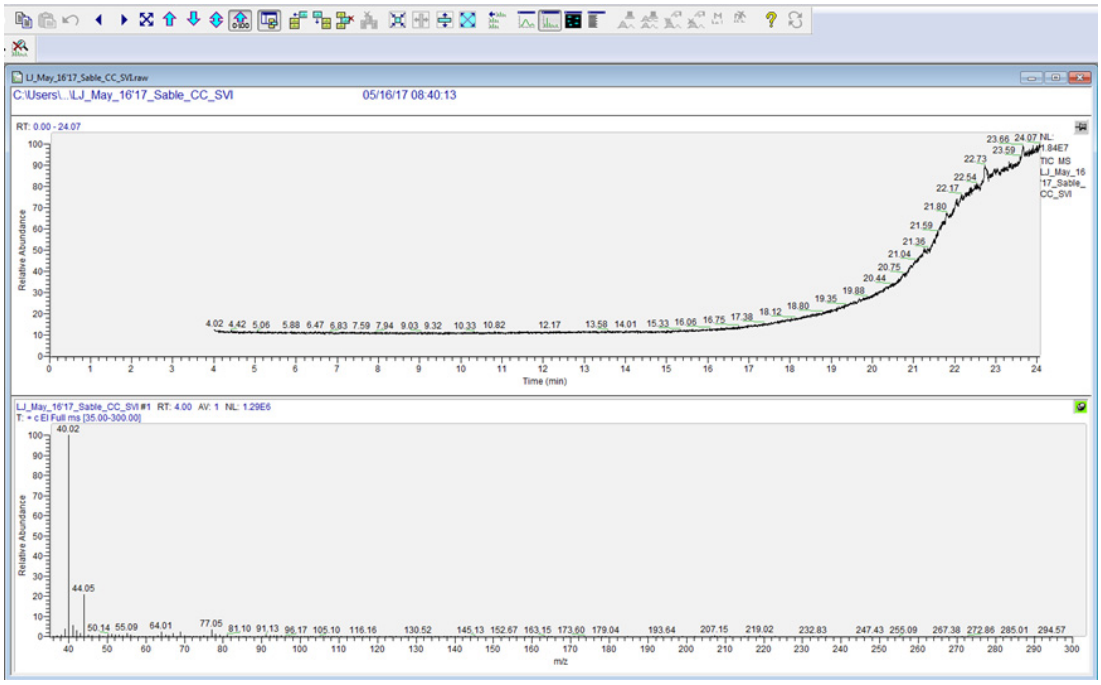


**Figure 32.** A sample run of a control TDT, containing no VOCs.

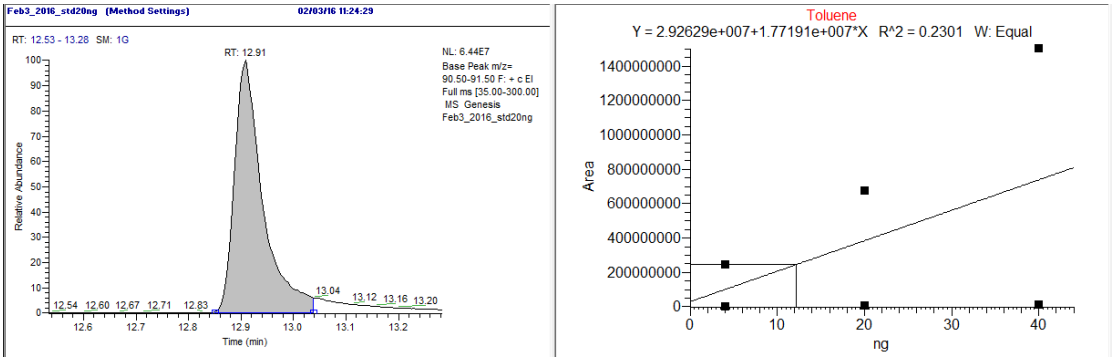


**Figure 33.** Calibration curve for Toluene. Left panel = Toluene peak, Right panel = Calibration curve.

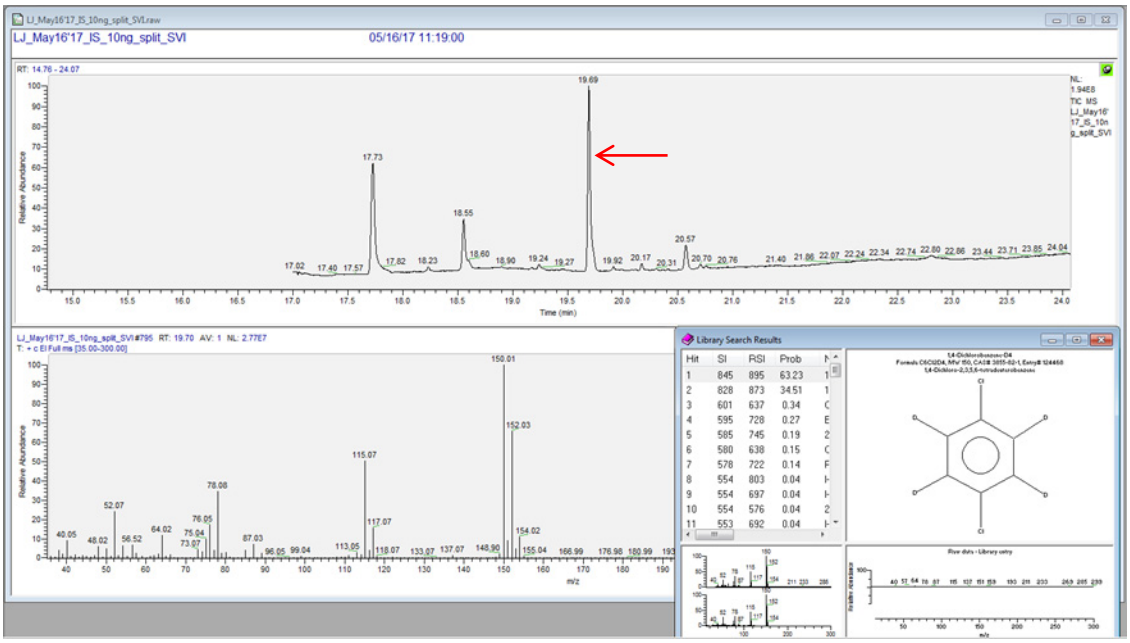


**Figure 34.** Mass spectra of an internal standard run, showing deuterated 1,4-Dichlorobenzene.

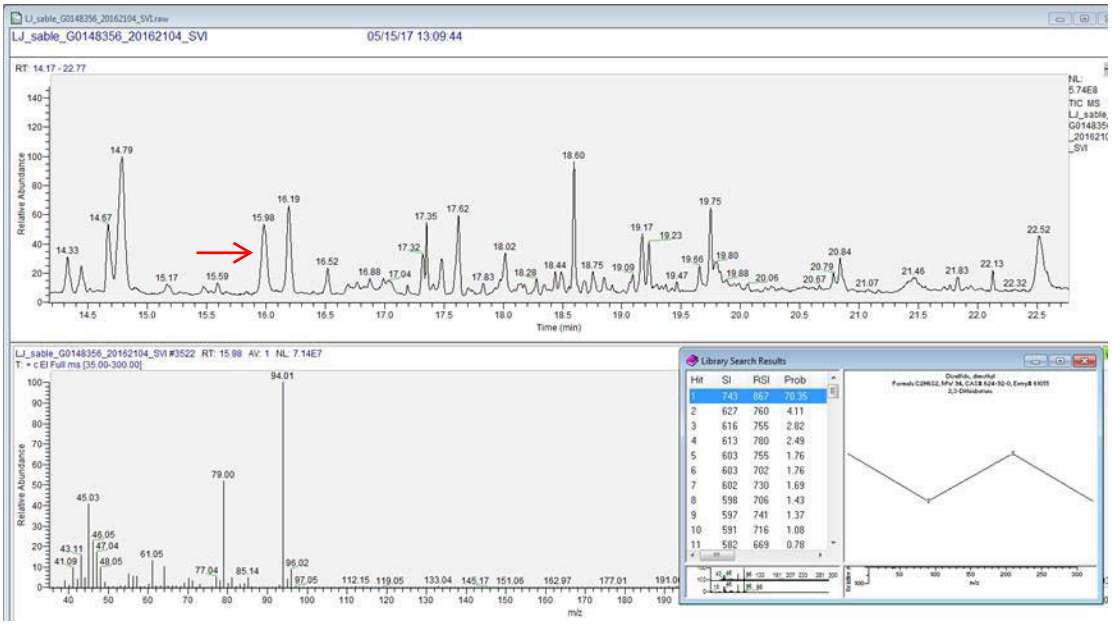


**Figure 35.** Mass spectra of a full sample run, showing Dimethyl disulfide.

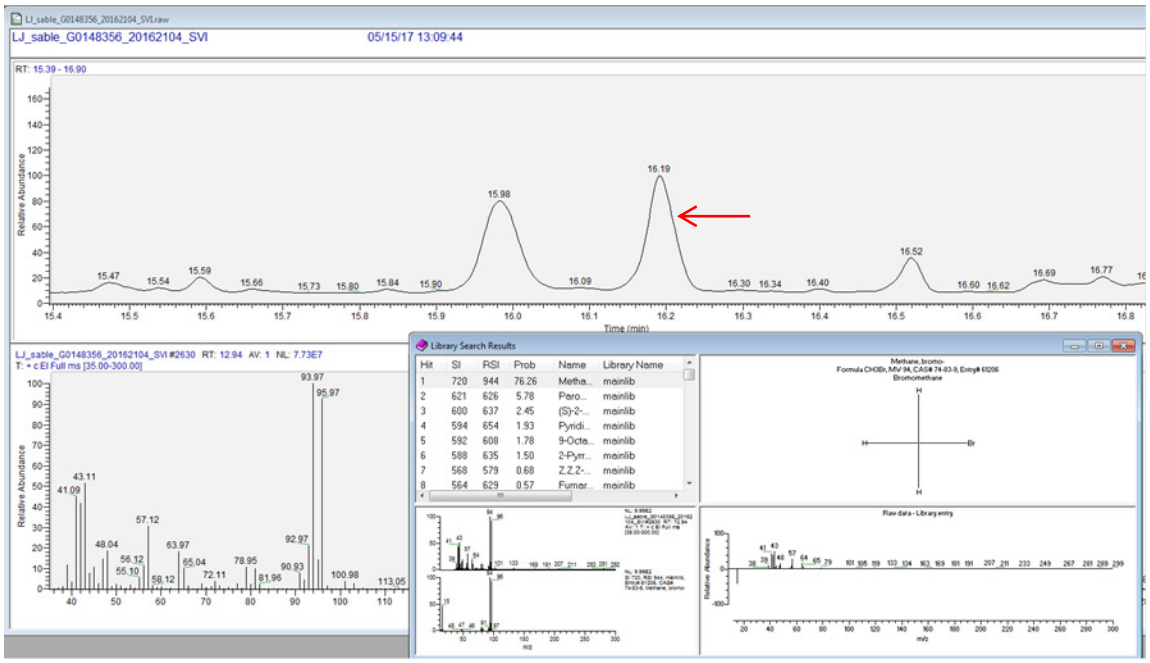


**Figure 36.** Enlarged mass spectra of a full sample run, showing Bromomethane.

**Table 11.** Possible sources of the most commonly detected compounds on Sable Island. A = Anthropogenic, M = Marine, T = Terrestrial, (?) = Most likely source.

| VOC | Source | Citation |
|---|---|---|
| 1,2-Dichlorobenzene | A/M | (Colomb et al., 2008; Howard, 1990) |
| 1-Hexanol | M / T | (Evans, 1994; Holopainen, 2004) |
| 1-Trichlorotrifuoroethane | A | (Walker et al., 2000) |
| 2-Bromoheptane | M (?) | N.A |
| 2-Bromooctadecanal | A | (Kaska et al., 1991; Yang et al., 2015) |
| 2-Chlorooctane | M | (Sabolis, 2010) |
| 3-Chlorobenzotrifluoride | M (?) | N.A |
| 4-Chloroheptane | M (?) | N.A |
| *a*-methylstyrene | A | (Miller et al., 1994) |
| *a*-pinene | M / T | (Palani et al., 2011; Sabolis, 2010) |
| Benzene | A | (Wallace, 1990) |
| Benzene-1-chloro-4-trifluoromethyl | A | (Lee et al., 2015) |
| Bromodichloromethane | M | (Goodwin et al., 1997) |
| Bromomethane | M | (Kladi et al., 2004; Moore and Tokarczyk, 1993) |
| Camphene | M / T | (Meskhidze et al., 2015; Sabolis, 2010) |
| Carbon disulfide | M | (Kim and Andreae, 1987). |
| Cumene | A | (Harrison et al., 1975) |

| | | |
|---|---|---|
| Decane | A | (Harrison et al., 1975) |
| Dichloromethane | M | (Kladi et al., 2004; Moore and Tokarczyk, 1993) |
| Dimethyl disulfide | T/ M (?) | (Trabue et al., 2008) |
| Dimethyl trisulfide | T/ M (?) | (Trabue et al., 2008) |
| Ethylbenzene | A | (Liu et al., 2005) |
| Heptanal | T/ M (?) | (Dąbrowska et al., 2014) |
| Hexanal | M / T | (Evans, 1994; Holopainen and Gershenzon, 2010) |
| m-xylene | A | (Liu et al., 2005) |
| Naphthalene | A | (Harrison et al., 1975) |
| Nonane | A | (Harrison et al., 1975) |
| Octanal | T | (Holopainen, 2004) |
| *p*-cymene | T | (Holopainen, 2004) |
| Styrene | A/ M | (Jüttner et al., 1986; Miller et al., 1994) |
| Tetrachloroethene | M | (Colomb et al., 2008; Meskhidze et al., 2015; Sabolis, 2010) |
| Tetrachloromethane | A | (Walker et al., 2000) |
| Thiophene | A | (Sumpter, 1944) |
| Toluene | A | (Gelencsér et al., 1997; Liu et al., 2005; White et al., 2009) |
| Trichloroethene | M | (Abrahamsson et al., 1995) |
| Tricyclene | T/ M (?) | (Jüttner et al., 1986; Spanke et al., 2001) |

From the probable emission sources listed above, it was found that marine emissions contributed the most to the VOC species (41%), followed by anthropogenic and terrestrial sources respectively (Figure 37).

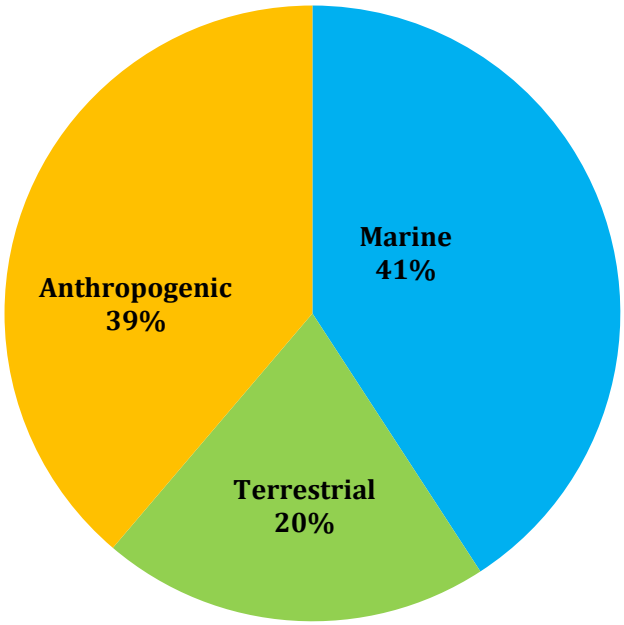


**Figure 37.** Percent contribution per category of VOC species based solely on literature survey of emission sources.

When literature-based source emissions were combined with HYSPLIT air mass back trajectories, the contribution of both marine and anthropogenic sources were equivalent at 38% each, while terrestrial sources contributed to 24% of all measured VOC species (Figure 38).

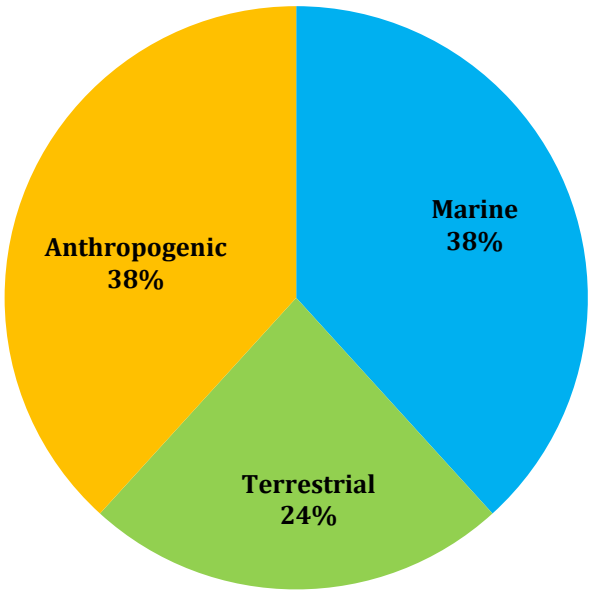


**Figure 38.** Percent contribution per category of VOC species, based on literature survey of emission sources combined with HYSPLIT air mass back trajectories.

HYSPLIT air mass back trajectory analyses were also conducted along with VOC species source emissions to calculate the percent contribution of each source to every VOC species (Figure 39). 48% of all emissions were attributed to marine sources, 40% to terrestrial sources and 11% to anthropogenic sources.

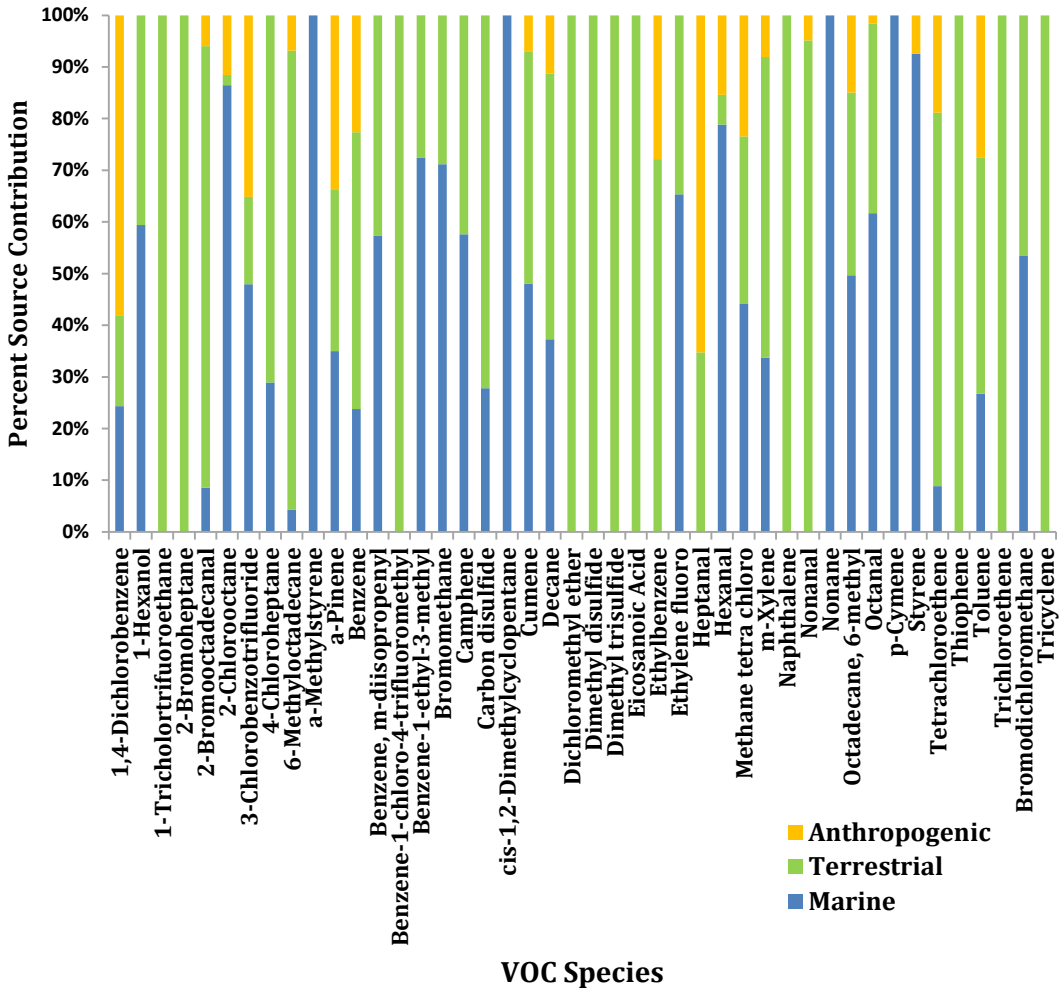


**Figure 39.** Percent contribution of the three sources to each VOC species analyzed.

Additionally, total VOC concentrations in ng/m$^3$ and µg/m$^3$ were calculated for each VOC species analyzed, and attributed to one or more of the three sources depending on its air mass back trajectory and possible emission sources (Figures 40, 41).

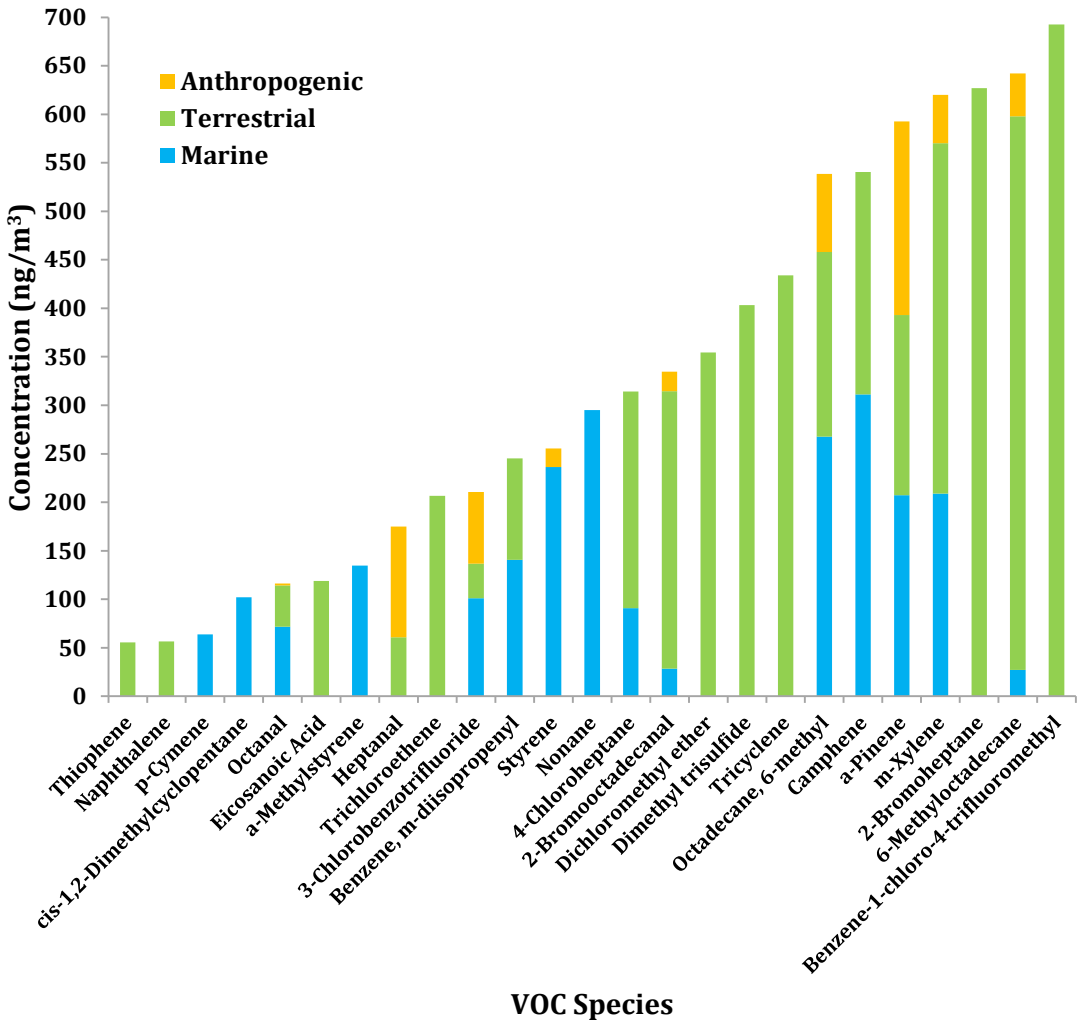


**Figure 40.** VOC source contributions to ng/m$^3$ concentrations of Thiophene, Naphthalene, p-Cymene, cis-1,2-Dimethylcyclopentane, Octanal, Eicosanoic Acid, a-Methylstyrene, Heptanal, Trichloroethene, 3-Chlorobenzotrifluoride, Benzene- m-diisopropenyl, Styrene, Nonane, 4-Chloroheptane, 2-Bromooctadecanal, Dichloromethyl ether, Dimethyl trisulfide, Tricyclene, Octadecane, 6-methyl, Camphene, a-Pinene, m-Xylene, 2-Bromoheptane, 6-Methyloctadecane and Benzene-1-chloro-4-trifluoromethyl.

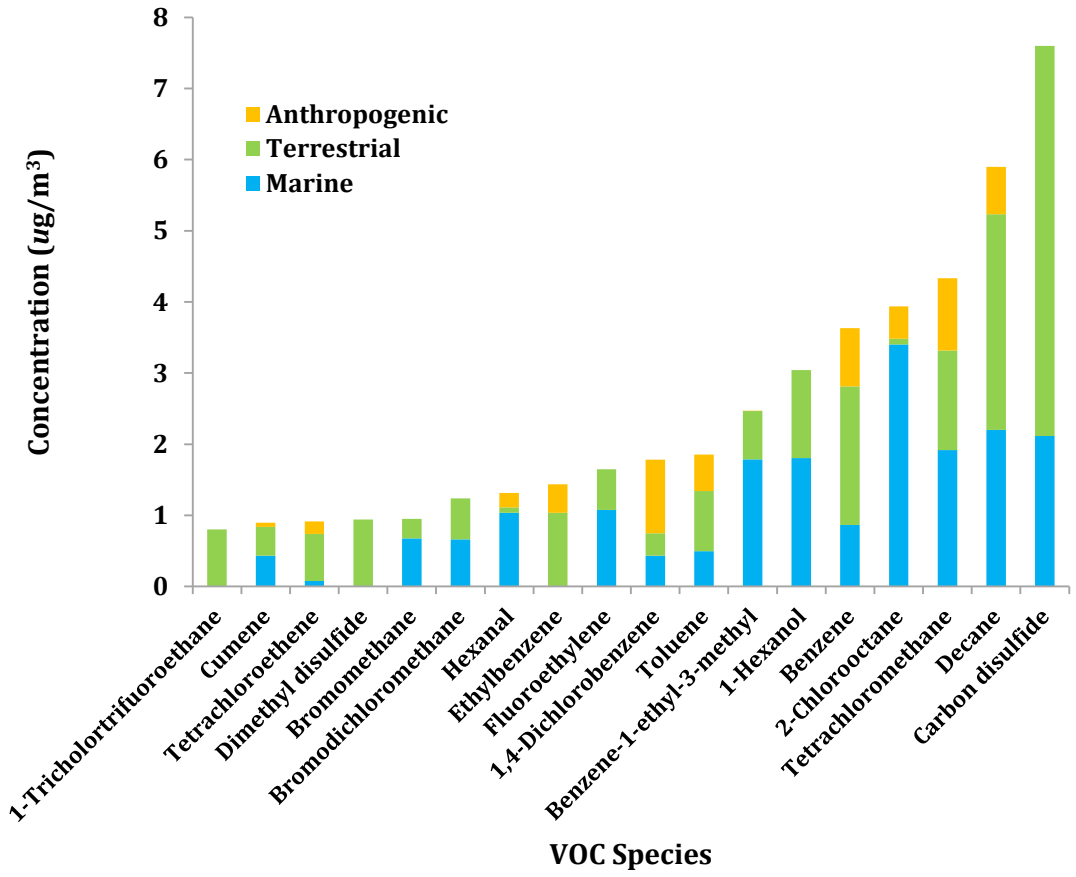


**Figure 41.** VOC source contributions to µg/m$^3$ concentrations of 1-Tricholortrifuoroethane, Cumene, Tetrachloroethene, Dimethyl disulfide, Bromomethane, Bromodichloromethane, Hexanal, Ethylbenzene, Fluoroethylene, 1,4-Dichlorobenzene, Toluene, Benzene-1-ethyl-3-methyl, 1-Hexanol, Benzene, 2-Chlorooctane, Tetrachloromethane, Decane and Carbon disulfide.

### 4.5 Remote Sensing

The images below capture *Chl-a* concentration around Sable Island, corresponding to spikes in VOC concentrations measured on the island. Warmer colors (e.g. yellows, oranges and reds) signify high photosynthetic activity, while colder colors (e.g. blues and violets) represent low photosynthetic activity (Figure 42).

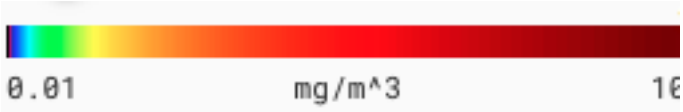


**2016-05-12 (Spike 1)**

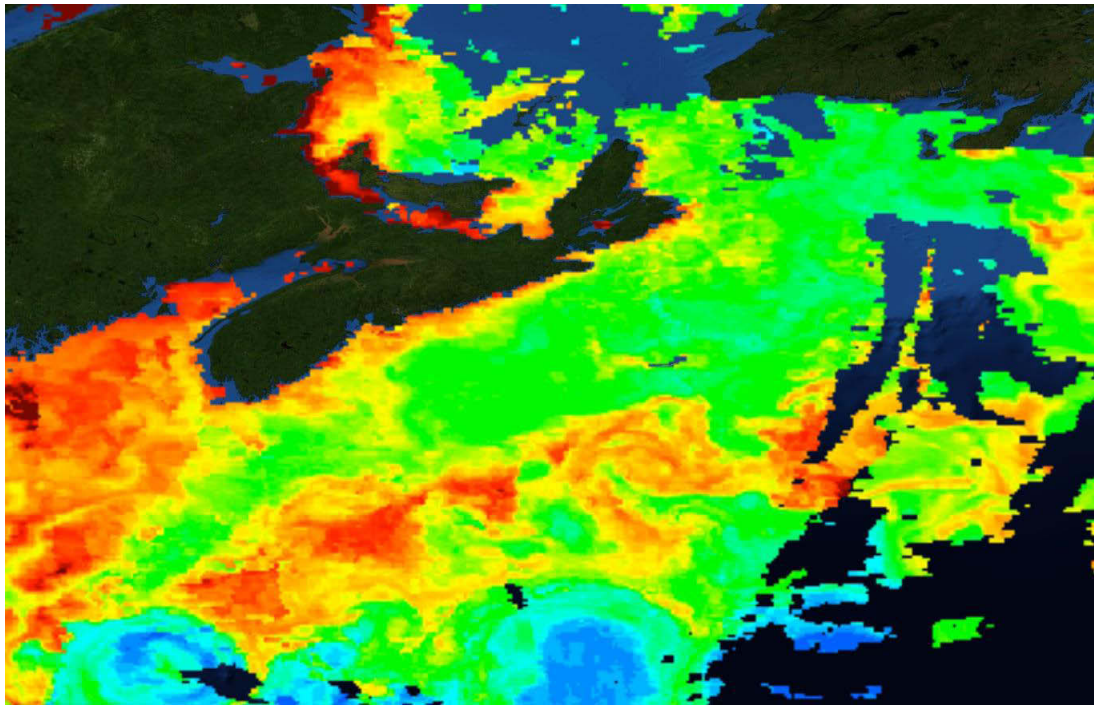

**2016-05-23 (Spike 2)**

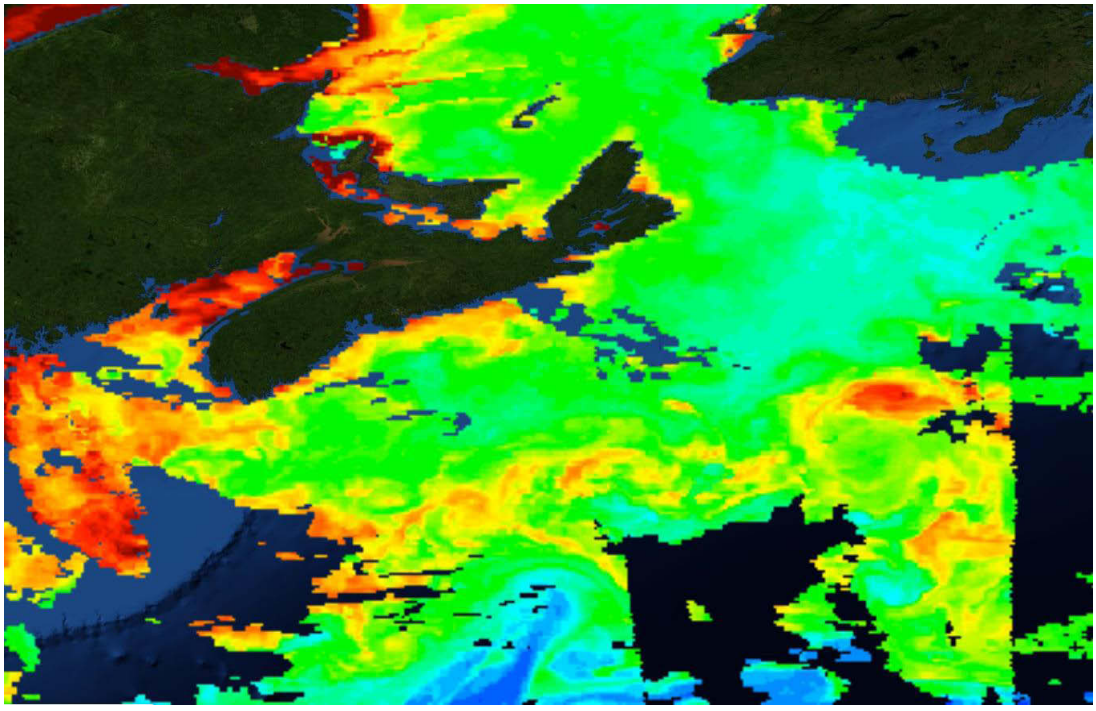

**2016-06-03 (Spike 3)**

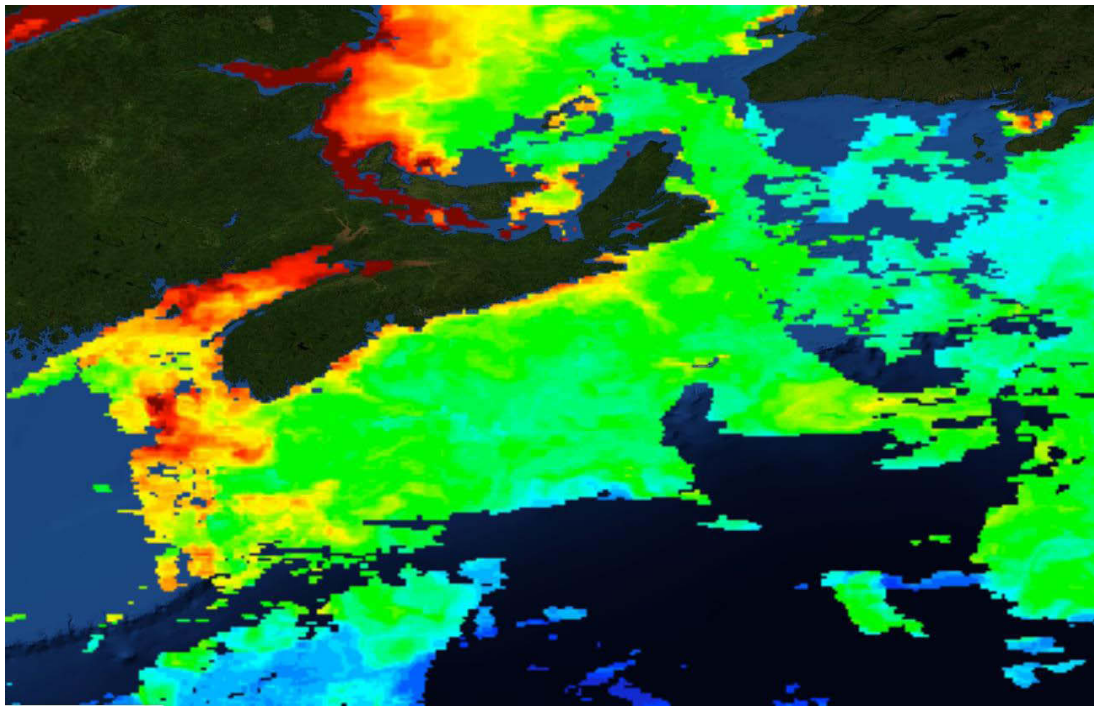

**2016-06-18 (Spike 4)**

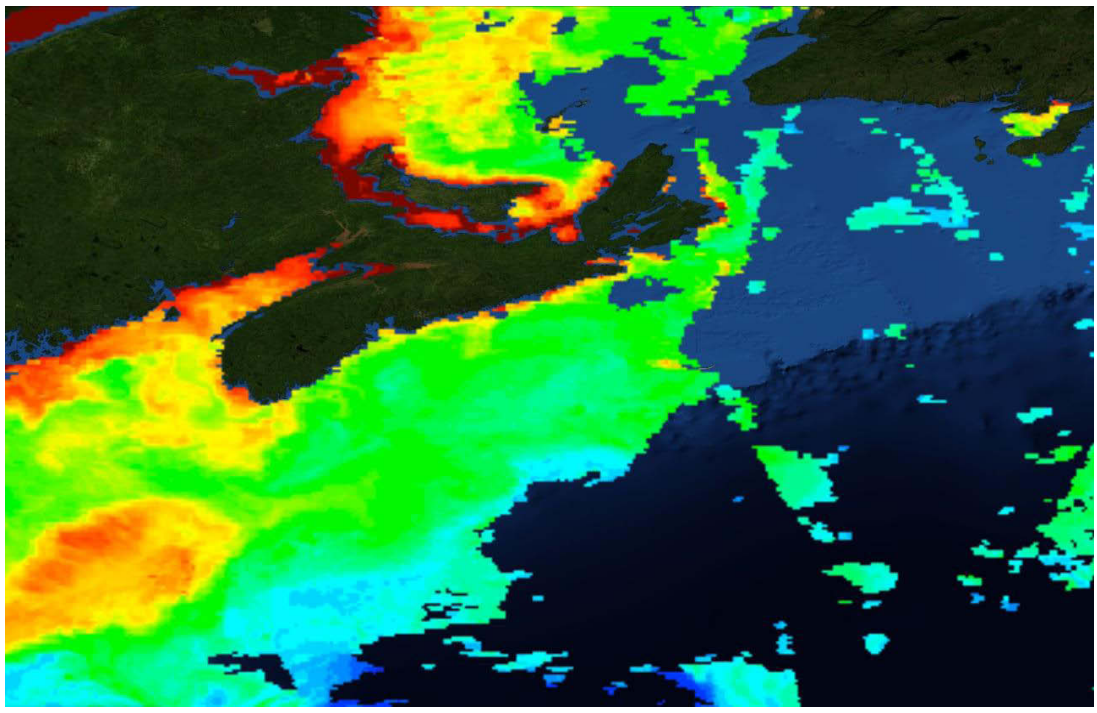

**2016-07-01 (Spike 5)**

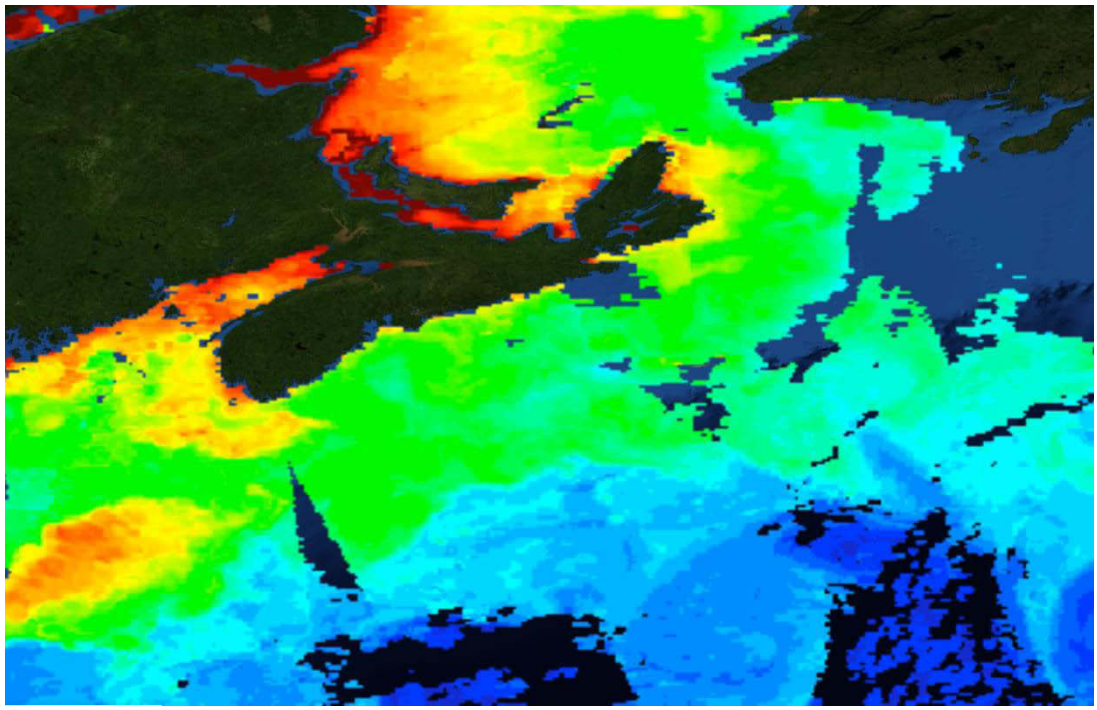

**2016-07-13 (Spike 6)**

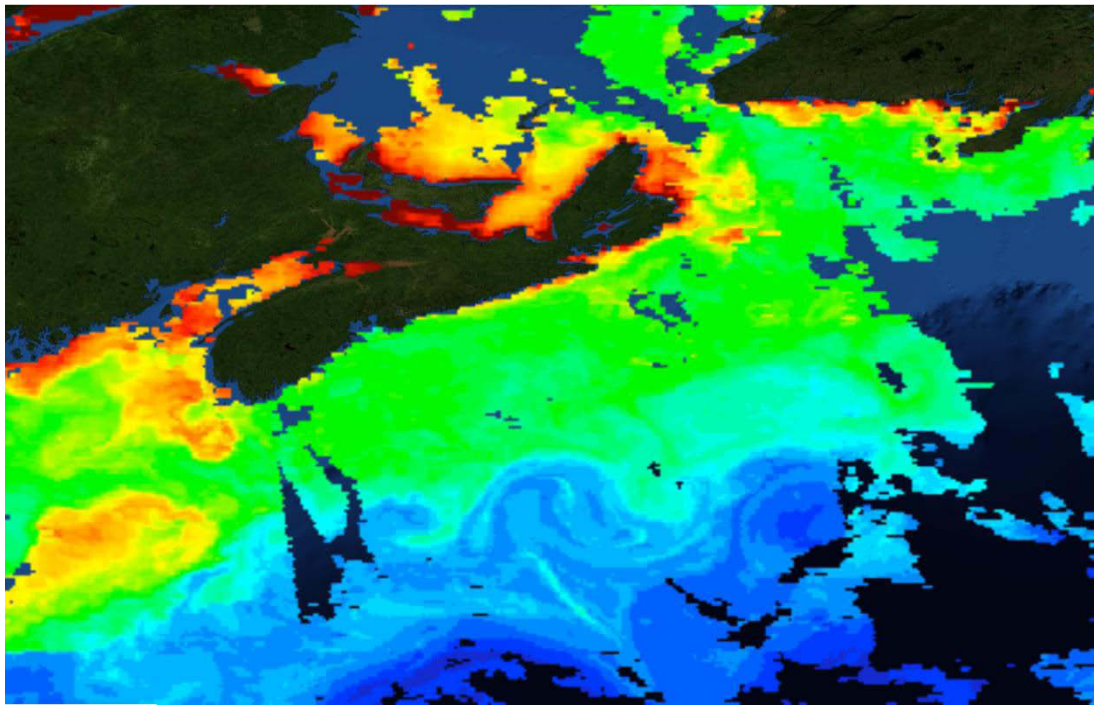

**2016-07-16 (Spike 7)**

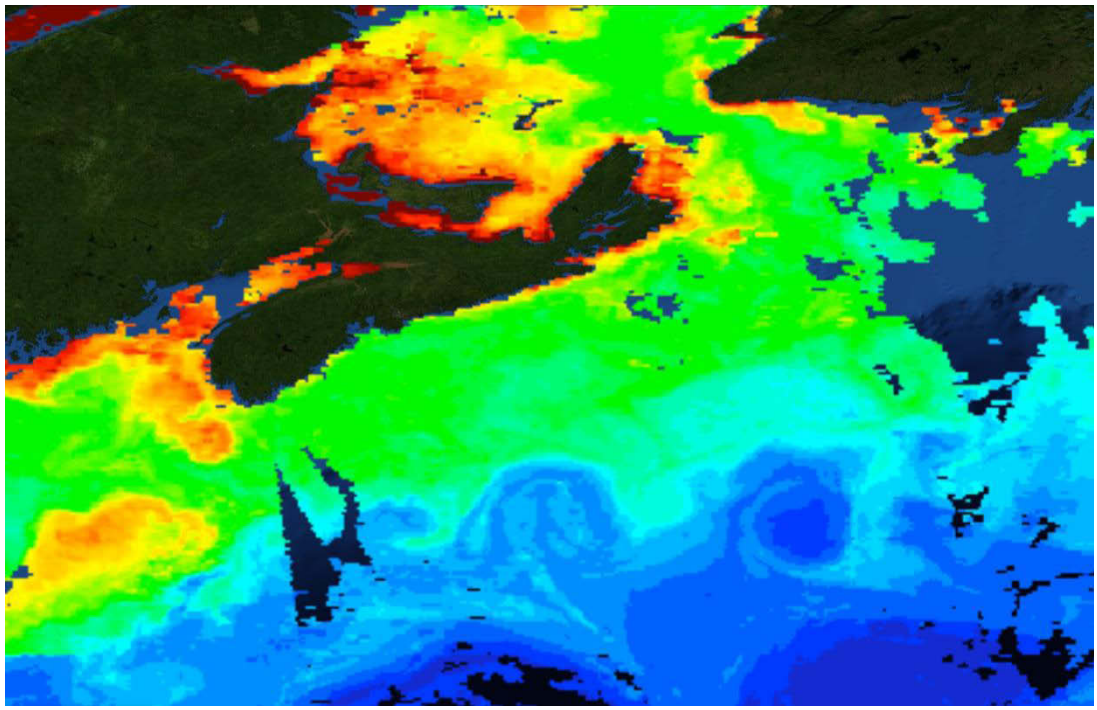

**2016-07-25 (Spike 8)**

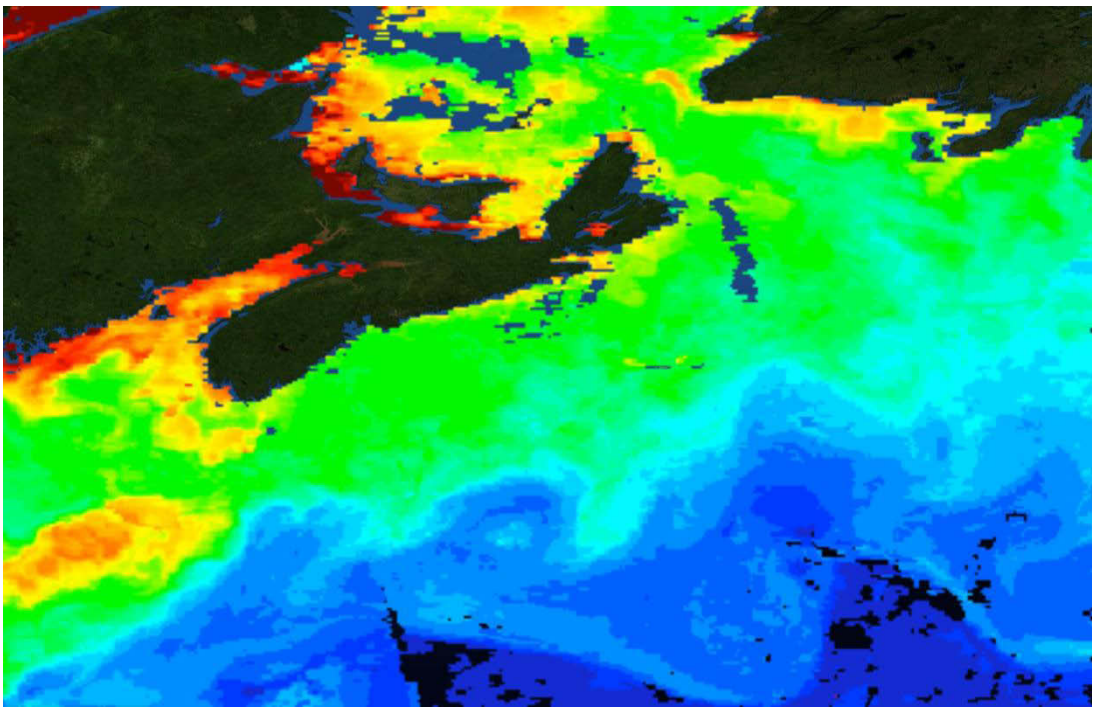

**2016-08-11 (Spike 9)**

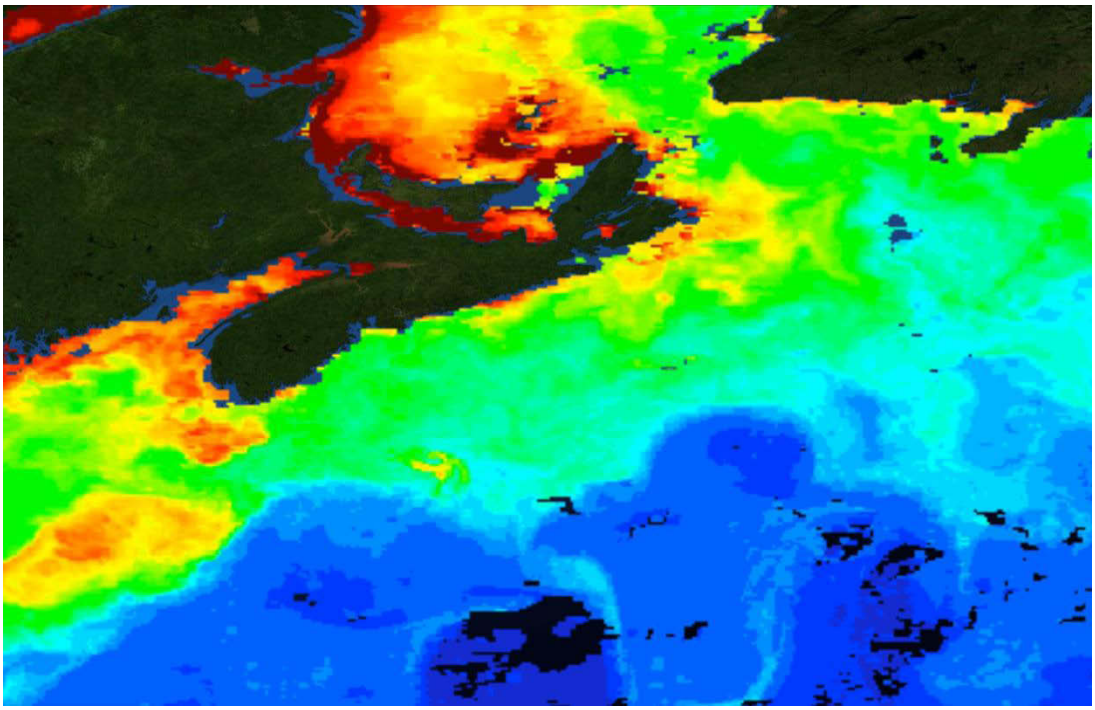

**2016-08-24 (Spike 10)**

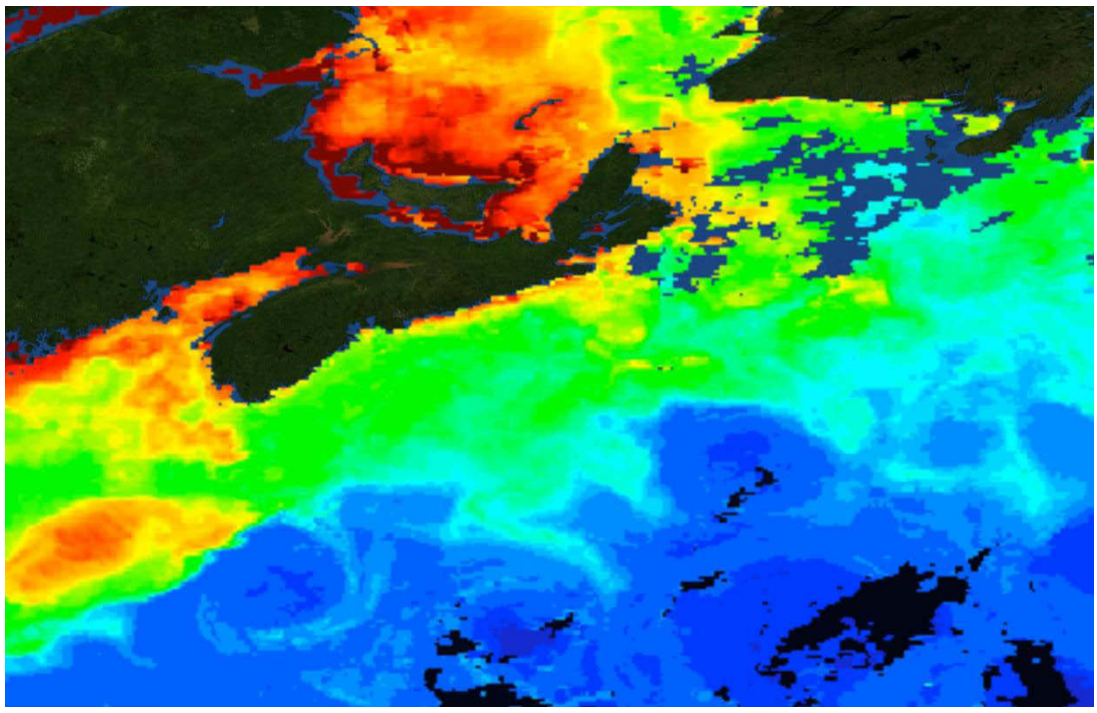

**2016-08-27 (Spike 11)**

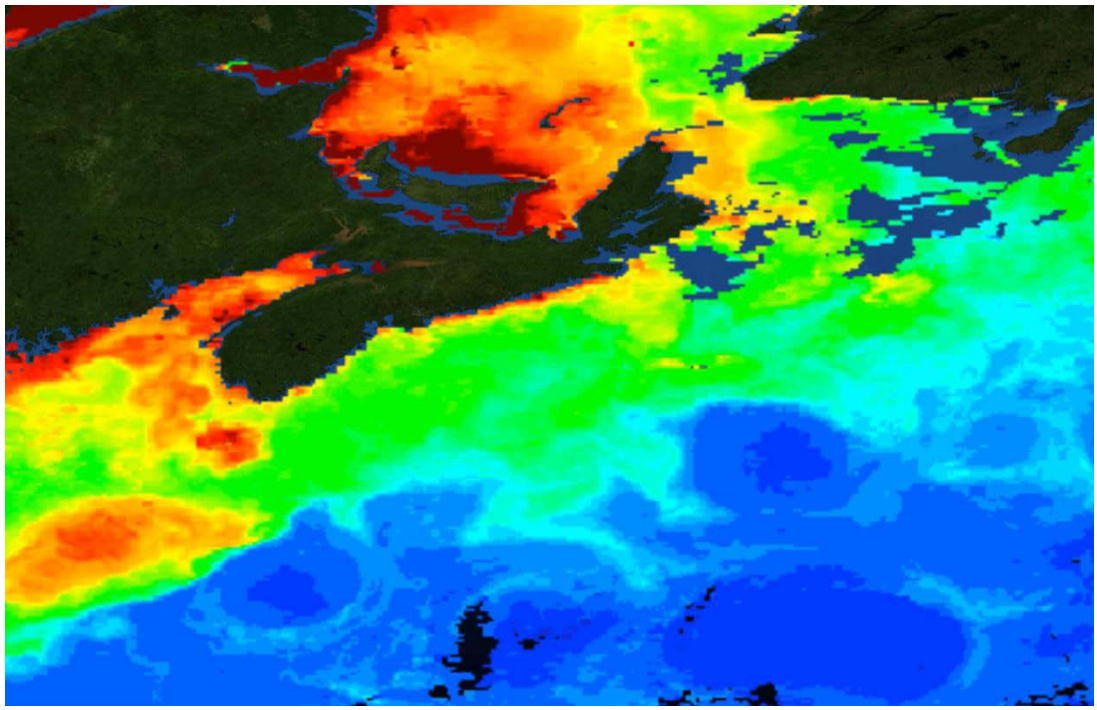

**2016-09-12 (Spike 12)**

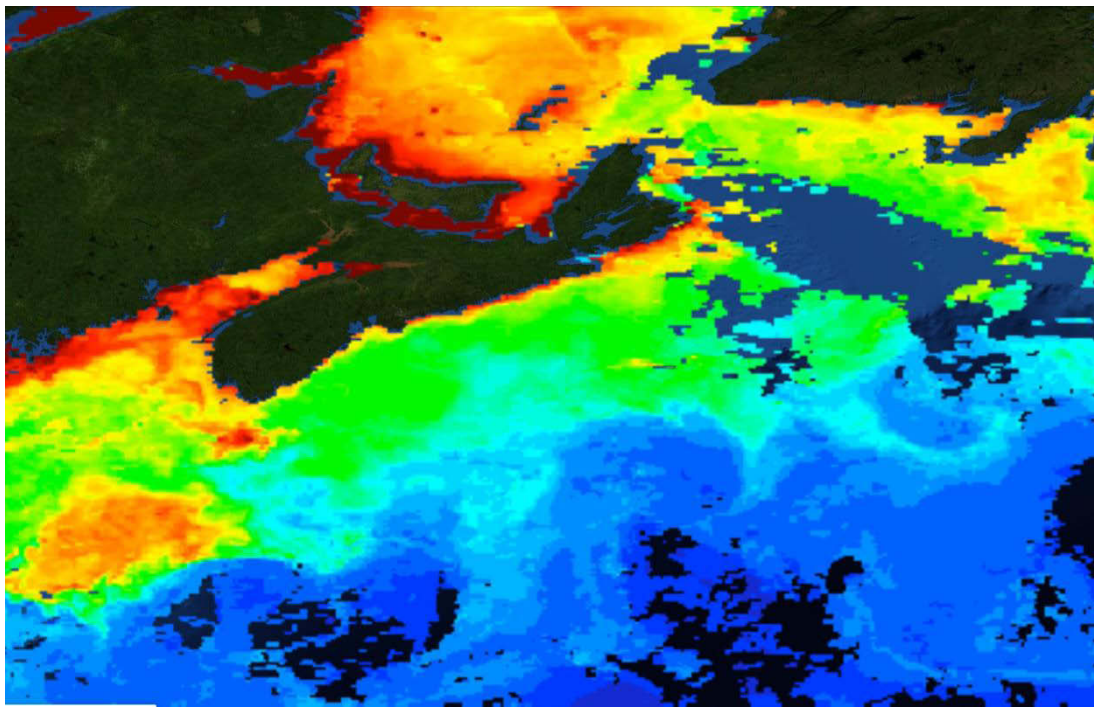

**2016-09-18 (Spike 13)**

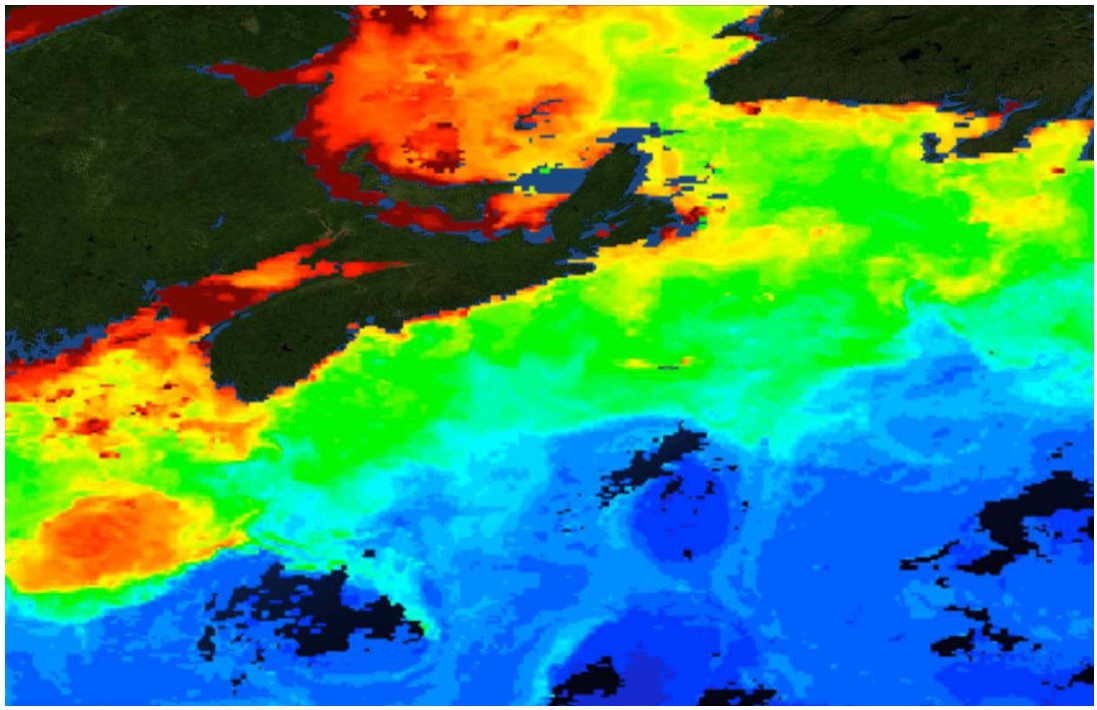

**2016-09-26 (Spike 14)**

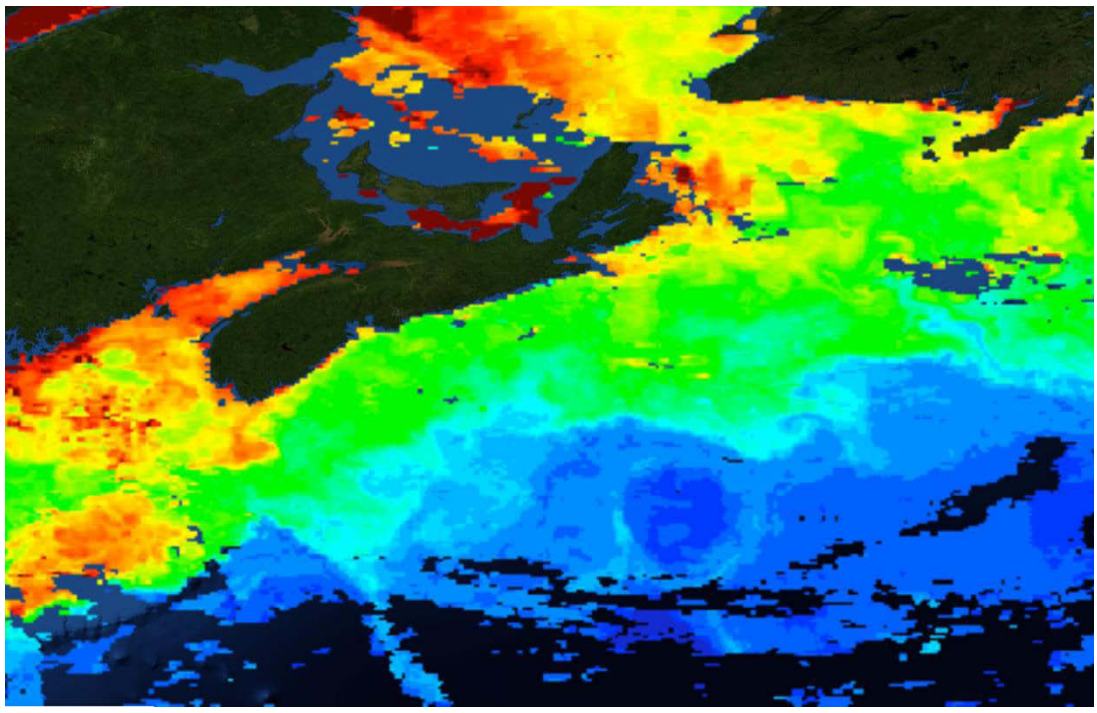

**2016-10-10 (Spike 15)**

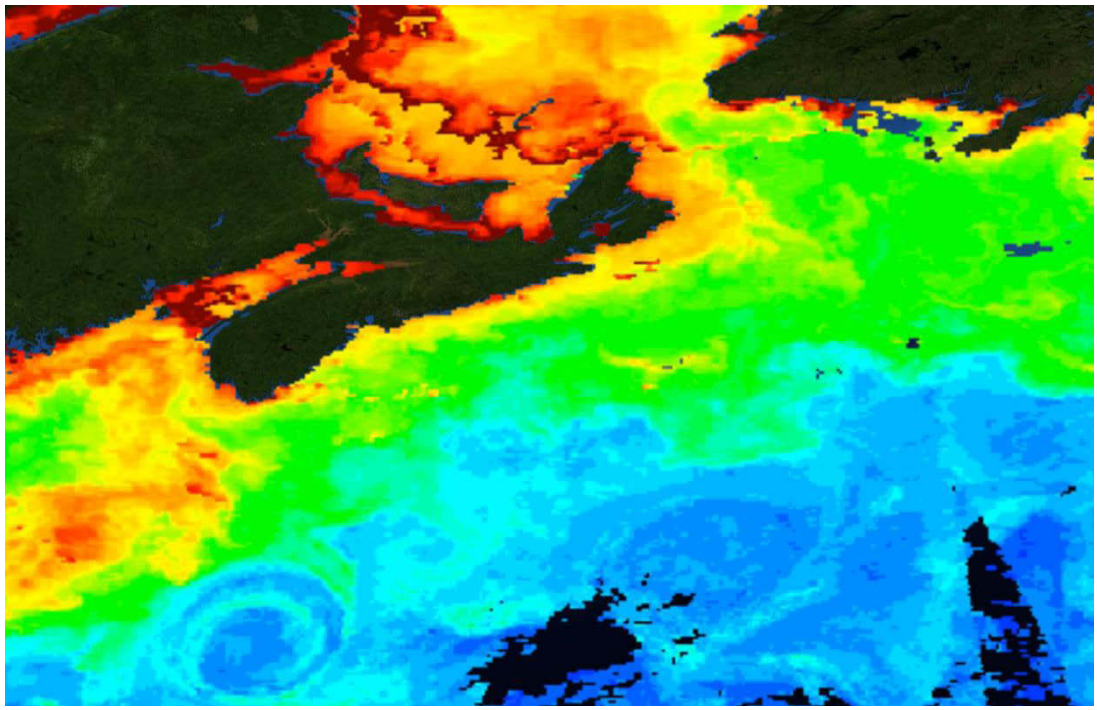

**2016-10-22 (Spike 16)**

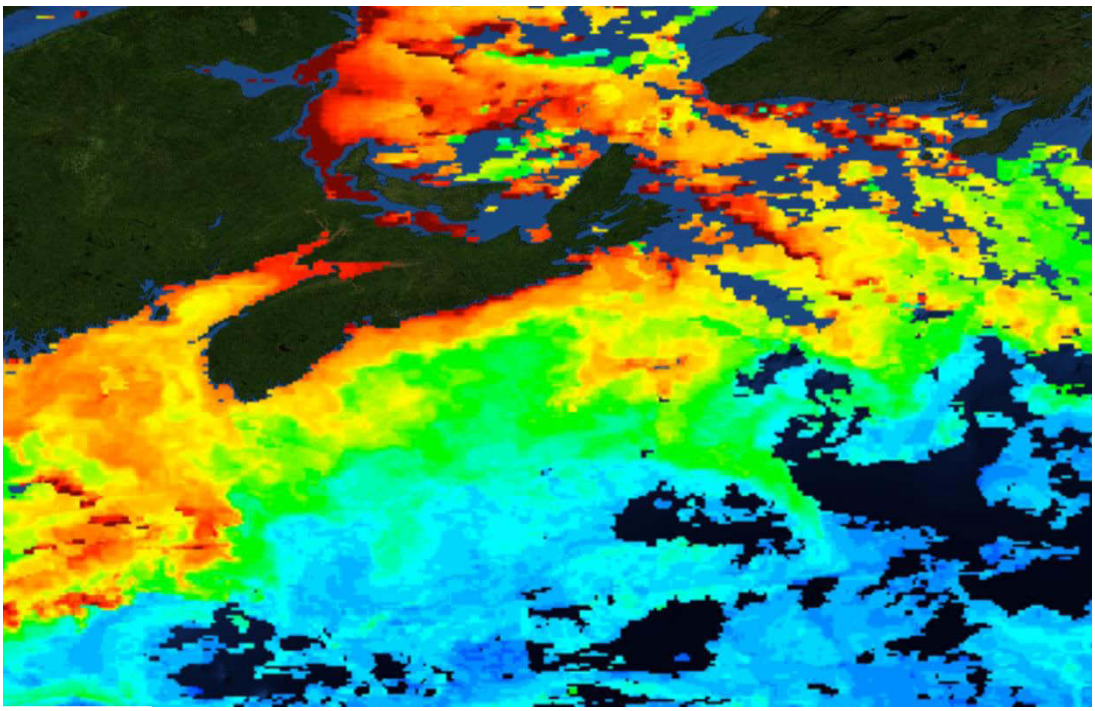

**Figure 42.** 16 separate MODIS-Aqua chlorophyll-*a* concentration images around Sable Island for periods corresponding to spikes in VOCs.

# CHAPTER 5 DISCUSSION

The purpose of this study was to analyze long-term temporal trends in total marine volatile organic compound (VOC) emissions on Sable Island and to use an amalgamation of scientific tools to identify and separate VOC species into their appropriate emission sources.

## 5.1 Meteorology

The temperature profile on Sable Island was relatively mild during winter months considering its Northern Atlantic location (Table 3). This is in part due to the island's proximity to the Gulf Stream, which exposes the island to warmer waters and wind (Taylor and Stephens, 1998). A similar temperature trend was also observed in 2015 (Qadoumi, 2016), except the mean annual temperature in 2016 (9.43°C) was 0.4°C warmer than in the 2015 study.

Interestingly, the seemingly unnatural maximum temperature of 53.8°C also appeared in 2015, and a review of online weather data sources confirmed this unusual value. With that said, an instrument malfunction is a probable cause for this error (Forbes, 2017- personal communication), and outliers were taken into consideration during data analysis.

As expected, local wind blew in a general WSW direction into Sable Island (Figure 16), consistently with previous wind patterns experienced on Sable Island and the Maritimes (Barnett, 2016; Qadoumi, 2016; Waugh et al., 2010). This is also confirmed with the HYSPLIT model for long range wind direction, showing that local wind often blew from a WSW direction, regardless of the previous pathway taken (Figure 43). Wind

speed was not fully examined in this study; however, it may be beneficial to inspect the relationship between wind and marine emissions as higher wind speeds can cause an increased rate of wave breaks, contributing to a higher release of VOC from the ocean's surface (Turner et al., 1996).

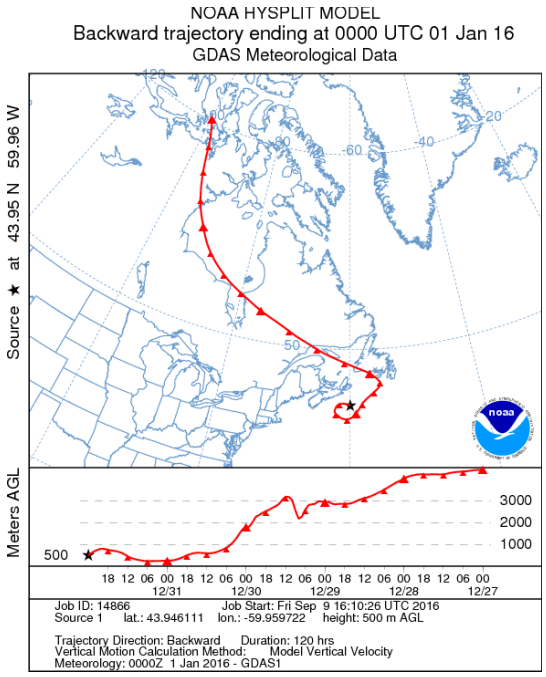


**Figure 43.** An example of NOAA HYSPLIT model showing a northern long range direction with a local WSW direction.

### 5.2 Temporal Patterns in VOC Concentrations

To my knowledge, this is the first study to examine long-term temporal trends of total marine VOC emissions. Distinct seasonal variations were measured where spring and summer had significantly higher VOC concentrations than autumn and winter. The increase in VOCs during the spring coincides with the annual northern Atlantic phytoplankton spring bloom, which has been observed for many years (Craig et al., 2015; Mahadevan et al., 2012; Siegel et al., 2002). Remote sensing data also show a substantial amount of chlorophyll-*a* around Sable Island on May 12$^{th}$, 2016 (Figure 44), signifying

high phytoplankton presence. This occurs around the same time period during which the first sharp increase in VOC concentrations was observed (Figure 25). Additionally, laboratory and mesocosm studies show that increases in phytoplankton populations carry with them a rise in physiological and chemical reactions (Turner et al., 1996), further supporting the relationship between total VOCs and phytoplankton observed in this study.

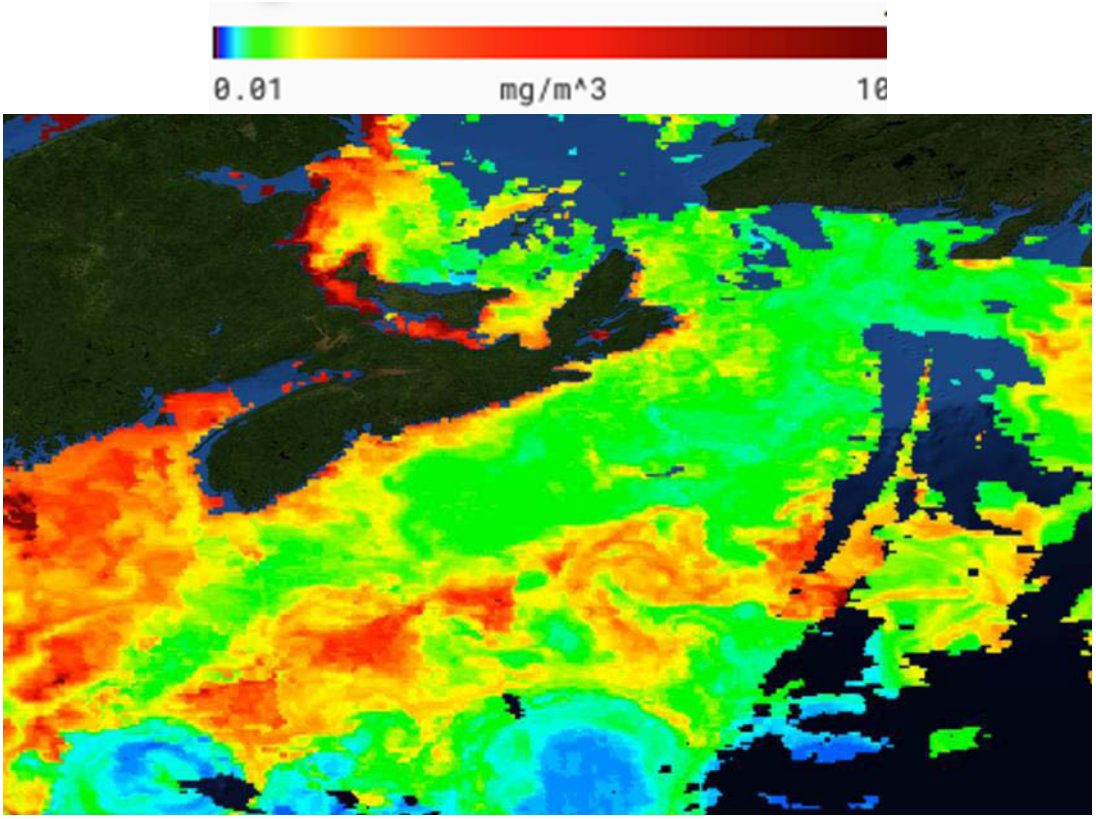


**Figure 44.** MODIS-Aqua chlorophyll-*a* concentrations showing substantial phytoplankton presence around Sable Island on May 12th, 2016.

Following the spring season, summer had the largest spikes and highest VOC concentrations of all seasons, with the highest concentration peaking at 20,029 ppb on August 22nd, 2017. Interestingly however, remote sensing data show a marked decrease in *chl-a* concentration during this period (Figure 42), suggesting that phytoplankton presence is reduced. This decrease in *chl-a* was also observed by Craig et al. (2015), and they noted that the comparatively low *chl-a* concentration during this period (< 1 mg $m^{-3}$) does not reflect the maximum numerical abundance of small cells and dinoflagellates observed consistently over the long-term Atlantic Zone Monitoring Program (AZMP; http://www.meds-sdmm.dfo-mpo.gc.ca/isdm-gdsi/azmp-pmza/index-eng.html). In other words, the intracellular chlorophyll concentration of small cells is very low compared to the large diatom cells that dominate the spring bloom. Therefore, even when present in very high numbers, bulk chlorophyll concentration will remain relatively low. Dinoflagellate numerical abundance also reaches its maximum in this period, but their numbers are orders of magnitude less than the small cells. It is probable that the high numerical abundance of these small cells contributes to the peak VOC concentrations observed in this late summer period.

It should also be noted that the shallow mixed layer depth (~9 m) during the summer period (Craig et al. 2015) forces the phytoplankton to stay in high irradiance conditions near the surface and may induce photo-acclimation that is known to reduce intracellular chlorophyll (MacIntyre et al., 2002; Moore et al., 2006). This is a common phenomenon also exhibited by terrestrial plants when exposed to strong sunlight (Østrem et al., 2015).

Strong diurnal fluctuations of total VOCs were most apparent during summer months, with concentrations peaking during the day and early afternoon (Figures 21-24). This can be explained by phytoplankton's dependence on light and their increased photosynthetic activity with light availability. However, a large portion of phytoplankton emissions are not released by regular metabolic activity, but instead when cells are under physical, chemical or biological stress (Meskhidze et al., 2015). Tamburic et al. found that phytoplankton exhibit photosystem damage around mid-day due to intense sunlight and temperatures, better explaining the diurnal spikes in VOC concentrations seen in this study (Tamburic et al., 2014). Furthermore, a somewhat puzzling "bump" was consistently observed later in the afternoon in diurnal total VOC plots (Figure 45). These spikes coincide with periods of high physiological activity by phytoplankton and increased cell death, which can cause phytoplankton to release more volatile compounds (Berges and Falkowski, 1998; Veldhuis et al., 2001). The phytoplankton assemblage during this period is also strongly associated with a recycling system (Ward et al., 2012) with high rates of grazing by micro-zooplankton that, along with the likely stress caused by high irradiance and low nutrients, may contribute to the VOC inventory.

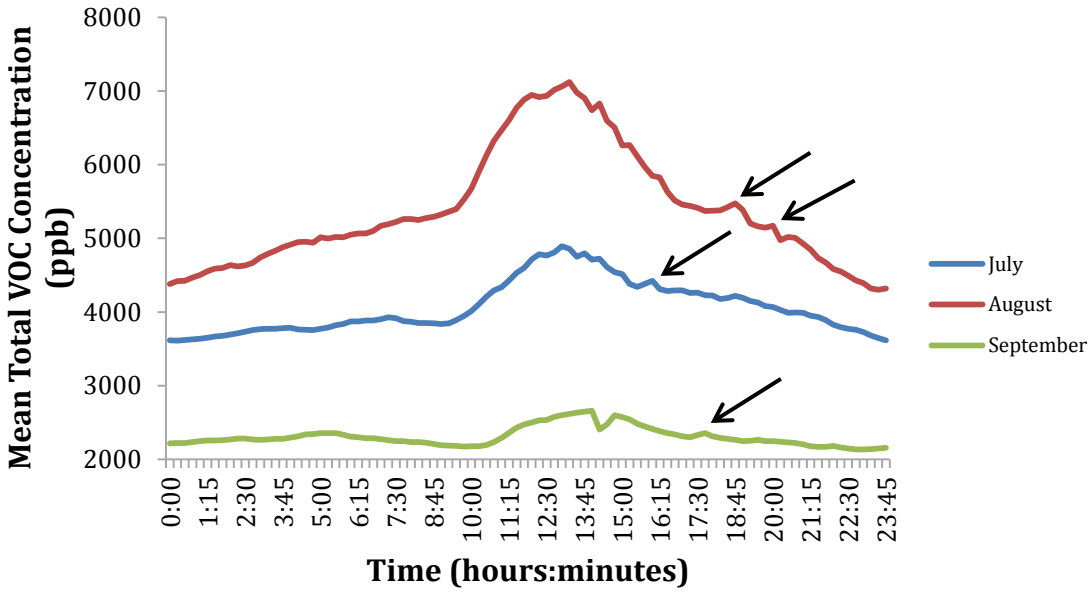


**Figure 45.** Example of VOC "bumps" in the later afternoon hours in July, August and September.

Further evidence of phytoplankton emission of VOCs is seen in the close relationship between temporal variations in temperature and changes in total VOC concentrations (Figure 46). This is further supported by the positive correlation between small (pico- and nano-) phytoplankton concentration and temperature shown by Craig et al. (2015) and the increased rate of gas emissions in warmer water (Wiebe and Gaddy, 1940).

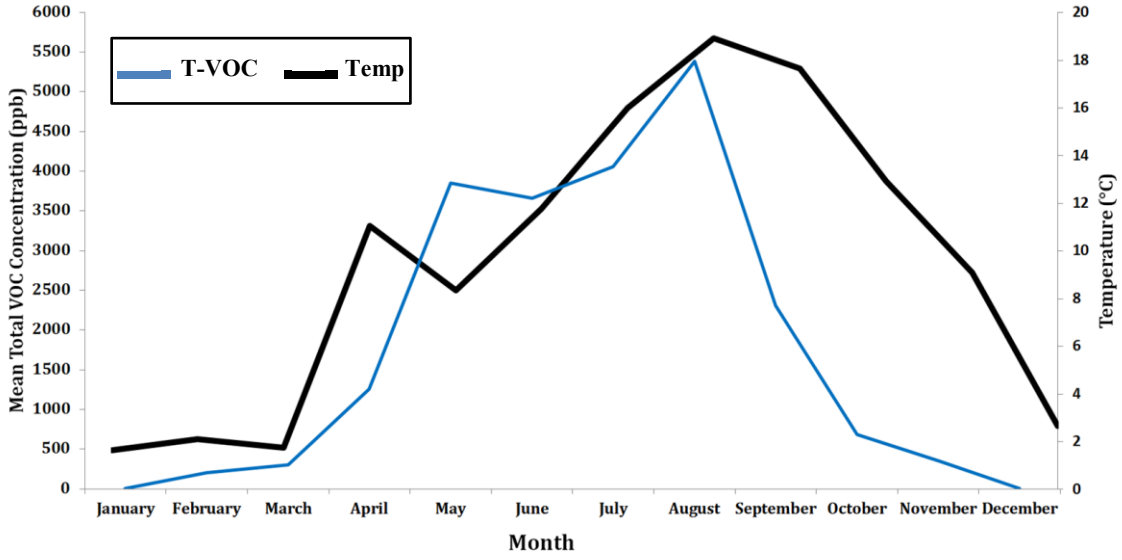


**Figure 46.** Temperature (°C) and Total VOC (T-VOC) concentration (ppb) in 2016 plotted against a common timeline (month).

Nevertheless, increases in temperature during the spring and summer seasons also bring with them a rise in terrestrial biogenic emissions (Seco et al., 2011), forest fires and anthropogenic activity; all of which can be sources of VOCs on Sable Island. Further inspection of VOCs and source sector analysis is, therefore, required.

### 5.3 Source Sector Analysis

A twice-daily Hybrid Single-Particle Lagrangian Integrated Trajectory (HYSPLIT) model showed that only 26.03 % of air trajectories passed solely over marine environments before reaching Sable Island in 2016 (Figure 27), with the rest of the trajectories passing over terrestrial and anthropogenic sources of VOCs; however, spring and summer seasons had significantly higher marine trajectories (~35%) than the other seasons (Figures 28, 29). When total VOC spikes were cross-examined with HYSPLIT analyses, it was shown that they were mostly associated with marine sources (68.75%),

followed by anthropogenic (18.75%) and terrestrial (12.5%) sources respectively (Figure 30). When HYSPLIT air mass back trajectories were cross-examined with specific VOC species identified using GC-MS, it was found that marine and anthropogenic sources contributed to 38% each to the total emissions and terrestrial sources contributed to 24% (Figures 38, 39). This apparent discrepancy can be due to several reasons.

The presence of offshore oil and gas platforms around Sable Island is likely to contribute to the total VOC concentrations measured in this study. Platforms Deep Panuk, Alma and Thebaud are located up wind of the island (based on wind patterns discussed previously) (Figure 47), and would be considered as 'Marine' sources using HYSPLIT analysis. Nonetheless, crude oil and refined fuel related compounds such as 2-bromooctadecanal, cumene and thiophene do not have natural marine sources, and it would therefore be incorrect to consider them as marine emissions.

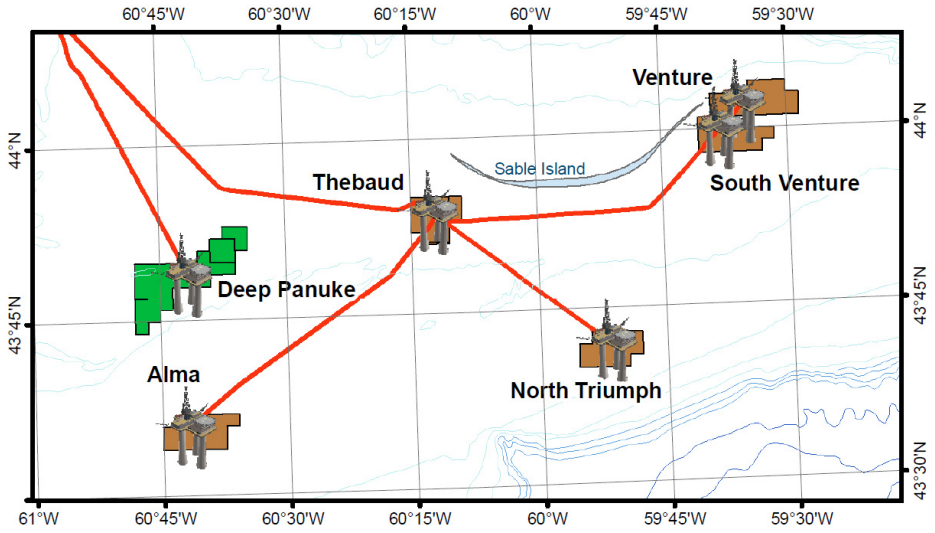


**Figure 47.** Map of oil and gas platforms surrounding Sable Island. (Canada-Nova Scotia Offshore Petroleum Board, http://www.cnsopb.ns.ca/pdfs/sable_area_platforms.pdf

Many VOC species also have several sources of emission and complex chemistry. For example, *a*-pinene is a compound produced widely by coniferous trees, has been shown to be emitted by marine algae (Sabolis, 2010); and 1-hexanol, a compound known for its "freshly cut grass" scent, can be produced by terrestrial and marine photosynthetic organisms (Evans, 1994); with air mass back trajectories showing both *a*-pinene and 1-hexanol to originate mostly from marine and mainland sources. While all of these sources are viable, both of the compounds have relatively short atmospheric lifetimes (Montenegro et al., 2012), which greatly reduces the amount reaching Sable Island from far terrestrial sources and increasing the likelihood of them being local emissions. Additionally, 1-hexanol may be released from damaged grass on the island due to grazing by horses or local insects (Scala et al., 2013), and some sulfur containing compounds including dimethyl disulfide may be emitted by horse feces; especially considering the

regular close proximity of horses to the instruments used in this study (Garner et al., 2007) (Figure 48). With that said, it is difficult to determine the true sources of compounds without considering all possible emitters, keeping in mind that all of the air mass back trajectories pass over at least 290 km of marine environments before reaching Sable Island, regardless of their original source.

**Figure 48.** Sable Island horses only meters away from the air chemistry building and air measurement instruments (Photo: Loay Jabre).

Marine biogenic VOCs are also notoriously difficult to analyse. Not only are they difficult to collect (i.e. chloromethane); many of them undergo rapid and complex chemical reactions when released into the atmosphere. For example, carbon disulfide, identified in this study as a mostly terrestrial VOC with substantial marine emissions (Figure 41), has been found in north Atlantic marine environments but has presented challenges in its identification and separation from DMS since it was first detected in

1971 (Kim and Andreae, 1987) - DMS was not detected in this study, but its presence is synonymous with phytoplankton blooms.

There is noteworthy phytoplankton activity in the winter months in the north Atlantic due to the uptake of nutrients in deep-ocean mixing (Behrenfeld, 2010; Eppley, 1972; Mahadevan et al., 2012). However, VOCs from these populations were not detected by our instruments. In addition to the relatively small phytoplankton concentration in winter, this can be explained by the less frequent calibration and maintenance trips during the winter because of bad weather, and several malfunctions of the instrument in December and January. Continuous, real-time identification and quantification of VOC species combined with Positive Matrix Factorization (PMF) models would help resolve these discrepancies, but due to logistical and technical issues and lack of funding, it was impossible to install an appropriate instrument on Sable Island for this study.

# CHAPTER 6 CONCLUSIONS AND RECOMMENDATIONS

## 6.1 Conclusions

A year-long study of total VOCs and air mass back trajectories as well as an intensive inspection of VOC species and remote sensing data were conducted on Sable Island, Nova Scotia, for 2016. Monthly and seasonal trends in VOC concentrations correlated strongly with temperature trends and phytoplankton blooming patterns, and were further supported by distinct diurnal patterns, showing elevated VOC concentrations during daytime and afternoon hours. Air mass back trajectories for periods of total VOC spikes throughout the year concluded that 68.75% of sources were from marine paths, while 18.75% originated from anthropogenic sources and 12.5% from natural terrestrial emissions. However, due to the presence of oil and gas platforms around Sable Island and the multi-source emissions of several compounds inspected, a meta-analysis of source emissions and HYSPLIT was conducted and concluded that 48% of emissions were marine, 11% were anthropogenic, and 40% were from natural terrestrial sources.

These results highlight the complex nature of air measurement studies, and offer useful insight into the presence of various compounds from numerous sources, even when performing remote region research. The tantalizing evidence of phytoplankton contribution to climate relevant VOCs along with obvious seasonal patterns in marine biogenic emissions show a possible link to water column structure and/or dominant phytoplankton species. This could provide insight into future ocean scenarios and may help future researchers in reaching more accurate decisions regarding the relationship between phytoplankton emissions and atmospheric chemistry.

## 6.2 Recommendations

It would be especially beneficial for this study to have real-time or incremental (i.e. 15 minutes) measurements of VOC species on Sable Island. This can be achieved by using an Air Server-Unity2-TD-GC-MS instrument or a Proton Transfer Reaction – Mass Spectrometer (PTR-MS), which sample air directly from the environment as opposed to collection on TDTs for 24 hours and subsequent analysis. This would provide a better temporal resolution of VOC species and would aid in the collection of highly volatile species that were not detected in this study (e.g. chloromethane).

It is also recommended that quantification and peak identification to be processed with newer and more powerful software such as TraceFinder™ to increase the reliability, precision and efficiency of data collection from mass spectra.

# REFERENCES


Abrahamsson, K., Ekdahl, A., Collen, J., and Pedersen, M. (1995). Marine algae-a source of trichloroethylene and perchloroethylene. Limnol. Oceanogr. *40*, 1321–1326.

Andreae, M., and Crutzen, P.J. (1997). Atmospheric aerosols: Biogeochemical sources and role in atmospheric chemistry. Science *276*, 1052–1058.

Arthur, C.L., and Pawliszyn, J. (1990). Solid phase microextraction with thermal desorption using fused silica optical fibers. Anal. Chem. *62*, 2145–2148.

Asamany, E.A., Gibson, M.D., and Pegg, M.J. (2017). Evaluating the potential of waste plastics as fuel in cement kilns using bench-scale emissions analysis. Fuel *193*, 178–186.

Ayers, G.P., Cainey, J.M., Gillett, R.W., and Ivey, J.P. (1997). Atmospheric sulphur and cloud condensation nuclei in marine air in the Southern Hemisphere. Philos. Trans. R. Soc. Lond. B Biol. Sci. *352*, 203–211.

Barnett, C. (2016). The Source Apportionment of Airborne Particulate Matter Composition on Sable Island, Nova Scotia, Canada. M.A.Sc. Dalhousie University.

Barton, A.D., Irwin, A.J., Finkel, Z.V., and Stock, C.A. (2016). Anthropogenic climate change drives shift and shuffle in North Atlantic phytoplankton communities. Proc. Natl. Acad. Sci. *113*, 2964–2969.

Batterman, S., Metts, T., Kalliokoski, P., and Barnett, E. (2002). Low-flow active and passive sampling of VOCs using thermal desorption tubes: theory and application at an offset printing facility. J. Environ. Monit. *4*, 361–370.

Behrenfeld, M.J. (2010). Abandoning Sverdrup's critical depth hypothesis on phytoplankton blooms. Ecology *91*, 977–989.

Behrenfeld, M.J., Boss, E., Siegel, D.A., and Shea, D.M. (2005). Carbon-based ocean productivity and phytoplankton physiology from space: PHYTOPLANKTON GROWTH RATES AND OCEAN PRODUCTIVITY. Glob. Biogeochem. Cycles *19*.

Behrenfeld, M.J., O'Malley, R.T., Siegel, D.A., McClain, C.R., Sarmiento, J.L., Feldman, G.C., Milligan, A.J., Falkowski, P.G., Letelier, R.M., and Boss, E.S. (2006). Climate-driven trends in contemporary ocean productivity. Nature *444*, 752–755.

Belviso, S., Kim, S.-K., Rassoulzadegan, F., Krajka, B., Nguyen, B.C., Mihalopoulos, N., and Buat-Menard, P. (1990). Production of dimethylsulfonium propionate (DMSP) and dimethylsulfide (DMS) by a microbial food web. Limnol. Oceanogr. *35*, 1810–1821.

Berges, J.A., and Falkowski, P.G. (1998). Physiological stress and cell death in marine phytoplankton: induction of proteases in response to nitrogen or light limitation. Limnol. Oceanogr. *43*, 129–135.

Bigg, G.R. (2005). Ocean-atmosphere interaction. In Encyclopedia of World Climatology, (Springer), pp. 540–546.

Blanchard, D.C., and Woodcock, A.H. (1957). Bubble Formation and Modification in the Sea and its Meteorological Significance. Tellus *9*, 145–158.

Bonsang, B., Polle, C., and Lambert, G. (1992). Evidence for marine production of Isoprene. Geophys. Res. Lett. *19*, 1129–1132.

Borbon, A., Gilman, J.B., Kuster, W.C., Grand, N., Chevaillier, S., Colomb, A., Dolgorouky, C., Gros, V., Lopez, M., Sarda-Esteve, R., et al. (2013). Emission ratios of anthropogenic volatile organic compounds in northern mid-latitude megacities: Observations versus emission inventories in Los Angeles and Paris: VOC EMISSION RATIOS IN MODERN MEGACITIES. J. Geophys. Res. Atmospheres *118*, 2041–2057.

Buckley, F.S.E., and Mudge, S.M. (2004). Dimethylsulphide and ocean–atmosphere interactions. Chem. Ecol. *20*, 73–95.

Capotondi, A., Alexander, M.A., Bond, N.A., Curchitser, E.N., and Scott, J.D. (2012). Enhanced upper ocean stratification with climate change in the CMIP3 models: CLIMATE CHANGE OF OCEAN STRATIFICATION. J. Geophys. Res. Oceans *117*, n/a-n/a.

Carlton, A.G., Wiedinmyer, C., and Kroll, J.H. (2009). A review of Secondary Organic Aerosol (SOA) formation from isoprene. Atmospheric Chem. Phys. *9*, 4987–5005.

CBC (2011). Sable Island named national park. CBC News.

Charlson, R., Lovelock, J., Andreae, M.O., and Warren, S. (1987). Oceanic phytoplankton, atmospheric sulphur, cloud albedo and climate. Nature *326*, 655–661.

Christaki, U., Lefevre, D., Georges, C., Colombet, J., Catala, P., Courties, C., Sime-Ngando, T., Blain, S., and Obernosterer, I. (2014). Microbial food web dynamics during spring phytoplankton blooms in the naturally iron-fertilized Kerguelen area (Southern Ocean). Biogeosciences *11*, 6739–6753.

Cochran, R.E., Laskina, O., Trueblood, J.V., Estillore, A.D., Morris, H.S., Jayarathne, T., Sultana, C.M., Lee, C., Lin, P., Laskin, J., et al. (2017). Molecular Diversity of Sea Spray Aerosol Particles: Impact of Ocean Biology on Particle Composition and Hygroscopicity. Chem *2*, 655–667.

Colomb, A., Yassaa, N., Williams, J., Peeken, I., and Lochte, K. (2008). Screening volatile organic compounds (VOCs) emissions from five marine phytoplankton species by head space gas chromatography/mass spectrometry (HS-GC/MS). J. Environ. Monit. *10*, 325.

Copolovici, L., Kännaste, A., Pazouki, L., and Niinemets, Ü. (2012). Emissions of green leaf volatiles and terpenoids from Solanum lycopersicum are quantitatively related to the severity of cold and heat shock treatments. J. Plant Physiol. *169*, 664–672.

Craig, S., Lohrenz, S., Lee, Z., Mahoney, K., Kirkpatrick, G., Schofield, O., and Steward, R. (2006). Use of hyperspectral remote sensing reflectance for detection and assessment of the harmful alga, Karenia bervis. Appl. Opt. *45*, 5414–5425.

Craig, S.E., Jones, C.T., Li, W.K.W., Lazin, G., Horne, E., Caverhill, C., and Cullen, J.J. (2012). Deriving optical metrics of coastal phytoplankton biomass from ocean colour. Remote Sens. Environ. *119*, 72–83.

Craig, S.E., Thomas, H., Jones, C.T., Li, W.K.W., Greenan, B.J.W., Shadwick, E.H., and Burt, W.J. (2015). The effect of seasonality in phytoplankton community composition on CO2 uptake on the Scotian Shelf. J. Mar. Syst. *147*, 52–60.

Dąbrowska, A., Nawrocki, J., and Szeląg-Wasielewska, E. (2014). Appearance of aldehydes in the surface layer of lake waters. Environ. Monit. Assess. *186*, 4569–4580.

Danielsdottir, M.G., Brett, M.T., and Arhonditsis, G.B. (2007). Phytoplankton food quality control of planktonic food web processes. Hydrobiologia *589*, 29–41.

von Dassow, P., and Montresor, M. (2011). Unveiling the mysteries of phytoplankton life cycles: patterns and opportunities behind complexity. J. Plankton Res. *33*, 3–12.

Dohoo, C., Read Guernsey, J., Gibson, M.D., and VanLeeuwen, J. (2015). Impact of biogas digesters on cookhouse volatile organic compound exposure for rural Kenyan farmwomen. J. Expo. Sci. Environ. Epidemiol. *25*, 167–174.

van Drooge, B.L., Nikolova, I., and Ballesta, P.P. (2009). Thermal desorption gas chromatography–mass spectrometry as an enhanced method for the quantification of polycyclic aromatic hydrocarbons from ambient air particulate matter. J. Chromatogr. A *1216*, 4030–4039.

Duderstadt, K.A., Carroll, M.A., Sillman, S., Wang, T., Albercook, G.M., Feng, L., Parrish, D.D., Holloway, J.S., Fehsenfeld, F.., Blake, D.R., et al. (1998). Photochemical production and loss rates of ozone at Sable Island, Nova Scotia during the North Atlantic Regional Experiment (NARE) 1993 summer intensive. J. Geophys. Res. *103*, 13531–13555.

ECCC (2013). Volatile Organic Compounds (VOCs).

ECCC (2016). Volatile Organic Compound Emissions.

Ekdahl, A., Pedersén, M., and Abrahamsson, K. (1998). A study of the diurnal variation of biogenic volatile halocarbons. Mar. Chem. *63*, 1–8.

Elbir, T., Cetin, B., Cetin, E., Bayram, A., and Odabasi, M. (2007). Characterization of Volatile Organic Compounds (VOCs) and Their Sources in the Air of Izmir, Turkey. Environ. Monit. Assess. *133*, 149–160.

Engelhart, G.J., Asa-Awuku, A., Nenes, A., and Pandis, S.N. (2008). CCN activity and droplet growth kinetics of fresh and aged monoterpene secondary organic aerosol. Atmospheric Chem. Phys. *8*, 3937–3949.

Eppley, R. (1972). Temperature and phytoplankton growth in the sea. Fish. Bull. *70*, 1063–1085.

Evans, W.G. (1994). Volatile organic chemicals of a shore-dwelling cyanobacterial mat community. J. Chem. Ecol. *20*, 219–230.

Falkowski, P.G., Katz, M.E., Knoll, A.H., Quigg, A., Raven, J.A., Schofield, O., and Taylor, F.J.R. (2004). The evolution of modern eukaryotic phytoplankton. Science *305*, 354–360.

Forster, C., Wandinger, U., Wotawa, G., James, P., Mattis, I., Althausen, D., Simmonds, P., Jager, H., and Stohl, A. (2001). Transport of boreal forest fire emissions from Canada to Europe. J. Geophys. Res. *106*, 22887–22906.

Fournier, R.O., Marra, J., Bohrer, R., and Det, M.V. (1977). Plankton dynamics and nutrient enrichment of the Scotian Shelf. J. Fish. Board Can. *34*, 1004–1018.

Friedland, K.D., Record, N.R., Asch, R.G., Kristiansen, T., Saba, V.S., Drinkwater, K.F., Henson, S., Leaf, R.T., Morse, R.E., Johns, D.G., et al. (2016). Seasonal phytoplankton blooms in the North Atlantic linked to the overwintering strategies of copepods. Elem. Sci. Anthr. *4*, 000099.

Garner, C.E., Smith, S., de Lacy Costello, B., White, P., Spencer, R., Probert, C.S.J., and Ratcliffe, N.M. (2007). Volatile organic compounds from feces and their potential for diagnosis of gastrointestinal disease. FASEB J. *21*, 1675–1688.

Gelencsér, A., Siszler, K., and Hlavay, J. (1997). Toluene- benzene concentration ratio as a tool for characterizing the distance from vehicular emission sources. Environ. Sci. Technol. *31*, 2869–2872.

Gibson, M., Guernsey, J.., Beauchamp, S., Waugh, D., Heal, M.R., Brook, J., Maher, R., Gagnon, G.., Bryden, B., McPherson, J., et al. (2009a). Quantifying the Spatial and Temporal Variation of Ground-Level Ozone in the Rural Annapolis Valley, Nova Scotia, Canada Using Nitrite-Impregnated Passive Samplers. J. Air Waste Manag. Assoc. *59*, 310–320.

Gibson, M.D., Heal, M.R., Bache, D.H., Hursthouse, A.S., Beverland, I.J., Craig, S.E., Clark, C.F., Jackson, M.H., Guernsey, J.R., and Jones, C. (2009b). Using Mass Reconstruction along a Four-Site Transect as a Method to Interpret $PM_{10}$ in West-Central Scotland,United Kingdom. J. Air Waste Manag. Assoc. *59*, 1429–1436.

Gibson, M.D., Pierce, J.R., Waugh, D., Kuchta, J.S., Chisholm, L., Duck, T.J., Hopper, J.T., Beauchamp, S., King, G.H., Franklin, J.E., et al. (2013). Identifying the sources driving observed $PM_{2.5}$ temporal variability over Halifax, Nova Scotia, during BORTAS-B. Atmospheric Chem. Phys. *13*, 7199–7213.

Gibson, M.D., Haelssig, J., Pierce, J.R., Parrington, M., Franklin, J.E., Hopper, J.T., Li, Z., and Ward, T.J. (2015). A comparison of four receptor models used to quantify the boreal wildfire smoke contribution to surface $PM_{2.5}$ in Halifax, Nova Scotia during the BORTAS-B experiment. Atmospheric Chem. Phys. *15*, 815–827.

Goodwin, K.D., North, W.J., and Lidstrom, M.E. (1997). Production of bromoform and dibromomethane by giant kelp: factors affecting release and comparison to anthropogenic bromine sources. Limnol. Oceanogr. *42*, 1725–1734.

Hader, D., and Schafer, J. (1994). Photosynthetic oxygen production of macroalgae and phytoplankton under solar irradiation*. J. Plant Physiol. *144*, 293–299.

Harrison, W., Winnik, M.A., Kwong, P.T., and Mackay, D. (1975). Crude oil spills. Disappearance of aromatic and aliphatic components from small sea-surface slicks. Environ. Sci. Technol. *9*, 231–234.

Hayes, A. (2014). Source apportionment of air quality on Sable Island. M.A.Sc. Dalhousie University.

He, N.P., Han, X.G., and Pan, Q.-M. (2005). Variations in the Volatile Organic Compound Emission Potential of Plant Functional Groups in the Temperate Grassland Vegetation of Inner Mongolia, China. J. Integr. Plant Biol. *47*, 13–19.

Herman, J.., Bhartia, P.., Ziemke, J., Ahmad, Z., and Larko, D. (1996). UV-B increases (1979-1992) from decreases in total ozone. Geophys. Res. Lett. *23*, 2117–2120.

Hilal, S.H., Karickhoff, S.W., and Carreira, L.A. (2003). Prediction of the Vapor Pressure Boiling Point, Heat of Vaporization and Diffusion Coefficient of Organic Compounds. QSAR Comb. Sci. *22*, 565–574.

Holopainen, J. (2004). Multiple functions of inducible plant volatiles. Trends Plant Sci. *9*, 529–533.

Holopainen, J.K., and Gershenzon, J. (2010). Multiple stress factors and the emission of plant VOCs. Trends Plant Sci. *15*, 176–184.

Howard, P.. (1990). Handbook of Environmental Fate and Exposure Data for Organic Chemiclas (Lewis Publishers, Chelsea, Michigan).

Jactel, H., Kleinhentz, M., Marpeau-Bezard, A., Marion-Poll, F., Menassieu, P., and Burban, C. (1996). Terpene variations in maritime pine constitutive oleoresin related to host tree selection byDioryctria sylvestrella RATZ.(Lepidoptera: Pyralidae). J. Chem. Ecol. *22*, 1037–1050.

Jardillier, L., Zubkov, M.V., Pearman, J., and Scanlan, D.J. (2010). Significant CO2 fixation by small prymnesiophytes in the subtropical and tropical northeast Atlantic Ocean. ISME J. *4*, 1180–1192.

Jenkins, W.J., and Goldman, J.C. (1985). Seasonal oxygen cycling and primary production in the Sargasso Sea. J. Mar. Res. *43*, 465–491.

Jüttner, F., Höflacher, B., and Wurster, K. (1986). Seasonal analysis of volatile organic biogenic substances (VOBS) in freshwater phytoplankton populations dominated by Dinobryon, Microcystis and Aphanizomenon. J. Phycol. *22*, 169–175.

Karlik, J.F., McKay, A.H., Welch, J.M., and Winer, A.M. (2002). A survey of California plant species with a portable VOC analyzer for biogenic emission inventory development. Atmos. Environ. *36*, 5221–5233.

Kaska, D.D., Polne-Fuller, M., and Gibor, A. (1991). Biotransformation of alkanes and haloalkanes by a marine amoeba. Appl. Microbiol. Biotechnol. *34*, 814–817.

Kiendler-Scharr, A., Wildt, J., Maso, M.D., Hohaus, T., Kleist, E., Mentel, T.F., Tillmann, R., Uerlings, R., Schurr, U., and Wahner, A. (2009). New particle formation in forests inhibited by isoprene emissions. Nature *461*, 381–384.

Kim, K.-H., and Andreae, M.O. (1987). Carbon disulfide in seawater and the marine atmosphere over the North Atlantic. J. Geophys. Res. Atmospheres *92*, 14733–14738.

Kladi, M., Vagias, C., and Roussis, V. (2004). Volatile halogenated metabolites from marine red algae. Phytochem. Rev. *3*, 337–366.

Le Quere, C., Andres, R.J., Boden, T., Conway, T., Houghton, R.A., House, J.I., Marland, G., Peters, G.P., van der Werf, G., Ahlstrem, A., et al. (2012). The global carbon budget 1959-2011. Earth Syst. Sci. Data Discuss. *5*, 1107–1157.

Lee, E.G., Lewis, B., Burns, D.A., Kashon, M.L., Kim, S.W., and Harper, M. (2015). Assessing Exposures to 1-chloro-4-(trifluoromethyl) Benzene (PCBTF) in U.S. Workplaces. J. Occup. Environ. Hyg. *12*, D123–D130.

Lelieveld, J., and Dentener, F. (2000). What controls tropospheric ozone? J. Geophys. Res. *105*, 3531–3551.

Li, W.K., and Glen Harrison, W. (2008). Propagation of an atmospheric climate signal to phytoplankton in a small marine basin. Limnol. Oceanogr. *53*, 1734–1745.

Li, W.K.., Glen Harrison, W., and Head, E.J.. (2006). Coherent assembly of phytoplankton communities in diverse temperate ocean ecosystems. Proc. R. Soc. B Biol. Sci. *273*, 1953–1960.

Lim, H.-J., Carlton, A.G., and Turpin, B.J. (2005). Isoprene Forms Secondary Organic Aerosol through Cloud Processing: Model Simulations. Environ. Sci. Technol. *39*, 4441–4446.

Liu, J., Li, N., Jiang, G., Liu, J., Jönsson, J.Å., and Wen, M. (2005). Disposable ionic liquid coating for headspace solid-phase microextraction of benzene, toluene, ethylbenzene, and xylenes in paints followed by gas chromatography–flame ionization detection. J. Chromatogr. A *1066*, 27–32.

Liu, Y., Shao, M., Fu, L., Lu, S., Zeng, L., and Tang, D. (2008). Source profiles of volatile organic compounds (VOCs) measured in China: Part I. Atmos. Environ. *42*, 6247–6260.

Liyana-Arachchi, T.P., Zhang, Z., Vempati, H., Hansel, A.K., Stevens, C., Pham, A.T., Ehrenhauser, F.S., Valsaraj, K.T., and Hung, F.R. (2014). Green Leaf Volatiles on Atmospheric Air/Water Interfaces: A Combined Experimental and Molecular Simulation Study. J. Chem. Eng. Data *59*, 3025–3035.

Lof, A., Wallen, M., and Bard, J. (2000). Concise International Chemical Assessment Document 28, Methyl Chloride.

Loreto, F., and Velikova, V. (2001). Isoprene Produced by Leaves Protects the Photosynthetic Apparatus against Ozone Damage, Quenches Ozone Products, and Reduces Lipid Peroxidation of Cellular Membranes. PLANT Physiol. *127*, 1781–1787.

MacIntyre, H., Kana, T., Anning, T., and Geider, R.J. (2002). PHOTOACCLIMATION OF PHOTOSYNTHESIS IRRADIANCE RESPONSE CURVES AND PHOTOSYNTHETIC PIGMENTS IN MICROALGAE AND CYANOBACTERIA. J Phycol *38*, 17–38.

Mackas, D.L. (2011). Does blending of chlorophyll data bias temporal trend? Nature *472*, E4.

Maggs, R.J., Joynes, P.L., Davies, A.J., and Lovelock, J.E. (1971). Electron capture detector. New mode of operation. Anal. Chem. *43*, 1966–1971.

Mahadevan, A., D'Asaro, E., Lee, C., and Perry, M.J. (2012). Eddy-driven stratification initiates North Atlantic spring phytoplankton blooms. Science *337*, 54–58.

Mahajan, A.S., Fadnavis, S., Thomas, M.A., Pozzoli, L., Gupta, S., Royer, S.-J., Saiz-Lopez, A., and Simó, R. (2015). Quantifying the impacts of an updated global dimethyl sulfide climatology on cloud microphysics and aerosol radiative forcing. J. Geophys. Res. Atmospheres *120*, 2524–2536.

Malin, G., and Kirst, G.O. (1997). Algal Production of Dimethyl Sulfide and Its Atmospheric Role. J. Phycol. *33*, 889–896.

Markes (2012). Unity-2 Operator's Manual.

Markes (2015). MTS-32 User's Manual.

Martinez-Levasseur, L.M., Birch-Machin, M.A., Bowman, A., Gendron, D., Weatherhead, E., Knell, R.J., and Acevedo-Whitehouse, K. (2013). Whales Use Distinct Strategies to Counteract Solar Ultraviolet Radiation. Sci. Rep. *3*.

Meskhidze, N., Sabolis, A., Reed, R., and Kamykowski, D. (2015). Quantifying environmental stress-induced emissions of algal isoprene and monoterpenes using laboratory measurements. Biogeosciences *12*, 637–651.

Miller, R., Newhook, R., and Poole, A. (1994). Styrene production, use and human exposure. Crit. Rev. Toxocology *24*, S1–S10.

Monks, P.., Granier, C., Fuzzi, S., Stohl, A., Williams, M., Akimoto, H., and Amann, M. (2009). Atmospheric composition change - global and regional air quality. Atmos. Environ. *43*, 5268–5350.

Montenegro, A., Ishibashi, J.S.A., Lam, P., and Li, Z. (2012). Kinetics Study of Reactions of α-Pinene and β-Pinene with Hydroxyl Radical at 1–8 Torr and 240–340 K Using the Relative Rate/Discharge Flow/Mass Spectrometry Method. J. Phys. Chem. A *116*, 12096–12103.

Moore, R.M. (2000). The solubility of a suite of low molecular weight organochlorine compounds in seawater and implications for estimating the marine source of methyl chloride to the atmosphere. Chemosphere-Glob. Change Sci. *2*, 95–99.

Moore, R.M., and Tokarczyk, R. (1993). Volatile biogenic halocarbons in the northwest Atlantic. Glob. Biogeochem. Cycles *7*, 195–210.

Moore, C.M., Suggett, D.J., Hickman, A.E., Kim, Y.-N., Tweddle, J.F., Sharples, J., Geider, R.J., and Holligan, P.M. (2006). Phytoplankton photoacclimation and photoadaptation in response to environmental gradients in a shelf sea. Limnol. Oceanogr. *51*, 936–949.

Moore, R.M., Oram, D.E., and Penkett, S.A. (1994). Production of isoprene by marine phytoplankton cultures. Geophys. Res. Lett. *21*, 2507–2510.

Nardi, L. (2003). In-tube solid-phase microextraction sampler for long-term storage. J. Chromatogr. A *985*, 93–98.

NASA-MODIS (2016). MODIS. Moderate Resolution Imaging Spectroradiometer.

NRC (2017). Forest Fires.

O'Dowd, C.D., Smith, M.H., Consterdine, I.E., and Lowe, J.A. (1997). Marine aerosol, sea-salt, and the marine sulphur cycle: A short review. Atmos. Environ. *31*, 73–80.

O'Reilly, J., Maritorena, S., Mitchell, G., Siegel, D., Carder, K., and Garver, S. (1998). Oceab color chlorophyll algorithms for SeeWiFS. J. Geophys. Res. *103*, 24937–24953.

Østrem, L., Rapacz, M., Larsen, A., Dalmannsdottir, S., and Jørgensen, M. (2015). Influences of growth cessation and photoacclimation on winter survival of non-native Lolium–Festuca grasses in high-latitude regions. Environ. Exp. Bot. *111*, 21–31.

Palani, S., Raja, S., Kumar, R.., Selvaraj, R., and Kumar, B.. (2011). Evaluation of phytoconstituents and anti-nephrotoxic and antioxidant activities of Monochoria vaginalis. Pak J Pharm Sci *24*, 293–301.

Palmer, P.I., and Shaw, S. (2005). Quantifying global marine isoprene fluxes using MODIS chlorophyll observations. Geophys. Res. Lett. *32*.

Palmer, P.I., Parrington, M., Lee, J.D., Lewis, A.C., Rickard, A.R., Bernath, P.F., Duck, T.J., Waugh, D.L., Tarasick, D.W., Andrews, S., et al. (2013a). Quantifying the impact of BOReal forest fires on Tropospheric oxidants over the Atlantic using Aircraft and Satellites (BORTAS) experiment: design, execution and science overview. Atmospheric Chem. Phys. *13*, 6239–6261.

Palmer, P.I., Parrington, M., Lee, J.D., Lewis, A.C., Rickard, A.R., Bernath, P.F., Duck, T.J., Waugh, D.L., Tarasick, D.W., Andrews, S., et al. (2013b). Quantifying the impact of BOReal forest fires on Tropospheric oxidants over the Atlantic using Aircraft and Satellites (BORTAS) experiment: design, execution and science overview. Atmospheric Chem. Phys. *13*, 6239–6261.

Paul, C., and Pohnert, G. (2011). Production and role of volatile halogenated compounds from marine algae. Nat Prod Rep *28*, 186–195.

Pickering, K.E., Thompson, A.M., Scala, J.R., Tao, W.-K., Dickerson, R.R., and Simpson, J. (1992). Free tropospheric ozone production following entrainment of urban plumes into deep convection. J. Geophys. Res. Atmospheres *97*, 17985–18000.

Qadoumi, H. (2016). The Source Apportionment of Volatile Organic Compounds on Sable Island, Nova Scotia, Canada.

Quinn, P.K., and Bates, T.S. (2011). The case against climate regulation via oceanic phytoplankton sulphur emissions. Nature *480*, 51–56.

RAE Systems (2015). ppbRAE 3000 - Portable Handheld VOC Monitor.

Rasconi, S., Winter, K., and Kainz, M.J. (2017). Temperature increase and fluctuation induce phytoplankton biodiversity loss - Evidence from a multi-seasonal mesocosm experiment. Ecol. Evol. *7*, 2936–2946.

Ravanat, J.-L., Douki, T., and Cadet, J. (2001). Direct and indirect effects of UV radiation on DNA and its components. J. Photochem. Photobiol. B *63*, 88–102.

Reisch, C.R., Moran, M.A., and Whitman, W.B. (2011). Bacterial Catabolism of Dimethylsulfoniopropionate (DMSP). Front. Microbiol. *2*.

Riley, G.A. (1957). Phytoplankton of the north central Sargasso Sea, 1950–52. Limnol. Oceanogr. *2*, 252–270.

Ross, T., Craig, S.E., Comeau, A., Davis, R., Dever, M., and Beck, M. (2017). Blooms and subsurface phytoplankton layers on the Scotian Shelf: Insights from profiling gliders. J. Mar. Syst. *172*, 118–127.

Ryoo, J.-M., Waliser, D.E., and Fetzer, E.J. (2011). Trajectory analysis on the origin of air mass and moisture associated with Atmospheric Rivers over the west coast of the United States. Atmospheric Chem. Phys. Discuss. *11*, 11109–11142.

Sabolis, A.. (2010). Quantifying marine emissions of biogenic volatile organic compounds using laboratory measurments, field measurements and remote sensing data. Master of Science.

Sánchez, J.F., Fernández-Sevilla, J.M., Acién, F.G., Cerón, M.C., Pérez-Parra, J., and Molina-Grima, E. (2008). Biomass and lutein productivity of Scenedesmus almeriensis: influence of irradiance, dilution rate and temperature. Appl. Microbiol. Biotechnol. *79*, 719–729.

Scala, A., Allmann, S., Mirabella, R., Haring, M., and Schuurink, R. (2013). Green Leaf Volatiles: A Plant's Multifunctional Weapon against Herbivores and Pathogens. Int. J. Mol. Sci. *14*, 17781–17811.

Schmidbauer, N., and Oehme, M. (1988). Comparison of solid adsorbent and stainless steel canister sampling for very low ppt-concentrations of aromatic compounds (≥ C 6) in ambient air from remote areas. Fresenius J. Anal. Chem. *331*, 14–19.

Seco, R., Peñuelas, J., Filella, I., Llusià, J., Molowny-Horas, R., Schallhart, S., Metzger, A., Müller, M., and Hansel, A. (2011). Contrasting winter and summer VOC mixing ratios at a forest site in the Western Mediterranean Basin: the effect of local biogenic emissions. Atmospheric Chem. Phys. *11*, 13161–13179.

Shaw, S.L., Gantt, B., and Meskhidze, N. (2010). Production and Emissions of Marine Isoprene and Monoterpenes: A Review. Adv. Meteorol. *2010*, 1–24.

Shields-Zhou, G., and Och, L. (2011). The case for a Neoproterozoic Oxygenation Event: Geochemical evidence and biological consequences. GSA Today *21*, 4–11.

Siegel, D.A., Doney, S.C., and Yoder, J.. (2002). The North Alantic Spring Phytoplankton Bloom and Sverdrup's Critical Depth Hypothesis. Science *296*, 730–733.

Simpson, I.J., Akagi, S.K., Barletta, B., Blake, N.J., Choi, Y., Diskin, G.S., Fried, A., Fuelberg, H.E., Meinardi, S., Rowland, F.S., et al. (2011). Boreal forest fire emissions in fresh Canadian smoke plumes: $C_1$-$C_{10}$ volatile organic compounds (VOCs), $CO_2$, CO, $NO_2$, NO, HCN and $CH_3CN$. Atmospheric Chem. Phys. *11*, 6445–6463.

Sinha, V., Williams, J., Meyerhöfer, M., Riebesell, U., Paulino, A.I., and Larsen, A. (2006). Air-sea fluxes of methanol, acetone, acetaldehyde, isoprene and DMS from a Norwegian fjord following a phytoplankton bloom in a mesocosm experiment. Atmospheric Chem. Phys. Discuss. *6*, 9907–9935.

Soja-Woźniak, M., Craig, S., Kratzer, S., Wojtasiewicz, B., Darecki, M., and Jones, C. (2017). A Novel Statistical Approach for Ocean Colour Estimation of Inherent Optical Properties and Cyanobacteria Abundance in Optically Complex Waters. Remote Sens. *9*, 343.

Spanke, J., Rannik, Ü., Forkel, R., Nigge, W., and Hoffmann, T. (2001). Emission fluxes and atmospheric degradation of monoterpenes above a boreal forest: field measurements and modelling. Tellus B *53*, 406–422.

Strain, P.M., and Yeats, P.A. (2005). Nutrients in the gully, Scotian shelf, Canada. Atmosphere-Ocean *43*, 145–161.

Stramska, M., Marks, R., and Monahan, E. (1991). Bubble-mediated aerosol production as a consequence of wave breaking in supersaturated (hyperoxic) seawater. J. Geophys. Res. *95*, 18281–18288.

Su, H.-J., Chao, C.-J., Chang, H.-Y., and Wu, P.-C. (2007). The effects of evaporating essential oils on indoor air quality. Atmos. Environ. *41*, 1230–1236.

Sumpter, W.C. (1944). The chemistry of isatin. Chem. Rev. *34*, 393–434.

Tamburic, B., Guruprasad, S., Radford, D.T., Szabó, M., Lilley, R.M., Larkum, A.W.D., Franklin, J.B., Kramer, D.M., Blackburn, S.I., Raven, J.A., et al. (2014). The Effect of Diel Temperature and Light Cycles on the Growth of Nannochloropsis oculata in a Photobioreactor Matrix. PLoS ONE *9*, e86047.

Taylor, A.H., and Stephens, J.A. (1998). The North Atlantic Oscillation and the latitude of the Gulf Stream. Tellus Dyn. Meteorol. Oceanogr. *50*, 134–142.

Teramura, A.H. (1983). Effects of ultraviolet-B radiation on the growth and yield of crop plants. Physiol. Plant. *58*, 415–427.

Thermo Scientific (2012). ISQ User Guide.

Tholl, D., Boland, W., Hansel, A., Loreto, F., Röse, U.S.R., and Schnitzler, J.-P. (2006). Practical approaches to plant volatile analysis. Plant J. *45*, 540–560.

Trabue, S., Scoggin, K., Mitloehner, F., Li, H., Burns, R., and Xin, H. (2008). Field sampling method for quantifying volatile sulfur compounds from animal feeding operations. Atmos. Environ. *42*, 3332–3341.

Turner, S., Malin, G., Nightingale, P., and Liss, P. (1996a). Seasonal variation of dimethyl sulphide in the North Sea and an assessment of fluxes to the atmosphere. Mar. Chem. *54*, 245–262.

Turner, S., Malin, G., Nightingale, P., and Liss, P. (1996b). Seasonal variation of dimethyl sulphide in the North Sea and an assessment of fluxes to the atmosphere. Mar. Chem. *54*, 245–262.

USEPA (1999). Compendium Method TO-17: Determination of Volatile Organic Compounds in Ambient Air Using Active Sampling Onto Sorbent Tubes.

Veldhuis, M., Kraay, G., and Timmermans, K. (2001). Cell death in phytoplankton: correlation between changes in membrane permeability, photosynthetic activity, pigmentation and growth. Eur. J. Phycol. *36*, 167–177.

Walker, S., Weiss, R., and Salameh, P. (2000). Reconstructed histories of the annual mean atmospheric mole fractions for the halocarbons CFC-11. CFC-12, CFC-113 and carbon tetrachloride. J. Geophys. Res. *105*, 14285–14296.

Wallace, L. (1990). Major sources of exposure to benzene and other volatile organic chemicals. Risk Anal. *10*, 59–64.

Ward, B.A., Dutkiewicz, S., Jahn, O., and Follows, M.J. (2012). A size-structured food-web model for the global ocean. Limnol. Oceanogr. *57*, 1877–1891.

Warneke, C., Geiger, F., Edwards, P.M., Dube, W., Pétron, G., Kofler, J., Zahn, A., Brown, S.S., Graus, M., Gilman, J.B., et al. (2014). Volatile organic compound emissions from the oil and natural gas industry in the Uintah Basin, Utah: oil and gas well pad emissions compared to ambient air composition. Atmospheric Chem. Phys. *14*, 10977–10988.

Waugh, D.L., Inkpen, T., Hingston, M., Keast, S., McPherson, J., Worthy, D., and Forster, G. (2010). Sable Island air monitoring program report: 2003-2006 (Dartmouth: Environmental Studies Research Funds).

Waza, A. (2014). Effect of green leaf volatiles (GLVs) on secondary organic aerosol formation. University of Eastern Finland.

Wheeler, A.J., Xu, X., Kulka, R., You, H., Wallace, L., Mallach, G., Ryswyk, K.V., MacNeill, M., Kearney, J., Rasmussen, P.E., et al. (2011). Windsor, Ontario Exposure Assessment Study: Design and Methods Validation of Personal, Indoor, and Outdoor Air Pollution Monitoring. J. Air Waste Manag. Assoc. *61*, 324–338.

White, M.L., Russo, R.S., Zhou, Y., Ambrose, J.L., Haase, K., Frinak, E.K., Varner, R.K., Wingenter, O.W., Mao, H., Talbot, R., et al. (2009). Are biogenic emissions a significant source of summertime atmospheric toluene in the rural Northeastern United States? Atmospheric Chem. Phys. *9*, 81–92.

WHOI (2017). Woods Hole Oceanographic Institute. What are phytoplankton?

Wiebe, R., and Gaddy, V.L. (1940). The solubility of carbon dioxide in water at various temperatures from 12 to 40 and at pressures to 500 atmospheres. Critical phenomena. J. Am. Chem. Soc. *62*, 815–817.

Woodhouse, M.T., Carslaw, K.S., Mann, G.W., Vallina, S.M., Vogt, M., Halloran, P.R., and Boucher, O. (2010). Low sensitivity of cloud condensation nuclei to changes in the sea-air flux of dimethyl-sulphide. Atmospheric Chem. Phys. *10*, 7545–7559.

Woolf, D., Bowyer, P., and Monahan, E. (1987). Discriminating between the film drops and jet drops produced by a simulated whitecap. J. Geophys. Res. *92*, 5142–5150.

Yang, D., Shi, H., Li, L., Li, J., Jabeen, K., and Kolandhasamy, P. (2015). Microplastic Pollution in Table Salts from China. Environ. Sci. Technol. *49*, 13622–13627.

Yu, J., Cocker, D.R., Griffin, R.J., Flagan, R.C., and Seinfeld, J.H. (1999). Gas-phase ozone oxidation of monoterpenes: Gaseous and particulate products. J. Atmospheric Chem. *34*, 207–258.

Zhao, D., Toba, Y., Suzuki, Y., and Komori, S. (2003). Effect of wind waves on air–sea gas exchange: proposal of an overall CO2 transfer velocity formula as a function of breaking-wave parameter. Tellus B *55*, 478–487.

# APPENDIX

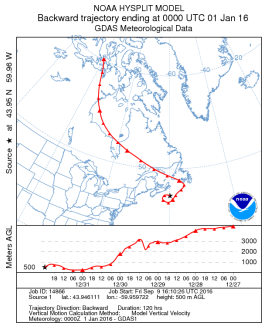
NOAA HYSPLIT MODEL
Backward trajectory ending at 0000 UTC 01 Jan 16
GDAS Meteorological Data

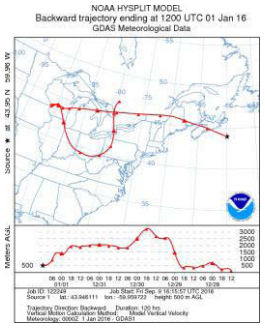
NOAA HYSPLIT MODEL
Backward trajectory ending at 1200 UTC 01 Jan 16
GDAS Meteorological Data

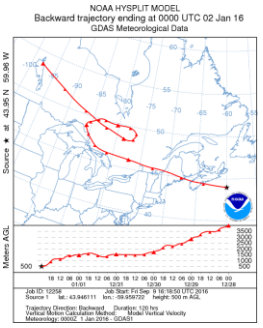
NOAA HYSPLIT MODEL
Backward trajectory ending at 0000 UTC 02 Jan 16
GDAS Meteorological Data

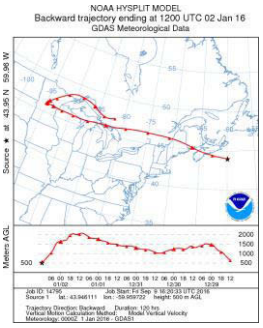
NOAA HYSPLIT MODEL
Backward trajectory ending at 1200 UTC 02 Jan 16
GDAS Meteorological Data

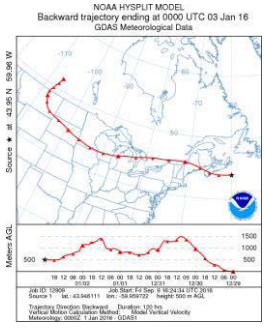
NOAA HYSPLIT MODEL
Backward trajectory ending at 0000 UTC 03 Jan 16
GDAS Meteorological Data

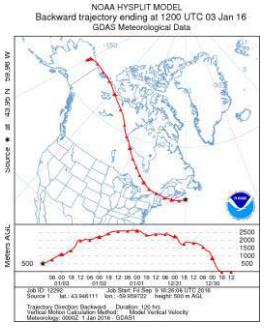
NOAA HYSPLIT MODEL
Backward trajectory ending at 1200 UTC 03 Jan 16
GDAS Meteorological Data

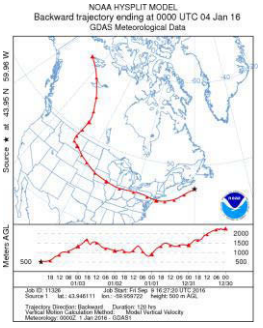
NOAA HYSPLIT MODEL
Backward trajectory ending at 0000 UTC 04 Jan 16
GDAS Meteorological Data

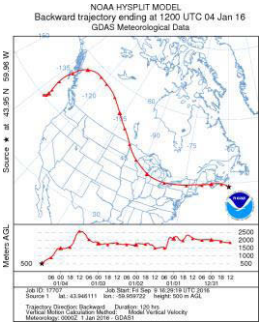
NOAA HYSPLIT MODEL
Backward trajectory ending at 1200 UTC 04 Jan 16
GDAS Meteorological Data

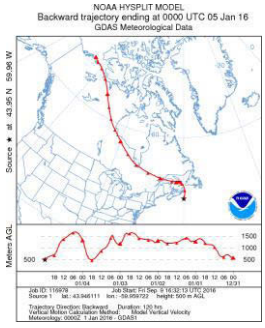
NOAA HYSPLIT MODEL
Backward trajectory ending at 0000 UTC 05 Jan 16
GDAS Meteorological Data

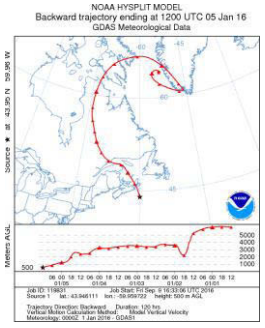
NOAA HYSPLIT MODEL
Backward trajectory ending at 1200 UTC 05 Jan 16
GDAS Meteorological Data

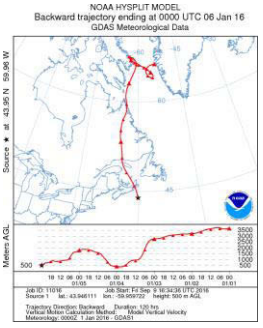
NOAA HYSPLIT MODEL
Backward trajectory ending at 0000 UTC 06 Jan 16
GDAS Meteorological Data

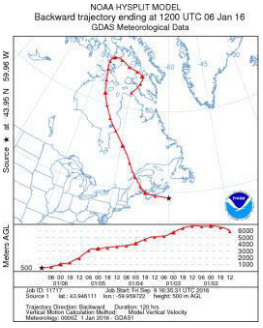
NOAA HYSPLIT MODEL
Backward trajectory ending at 1200 UTC 06 Jan 16
GDAS Meteorological Data

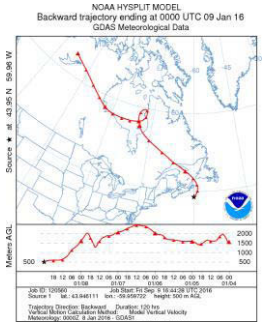
NOAA HYSPLIT MODEL
Backward trajectory ending at 0000 UTC 09 Jan 16
GDAS Meteorological Data

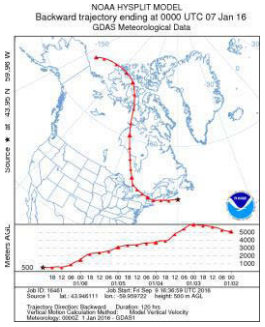
NOAA HYSPLIT MODEL
Backward trajectory ending at 0000 UTC 07 Jan 16
GDAS Meteorological Data

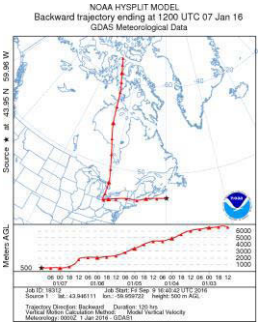
NOAA HYSPLIT MODEL
Backward trajectory ending at 1200 UTC 07 Jan 16
GDAS Meteorological Data

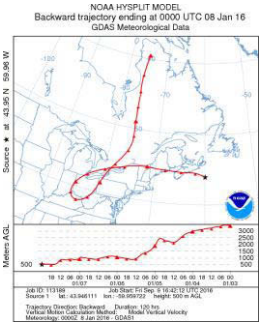
NOAA HYSPLIT MODEL
Backward trajectory ending at 0000 UTC 08 Jan 16
GDAS Meteorological Data

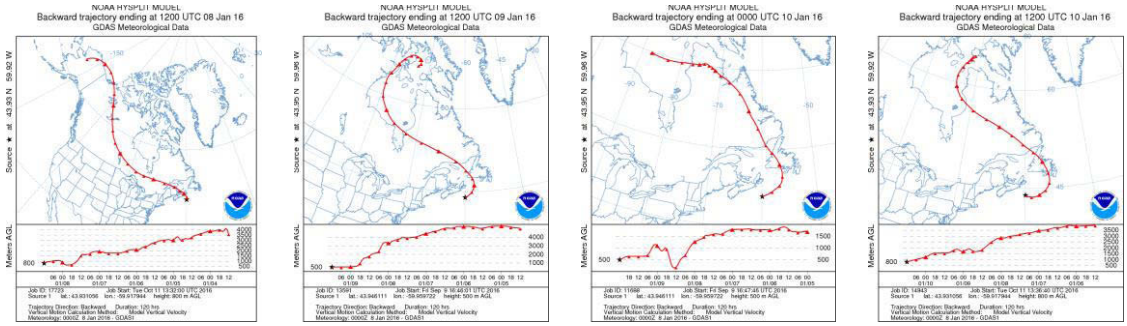


## January 01st – 10th, 2016

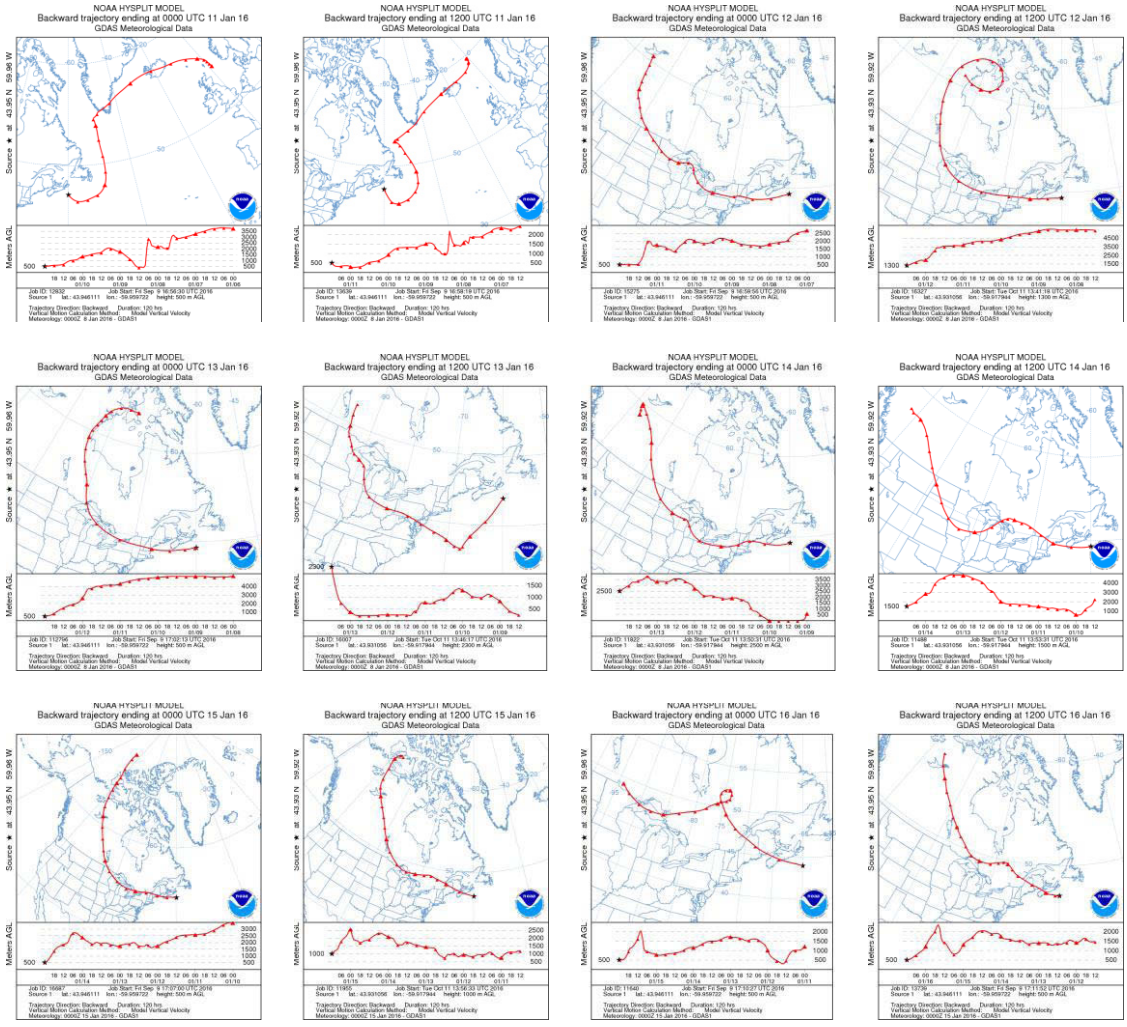

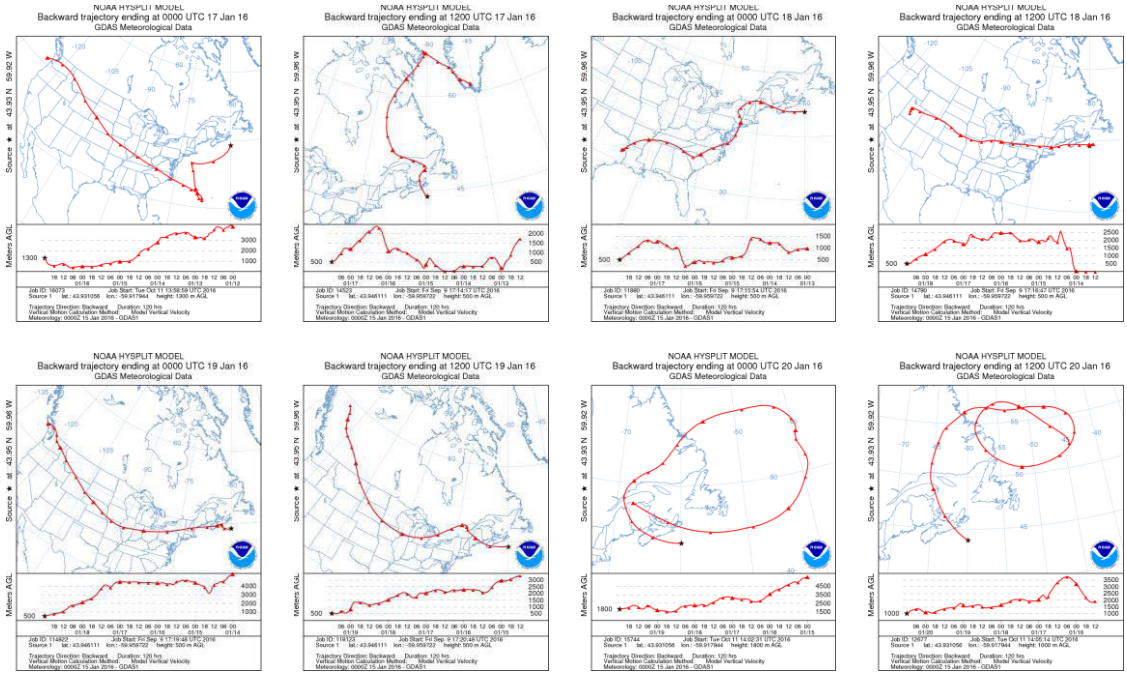


## January 11th – 20th, 2016

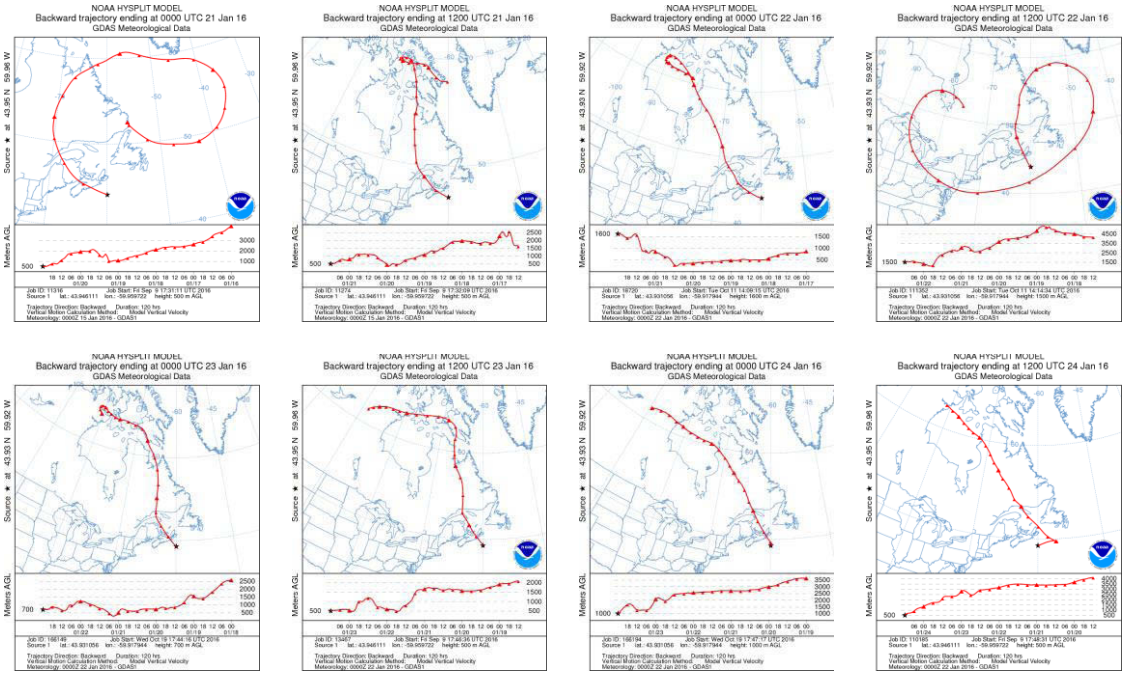

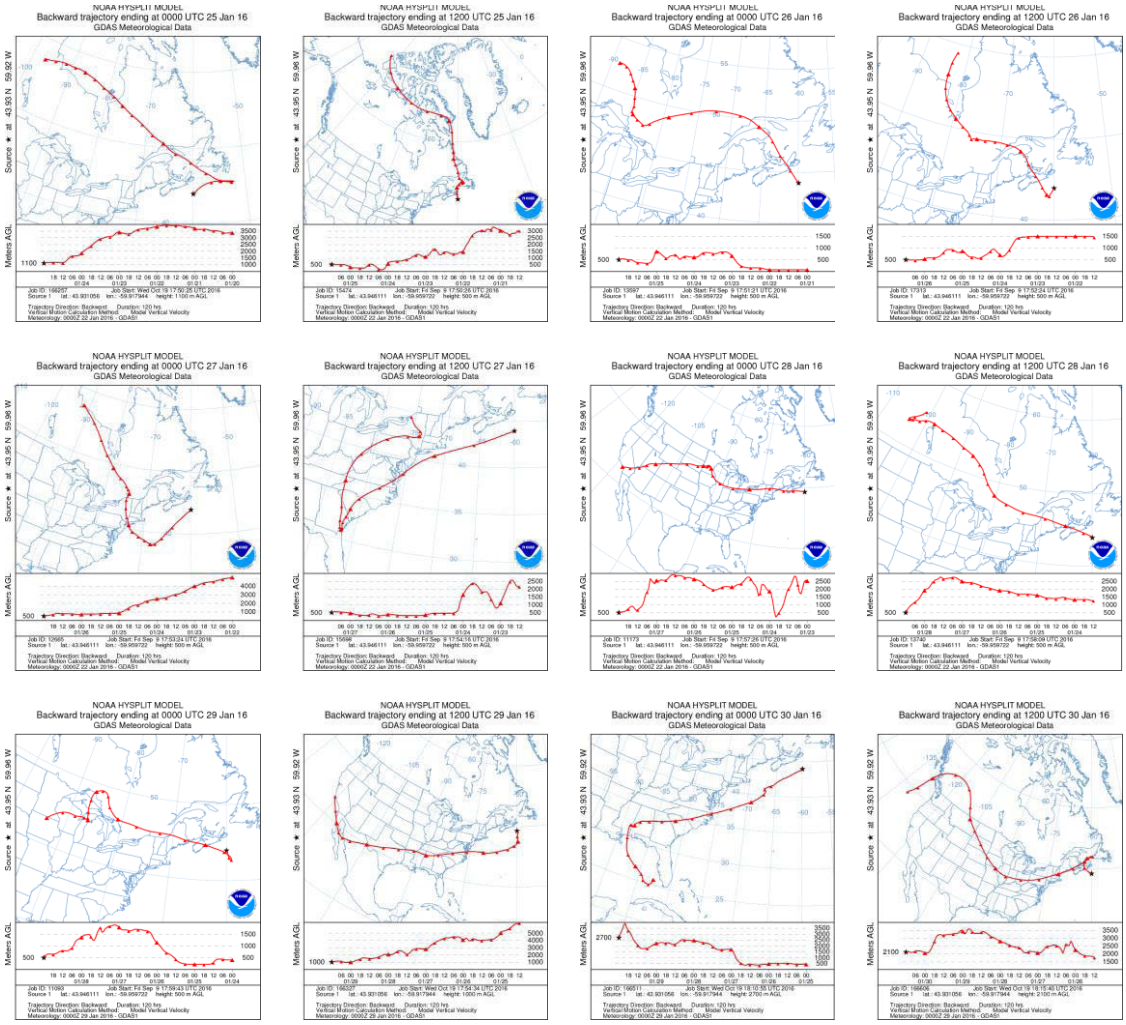


## January 21st – 30th, 2016

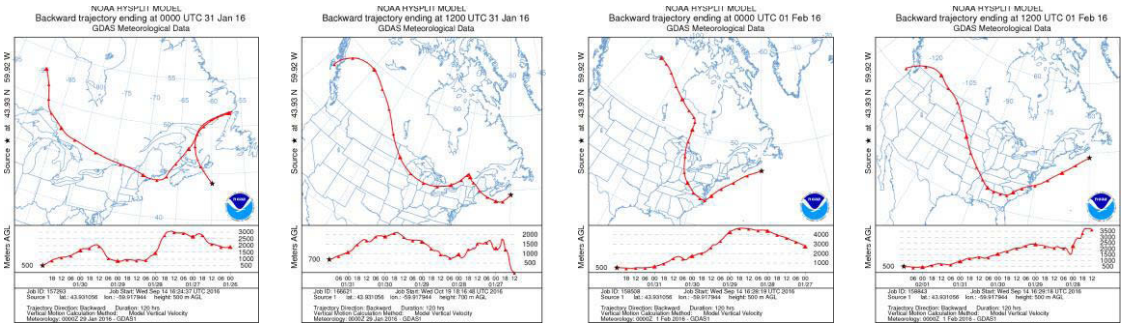

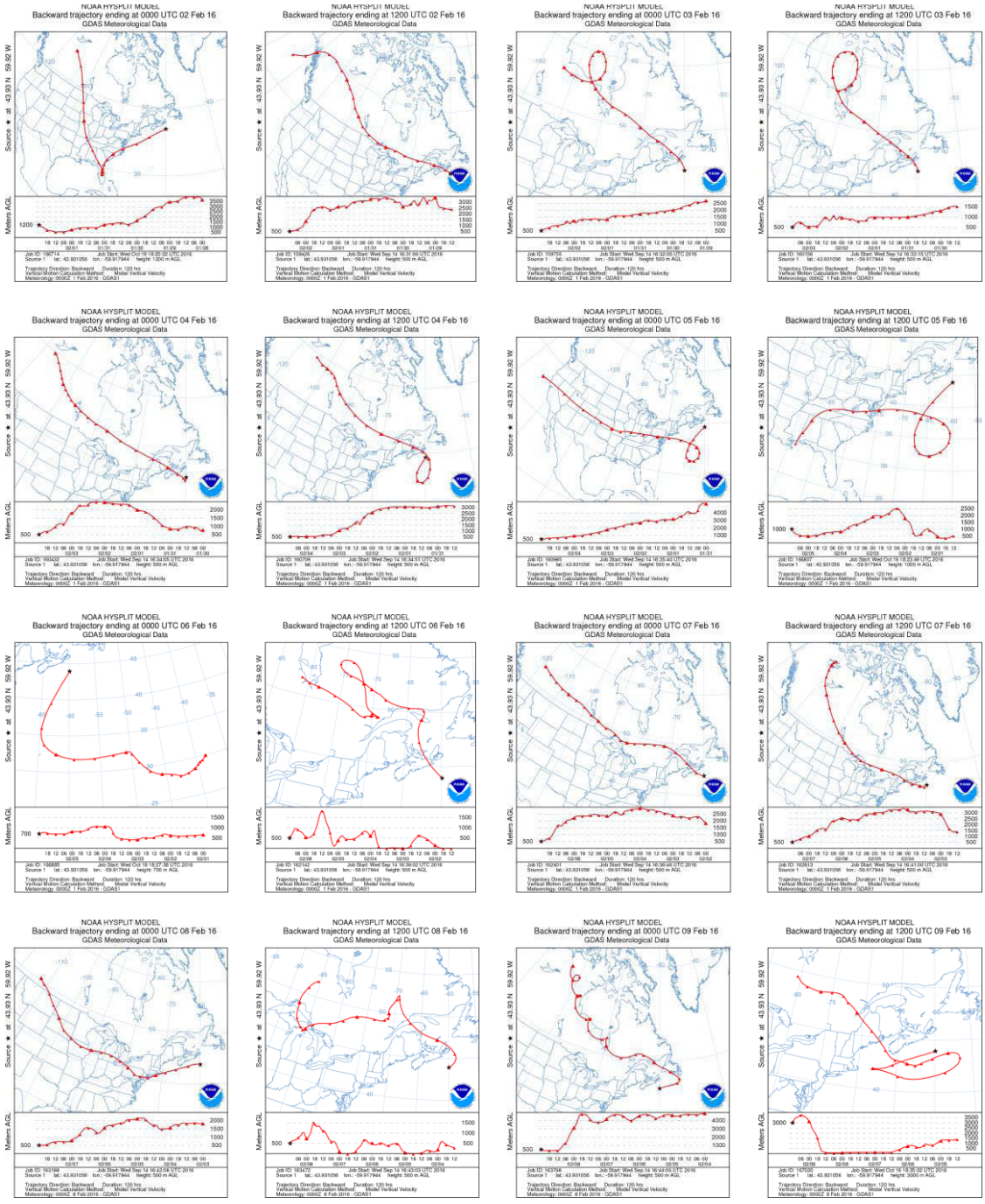


**January 31st – February 9th, 2016**

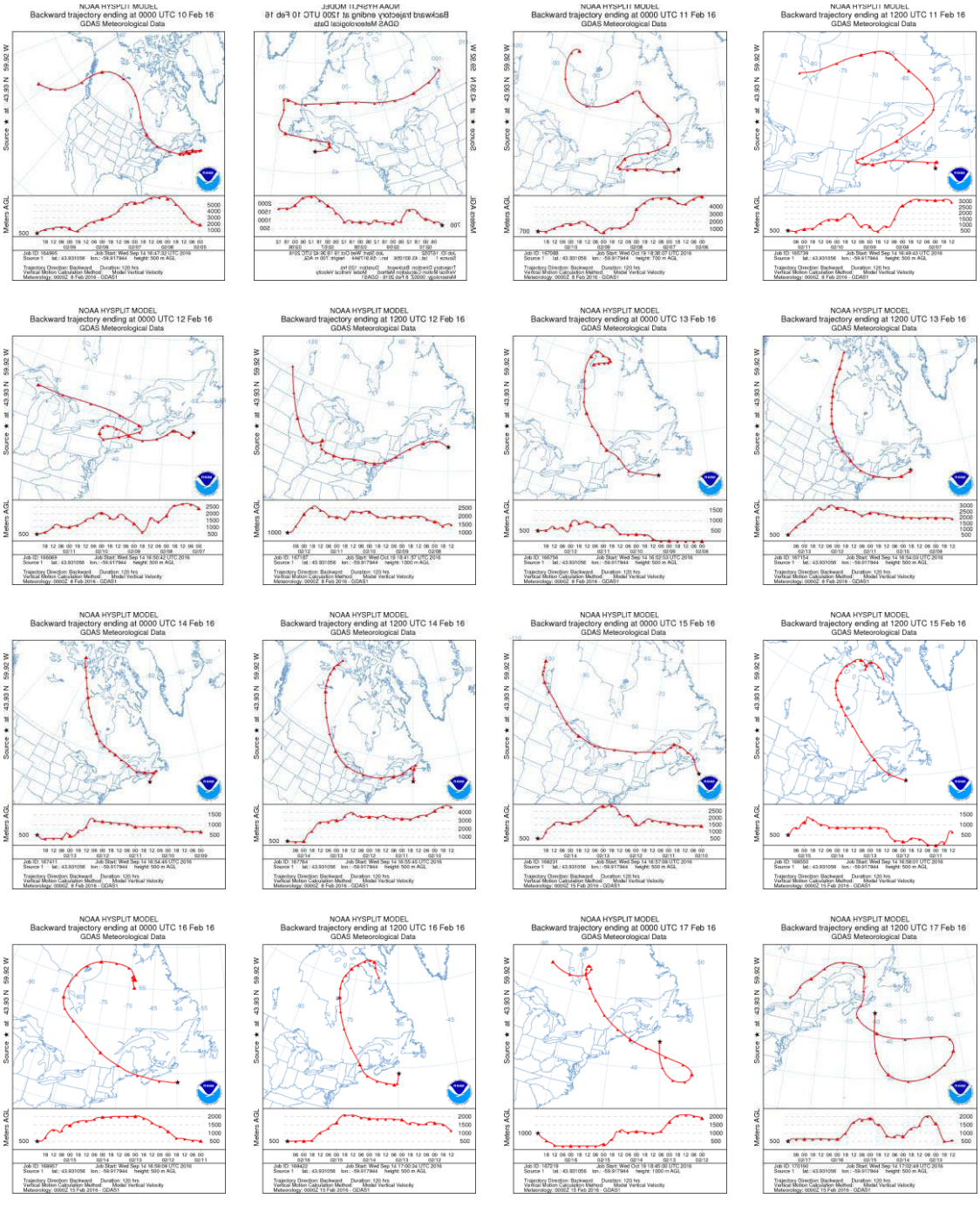
NOAA HYSPLIT MODEL
Backward trajectory ending at 0000 UTC 10 Feb 16
GDAS Meteorological Data
NOAA HYSPLIT MODEL
Backward trajectory ending at 1200 UTC 10 Feb 16
GDAS Meteorological Data
NOAA HYSPLIT MODEL
Backward trajectory ending at 0000 UTC 11 Feb 16
GDAS Meteorological Data
NOAA HYSPLIT MODEL
Backward trajectory ending at 1200 UTC 11 Feb 16
GDAS Meteorological Data
NOAA HYSPLIT MODEL
Backward trajectory ending at 0000 UTC 12 Feb 16
GDAS Meteorological Data
NOAA HYSPLIT MODEL
Backward trajectory ending at 1200 UTC 12 Feb 16
GDAS Meteorological Data
NOAA HYSPLIT MODEL
Backward trajectory ending at 0000 UTC 13 Feb 16
GDAS Meteorological Data
NOAA HYSPLIT MODEL
Backward trajectory ending at 1200 UTC 13 Feb 16
GDAS Meteorological Data
NOAA HYSPLIT MODEL
Backward trajectory ending at 0000 UTC 14 Feb 16
GDAS Meteorological Data
NOAA HYSPLIT MODEL
Backward trajectory ending at 1200 UTC 14 Feb 16
GDAS Meteorological Data
NOAA HYSPLIT MODEL
Backward trajectory ending at 0000 UTC 15 Feb 16
GDAS Meteorological Data
NOAA HYSPLIT MODEL
Backward trajectory ending at 1200 UTC 15 Feb 16
GDAS Meteorological Data
NOAA HYSPLIT MODEL
Backward trajectory ending at 0000 UTC 16 Feb 16
GDAS Meteorological Data
NOAA HYSPLIT MODEL
Backward trajectory ending at 1200 UTC 16 Feb 16
GDAS Meteorological Data
NOAA HYSPLIT MODEL
Backward trajectory ending at 0000 UTC 17 Feb 16
GDAS Meteorological Data
NOAA HYSPLIT MODEL
Backward trajectory ending at 1200 UTC 17 Feb 16
GDAS Meteorological Data

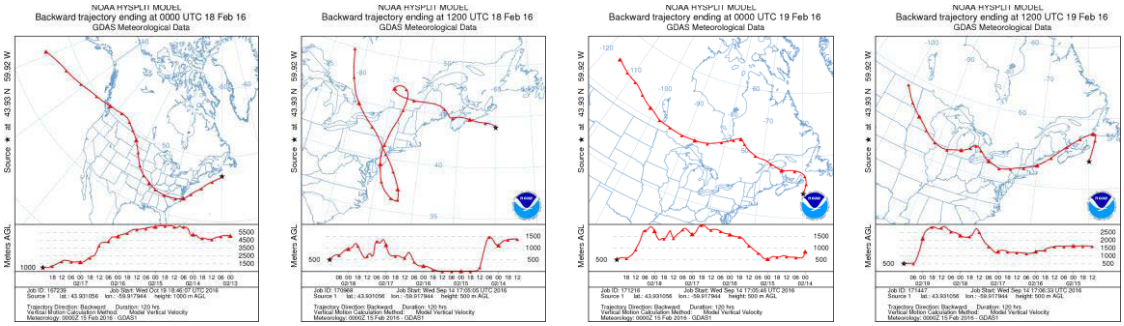


## February 10th – 19th, 2016

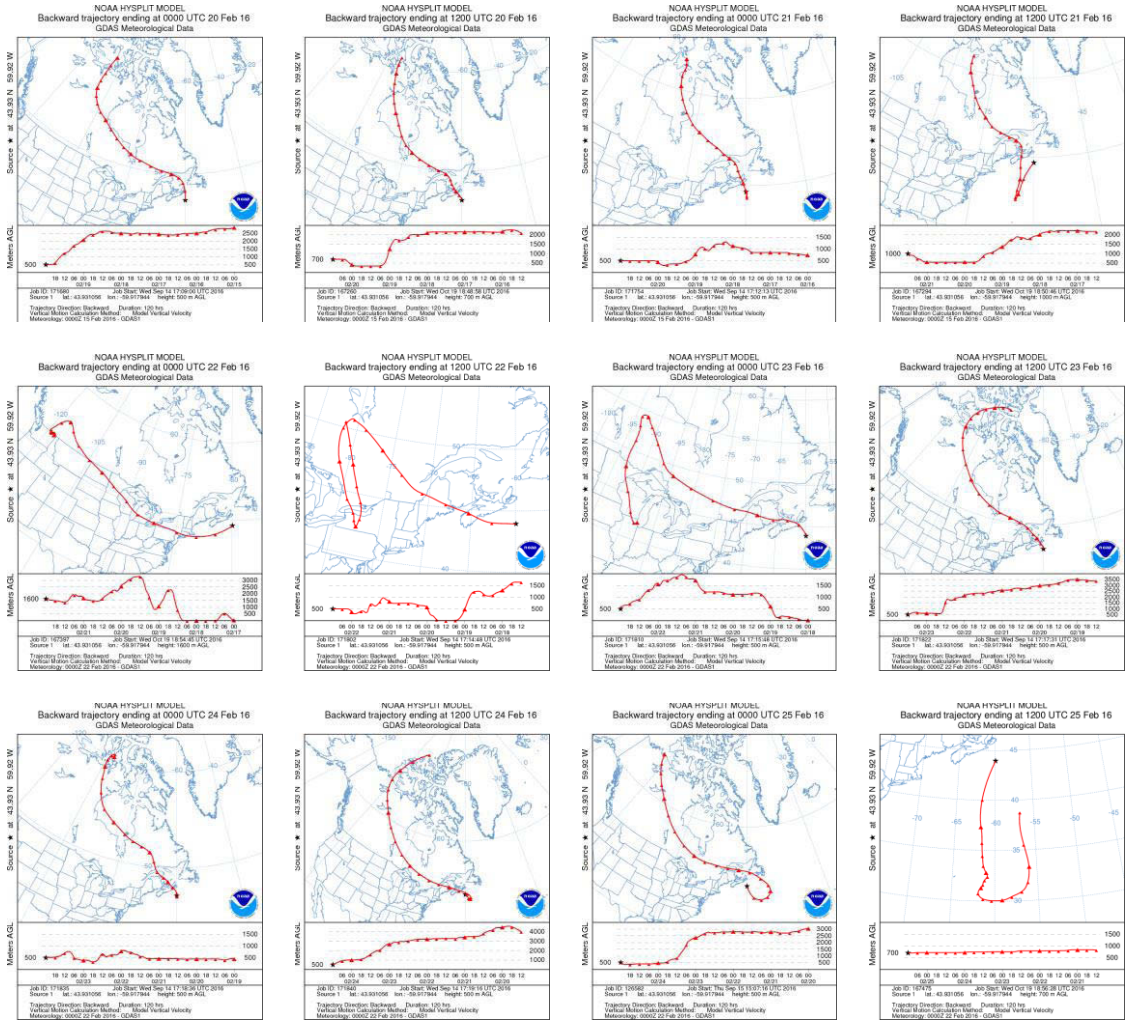

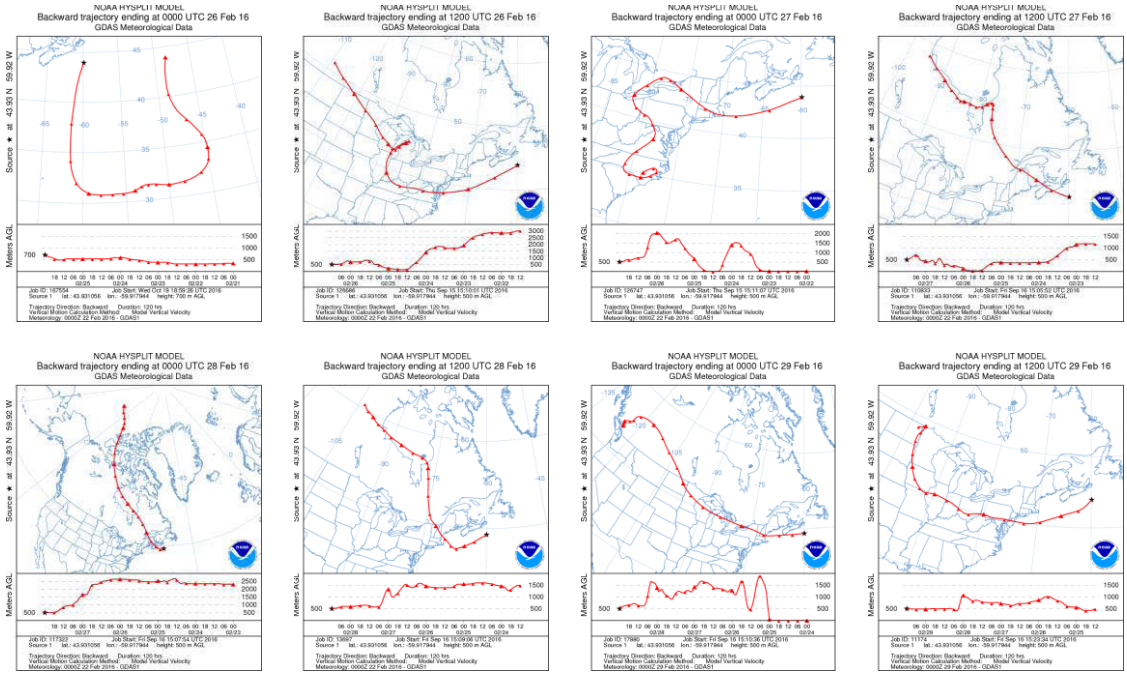


## February 20th – 29th, 2016

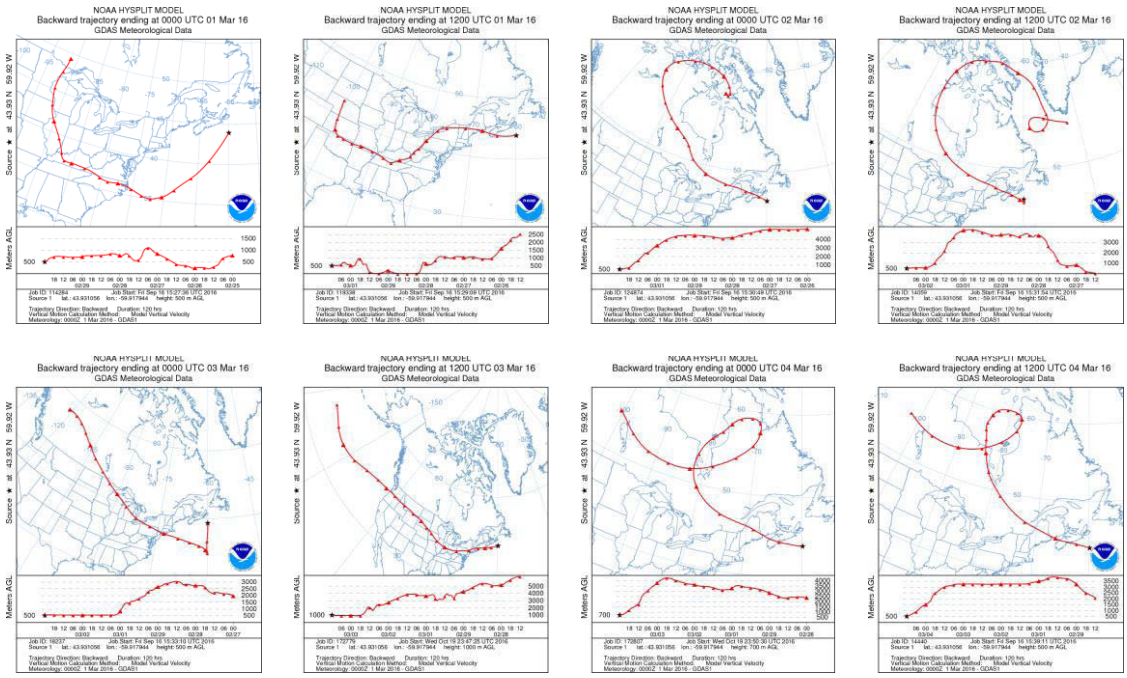

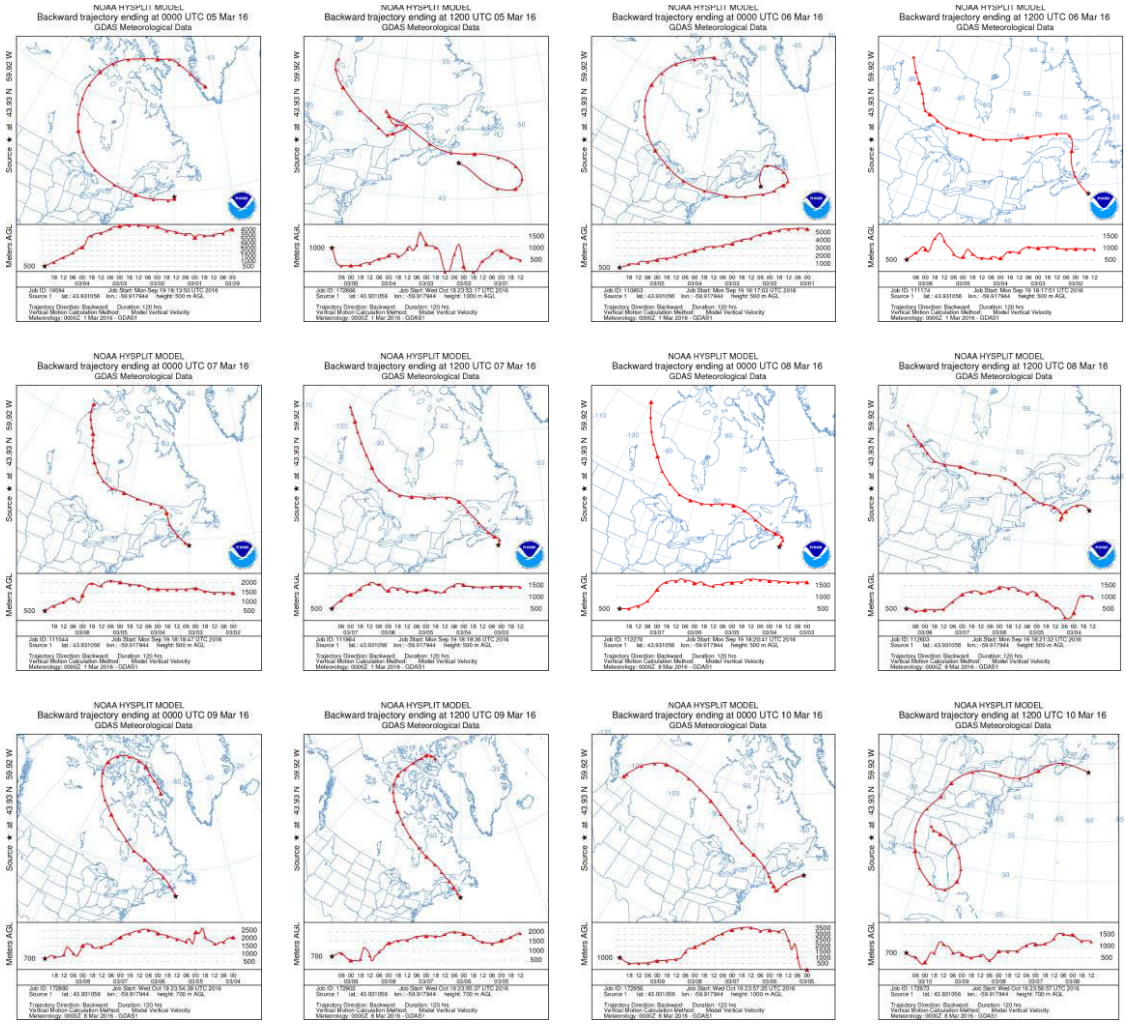


## March 1st – 10th, 2016

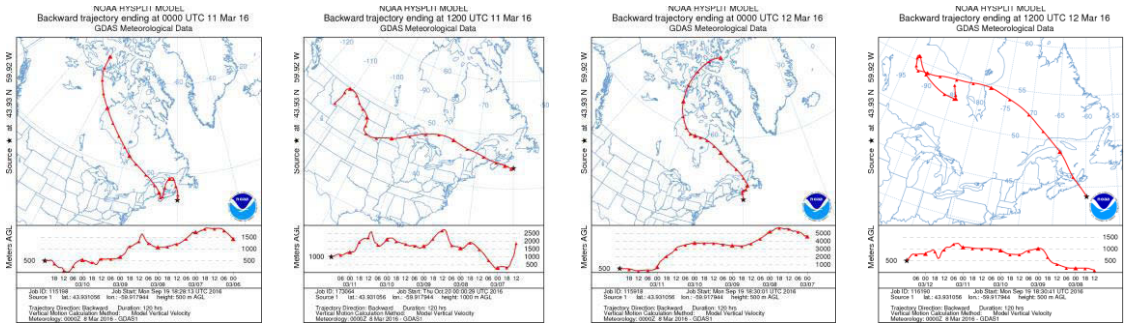

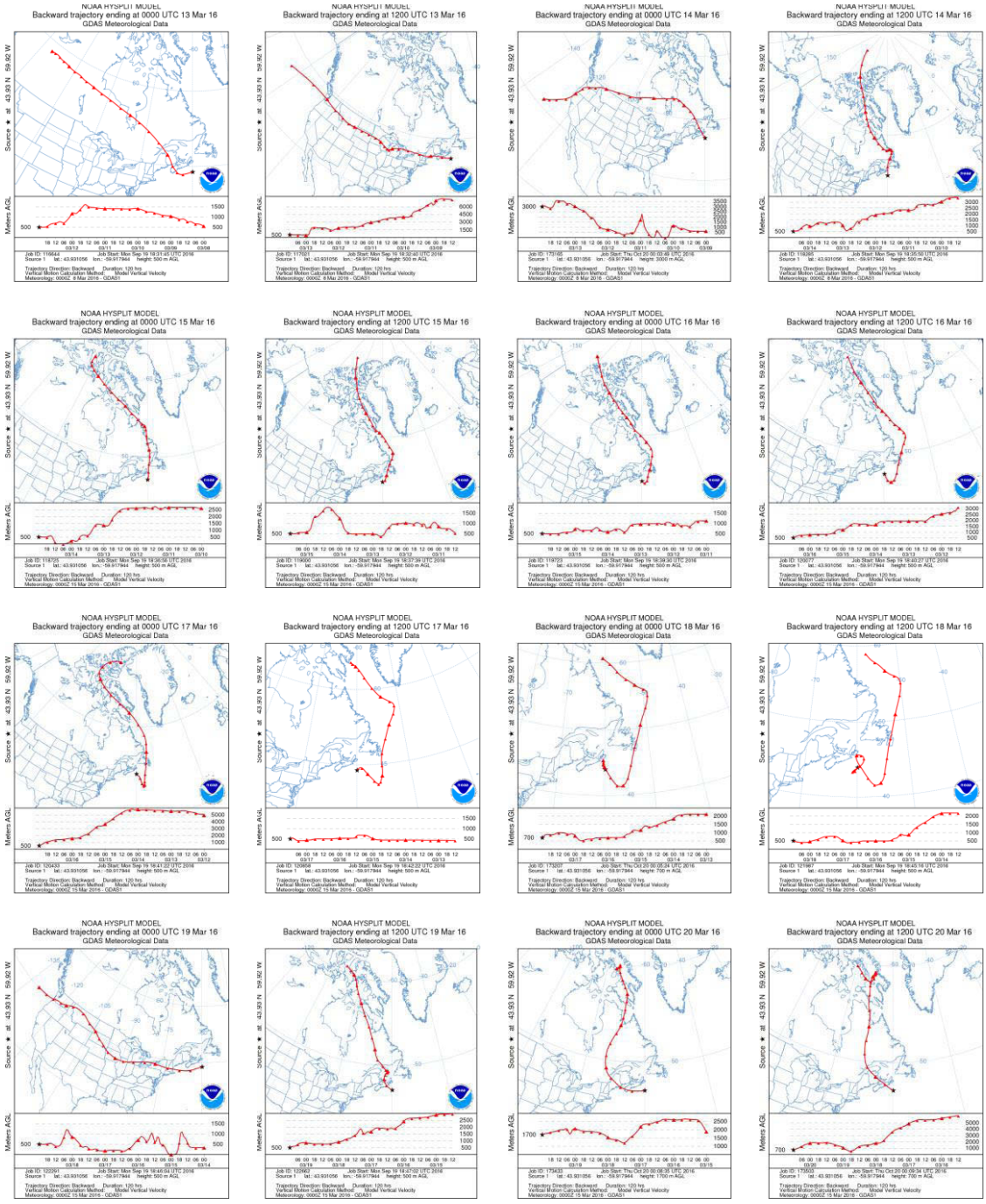


**March 11th – 20th, 2016**

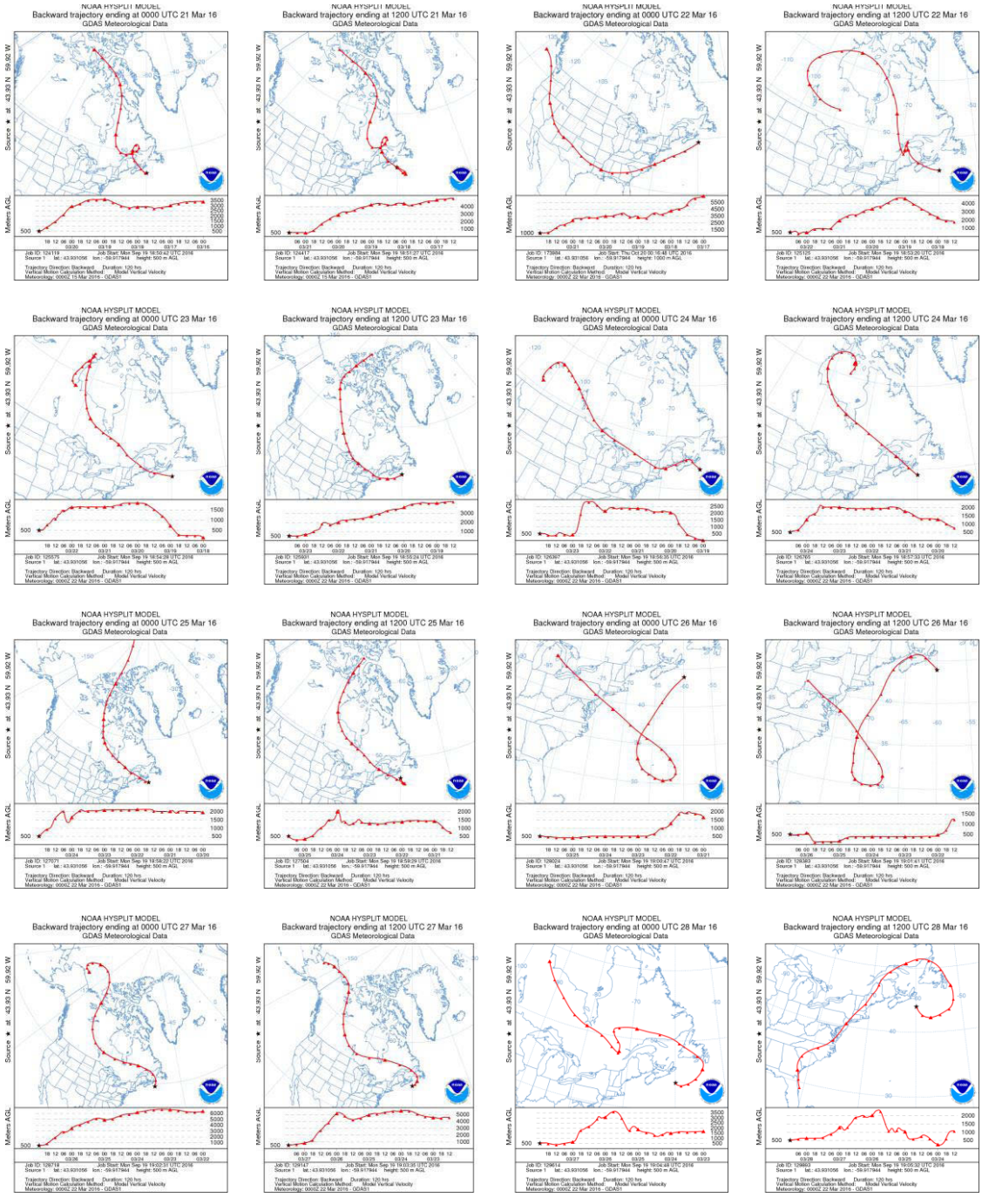
NOAA HYSPLIT MODEL
Backward trajectory ending at 0000 UTC 21 Mar 16
GDAS Meteorological Data
NOAA HYSPLIT MODEL
Backward trajectory ending at 1200 UTC 21 Mar 16
GDAS Meteorological Data
NOAA HYSPLIT MODEL
Backward trajectory ending at 0000 UTC 22 Mar 16
GDAS Meteorological Data
NOAA HYSPLIT MODEL
Backward trajectory ending at 1200 UTC 22 Mar 16
GDAS Meteorological Data
NOAA HYSPLIT MODEL
Backward trajectory ending at 0000 UTC 23 Mar 16
GDAS Meteorological Data
NOAA HYSPLIT MODEL
Backward trajectory ending at 1200 UTC 23 Mar 16
GDAS Meteorological Data
NOAA HYSPLIT MODEL
Backward trajectory ending at 0000 UTC 24 Mar 16
GDAS Meteorological Data
NOAA HYSPLIT MODEL
Backward trajectory ending at 1200 UTC 24 Mar 16
GDAS Meteorological Data
NOAA HYSPLIT MODEL
Backward trajectory ending at 0000 UTC 25 Mar 16
GDAS Meteorological Data
NOAA HYSPLIT MODEL
Backward trajectory ending at 1200 UTC 25 Mar 16
GDAS Meteorological Data
NOAA HYSPLIT MODEL
Backward trajectory ending at 0000 UTC 26 Mar 16
GDAS Meteorological Data
NOAA HYSPLIT MODEL
Backward trajectory ending at 1200 UTC 26 Mar 16
GDAS Meteorological Data
NOAA HYSPLIT MODEL
Backward trajectory ending at 0000 UTC 27 Mar 16
GDAS Meteorological Data
NOAA HYSPLIT MODEL
Backward trajectory ending at 1200 UTC 27 Mar 16
GDAS Meteorological Data
NOAA HYSPLIT MODEL
Backward trajectory ending at 0000 UTC 28 Mar 16
GDAS Meteorological Data
NOAA HYSPLIT MODEL
Backward trajectory ending at 1200 UTC 28 Mar 16
GDAS Meteorological Data

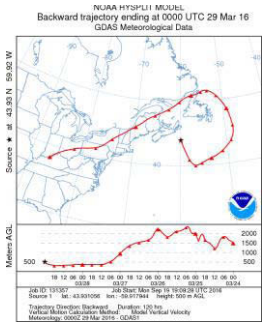


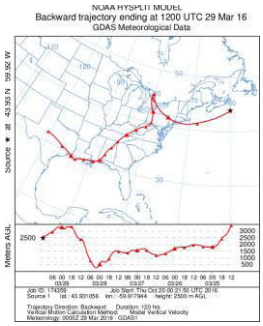


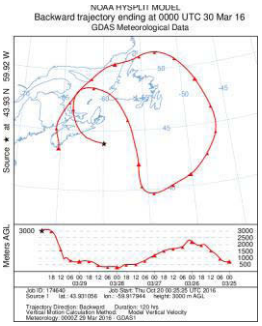


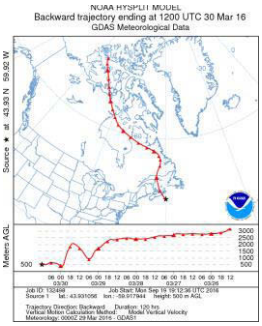


## March 21st – 30th, 2016

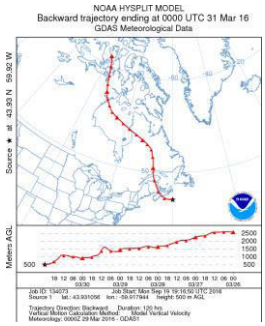


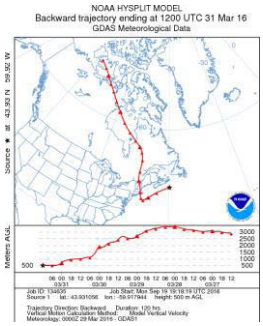


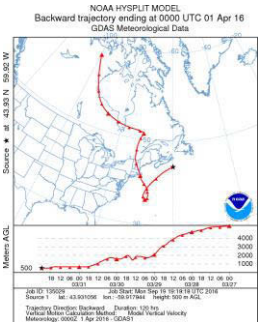


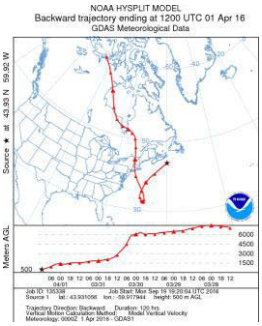


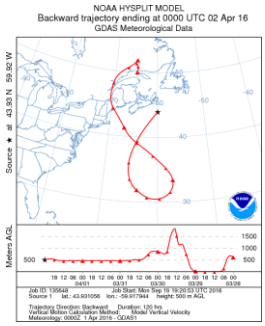


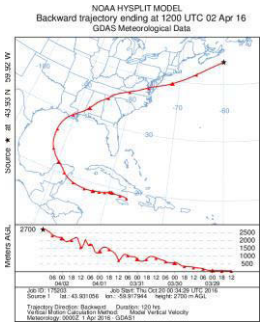


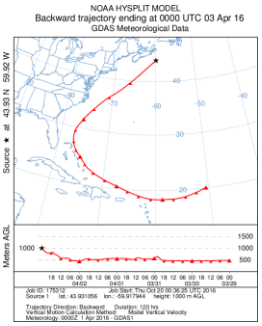


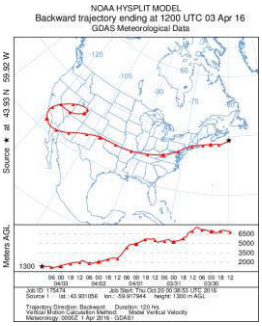


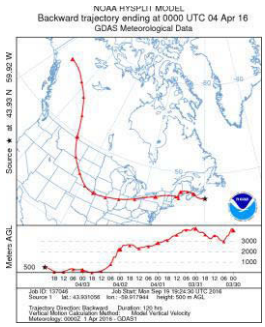


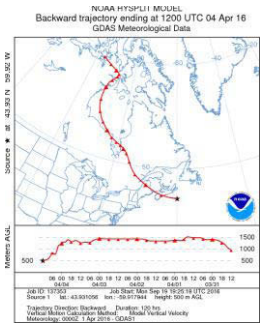


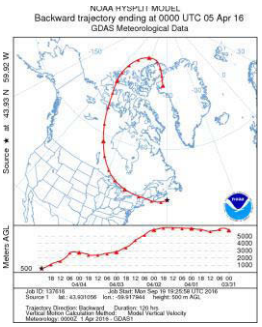


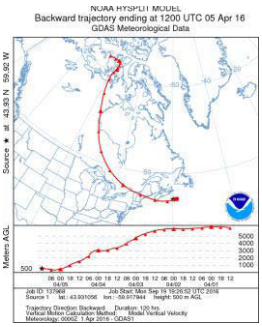

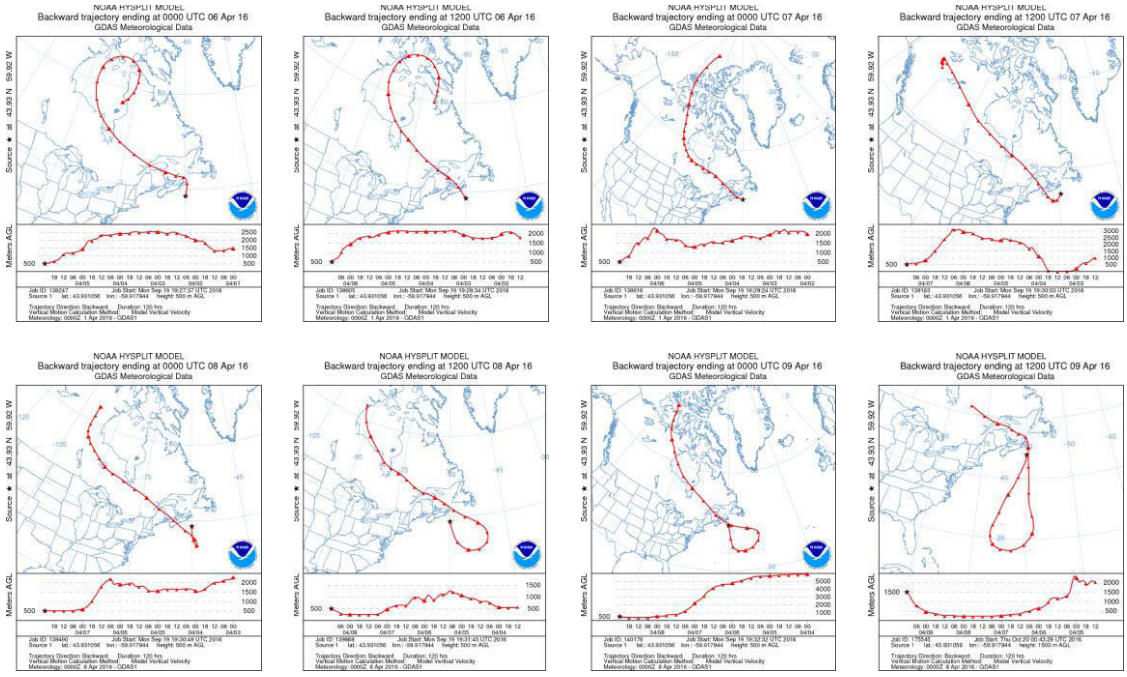


## March 31st – April 9th, 2016

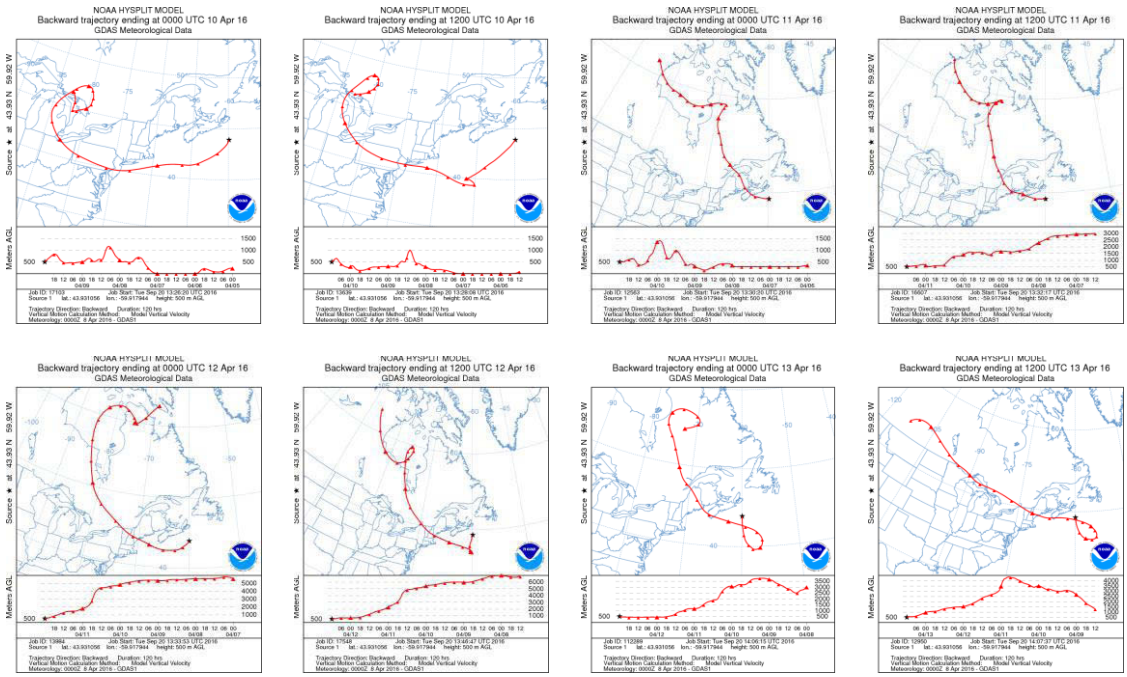

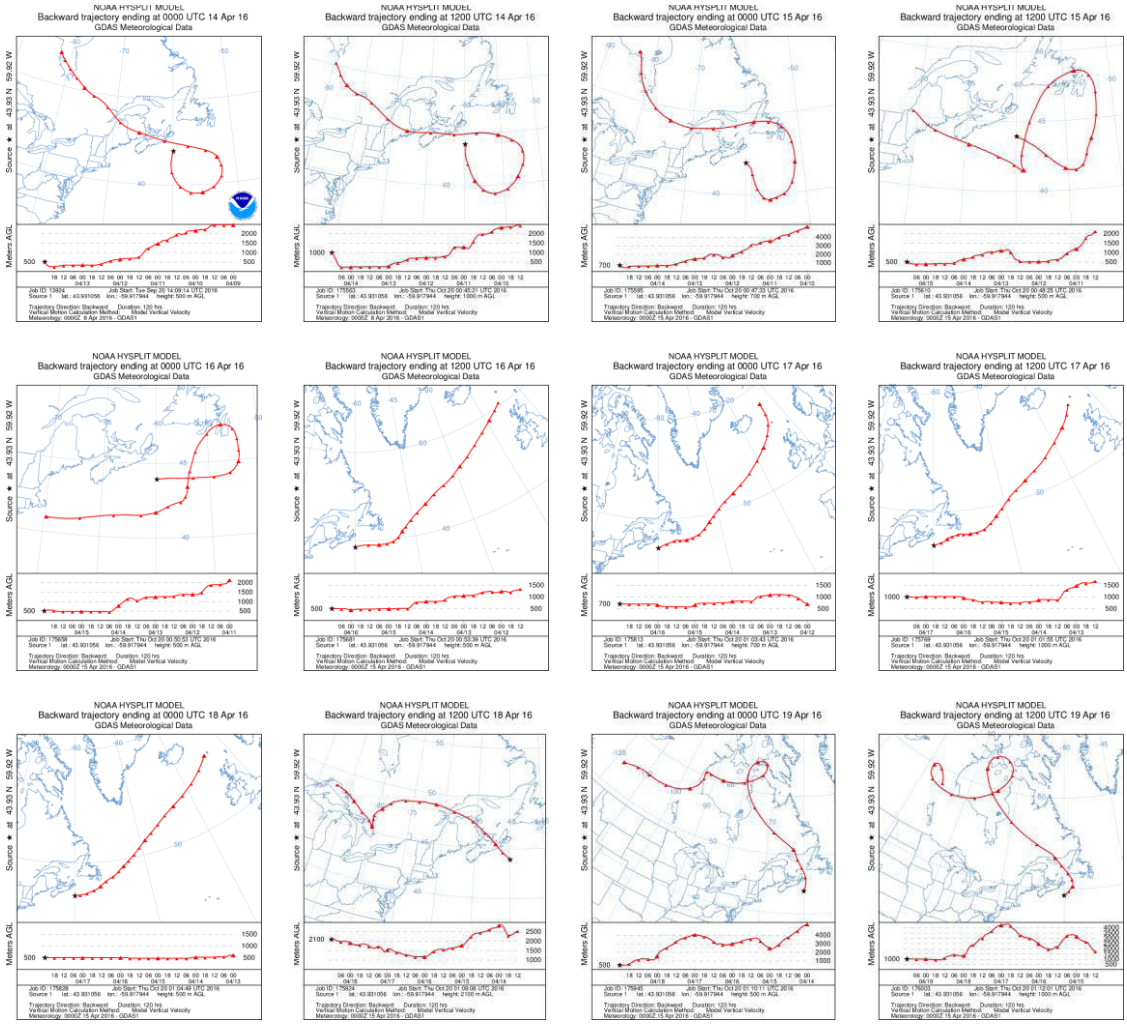


## April 10th – 19th, 2016

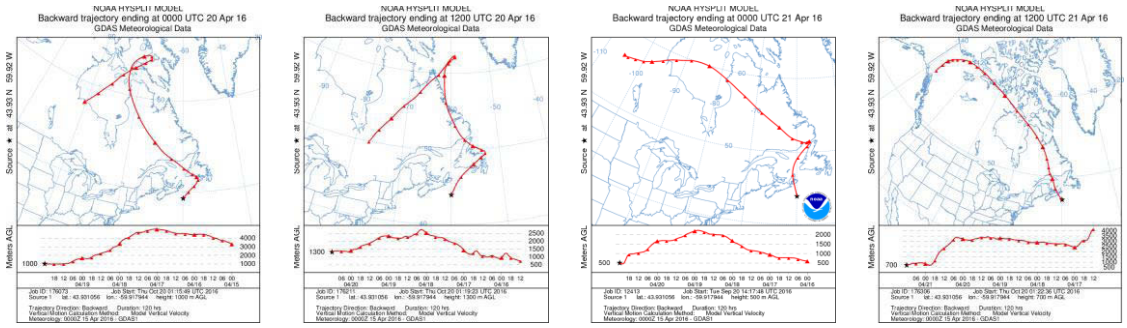

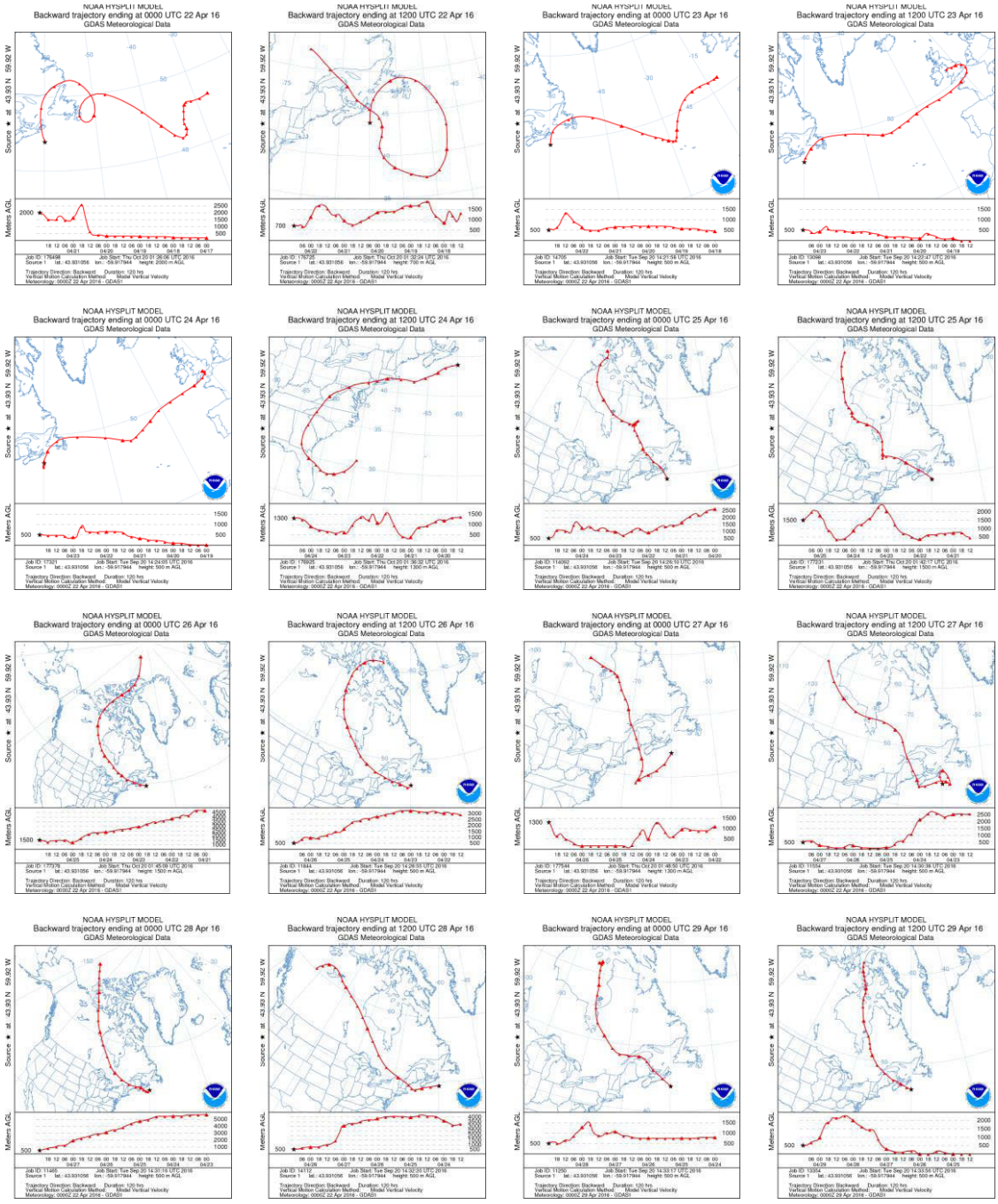


**April 20th – 29th, 2016**

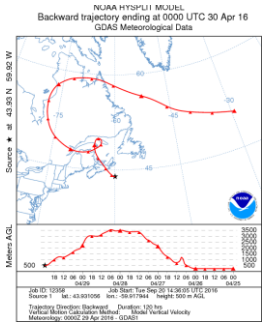
NOAA HYSPLIT MODEL
Backward trajectory ending at 0000 UTC 30 Apr 16
GDAS Meteorological Data

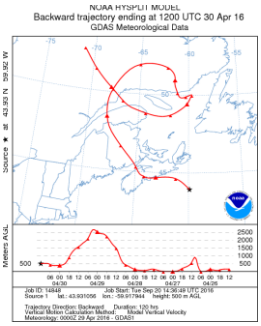
NOAA HYSPLIT MODEL
Backward trajectory ending at 1200 UTC 30 Apr 16
GDAS Meteorological Data

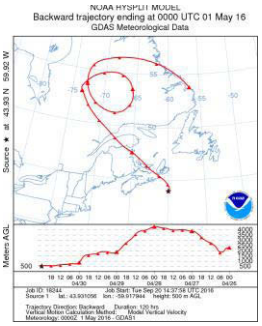
NOAA HYSPLIT MODEL
Backward trajectory ending at 0000 UTC 01 May 16
GDAS Meteorological Data

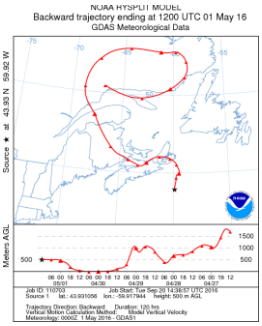
NOAA HYSPLIT MODEL
Backward trajectory ending at 1200 UTC 01 May 16
GDAS Meteorological Data

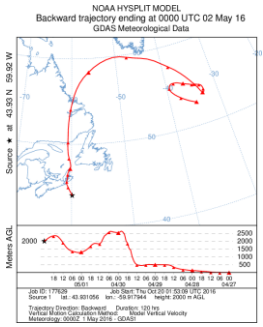
NOAA HYSPLIT MODEL
Backward trajectory ending at 0000 UTC 02 May 16
GDAS Meteorological Data

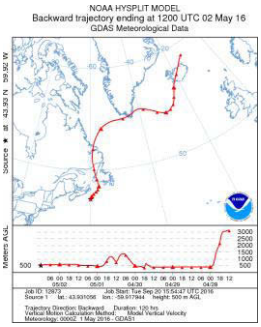
NOAA HYSPLIT MODEL
Backward trajectory ending at 1200 UTC 02 May 16
GDAS Meteorological Data

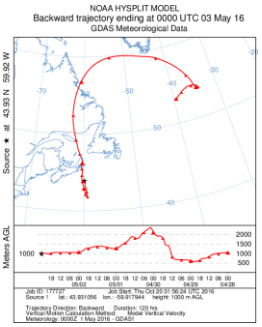
NOAA HYSPLIT MODEL
Backward trajectory ending at 0000 UTC 03 May 16
GDAS Meteorological Data

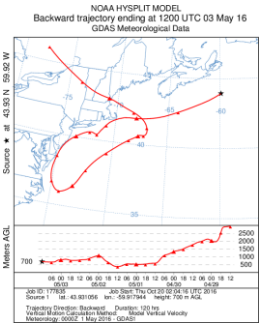
NOAA HYSPLIT MODEL
Backward trajectory ending at 1200 UTC 03 May 16
GDAS Meteorological Data

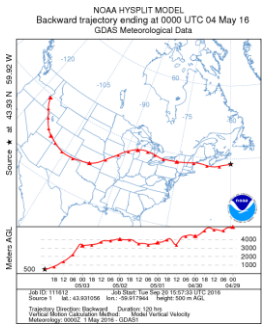
NOAA HYSPLIT MODEL
Backward trajectory ending at 0000 UTC 04 May 16
GDAS Meteorological Data

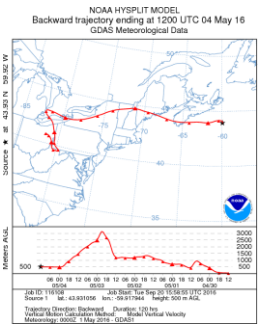
NOAA HYSPLIT MODEL
Backward trajectory ending at 1200 UTC 04 May 16
GDAS Meteorological Data

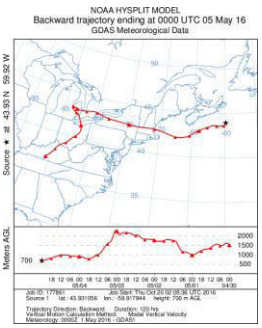
NOAA HYSPLIT MODEL
Backward trajectory ending at 0000 UTC 05 May 16
GDAS Meteorological Data

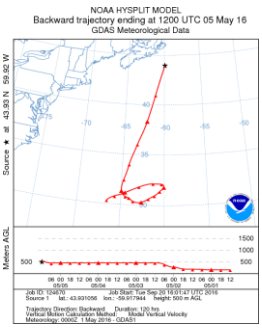
NOAA HYSPLIT MODEL
Backward trajectory ending at 1200 UTC 05 May 16
GDAS Meteorological Data

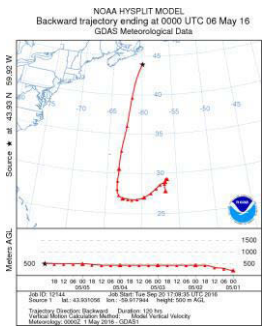
NOAA HYSPLIT MODEL
Backward trajectory ending at 0000 UTC 06 May 16
GDAS Meteorological Data

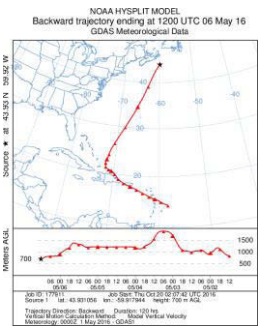
NOAA HYSPLIT MODEL
Backward trajectory ending at 1200 UTC 06 May 16
GDAS Meteorological Data

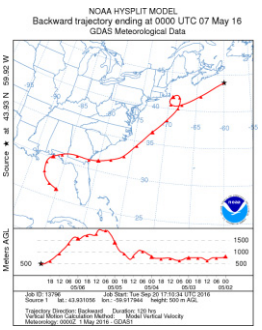
NOAA HYSPLIT MODEL
Backward trajectory ending at 0000 UTC 07 May 16
GDAS Meteorological Data

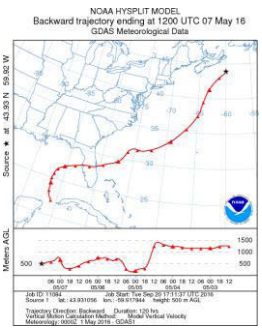
NOAA HYSPLIT MODEL
Backward trajectory ending at 1200 UTC 07 May 16
GDAS Meteorological Data

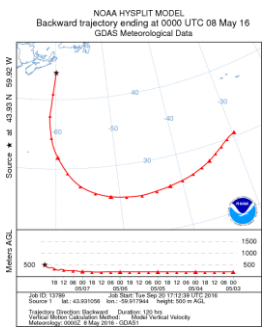
NOAA HYSPLIT MODEL
Backward trajectory ending at 0000 UTC 08 May 16
GDAS Meteorological Data

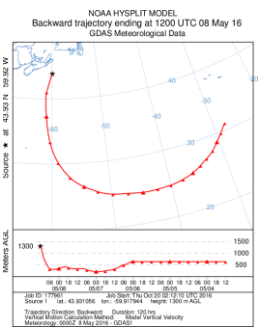
NOAA HYSPLIT MODEL
Backward trajectory ending at 1200 UTC 08 May 16
GDAS Meteorological Data

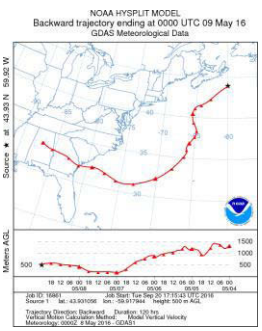
NOAA HYSPLIT MODEL
Backward trajectory ending at 0000 UTC 09 May 16
GDAS Meteorological Data

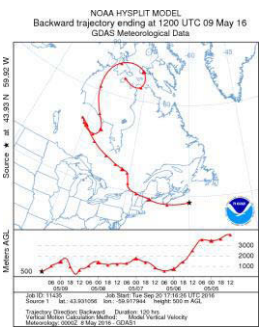
NOAA HYSPLIT MODEL
Backward trajectory ending at 1200 UTC 09 May 16
GDAS Meteorological Data

## April 30th – May 9th, 2016

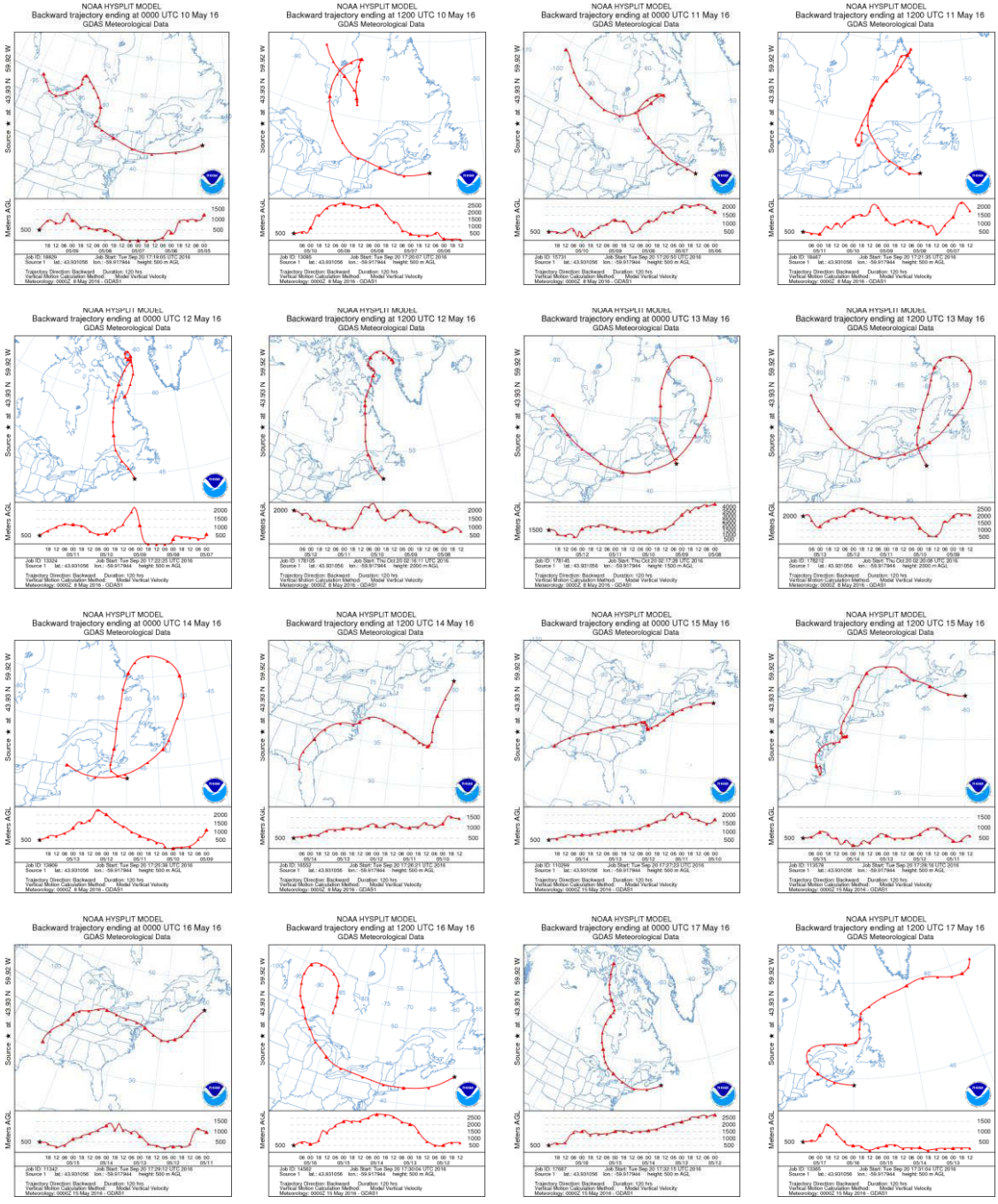

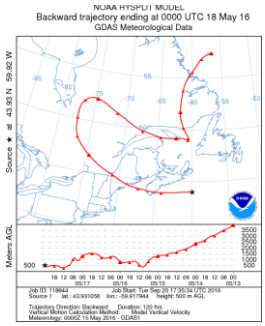


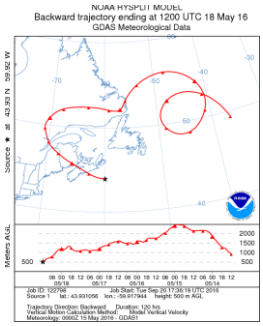


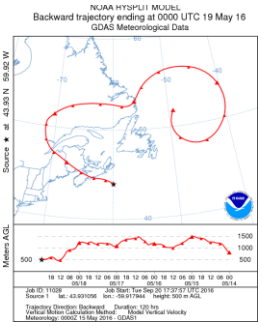


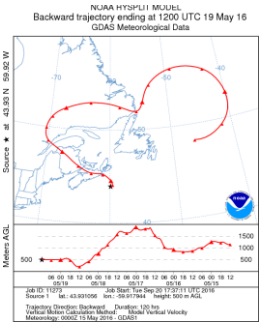


## May 10th – 19th, 2016

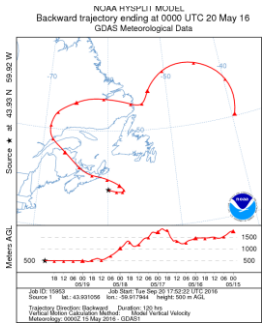


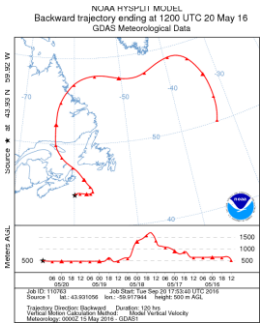


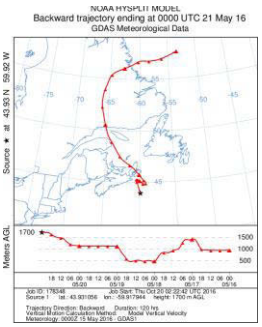


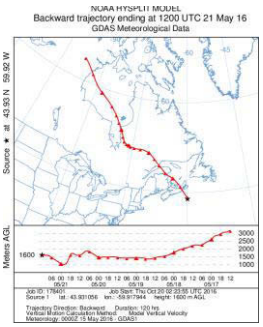


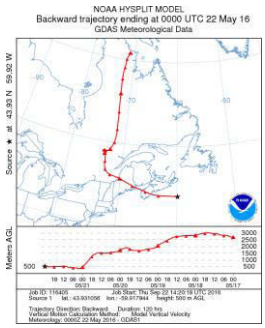


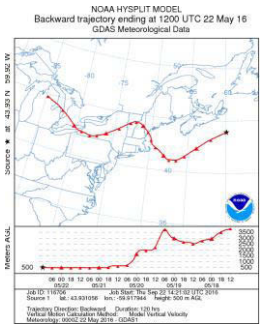


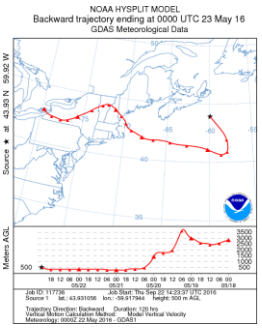


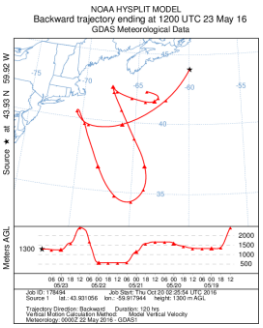


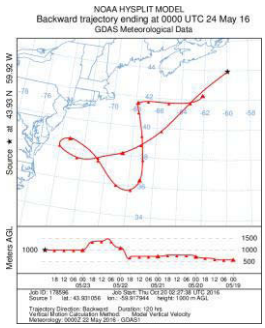


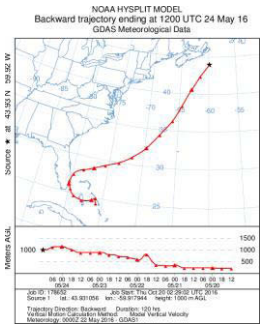


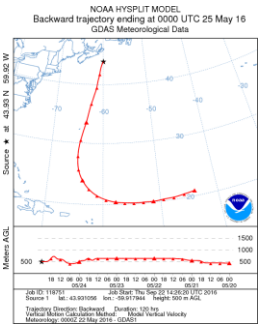


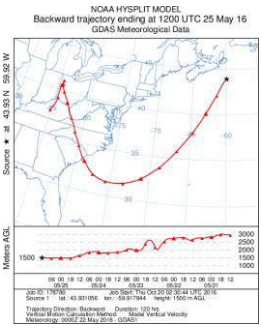

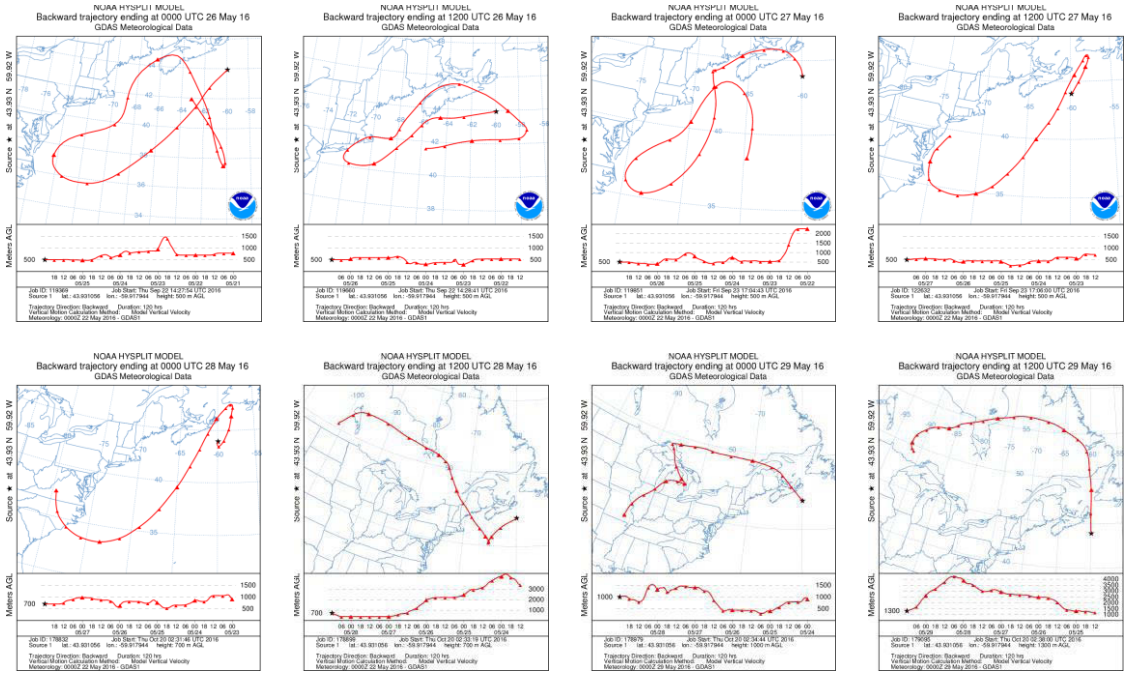


## May 20th – 29th, 2016

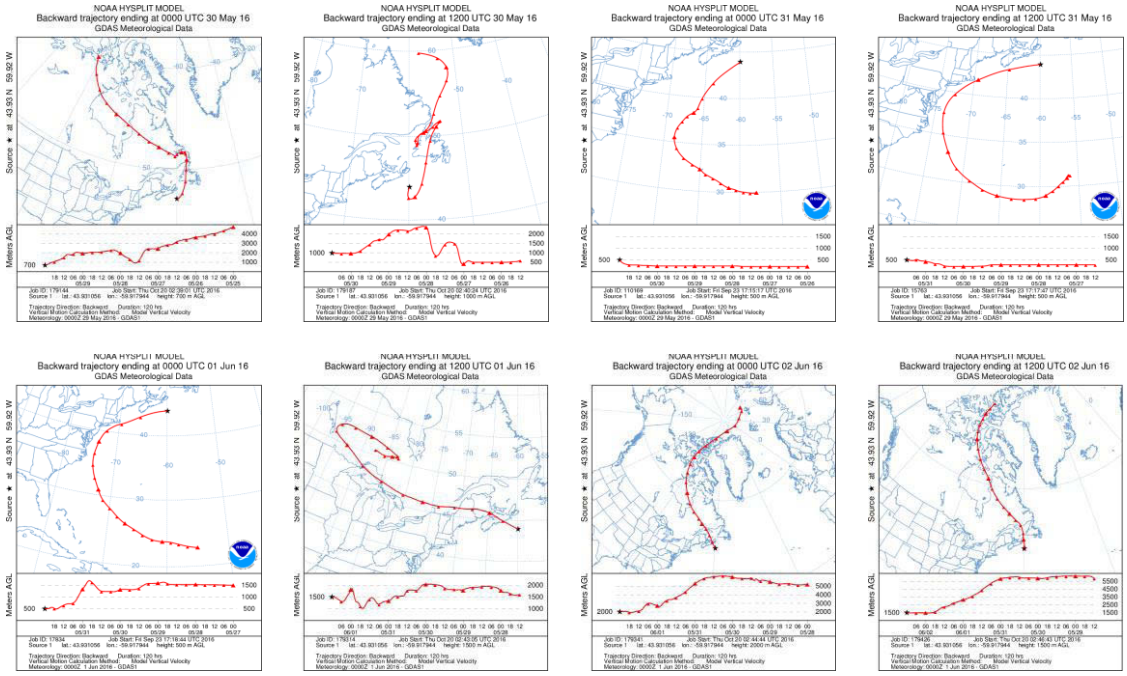

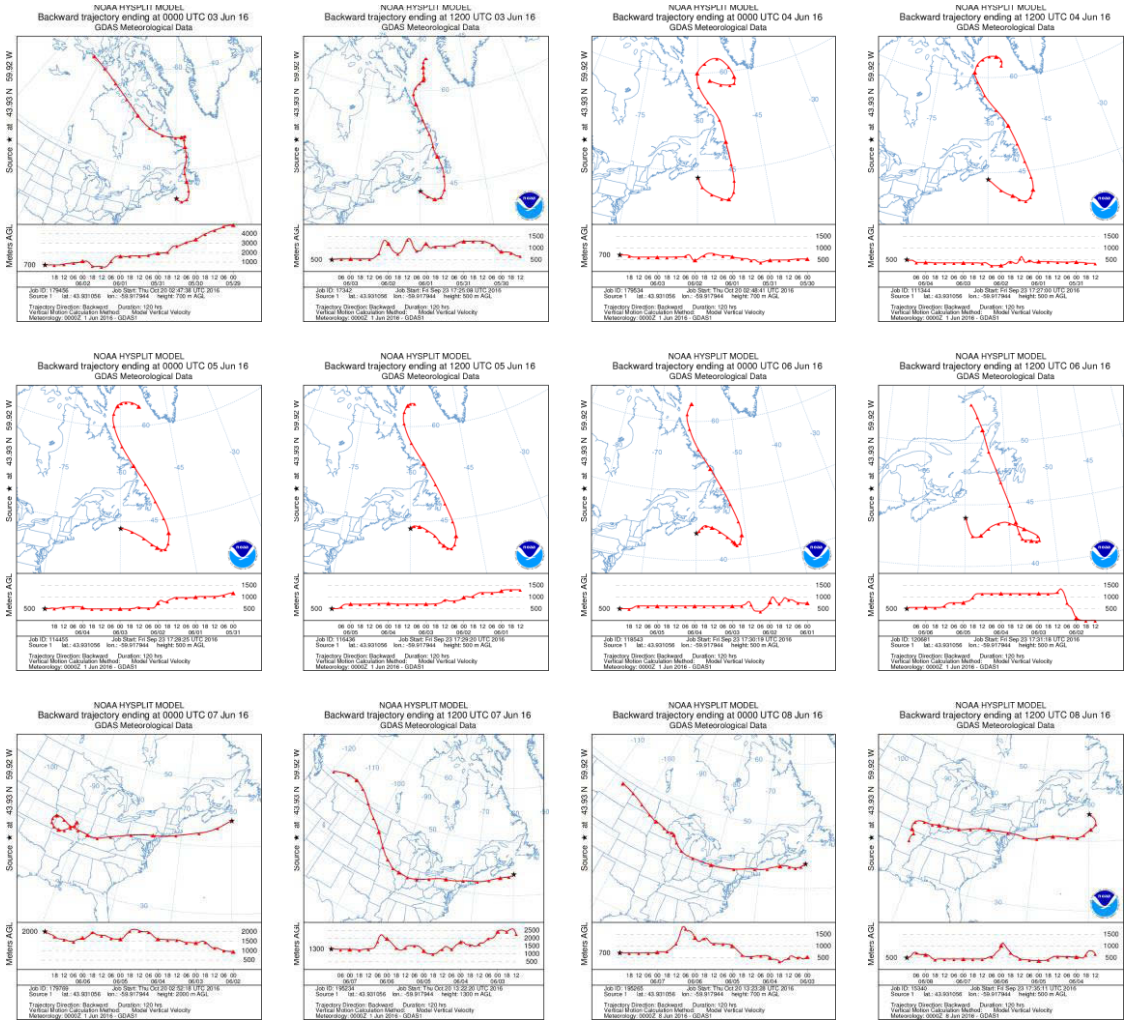


## May 30th – June 8th, 2016

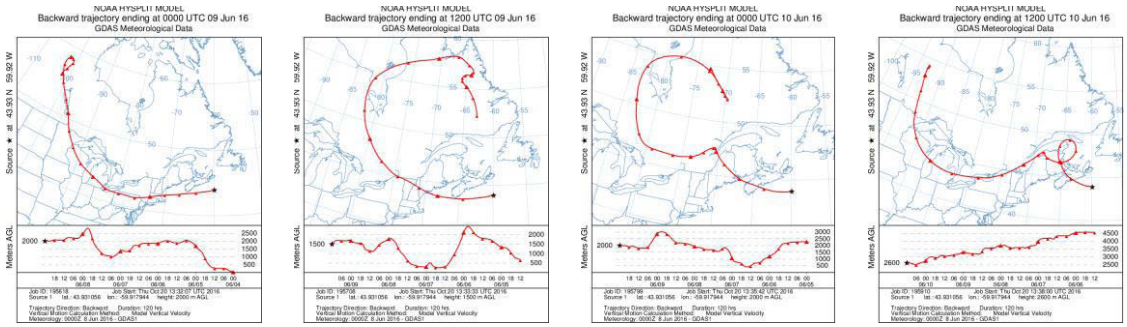

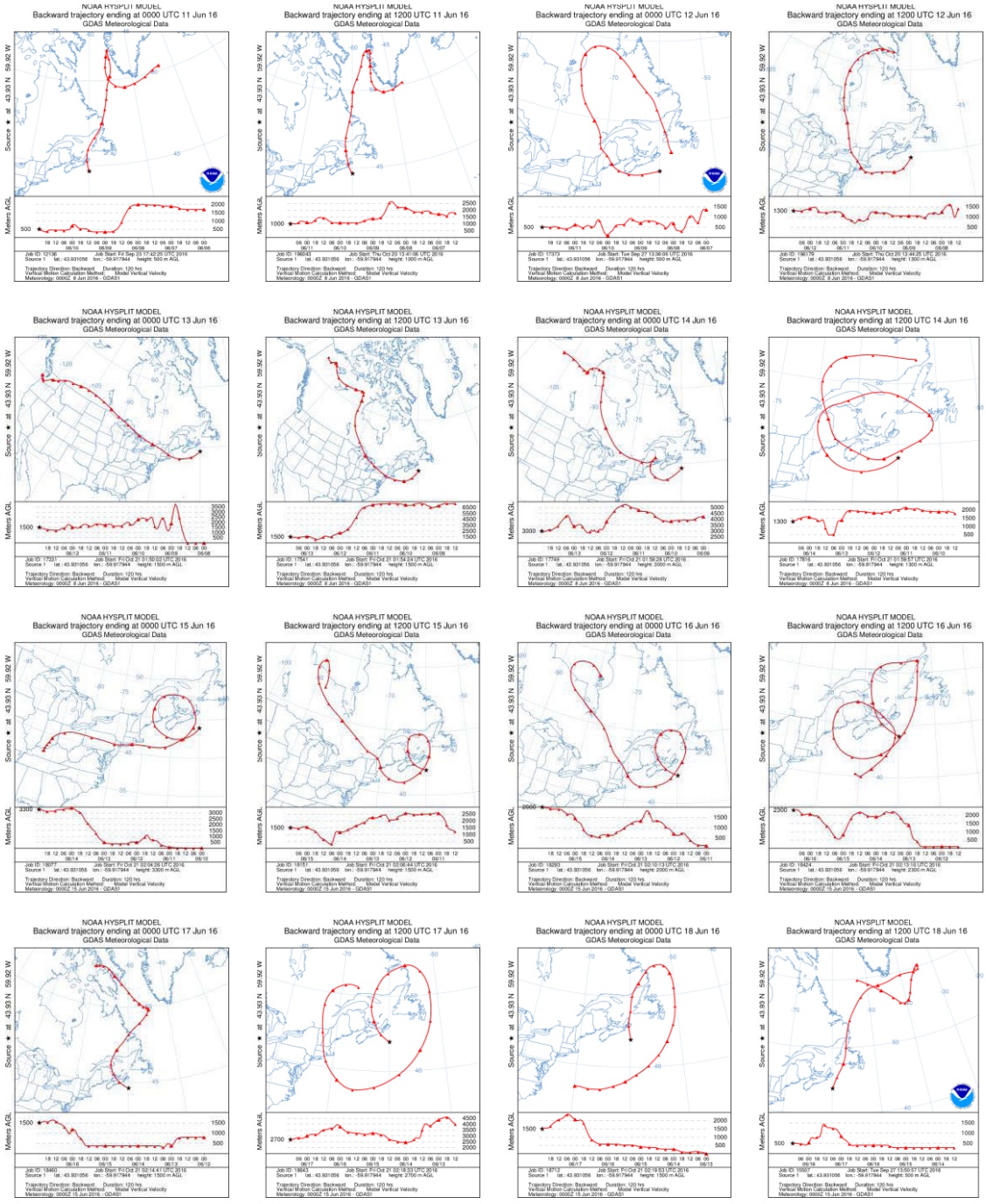


**June 9th – 18th, 2016**

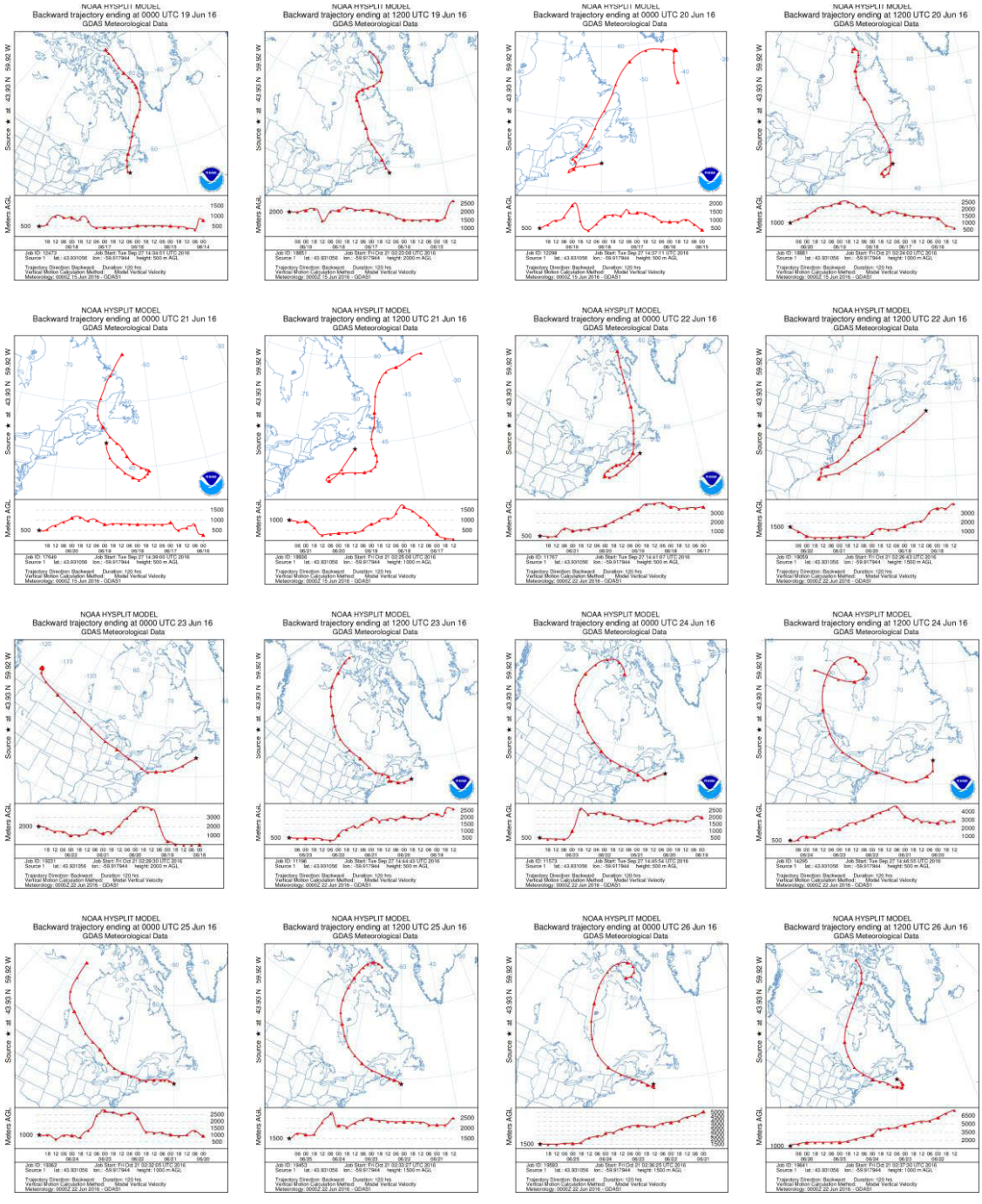
NOAA HYSPLIT MODEL
Backward trajectory ending at 0000 UTC 19 Jun 16
GDAS Meteorological Data
NOAA HYSPLIT MODEL
Backward trajectory ending at 1200 UTC 19 Jun 16
GDAS Meteorological Data
NOAA HYSPLIT MODEL
Backward trajectory ending at 0000 UTC 20 Jun 16
GDAS Meteorological Data
NOAA HYSPLIT MODEL
Backward trajectory ending at 1200 UTC 20 Jun 16
GDAS Meteorological Data
NOAA HYSPLIT MODEL
Backward trajectory ending at 0000 UTC 21 Jun 16
GDAS Meteorological Data
NOAA HYSPLIT MODEL
Backward trajectory ending at 1200 UTC 21 Jun 16
GDAS Meteorological Data
NOAA HYSPLIT MODEL
Backward trajectory ending at 0000 UTC 22 Jun 16
GDAS Meteorological Data
NOAA HYSPLIT MODEL
Backward trajectory ending at 1200 UTC 22 Jun 16
GDAS Meteorological Data
NOAA HYSPLIT MODEL
Backward trajectory ending at 0000 UTC 23 Jun 16
GDAS Meteorological Data
NOAA HYSPLIT MODEL
Backward trajectory ending at 1200 UTC 23 Jun 16
GDAS Meteorological Data
NOAA HYSPLIT MODEL
Backward trajectory ending at 0000 UTC 24 Jun 16
GDAS Meteorological Data
NOAA HYSPLIT MODEL
Backward trajectory ending at 1200 UTC 24 Jun 16
GDAS Meteorological Data
NOAA HYSPLIT MODEL
Backward trajectory ending at 0000 UTC 25 Jun 16
GDAS Meteorological Data
NOAA HYSPLIT MODEL
Backward trajectory ending at 1200 UTC 25 Jun 16
GDAS Meteorological Data
NOAA HYSPLIT MODEL
Backward trajectory ending at 0000 UTC 26 Jun 16
GDAS Meteorological Data
NOAA HYSPLIT MODEL
Backward trajectory ending at 1200 UTC 26 Jun 16
GDAS Meteorological Data

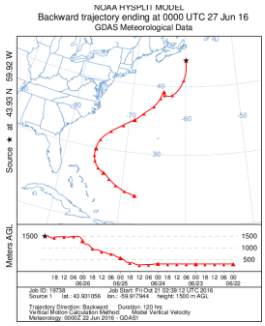


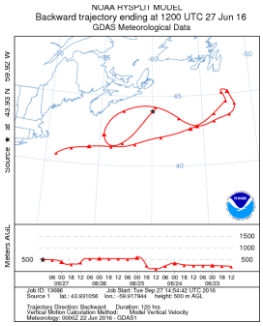


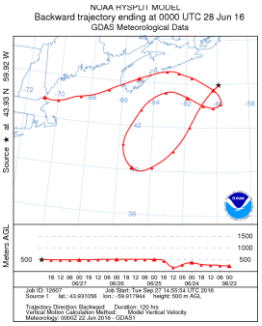


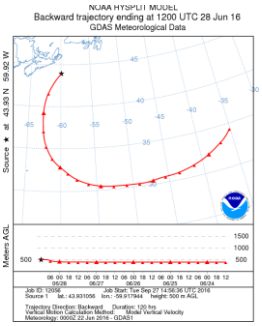


## June 19th – 28th, 2016

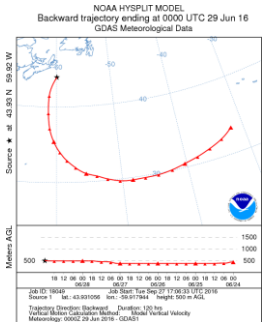


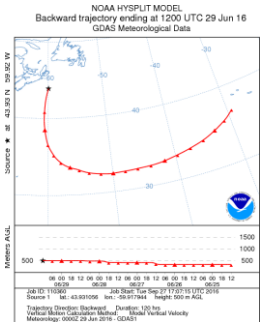


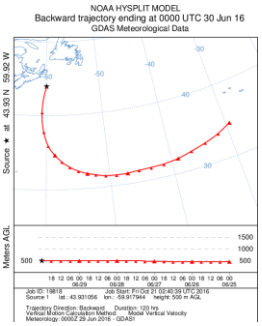


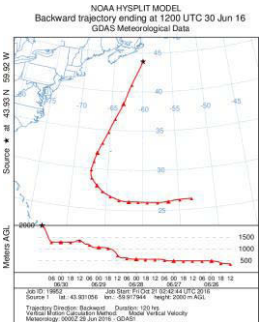


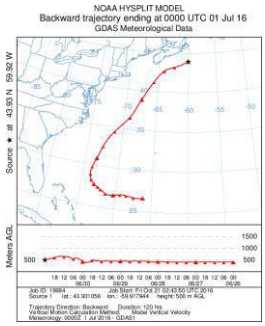


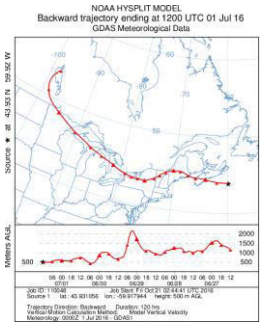


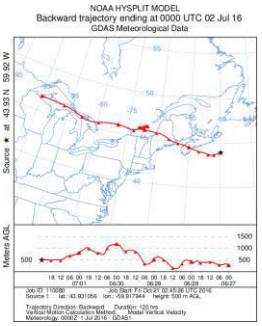


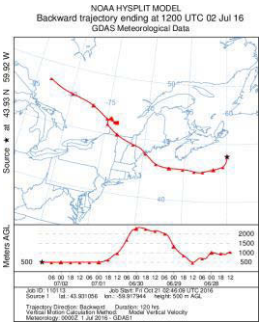


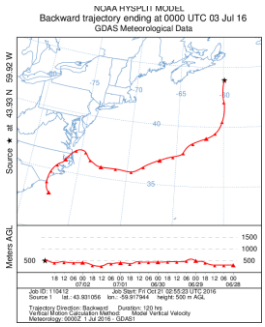


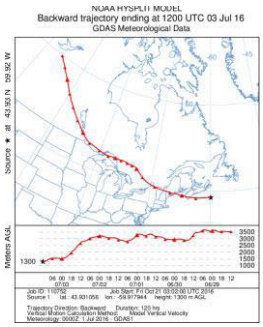


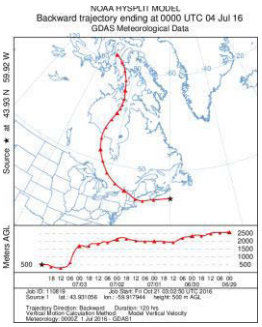


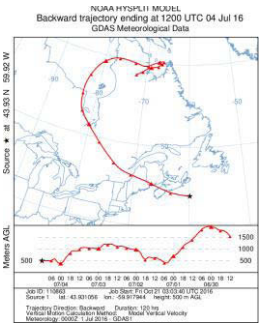

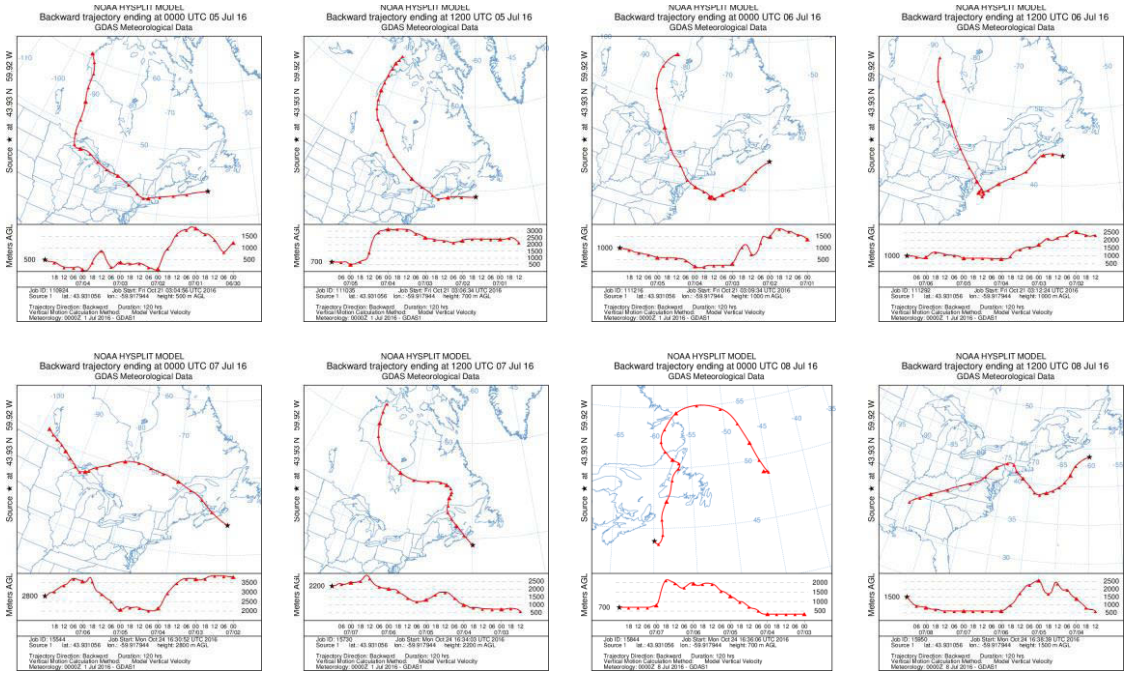


## June 29th – July 8th, 2016

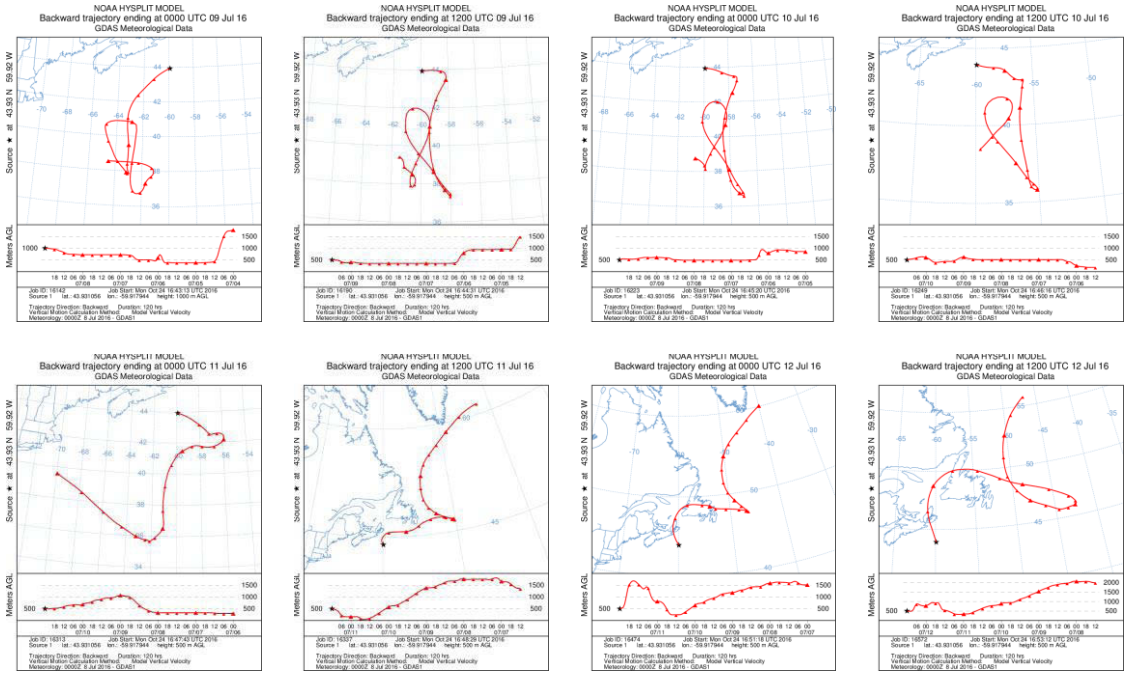

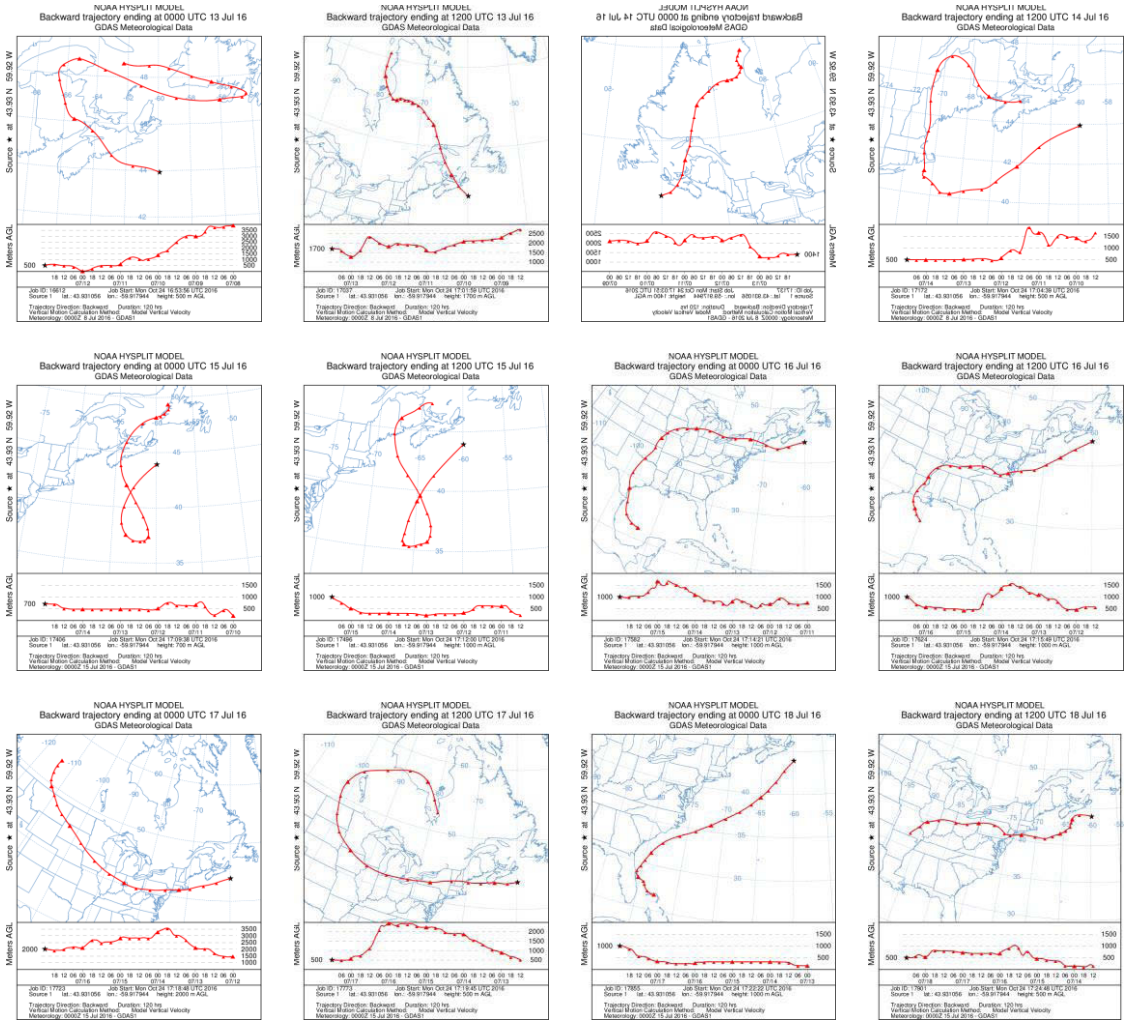


## July 9th – 18th, 2016

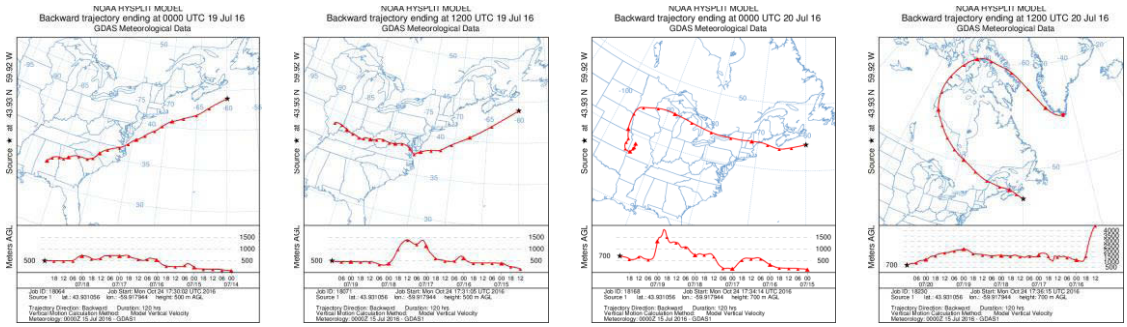

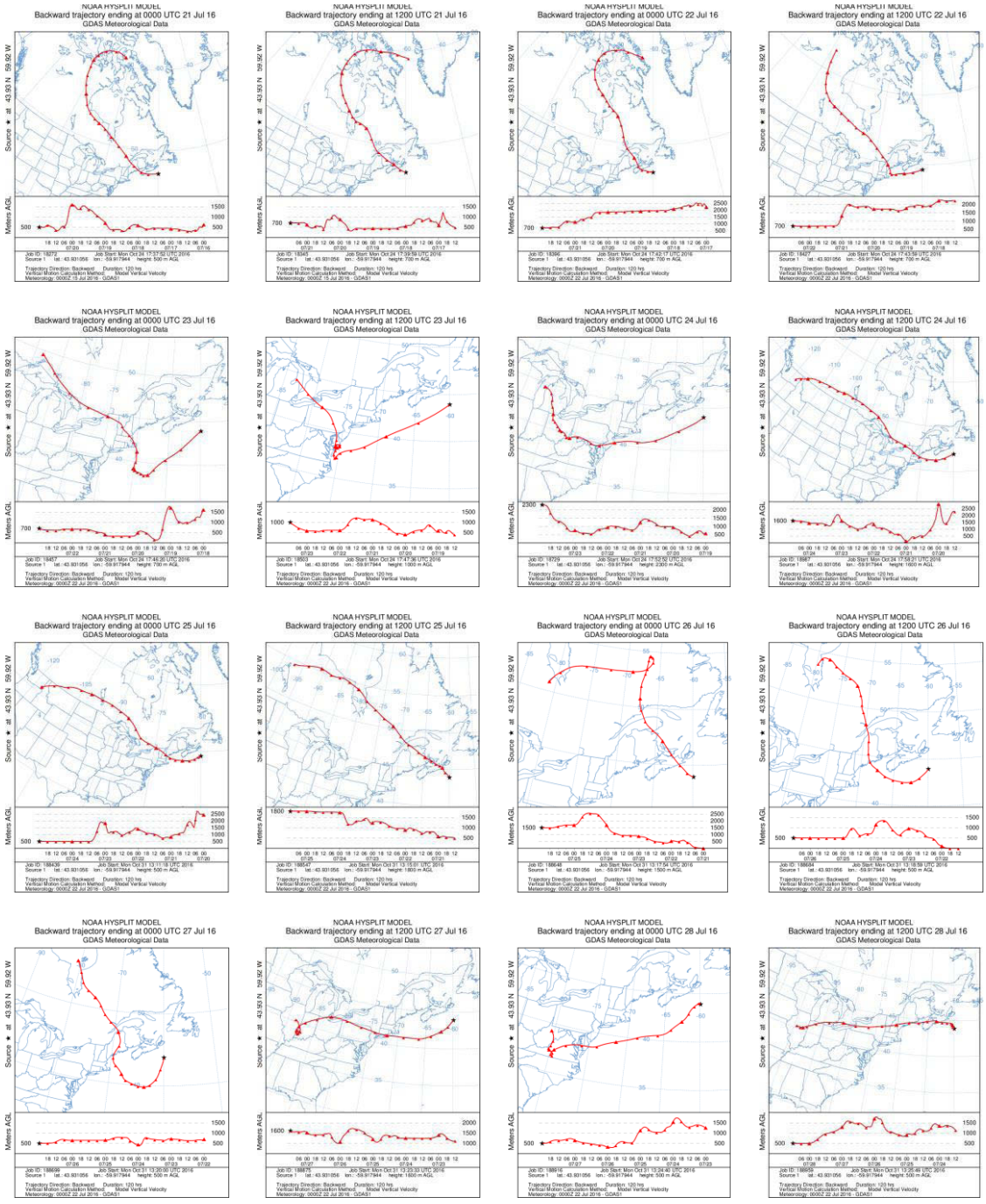


**July 19th – 28th, 2016**

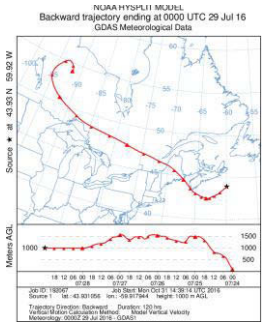
NOAA HYSPLIT MODEL
Backward trajectory ending at 0000 UTC 29 Jul 16
GDAS Meteorological Data

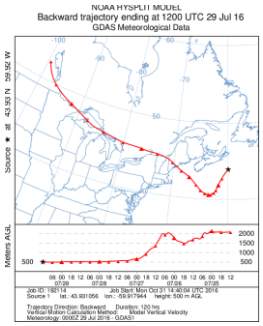
NOAA HYSPLIT MODEL
Backward trajectory ending at 1200 UTC 29 Jul 16
GDAS Meteorological Data

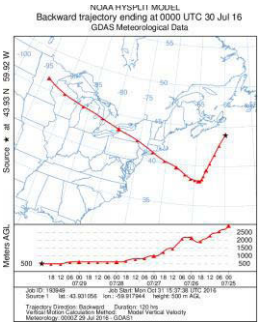
NOAA HYSPLIT MODEL
Backward trajectory ending at 0000 UTC 30 Jul 16
GDAS Meteorological Data

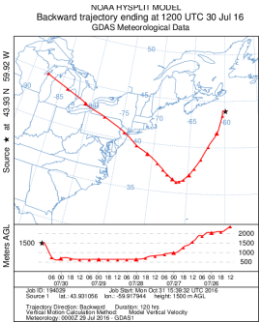
NOAA HYSPLIT MODEL
Backward trajectory ending at 1200 UTC 30 Jul 16
GDAS Meteorological Data

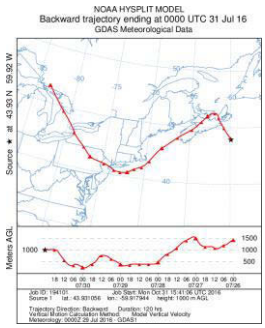
NOAA HYSPLIT MODEL
Backward trajectory ending at 0000 UTC 31 Jul 16
GDAS Meteorological Data

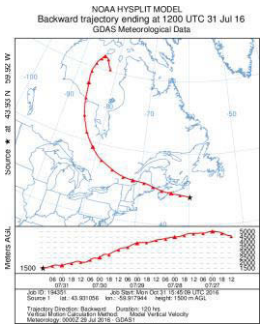
NOAA HYSPLIT MODEL
Backward trajectory ending at 1200 UTC 31 Jul 16
GDAS Meteorological Data

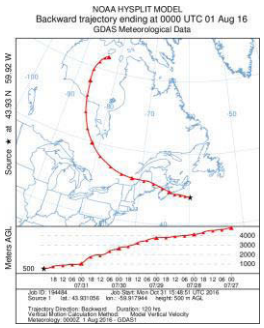
NOAA HYSPLIT MODEL
Backward trajectory ending at 0000 UTC 01 Aug 16
GDAS Meteorological Data

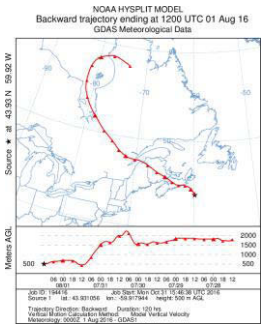
NOAA HYSPLIT MODEL
Backward trajectory ending at 1200 UTC 01 Aug 16
GDAS Meteorological Data

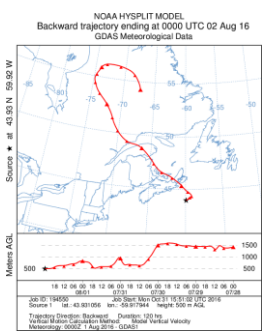
NOAA HYSPLIT MODEL
Backward trajectory ending at 0000 UTC 02 Aug 16
GDAS Meteorological Data

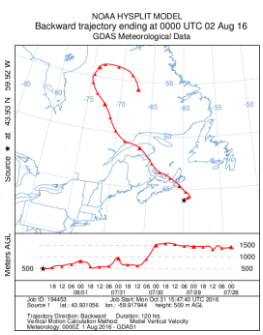
NOAA HYSPLIT MODEL
Backward trajectory ending at 0000 UTC 02 Aug 16
GDAS Meteorological Data

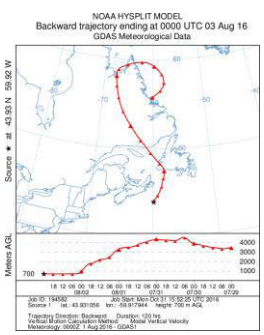
NOAA HYSPLIT MODEL
Backward trajectory ending at 0000 UTC 03 Aug 16
GDAS Meteorological Data

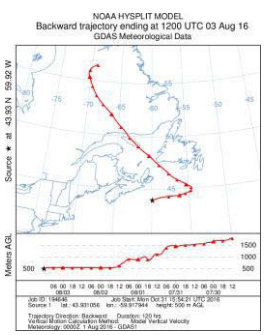
NOAA HYSPLIT MODEL
Backward trajectory ending at 1200 UTC 03 Aug 16
GDAS Meteorological Data

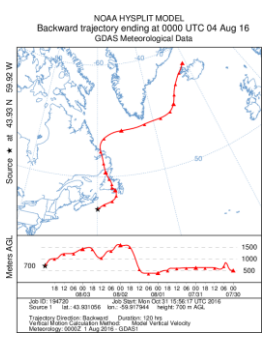
NOAA HYSPLIT MODEL
Backward trajectory ending at 0000 UTC 04 Aug 16
GDAS Meteorological Data

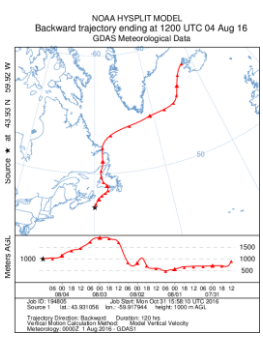
NOAA HYSPLIT MODEL
Backward trajectory ending at 1200 UTC 04 Aug 16
GDAS Meteorological Data

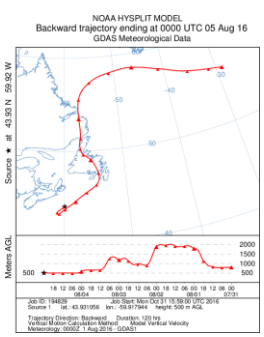
NOAA HYSPLIT MODEL
Backward trajectory ending at 0000 UTC 05 Aug 16
GDAS Meteorological Data

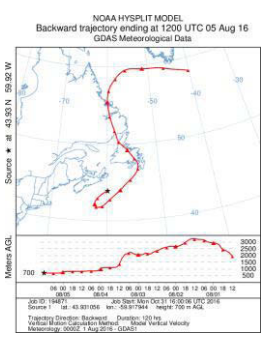
NOAA HYSPLIT MODEL
Backward trajectory ending at 1200 UTC 05 Aug 16
GDAS Meteorological Data

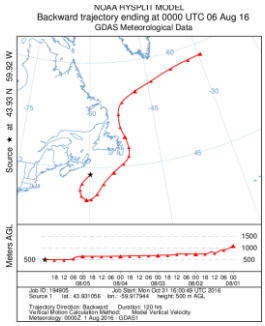


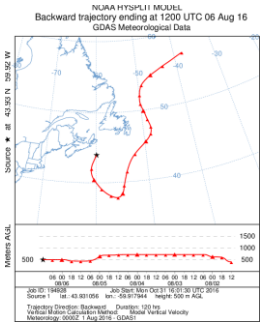


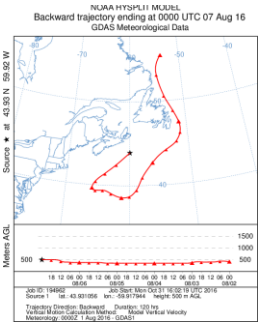


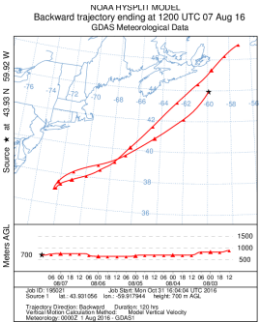


## July 29th – August 7th, 2016

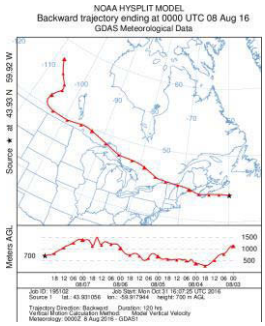


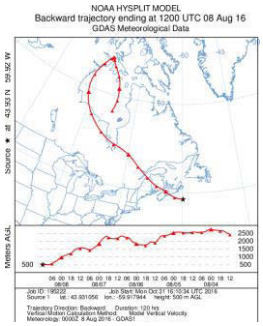


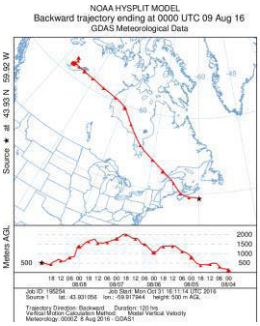


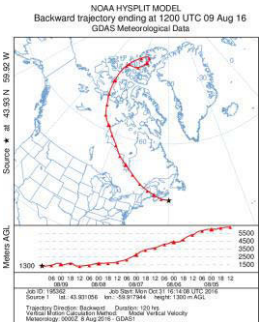


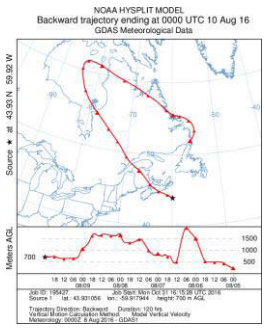


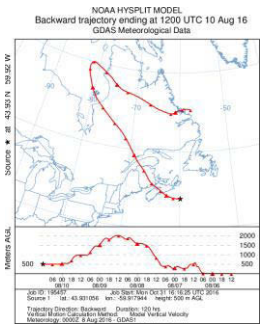


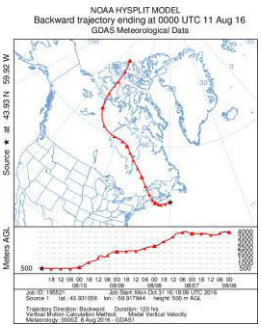


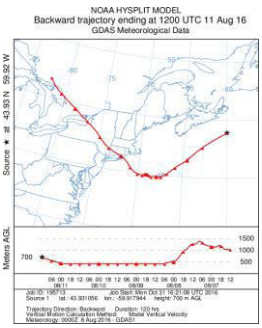


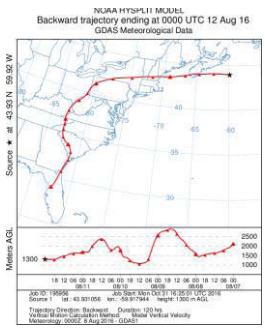


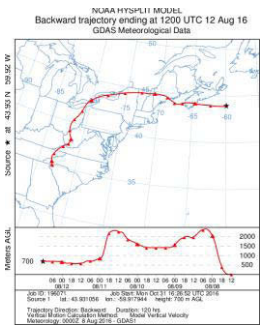


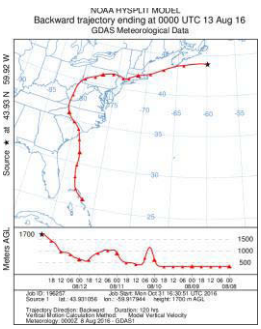


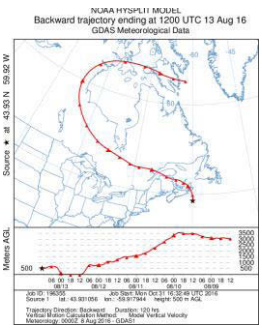

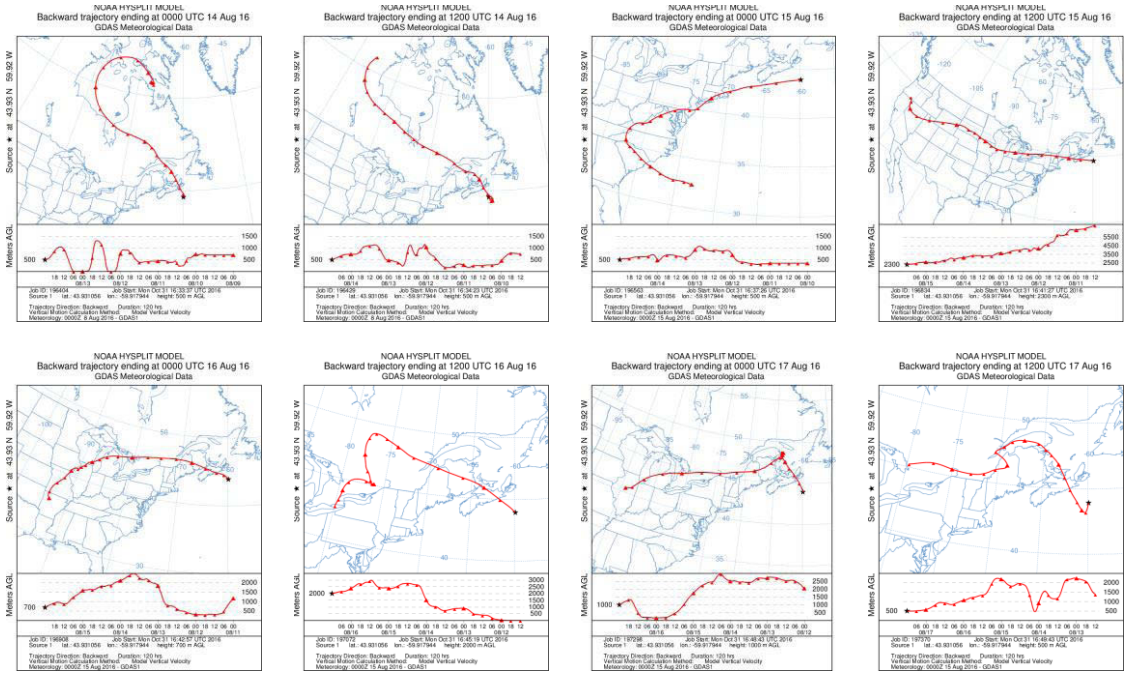


## August 8th – 17th, 2016

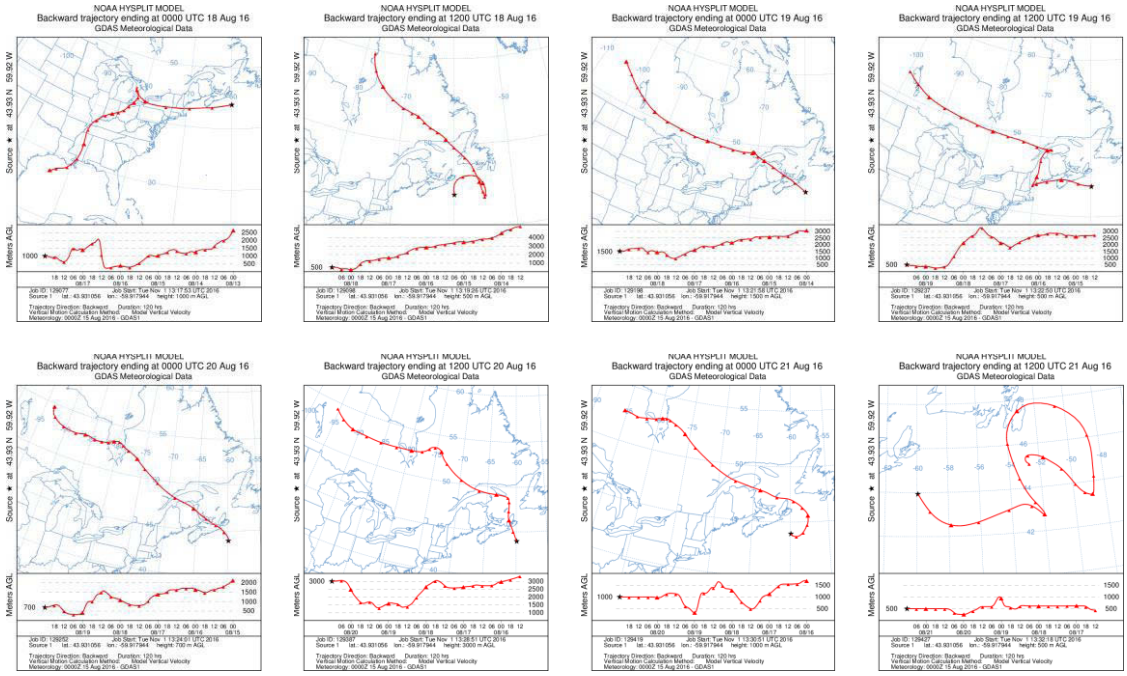

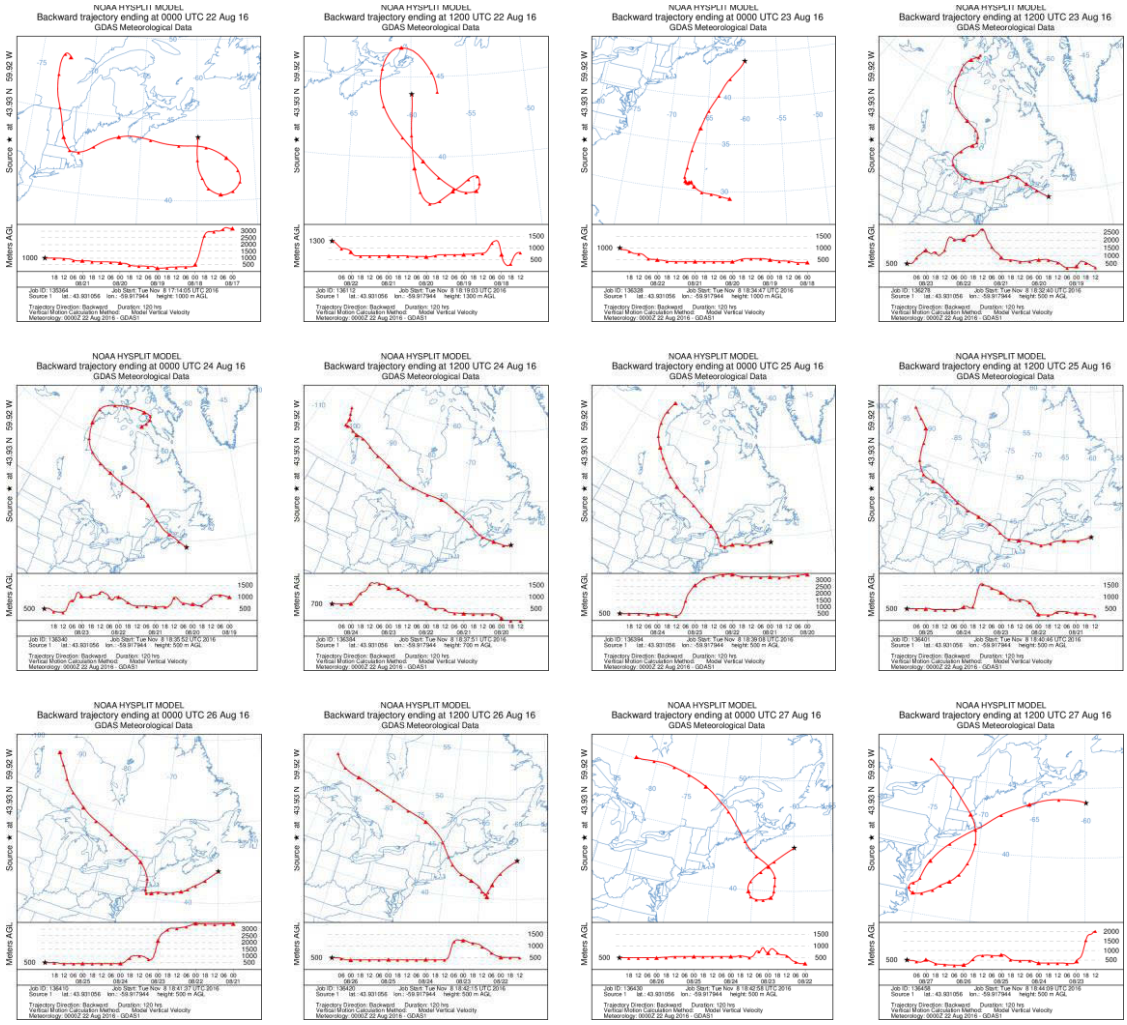


## August 18th – 27th, 2016

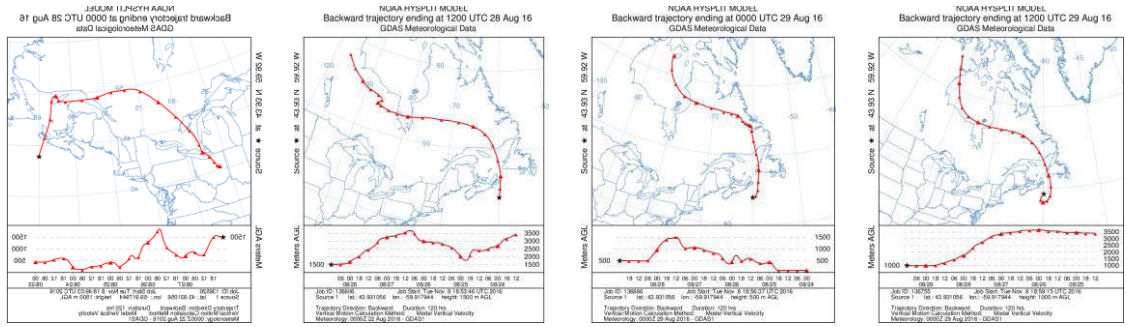

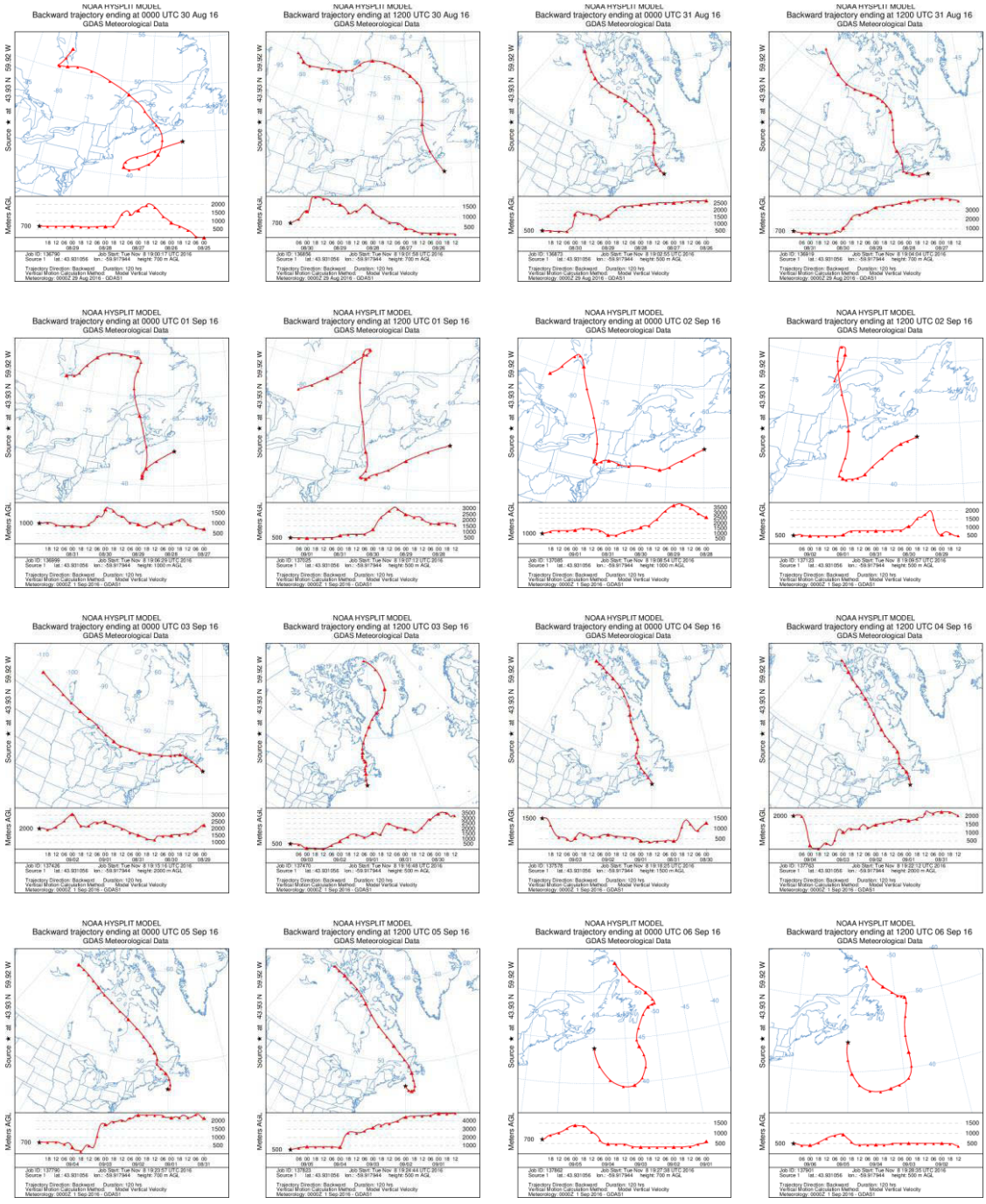


**August 28th – September 6th, 2016**

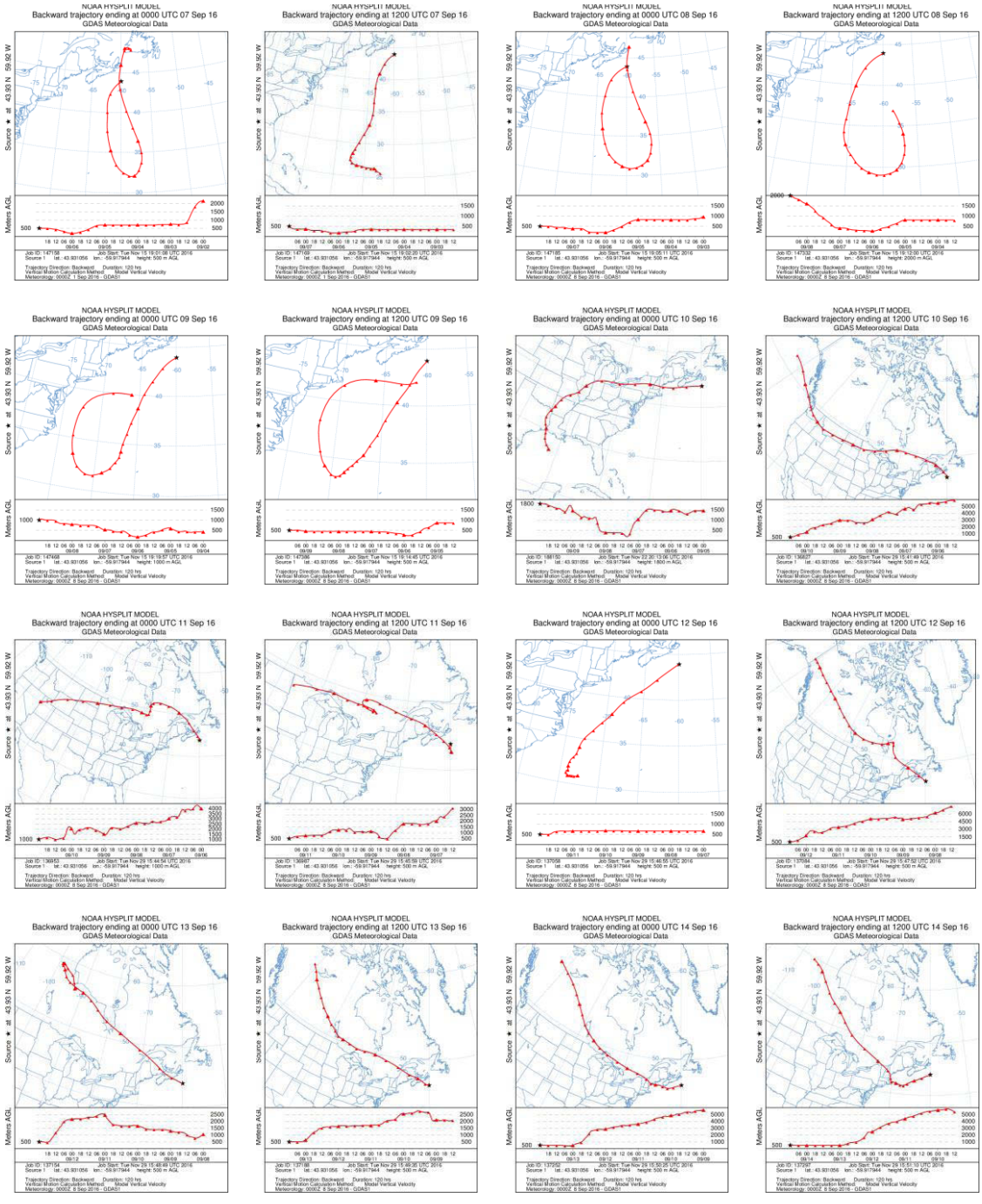
NOAA HYSPLIT MODEL
Backward trajectory ending at 0000 UTC 07 Sep 16
GDAS Meteorological Data
NOAA HYSPLIT MODEL
Backward trajectory ending at 1200 UTC 07 Sep 16
GDAS Meteorological Data
NOAA HYSPLIT MODEL
Backward trajectory ending at 0000 UTC 08 Sep 16
GDAS Meteorological Data
NOAA HYSPLIT MODEL
Backward trajectory ending at 1200 UTC 08 Sep 16
GDAS Meteorological Data
NOAA HYSPLIT MODEL
Backward trajectory ending at 0000 UTC 09 Sep 16
GDAS Meteorological Data
NOAA HYSPLIT MODEL
Backward trajectory ending at 1200 UTC 09 Sep 16
GDAS Meteorological Data
NOAA HYSPLIT MODEL
Backward trajectory ending at 0000 UTC 10 Sep 16
GDAS Meteorological Data
NOAA HYSPLIT MODEL
Backward trajectory ending at 1200 UTC 10 Sep 16
GDAS Meteorological Data
NOAA HYSPLIT MODEL
Backward trajectory ending at 0000 UTC 11 Sep 16
GDAS Meteorological Data
NOAA HYSPLIT MODEL
Backward trajectory ending at 1200 UTC 11 Sep 16
GDAS Meteorological Data
NOAA HYSPLIT MODEL
Backward trajectory ending at 0000 UTC 12 Sep 16
GDAS Meteorological Data
NOAA HYSPLIT MODEL
Backward trajectory ending at 1200 UTC 12 Sep 16
GDAS Meteorological Data
NOAA HYSPLIT MODEL
Backward trajectory ending at 0000 UTC 13 Sep 16
GDAS Meteorological Data
NOAA HYSPLIT MODEL
Backward trajectory ending at 1200 UTC 13 Sep 16
GDAS Meteorological Data
NOAA HYSPLIT MODEL
Backward trajectory ending at 0000 UTC 14 Sep 16
GDAS Meteorological Data
NOAA HYSPLIT MODEL
Backward trajectory ending at 1200 UTC 14 Sep 16
GDAS Meteorological Data

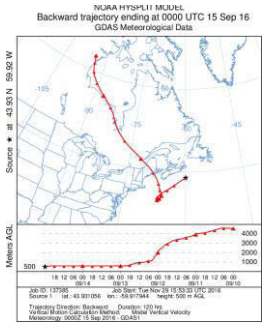


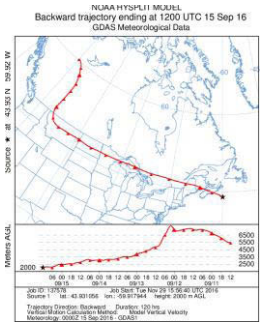


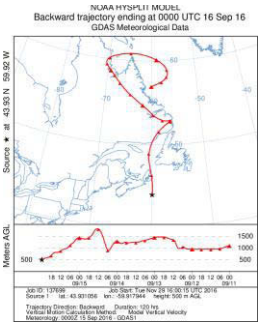


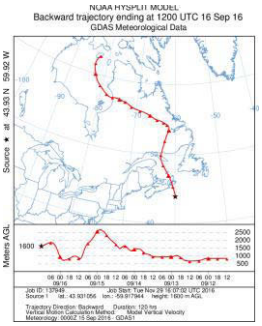


## September 7th-16th, 2016

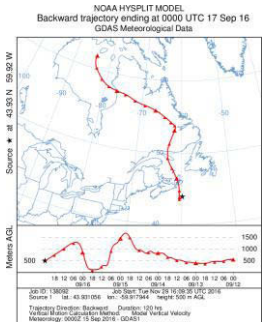


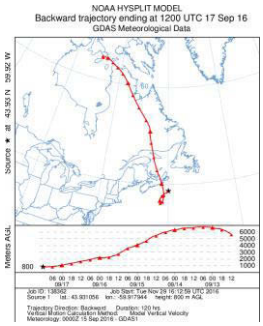


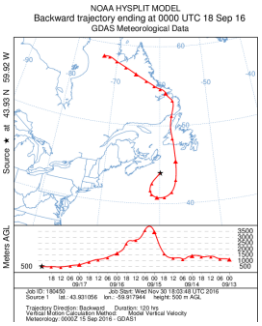


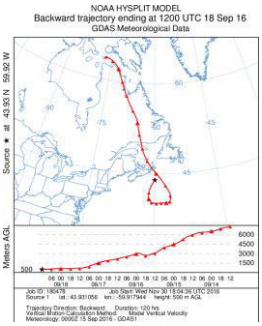


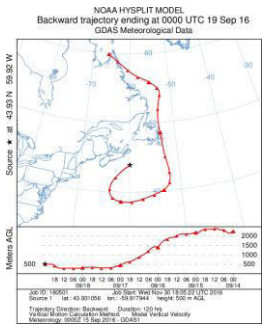


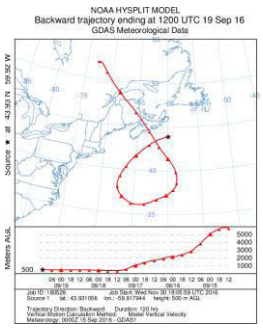


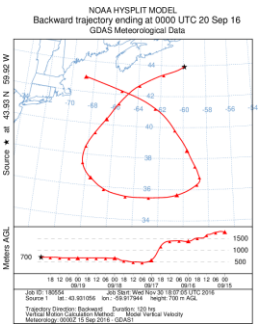


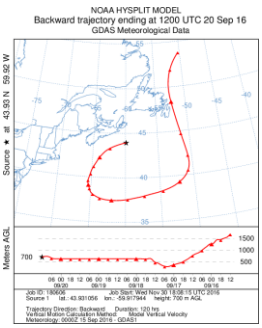


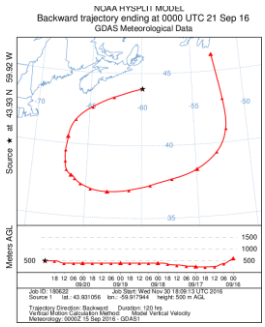


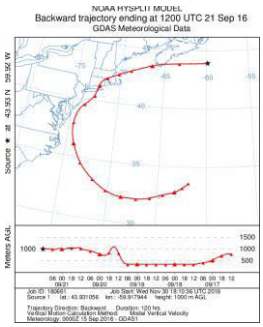


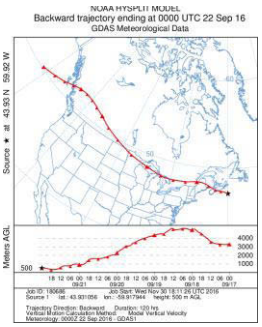


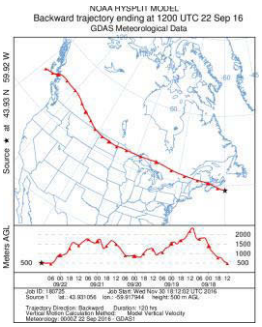

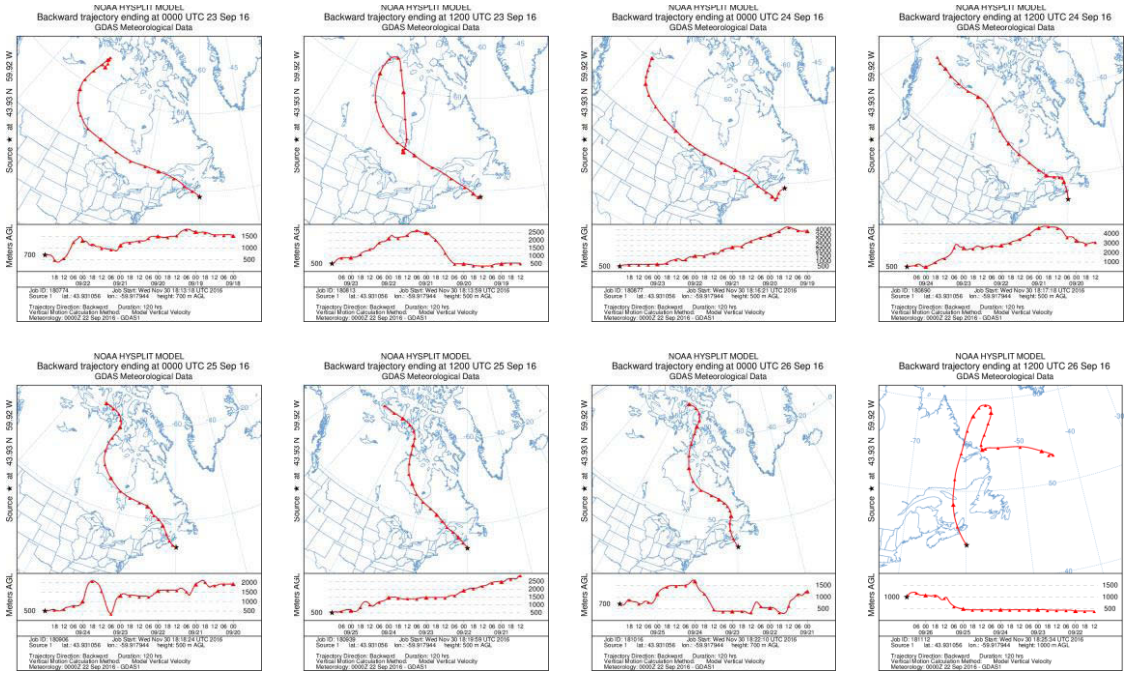


## September 17th – 26th, 2016

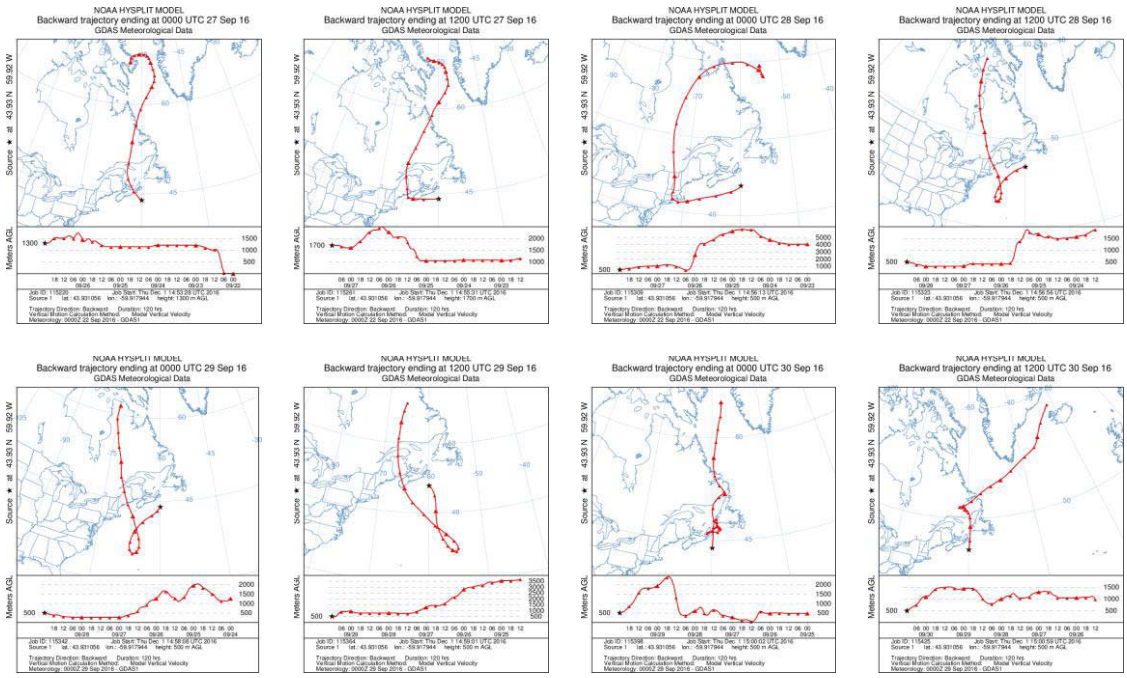

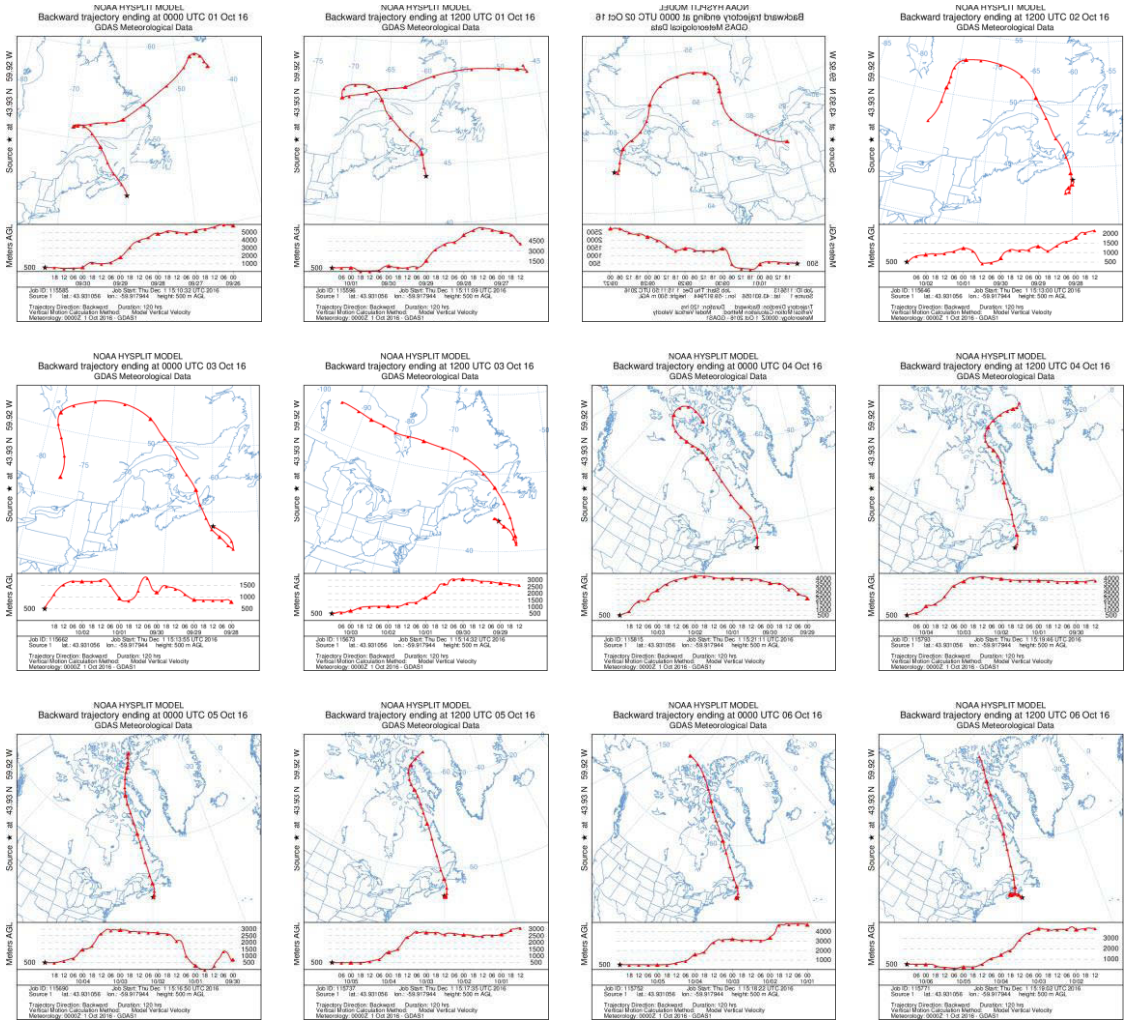


**September 27th – October 6th, 2016**

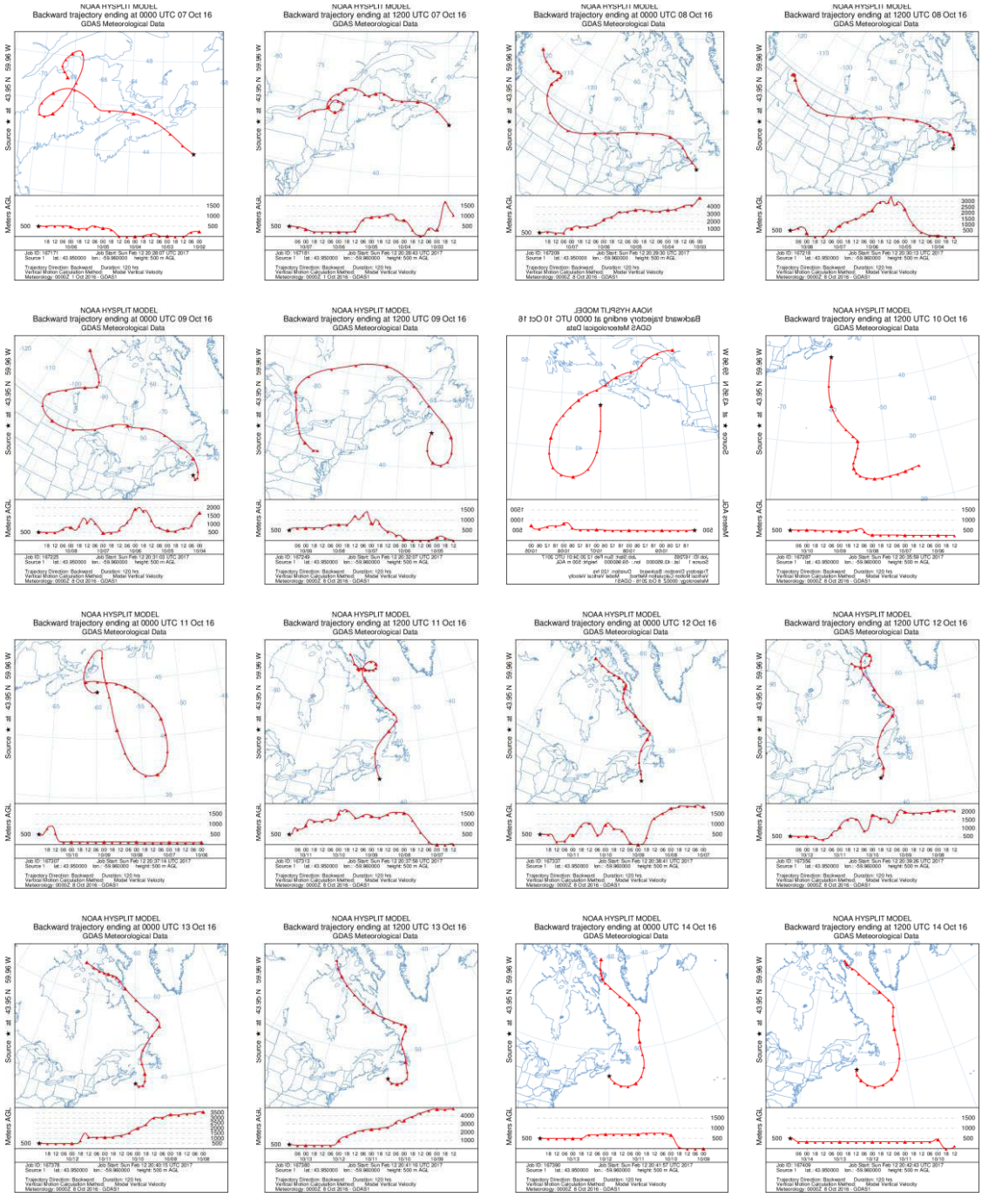
NOAA HYSPLIT MODEL
Backward trajectory ending at 0000 UTC 07 Oct 16
GDAS Meteorological Data
NOAA HYSPLIT MODEL
Backward trajectory ending at 1200 UTC 07 Oct 16
GDAS Meteorological Data
NOAA HYSPLIT MODEL
Backward trajectory ending at 0000 UTC 08 Oct 16
GDAS Meteorological Data
NOAA HYSPLIT MODEL
Backward trajectory ending at 1200 UTC 08 Oct 16
GDAS Meteorological Data
NOAA HYSPLIT MODEL
Backward trajectory ending at 0000 UTC 09 Oct 16
GDAS Meteorological Data
NOAA HYSPLIT MODEL
Backward trajectory ending at 1200 UTC 09 Oct 16
GDAS Meteorological Data
NOAA HYSPLIT MODEL
Backward trajectory ending at 0000 UTC 10 Oct 16
GDAS Meteorological Data
NOAA HYSPLIT MODEL
Backward trajectory ending at 1200 UTC 10 Oct 16
GDAS Meteorological Data
NOAA HYSPLIT MODEL
Backward trajectory ending at 0000 UTC 11 Oct 16
GDAS Meteorological Data
NOAA HYSPLIT MODEL
Backward trajectory ending at 1200 UTC 11 Oct 16
GDAS Meteorological Data
NOAA HYSPLIT MODEL
Backward trajectory ending at 0000 UTC 12 Oct 16
GDAS Meteorological Data
NOAA HYSPLIT MODEL
Backward trajectory ending at 1200 UTC 12 Oct 16
GDAS Meteorological Data
NOAA HYSPLIT MODEL
Backward trajectory ending at 0000 UTC 13 Oct 16
GDAS Meteorological Data
NOAA HYSPLIT MODEL
Backward trajectory ending at 1200 UTC 13 Oct 16
GDAS Meteorological Data
NOAA HYSPLIT MODEL
Backward trajectory ending at 0000 UTC 14 Oct 16
GDAS Meteorological Data
NOAA HYSPLIT MODEL
Backward trajectory ending at 1200 UTC 14 Oct 16
GDAS Meteorological Data

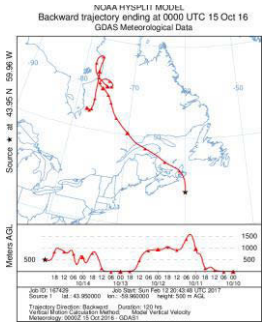


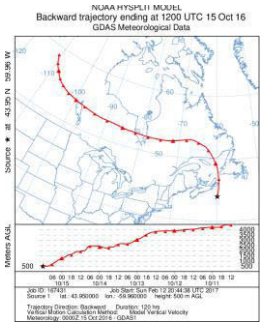


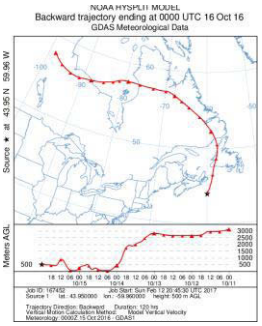


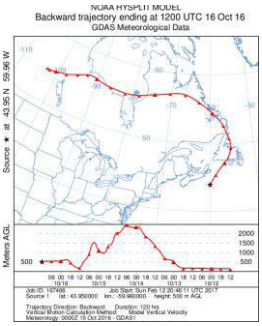


## October 7th – 16th, 2016

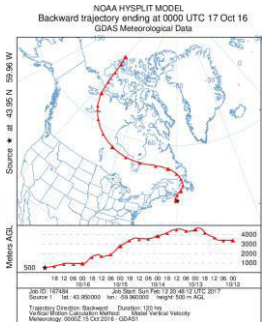


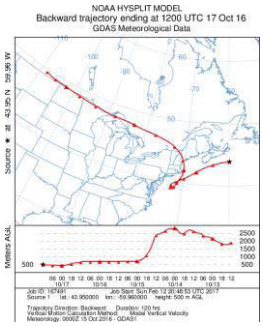


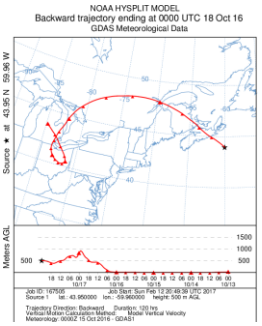


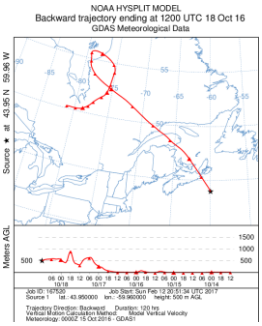


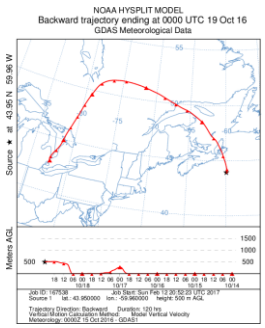


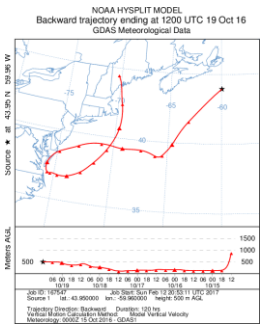


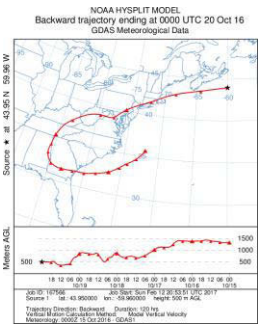


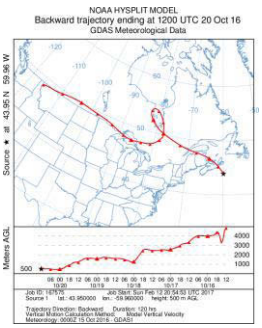


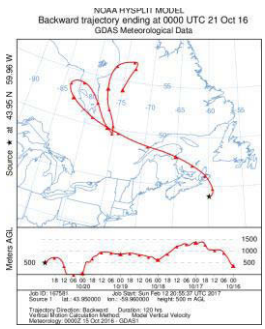


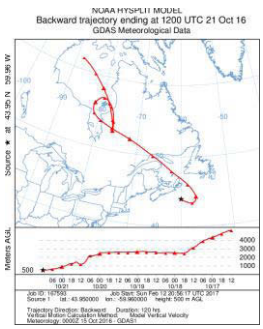


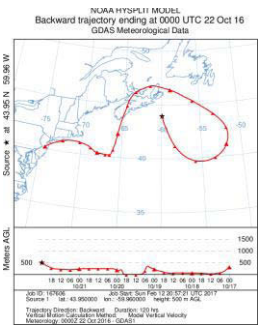


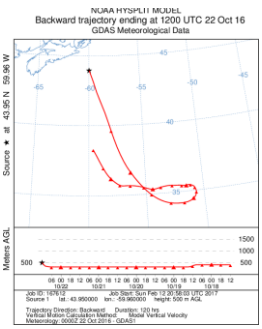

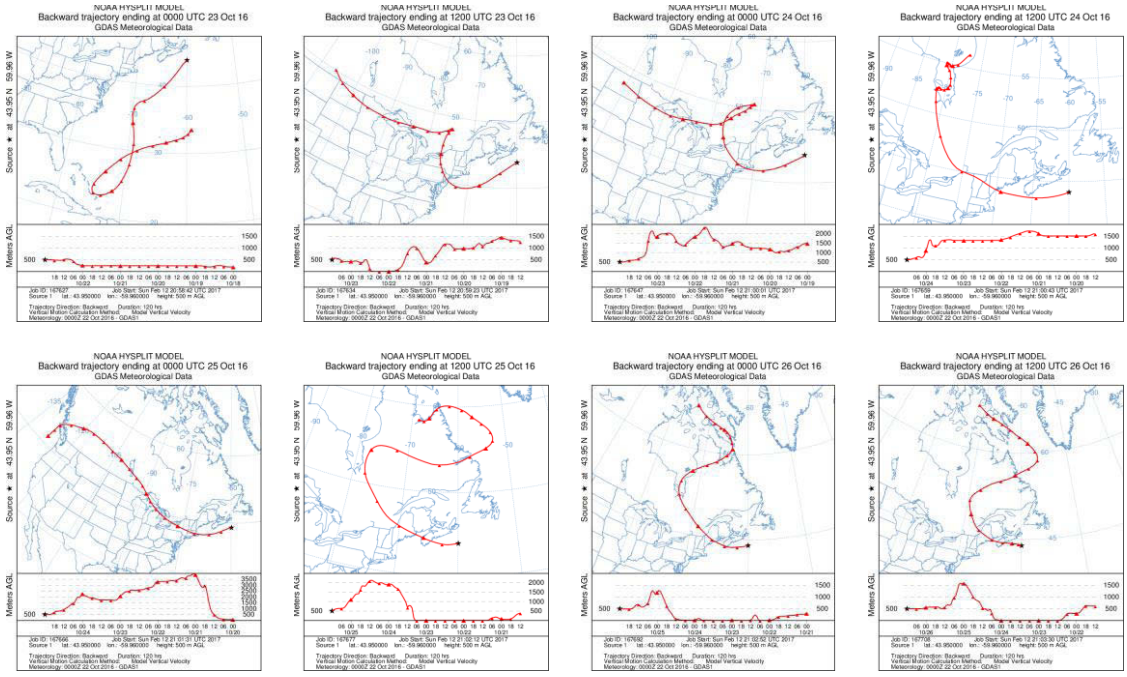


## October 17th – 26th, 2016

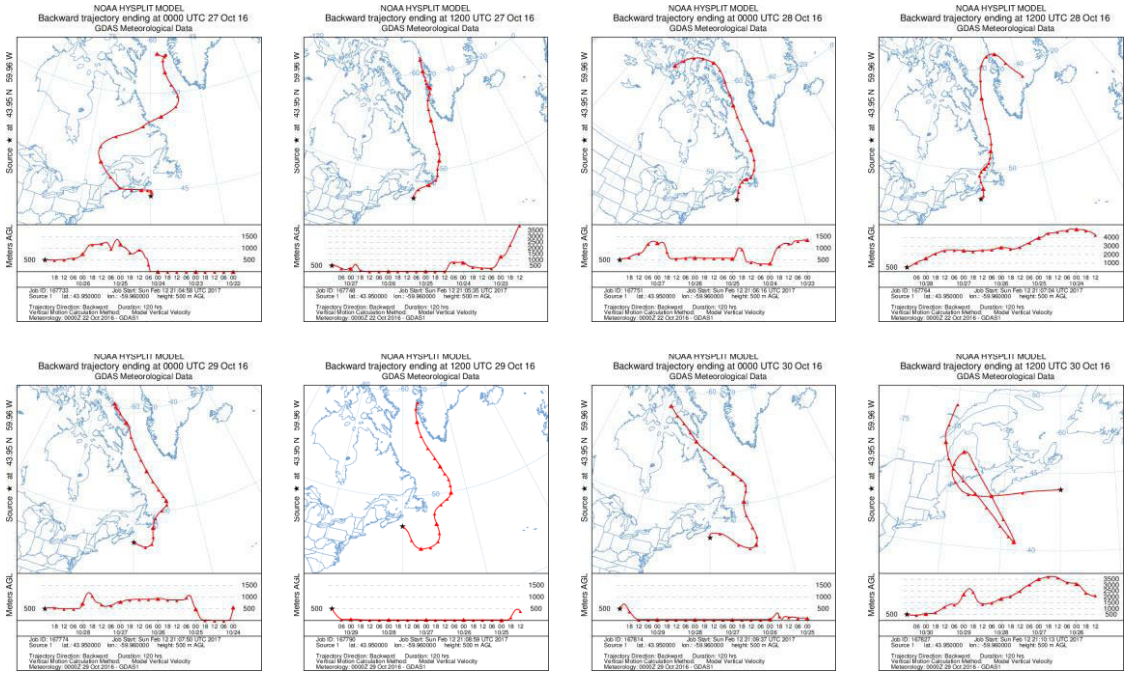

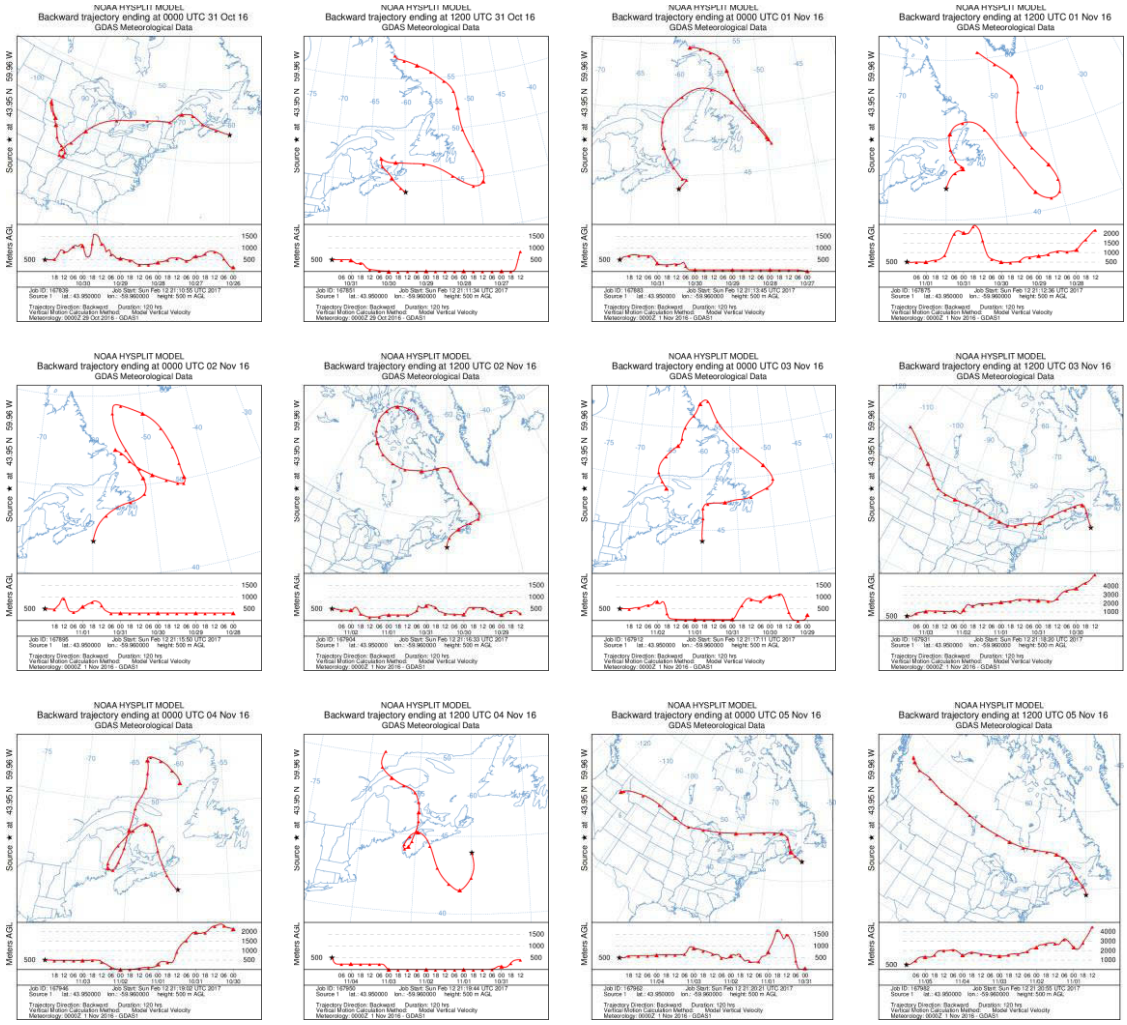


## October 27th – November 5th, 2016

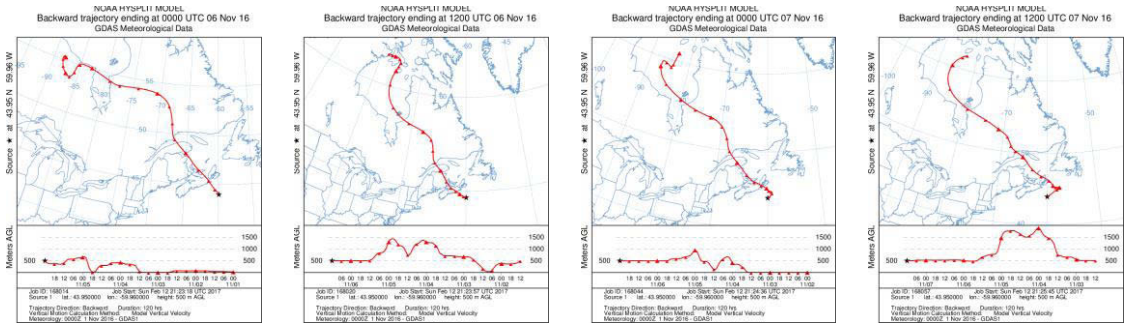

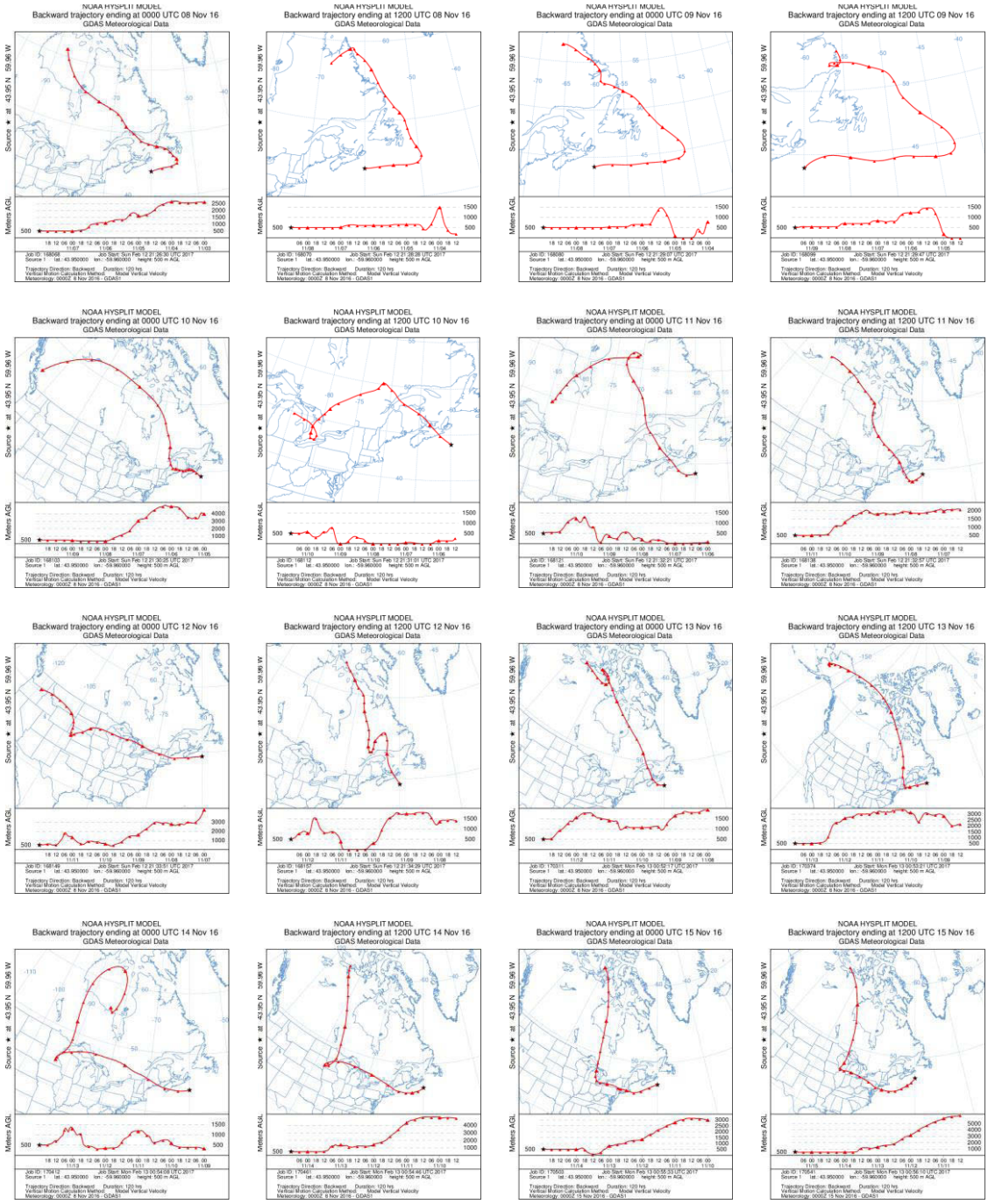


**November 6th – 15th, 2016**

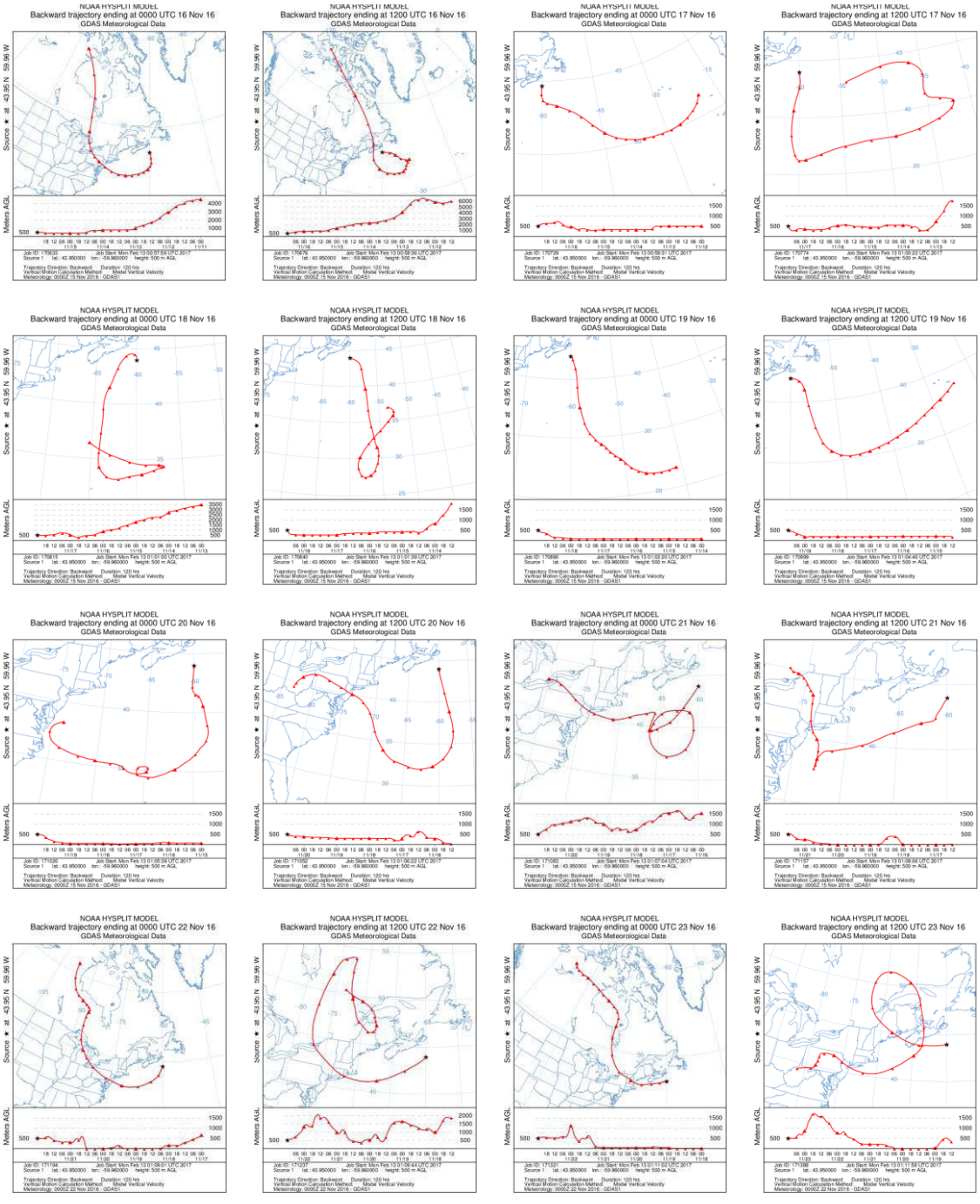
NOAA HYSPLIT MODEL
Backward trajectory ending at 0000 UTC 16 Nov 16
GDAS Meteorological Data
NOAA HYSPLIT MODEL
Backward trajectory ending at 1200 UTC 16 Nov 16
GDAS Meteorological Data
NOAA HYSPLIT MODEL
Backward trajectory ending at 0000 UTC 17 Nov 16
GDAS Meteorological Data
NOAA HYSPLIT MODEL
Backward trajectory ending at 1200 UTC 17 Nov 16
GDAS Meteorological Data
NOAA HYSPLIT MODEL
Backward trajectory ending at 0000 UTC 18 Nov 16
GDAS Meteorological Data
NOAA HYSPLIT MODEL
Backward trajectory ending at 1200 UTC 18 Nov 16
GDAS Meteorological Data
NOAA HYSPLIT MODEL
Backward trajectory ending at 0000 UTC 19 Nov 16
GDAS Meteorological Data
NOAA HYSPLIT MODEL
Backward trajectory ending at 1200 UTC 19 Nov 16
GDAS Meteorological Data
NOAA HYSPLIT MODEL
Backward trajectory ending at 0000 UTC 20 Nov 16
GDAS Meteorological Data
NOAA HYSPLIT MODEL
Backward trajectory ending at 1200 UTC 20 Nov 16
GDAS Meteorological Data
NOAA HYSPLIT MODEL
Backward trajectory ending at 0000 UTC 21 Nov 16
GDAS Meteorological Data
NOAA HYSPLIT MODEL
Backward trajectory ending at 1200 UTC 21 Nov 16
GDAS Meteorological Data
NOAA HYSPLIT MODEL
Backward trajectory ending at 0000 UTC 22 Nov 16
GDAS Meteorological Data
NOAA HYSPLIT MODEL
Backward trajectory ending at 1200 UTC 22 Nov 16
GDAS Meteorological Data
NOAA HYSPLIT MODEL
Backward trajectory ending at 0000 UTC 23 Nov 16
GDAS Meteorological Data
NOAA HYSPLIT MODEL
Backward trajectory ending at 1200 UTC 23 Nov 16
GDAS Meteorological Data
Source ★ at 43.95 N 59.96 W
Meters AGL

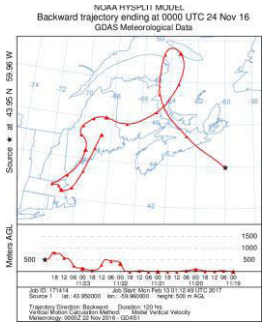

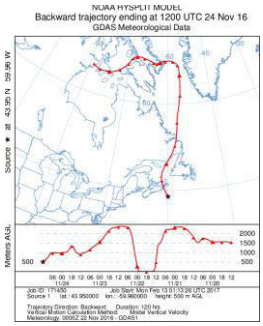

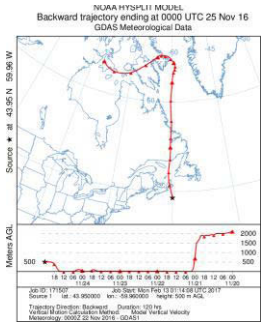

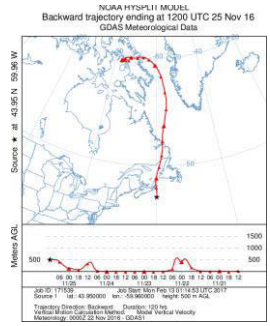


## November 16th – 25th, 2016

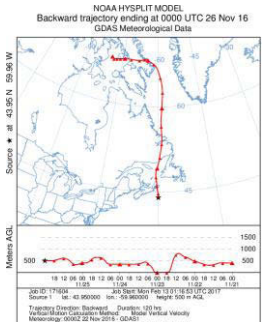

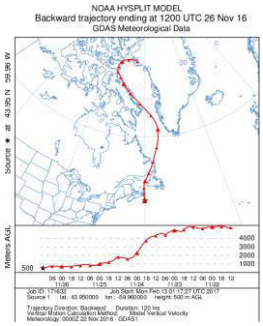

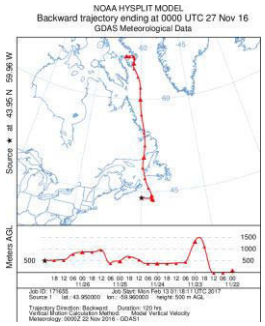

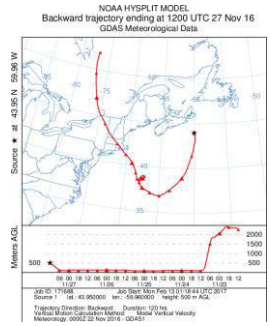

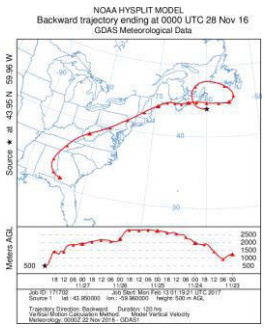

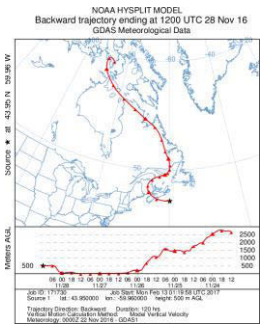

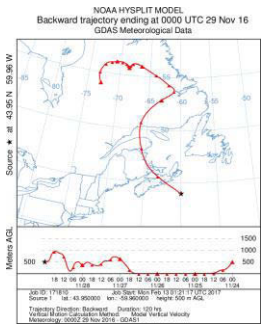

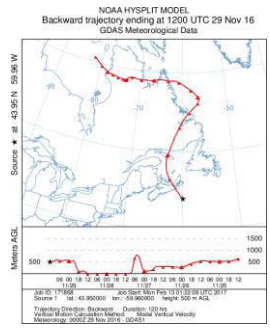

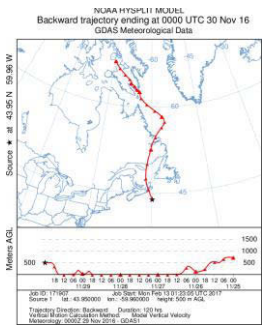

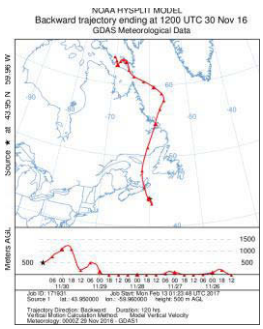

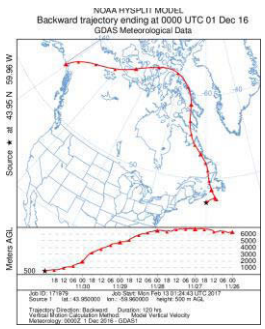

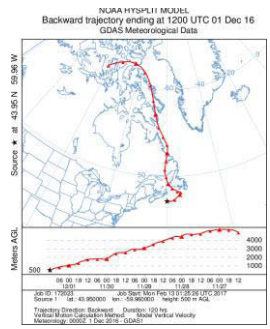

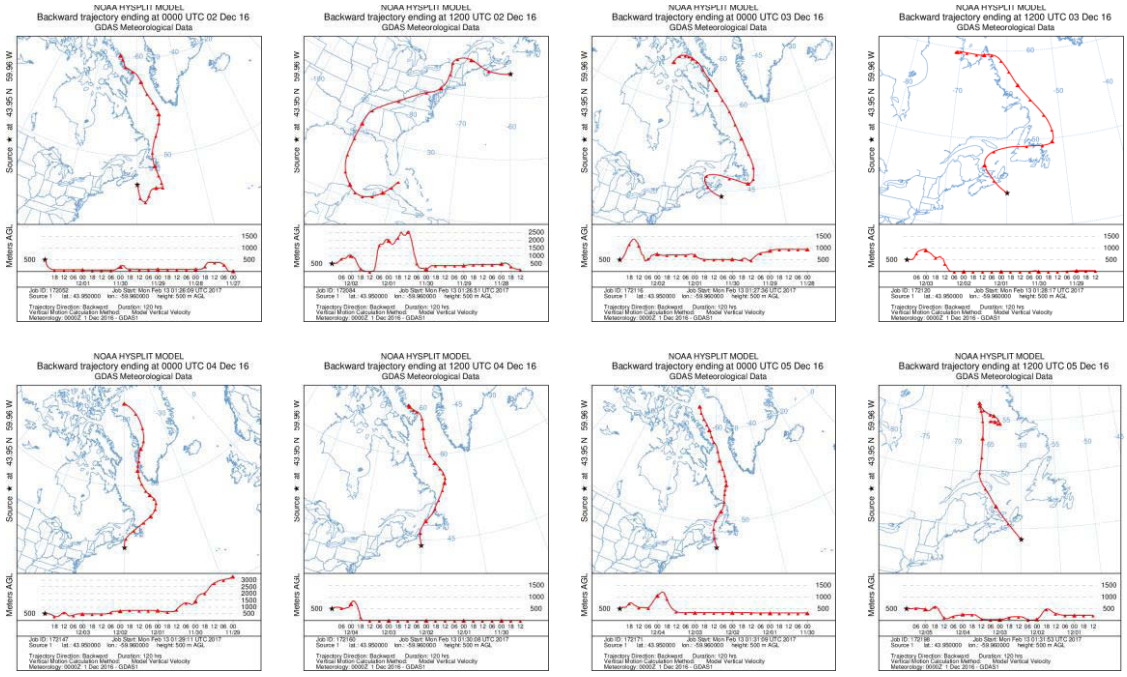


## November 26th – December 5th, 2016

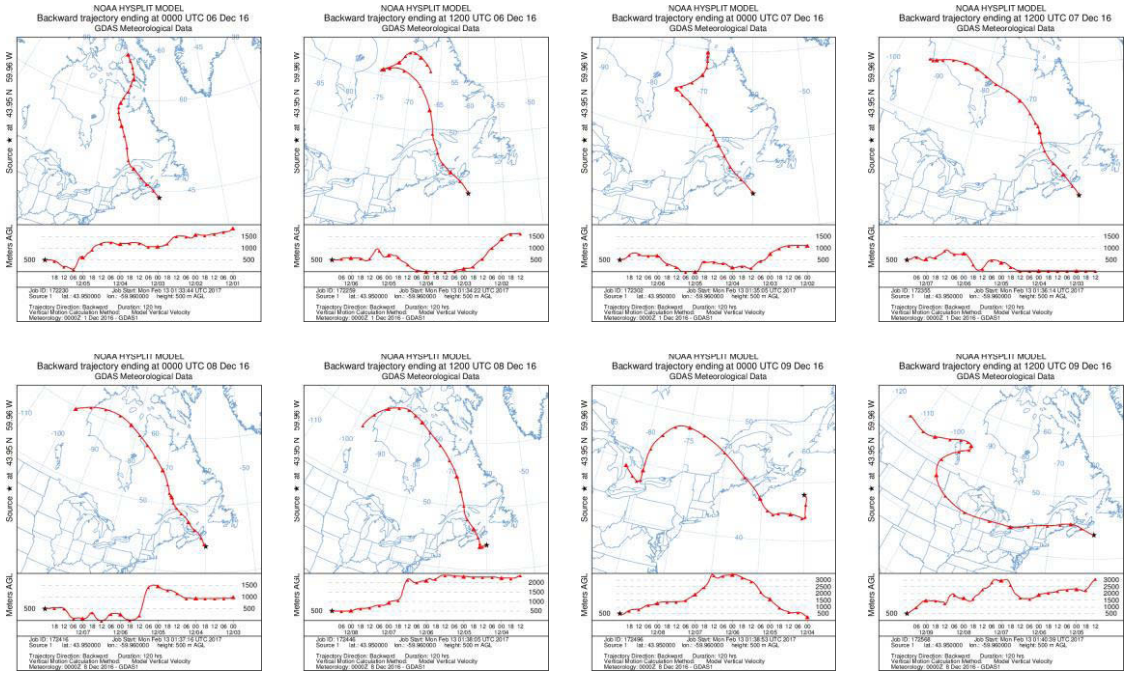

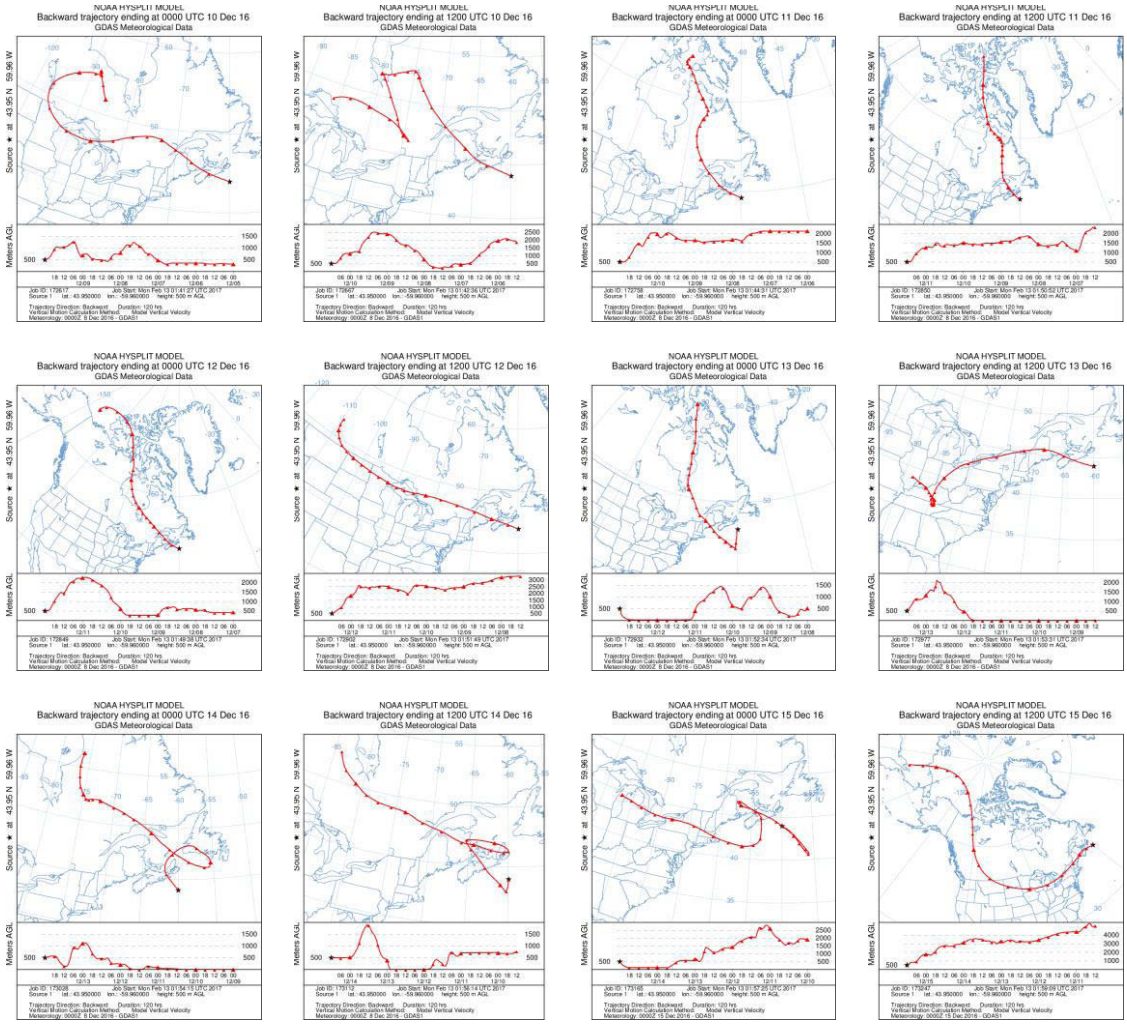


## December 6th – 15th, 2016

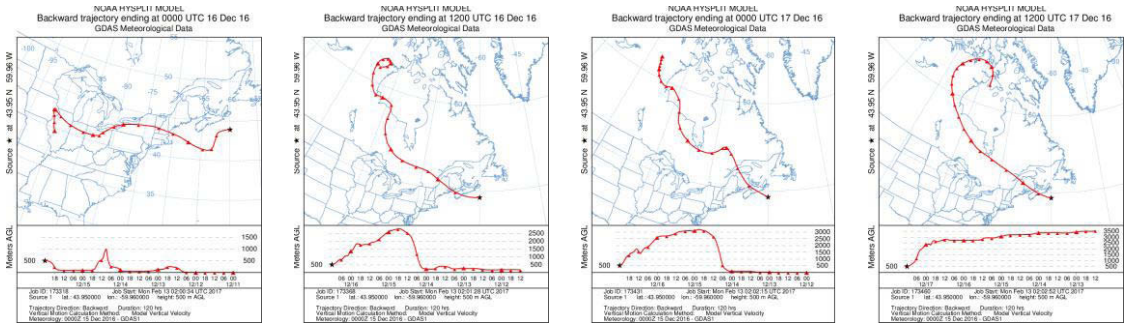

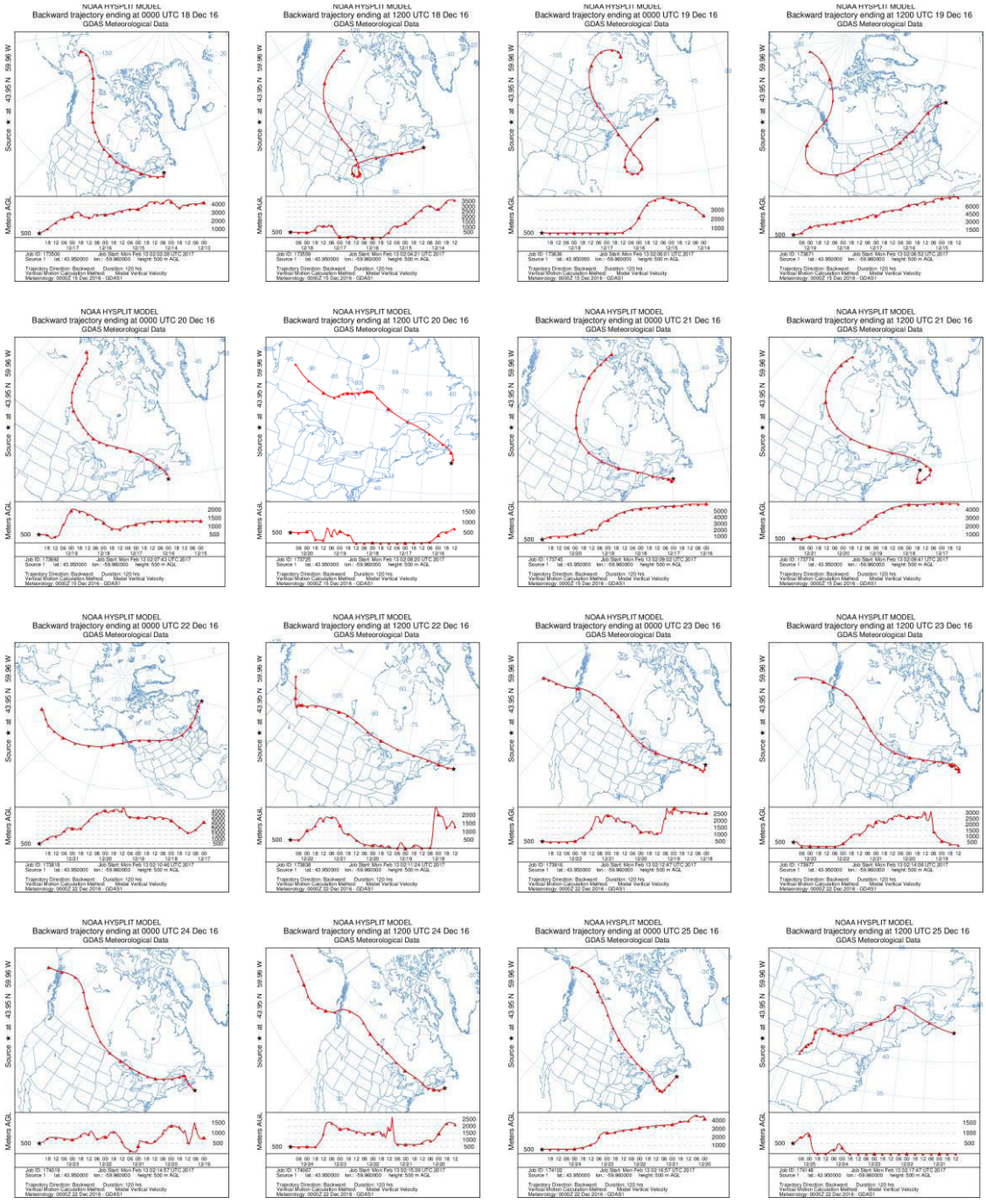


**December 16th – 25th, 2016**

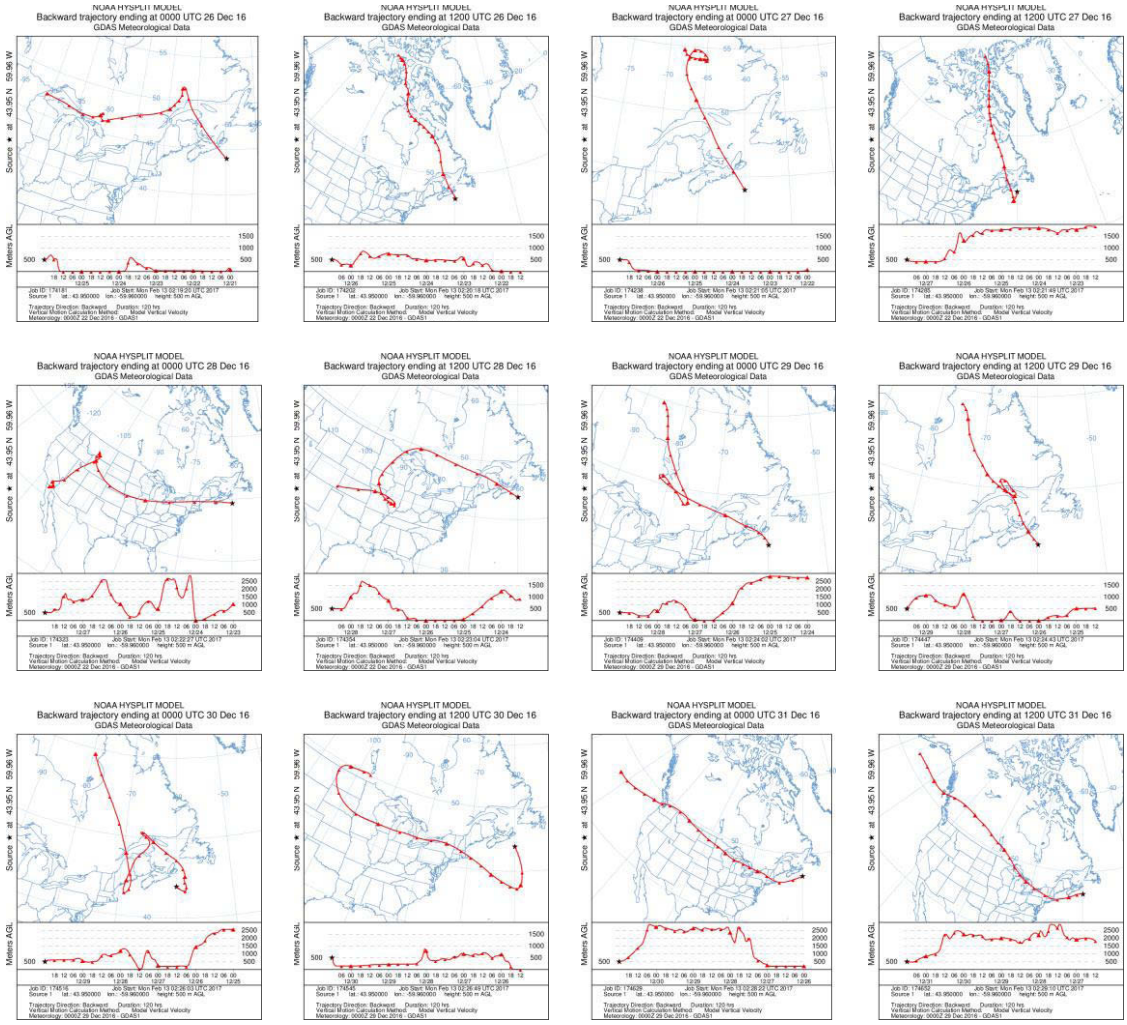


**December 26th – 31st, 2016**